Title

Controlled Assembly of Endohedrally-Functionalized Metal-Ligand Supramolecular Complexes

Permalink

https://escholarship.org/uc/item/2r5514mh

Author

Johnson, Amber

Publication Date

2014

UNIVERSITY OF CALIFORNIA
RIVERSIDE

Controlled Assembly of Endohedrally-Functionalized Metal-Ligand Supramolecular Complexes

A Dissertation submitted in partial satisfaction
of the requirements for the degree of

Doctor of Philosophy

in

Chemistry

by

Amber Marie Johnson

August 2014

Dissertation Committee:
    Dr. Richard J. Hooley, Chairperson
    Dr. Catharine Larsen
    Dr. Thomas Morton

The Dissertation of Amber Marie Johnson is approved:

Committee Chairperson

University of California, Riverside

Acknowledgements

I would like to start by thanking my advisor, Professor Richard J. Hooley. His guidance and encouragement has helped increase my confidence in myself and my chemistry. I had no idea what to expect when accepting a summer research offer, but I have enjoyed my research from that very first summer and know that I made a good decision in coming to UCR. Thanks for being available to discuss chemistry and look at endless NMR spectra, particularly for helping me see the big picture when I was caught up in minute details or experimental inconsistencies.

Graduate school has been a great experience and I would like to thank the members of the Hooley group, past and present, for making the lab an enjoyable place to work. I would also like to thank the members of the Morton and Larsen labs for keeping things in our hallway interesting. I would particularly like to thank Dr. Mike Young for his friendship and support throughout graduate school. I would not have been nearly as successful without your encouragement to work harder and the feeling of competition that comes with being in the same year.

I would like to finish by thanking my family for being supportive of my education and always believing in me. Your encouragement has meant a lot to me. I would also like to include a special thanks to Dr. Gaël Ung for helping me enjoy life outside of the lab.

The text of this dissertation, in part or in full, is a reprint of the material as it appears in *Chem. Commun.* **2010**, *46*, 4932-4934, *Inorg. Chem.* **2011**, *50*, 4671-4673, *Inorg. Chem.* **2011**, *50*, 9430-9442, *Dalton Trans.* **2013**, *42*, 8394-8401, and *J. Am. Chem. Soc.* **2013**, *135*, 17723-17726. The co-author Richard J. Hooley listed in these publications directed and supervised the research which forms the basis for this dissertation. All other co-authors listed in these publications contributed technical expertise.

Chem. Commun. **2010**, *46*, 4932-4934—Reproduced by permission of The Royal Society of Chemistry. Adapted with permission from *Inorg. Chem.* **2011**, *50*, 4671-4673. Copyright 2011 American Chemical Society. Adapted with permission from *Inorg. Chem.* **2011**, *50*, 9430-9442. Copyright 2011 American Chemical Society. *Dalton Trans.* **2013**, *42*, 8394-8401—Reproduced by permission of The Royal Society of Chemistry. Adapted with permission from *J. Am. Chem. Soc.* **2013**, *135*, 17723-17726. Copyright 2013 American Chemical Society.

Dedication

In memory of my grandparents, George and Patricia Johnson, for helping cultivate and encourage my lifelong love of learning.

ABSTRACT OF THE DISSERTATION

Controlled Assembly of Endohedrally-Functionalized Metal-Ligand Supramolecular Complexes

by

Amber Marie Johnson

Doctor of Philosophy, Graduate Program in Chemistry
University of California, Riverside, August 2014
Dr. Richard J. Hooley, Chairperson

An area of supramolecular chemistry that has recently been growing in popularity is the synthesis of metal-ligand cages. These are most commonly comprised of organic ligands and transition metal ions. Cage complexes often take the form of geometric polyhedra such as tetrahedra and octahedra, where the ligands act as the edges or faces and the metals serve as the vertices. Because these complexes have a polyhedral design, there is a central cavity in the cage, and this has been exploited for guest binding. Many types of guests have been bound inside supramolecular cage complexes, and binding is dependent on the environment inside the cage. Encapsulated guests can also react, either with themselves or with a coencapsulated guest.

Host-guest chemistry is often inspired by the selectivity of enzymes for their substrates, and the development of biomimetic systems is one of the goals for these assemblies. While encapsulation has been effective for promoting reactions and accessing novel reactivity, reactions are limited to those that require no additional reagents such as cycloadditions. No functional groups are present to direct reactivity, and reactivity is promoted by an increased effective concentration of guest molecules in the confined interior of a host. Introducing functional groups to cages can mimic the side chains of amino acids that are present in enzyme active sites, and this strategy can lead to more specialized, truly biomimetic reactivity.

This work presents a series of supramolecular cage complexes with varied geometries and assembly properties. Endohedral functionality could be introduced to a series of palladium-pyridine “paddle-wheel” complexes, and functional groups were able to influence assembly. Bidentate hydroxamic acid ligands were shown to complex bismuth and praseodymium, and attempts toward endohedrally-functionalizing these assemblies are discussed. Variable assembly was observed in complexes with 9-coordinate bismuth, and assembly was primarily dependent on metal concentration. Lanthanide complexes were also synthesized, and cooperative, thermodynamic control of selectivity between metal ions was observed. Fluorene-based ligands were combined with lanthanide ions, and complexes differing only in endohedral functionality narcissistically self-sorted despite identical ligand geometry and metal coordinating motif.

Table of Contents

Chapter One: Background

Chapter Two: Self-Sorting in Aniline-Functionalized Paddle-Wheel Complexes

Chapter Three: Bidentate Hydroxamic Acid Ligands and Synthesis of Functionalized Ligand Cores

Chapter Four: Tridentate Indazole Ligands

Chapter Five: Variable Assembly in Bismuth Complexes

Chapter Six: Cooperative Thermodynamic Control of Selectivity in the Self-Assembly of Rare Earth Metal-Ligand Helices

Chapter Seven: Narcissistic Self-Sorting in Fluorene-Based Lanthanide Assemblies

Chapter Eight: Experimental

List of Figures

Chapter One: Background

Chapter Two: Self-Sorting in Aniline-Functionalized Paddle-Wheel Complexes

Chapter Three: Bidentate Hydroxamic Acid Ligands and Synthesis of Functionalized Ligand Cores

Chapter Four: Tridentate Indazole Ligands

Chapter Five: Variable Assembly in Bismuth Complexes

Chapter Six: Cooperative Thermodynamic Control of Selectivity in the Self-Assembly of Rare Earth Metal-Ligand Helices

Chapter Seven: Narcissistic Self-Sorting in Fluorene-Based Lanthanide Assemblies

Chapter Eight: Experimental

List of Tables

Chapter Six: Cooperative Thermodynamic Control of Selectivity in the Self-Assembly of Rare Earth Metal-Ligand Helices

Chapter Eight: Experimental

Chapter One: Background

1.1 Rational Design of Metal-Ligand Supramolecular Cage Complexes

An area of supramolecular chemistry that has recently been growing in popularity is the synthesis of metal-ligand cages. These are commonly composed of organic ligands and transition metal ions. Cage complexes often take the form of geometric polyhedra such as tetrahedra and octahedra, where the ligands act as the edges or faces and the metals serve as the vertices. There are many reviews on the rational design of these complexes,[1] and a complex with a desired geometry can be synthesized by combining a metal and ligand with complementary geometry. Figure 1.1 shows the design of two well-known supramolecular cages.

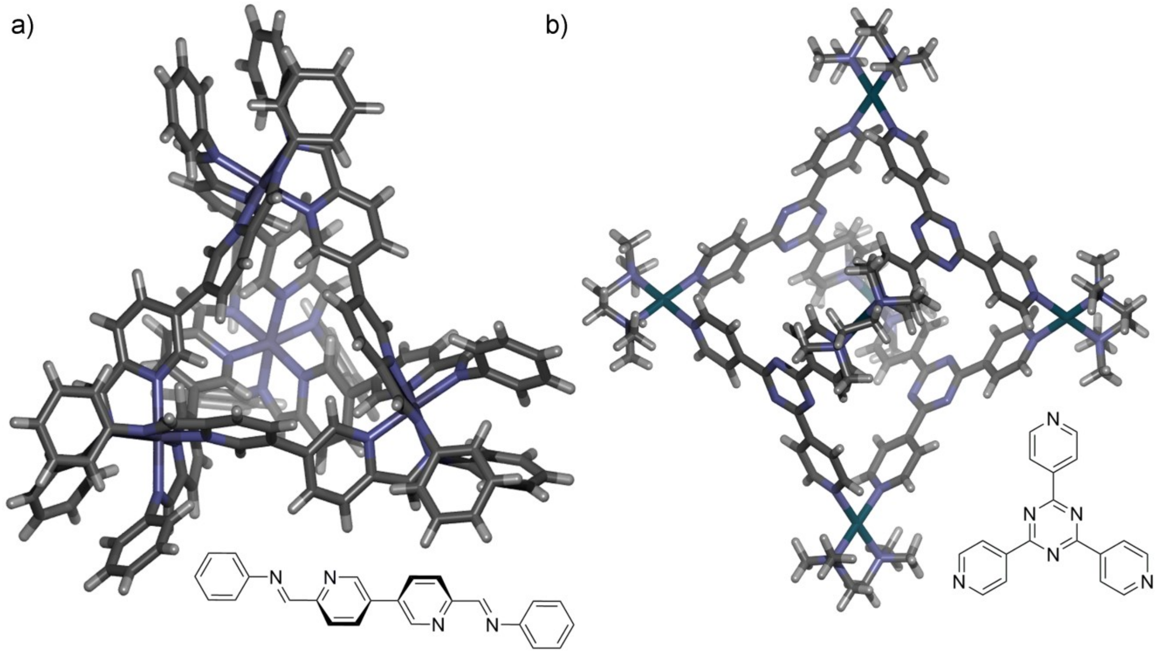

Figure 1.1: Self-assembled supramolecular cages: a) M_4L_6 tetrahedron; b) M_6L_4 octahedron.

The first, by the Nitschke group, combines bis-bidentate iminopyridine ligands and octahedral Fe^{2+} to form a M_4L_6 tetrahedron.[2] Three ligands coordinate each metal ion and form a corner of the tetrahedron. Two coordination sites on each ligand allow for connection to a neighboring corner and construction of the supramolecular architecture. The second example is an M_6L_4 octahedron synthesized by the Fujita group.[3] The ligands in this example act as the faces rather than the edges of the polyhedron, and *tris*-monodentate pyridine ligands coordinate square planar Pd^{2+}. In contrast to the previous example, only two of the four sites of palladium are occupied by the structural ligand. The other two sites are occupied by an ethylenediamine ligand that prevents additional ligands, which do not contribute to the geometry of the complex, from coordinating.

To design complexes with a specific geometry, as shown in the previous examples, ligands and metal ions must possess certain qualities. Directional coordination is important, so the most commonly used metals are transition metal ions with known coordination geometries, such as square planar Pd^{2+} and octahedral Fe^{2+}. Coordinative saturation increases the stability of metal ions, so all coordination sites must be occupied by structural ligands or blocking ligands to prevent coordination polymers or oligomers from forming. Nondiscrete assemblies form when coordination conditions are not carefully controlled. Ligands must be rigid to take advantage of directional coordination, and aromatic rings and alkynes are often used to confer this rigidity. Limited conformations of the coordinator are also important to ensure that the ligand coordinates in the desired direction. When ligands are flexible, multiple conformations are possible. This makes it more difficult for the ligand to match the geometry of the metal ion, and "mismatches" in coordination can lead to undesired coordination polymers. Flexible ligands can also compromise the structural integrity of a three-dimensional complex.

Complexes self-assemble from their constituent ligands and metals, and simply mixing the components is commonly all that is required for assembly. Metal-ligand interactions are often reversible, and this is advantageous to the assembly process. Components must be able to dissociate and reassociate to form a discrete complex from oligomers that may form upon the first coordination events. Entropy favors the formation of discrete complexes because multiple, smaller assemblies are produced.

1.2 Applications of Supramolecular Cage Complexes

Because these complexes have a polyhedral design with metals and ligands making up the edges/faces and vertices, there is a central cavity in the cage. This has been exploited for guest binding. Host-guest chemistry is often inspired by the selectivity of enzymes for their substrates, and the development of biomimetic systems is one of the goals for these assemblies.[4] Many types of guests have been bound inside supramolecular cage complexes including anions,[5] cations,[6] organic molecules,[7] organometallic complexes,[8] and reactive species.[9] Guest binding is dependent on the supramolecular environment inside the cage: anions bind inside cationic cages and cations bind inside anionic cages. The hydrophobic effect plays a role in the binding of organic molecules, and organic molecules can be shielded from an aqueous solvent by encapsulation within a complex.

In addition to simply being bound, guests can react, either with themselves or with a coencapsulated guest. One of the advantages of performing reactions inside cages is the potential for novel reactivity. A notable example is a Diels-Alder reaction with anthracene which proceeds at the terminal 1,4-position rather than the central 9,10-position (Figure 1.2).[10] This unusual regiochemistry occurs because of the conformations of the encapsulated guests. The anthracene and maleimide reactants are preorganized into a conformation that is favorable only for reaction at the 1,4-position. This cage also promoted Diels-Alder reactions of naphthalene and perylene, aromatics that are usually unreactive toward dienophiles.[11]

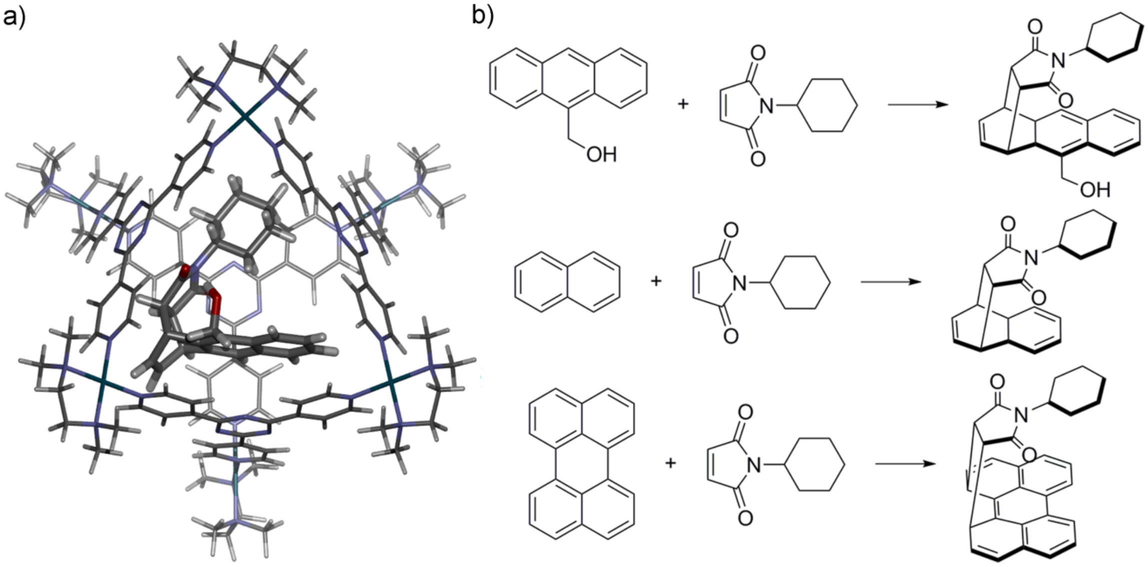

Figure 1.2: Diels-Alder reactions within an octahedral cage: a) Unusual reactivity of anthracene; b) Examples of Diels-Alder reactions promoted by octahedral cage.

Another example of reactivity inside a supramolecular cage is the catalysis of an aza-Cope rearrangement.[12] Cationic aza-Cope substrates are bound inside the anionic cage, and the molecule is forced into a reactive conformation upon encapsulation (Figure 1.3). This cage can be used as a catalyst because the product of the rearrangement is hydrolyzed to the aldehyde, which has a much lower affinity for the cage. When enantiopure cage is utilized, the reaction occurs asymmetrically, and an *ee* of 78% was observed.[13] This cage has also been used to accelerate a Nazarov cyclization,[14] and it can host organometallic reagents for the catalysis of organic reactions.[15]

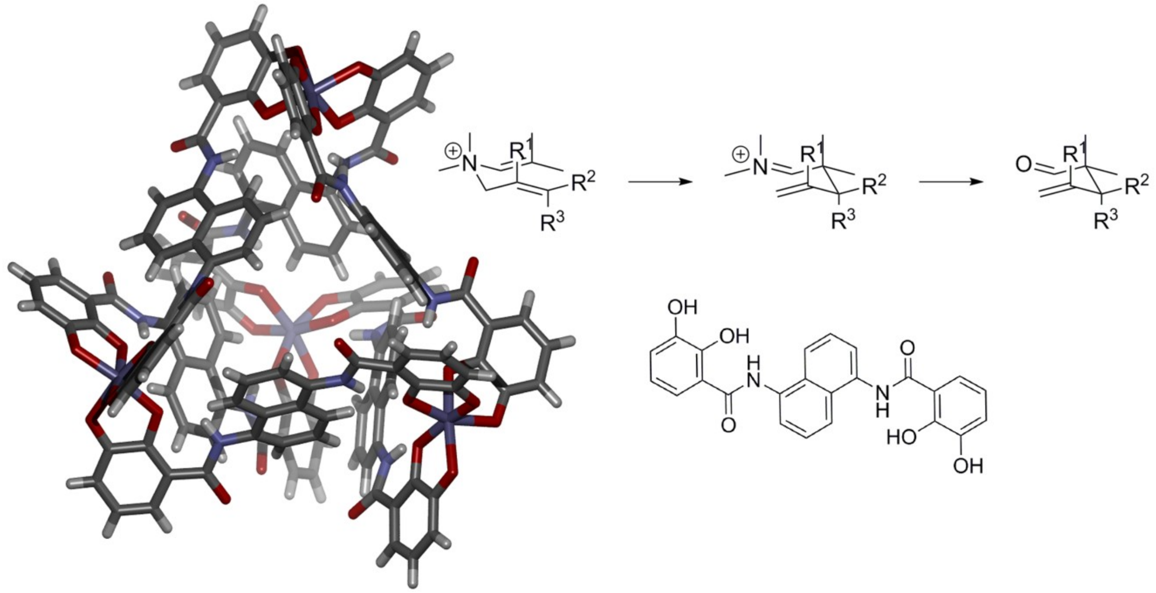

Figure 1.3: Catalysis of the aza-Cope rearrangement within a supramolecular cage.

1.3 Endohedral Functionalization of Cages

The inspiration for reactivity inside cages is often biology, particularly the highly selective reactivity of enzymes. The previously-described examples highlight the remarkable reactivity that can be performed upon supramolecular encapsulation, but these complexes lack truly biomimetic features. No functional groups are present to direct reactivity, and only differences in electron density differentiate one position from another. Reactivity is promoted by increased effective concentration of guest molecules in the confined interior of a host. The position of reactivity is directed by the conformation of the encapsulated guests and the proximity of their reactive sites. Reactions are limited to those with reagents that spontaneously react upon close contact, such as the previously-described cycloadditions. Reactions that require additional reagents, such as acids, are difficult to perform inside cages because external reagents may not be able to reach the bound reagents. Enzymes, on the other hand, promote reactivity through the use of amino acid sidechains in their active site, and this functionality is optimized for reactivity. For truly biomimetic reactivity, cages must be synthesized with defined functionality that is oriented to the interior of the cage.

When designing cages with endohedral functionality, additional design considerations are required beyond those of rational design. Many complexes have aromatic walls, and this approach is limited because the face of an aromatic ring cannot be functionalized. Most examples of cages with functionalized ligands avoid the “molecular paneling” approach, and the edges rather than the faces of aromatic rings are directed toward the interior of the complex. This approach allows for functionalization along the edges of the ring. Bent, “v-shaped” ligands are typically employed as they contain a central functional group or a site for covalent introduction of a functional group. This shape does not allow for rotation, which keeps the functional group static and pointed toward the interior of the cage. This core can then be derivatized with rigid spacers to tune the size of the final assembly, and metal coordinators can be added at the ends of the ligand. Another factor influencing ligand design is the compatibility of functional groups with the metal coordinator. Functional groups must not interfere with assembly, so potential coordinating groups must be introduced with caution. Weak metal-ligand interactions are less tolerant to reactive functional groups, so more inert groups must be incorporated.

While many different combinations of metals and ligands have been utilized to rationally design unfunctionalized cages, there has been much less variation in the synthesis of endohedrally-functionalized complexes. Two main coordination motifs have been explored, and these are relatively stable and simple to synthesize. The most common ligand is a monodentate pyridine, and this favors coordination to late transition metal ions such as Pd^{2+}, Pt^{2+}, or Hg^{2+}. Bidentate chelators such as iminopyridines or 2,2'-bipyridines have also been utilized, and these are often combined with Fe^{2+}, Ni^{2+}, or Cu^{+}. These coordinators are shown on the ligands in Figure 1.4 which provide complexes with small functional groups when assembled.

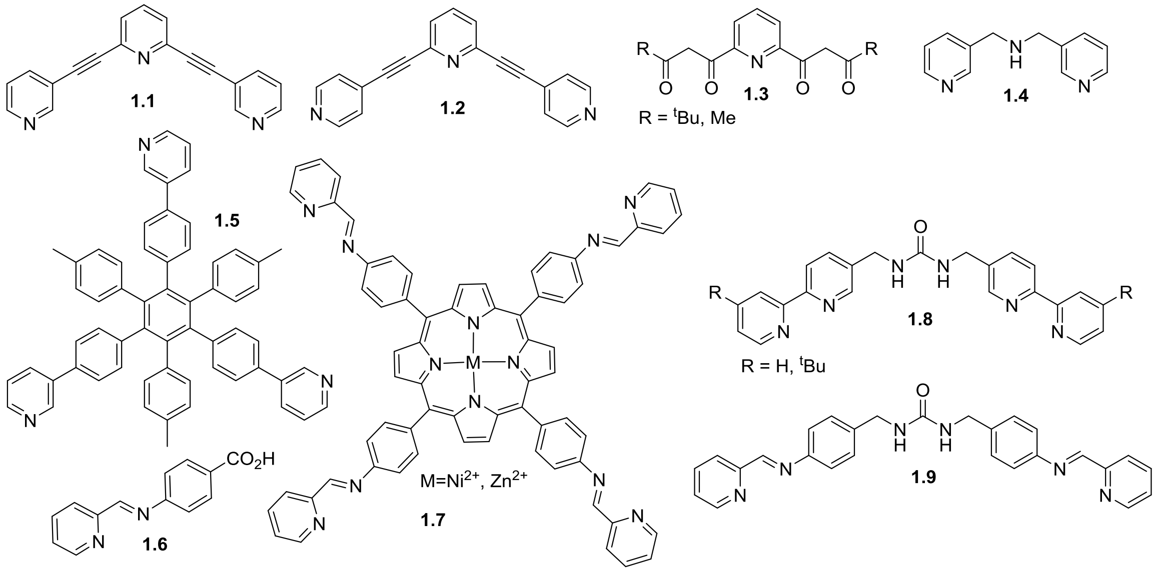

Figure 1.4: Ligands with small endohedral functional groups such as lone pairs, hydrogen bonds, and empty orbitals.

1.4 Cages with Endohedral Lone Pairs

Functional groups do not need to be large to provide functionality to complexes. The smallest groups that can be directed endohedrally include empty orbitals or coordination sites from a structural metal. Other small groups include acidic hydrogen atoms or hydrogen bond donors that can interact with electron rich guests. Lone pairs are useful for interacting with cationic or electron deficient guests.

Most cages displaying endohedral functionality have neutral nitrogen ligands that coordinate metal cations, which results in positively-charged complexes. This makes cation binding less common in the literature than anion binding, but it can be achieved with endohedral functionality. Endohedral pyridines can be introduced, and these have a lone pair of electrons that can interact with cationic guests. Complex (**1.1**)$_4$Pd$_2$ can encapsulate two molecules of cisplatin through hydrogen bonding with the endohedral pyridine.[16] No binding was observed in competitive hydrogen bonding solvents such as water or in the absence of the hydrogen bond accepting pyridine. The cisplatin guest could be released upon the addition of a competitive ligand for Pd^{2+} such as DMAP or chloride.

Ligand **1.2** orientates the structural pyridines *para* to the central ring for the formation of larger pyridine-palladium cages. The most commonly formed cages from this ligand are $M_{12}L_{24}$ "nanospheres" developed by the Fujita group.[17] Complex (**1.2**)$_{24}$Pd$_{12}$ has the lone pairs of all 24 pyridines pointing toward the center of the cage, and a silver ion is coordinated to each of the pyridines. Weakly coordinating nitromethane was required as a solvent for binding of the silver cations, and no binding was observed with competitively coordinating solvents such as DMSO or acetonitrile. Another example of cation binding is presented by ligand **1.3**.[18] A neutral (**1.3**)$_3$Fe$_2$ helix is formed which can coordinate potassium, strontium, and lanthanum cations through the nine coordination sites formed by the internal pyridine and inner carbonyls of the β-diketone coordinator.

1.5 Cages with Endohedral Coordination Sites

Endohedral coordination sites can be introduced two ways. Unoccupied orbitals from the structural metals can be directed toward the interior of the complex, or a second metal can be incorporated into the ligand. The second strategy is far more common than the first, as effective assembly usually requires coordinatively saturated metal centers.

An example by the Shionoya group uses Hg^{2+} as a structural metal in a M_6L_8 octahedron.[19] Only four of the six coordination sites are occupied by ligand **1.5**, and the axial sites are occupied by two triflate counterions (Figure 1.5a). The internal triflates can be selectively displaced by other sulfonate ligands such as tosylates, and a ditopic sulfonate ligand was designed to selectively bridge two of the mercury atoms. One or two equivalents of the ligand could be bound, and bridging opposing mercury centers was more favorable than bridging adjacent centers.

The Nitschke group has incorporated empty coordination sites through the use of two different metals in self assembly. Ligand **1.7** coordinates iron as a structural metal, but contains a porphyrin where a second metal can be added.[20] The $(\mathbf{1.7})_6Fe_8$ cubic cage encapsulates fullerenes or coronene, and favorable interactions are present when the porphyrin is metallated. A more exciting example utilized two different structural metals, which is extremely rare in solution-phase assemblies. A $(\mathbf{1.6})_{24}Fe_8Mo_{12}$ cube could be constructed by coordination of **1.6** to $Mo(CO)_6$ followed by combination with $Fe(OTf)_2$ and 2-formylpyridine.[21] Iron is at the corners of the cube, and molybdenum is in the center of the faces (Figure 1.5b). An empty coordination site from molybdenum is present which binds triflate counterions that are present during assembly. These are weakly coordinated and can be displaced by halides, with iodine being the most effective. Neutral molecules such as ammonia, trimethylamine, and trimethylphosphine could also be bound. The binding affinity of different guests could be explained by steric and electronic effects. After the negatively-charged triflates were displaced by a neutral molecule, iodide had a greater affinity for the more positively-charged cage. Negative steric interactions could be present between bound triflates and halides, and this was alleviated when a smaller neutral molecule was bound instead of another triflate.

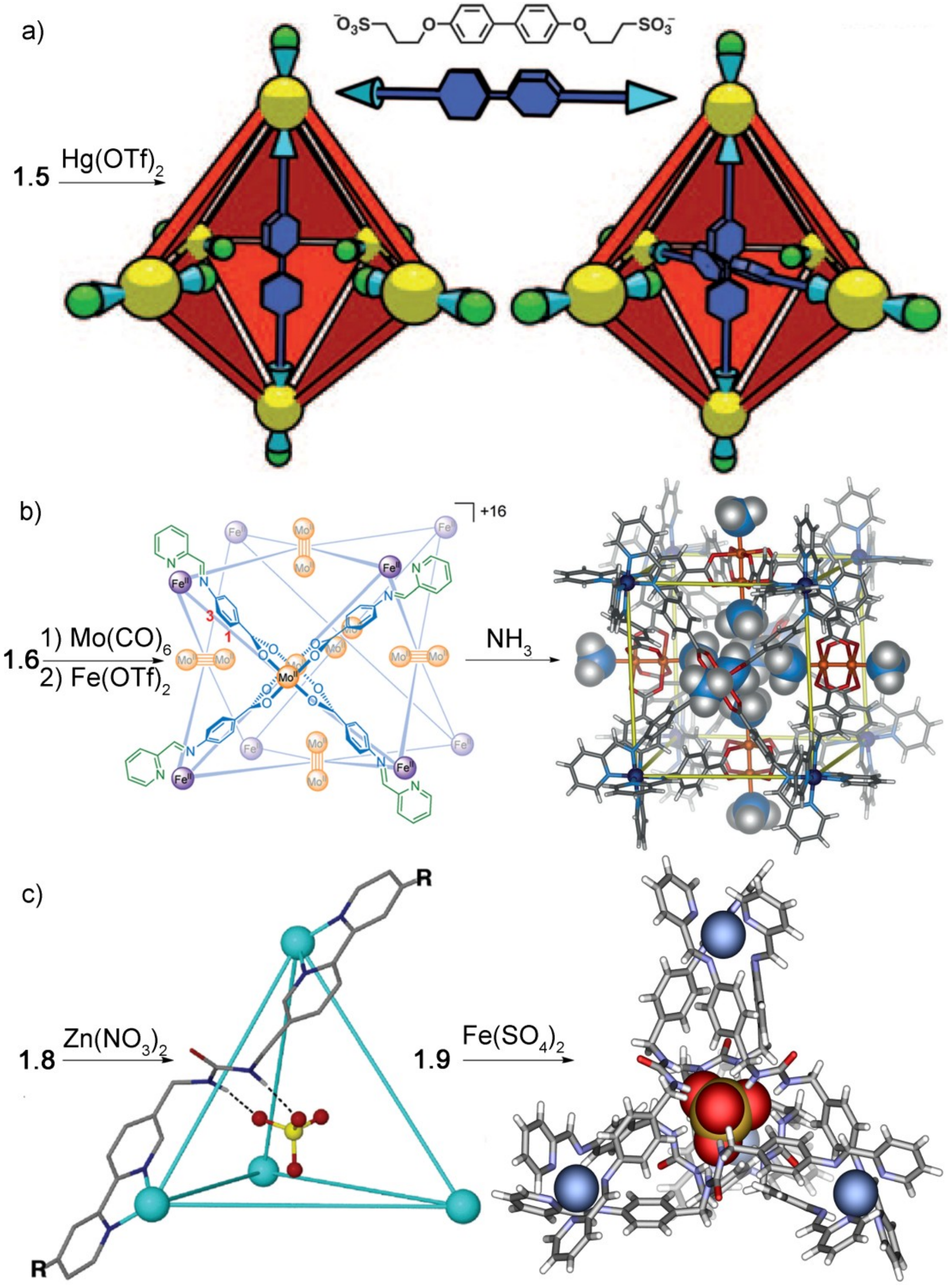

Figure 1.5: Guest binding in endohedraly-functionalized complexes: a) Octahedral $(\mathbf{1.5})_8\mathrm{Hg}_6$ binding one and two bis-sulfonate ligands; b) $(\mathbf{1.6})_{24}\mathrm{Fe}_8\mathrm{Mo}_{12}$ cube with bound ammonia; c) Sulfate-binding tetrahedra $(\mathbf{1.8})_6\mathrm{Zn}_4$ and $(\mathbf{1.9})_6\mathrm{Fe}_4$.

1.6 Cages with Endohedral Hydrogen Bonding Groups

Anions are common guests in cages, particulary cationic cages, due to size and charge complementarity. Anion selectivity can be an issue with larger cages, however, and endohedral functionality can assist in increasing in the affinity and selectivity of cages for anions. An example of this is the use of a urea-containing ligand to selectively encapsulate sulfate ions through directed hydrogen bonding. The Custelcean group used molecular modeling to assist in designing a tetrahedral ($\mathbf{1.8}$)$_6$Ni$_4$ complex.[22] The tetrahedral complex is complementary to the shape of the tetrahedral sulfate guest, and the urea hydrogen bond donor is pointed directly at the encapsulated sulfate anion (Figure 1.5c). Sulfate affinity was comparable to that of a sulfate-binding protein and was a result of both the charge of the cage and the presence of the hydrogen bonds. This work was extended to include cages with zinc and the tetrahedral oxoanions of sulfur, selenium, chromium, molybdenum, tungsten, and phosphorus.[23] A tetrahedral anion was required to template the tetrahedral cage, and a smaller ($\mathbf{1.8}$)$_3$Zn$_2$ helical complex was formed in the absence of templating guest. Anion exchange was observed via ^{77}Se NMR, and equilibrium constants between various anions and $^{77}SeO_4^{2-}$ were compared to give the order of binding strength as $PO_4^{3-} >> CrO_4^{2-} > SO_4^{2-} > SeO_4^{2-} > MoO_4^{2-} > WO_4^{2-}$. Binding strength was based on several factors such as the charge, size, and basicity of the guest.

A similar sulfate-binding tetrahedron was formed from **1.9** and Fe^{2+} or Ni^{2+}.[24] Sulfate was required as a template for assembly, and no cage formation was observed with other anions. The cage could be irreversibly disassembled to release the anion by addition of a competitively coordinating ligand such as tris(2-aminoethyl)amine. Reversible disassembly-reassembly was possible through reactivity of the imine coordinator upon treatment with acid or base. The cage could also be transferred to a nonaqueous solvent through counterion exchange. A ligand with a secondary amine rather than a urea for hydrogen bonding was also developed.[25] Ligand **1.4** assembled into a M_2L_4 cage with $Cu(NO_3)_2$, and a nitrate counterion was bound. The bound nitrate interacts with the cationic copper, and additional nitrates are bound in the space between ligands via hydrogen bonding with the nitrogen of the ligand which is protonated during assembly.

1.7 Cages with Inert, Space-Filling Functionality

As described in the previous sections, small groups can confer functionality on assemblies. These active groups, however, may not always be compatible with the overall assembly. By introducing nonreactive groups, the scope of internal functionalization can be expanded while retaining the potential applications of the cage. The Fujita group has introduced many functional groups to cages by utilizing the ligands in Figure 1.6. Functional groups could introduced by covalently modifying the central, phenol-containing aromatic ring. These ligands can be combined with Pd^{2+} to form large $M_{12}L_{24}$ or $M_{24}L_{48}$ cages.

Because these cages are cationic, they are water soluble. By introducing functional groups, different environments are found inside and outside of the cage. When alkyl chains of varying length were introduced (ligand **1.10a**), the hydrophobicity of the cage interior was altered.[26] Chains of nine, twelve, and eighteen carbons were introduced and nile red, a hydrophobic dye, was used to measure hydrophobicity. As the hydrophobicity inside the cage increased, so did the solubility of the dye. The choice of solvent also had an effect on guest binding. When the polarity of the solvent was reduced, binding affinity decreased because the dye was not as attracted to the nonpolar interior of the cage.

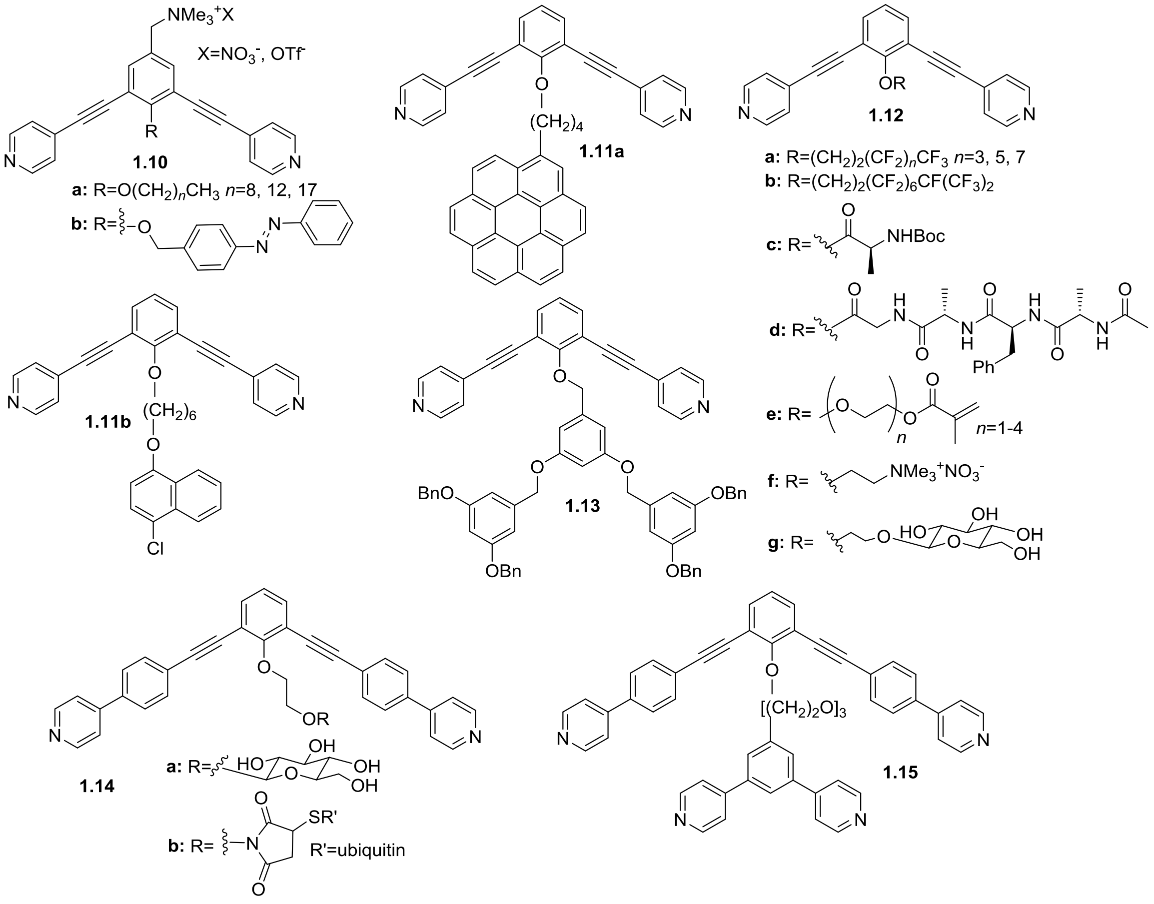

Figure 1.6: Functionalized ligands for the formation of $M_{12}L_{24}$ or $M_{24}L_{48}$ “nanoballs”.

Another example of internal hydrophobicity influencing guest binding is the introduction of coronene to a complex (ligand **1.11a**).[27] Incorporation of 24 coronene molecules created an aromatic “nanophase” which enhanced the binding of guests such as C_{60}. Other aromatic guests such as naphthalenediimide could be bound, but the aromatic environment was required for strong binding. Functionalization with chloronaphthalene (**1.11b**) resulted in a decrease in C_{60} binding, and no binding was observed in an unfunctionalized cage. When fluorinated alkyl chains were introduced, a fluorous "nanophase" could be created.[28] Chains of four, six, eight, and nine perfluorocarbons were introduced (ligand **1.12a**,**b**), and guest binding was dependent on chain length. Six perfluorooctane molecules could be bound in the cage with a six-carbon chain. Decreased binding was observed in cages with longer chains due to crowding within the cage, and shorter chains completely inhibited binding by not providing a suitable solubilizing environment.

Very large groups can be incorporated in cages as shown in an example with an inverse dendrimer.[29] Three sizes of dendrimer were incorporated and assembly was observed with all three. Ligand **1.13** depicts the middle-sized of the three. In comparison to traditional dendrimers, the "inverse dendrimer" inside the complex had increasing segment density toward the center of the cage with no density at the very center. A chiral environment could be created by the introduction of amino acids and peptides.[30] When ligands with the same chirality were assembled, an enhancement in the Cotton effect was observed for the complex over the free ligand. Multiple types of amino acids (**1.12c**) or peptides (**1.12d**) could be introduced, and up to 96 amino acid residues could be incorporated. The most complex group that has been introduced to a complex is the protein ubiquitin.[31] An N-substituted maleimide was introduced, which could be attached to a cysteine in ubiquitin (**1.14**). When combined with Pd^{2+} and 23 non-ubiquitin-containing ligands, the $M_{12}L_{24}$ cage assembled around the protein. Glucose-containing ligand **1.14b** was used to help crystallize the complex, as it filled more space and slowed the movement of the encapsulated protein. This is the most complex molecule encapsulated in a self-assembled cage to date, and the first encapsulated protein (Figure 1.7).

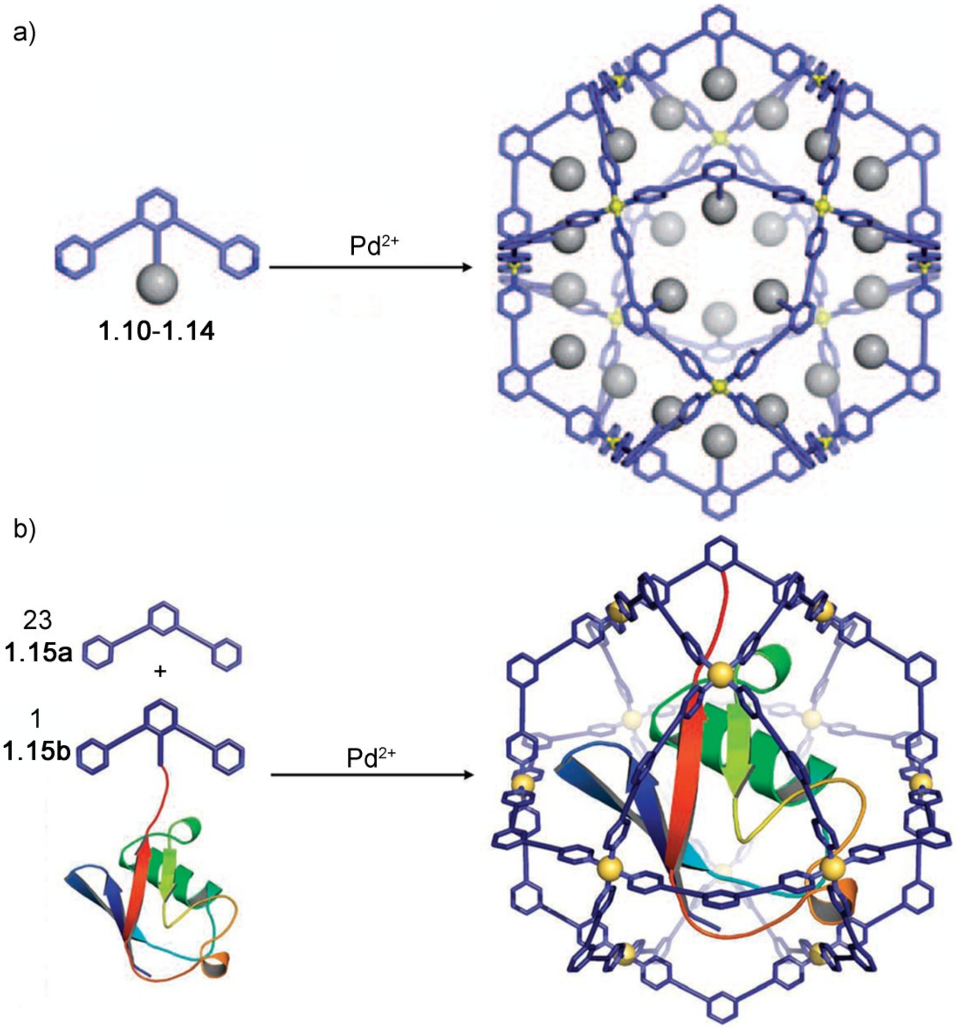

Figure 1.7: a) Assembly of endohedrally-functionalized $M_{12}L_{24}$ “nanoballs”; b) Encapsulation of ubiquitin.

More “active” functional groups can also be introduced into these types of cages. Guest binding could be controlled by the change in polarity associated with azobenzene isomerization.[32] Cage $(\mathbf{1.10b})_{24}Pd_{12}$ was assembled with the azobenzene in the favored *trans* isomer. Hydrophobic 1-pyrene-carboxaldehyde was bound, and binding affinity decreased when the cage was irradiated to switch to the more polar *cis* isomer. After thermal isomerization back to the *trans* isomer, stronger guest binding was again observed.

1.8 Self-Sorting and Stereocontrol through Endohedral Functionality

In addition to influencing guest binding, endohedral functionality can also be used to control the assembly process. Ligands with a dibenzosuberone core can form interpenetrated (**1.16a**)$_8$Pd$_4$ complexes which have been used in anion binding as shown in Figure 1.8. Suberone complex (**1.16a**)$_8$Pd$_4$ binds tetrafluoroborate anions and can serve as a template for the binding of other anions such as chloride.[33] When this ligand is derivatized with an aromatic ring (**1.16b**), the anion binding abilities of the complex change.[34] Steric crowding inside the complex prevents the formation of interpenetrated (**1.16b**)$_8$Pd$_4$ around a tetrafluoroborate anion, and the smaller, undimerized (**1.16b**)$_4$Pd$_2$ is formed instead. When assembly occurs around a smaller chloride anion, dimerization occurs, and the shape of the binding pocket changes to accommodate larger anions such as perrhenate (Figure 1.8b). The endohedral functionality also directed the stereochemistry of complex formation, and a single isomer of the cage was formed with all of the aromatic rings pointing in the same direction.

When octahedral metals are used instead of square planar metals, isomerism at the metal can be observed. Chiral groups on the exterior of the complex can control the stereochemistry,[35] as can endohedral groups. When functionalized linear ligands are used instead of the usual bent ligands, functional groups can be directed toward the inside or outside of the complex, because the functionality is no longer forced to be on the inside. In freely-rotating ligands, functionality can spend time inside and outside the complex as shown by (**1.17**)$_6$Fe$_4$ (Figure 1.8d). Ligand **1.17** contains chiral diols on a freely-rotating core, and the stereochemistry of these “arms” determines the stereochemistry of all metals in the complex. Only enantiomerically pure ΔΔΔΔ or ΛΛΛΛ were formed.[36] This tetrahedron could bind small hydrophobic guests, and the flexible alcohols could change the cavity size to adapt to the size of the guest.

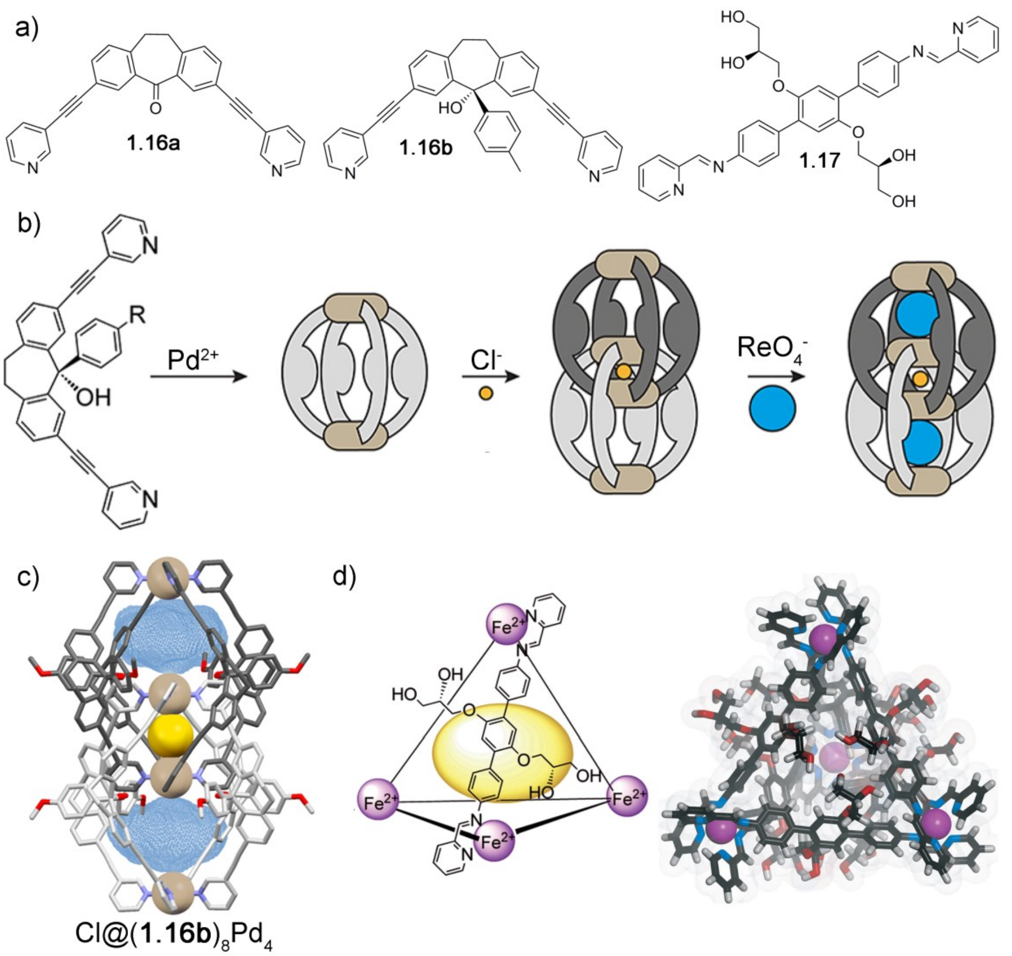

Figure 1.8: a) Ligands for control of self-sorting and stereocontrol in cages; b) Anion templation in interpenetrated cages; c) Interpenetrated cage ($\mathbf{1.16b}$)$_8$Pd$_4$ with bound chloride; d) Cartoon and model of ($\mathbf{1.17}$)$_6$Fe$_4$.

A very elegant example of endohedral functional controlling assembly is the formation of a “cage within a cage”.[37] Ligand **1.15** contains two different sized *bis*-

pyridine ligands connected by a triethyleneglycol linker. This allows for a smaller cage to assemble inside a larger cage (Figure 1.9a). The two connected ligands have the same coordination geometry and can assemble in identical stoichiometries with Pd^{2+}. Oligomers were formed upon initial addition of Pd^{2+}, but only the double cage is present after the correct stoichiometry for assembly is reached. Both cages are formed simultaneously, and the addition of 0.5 eq palladium resulted in a 1:1 mix of ligand and complex, showing that the double cage is favored over mixtures of intermediate structures.

1.9 Reactive Complexes

Biomimicry is one of the primary goals of self-assembled complexes, and endohedrally-functionalized cages that can direct reactivity are beginning to be developed. An endohedrally-functionalized nanosphere from the Fujita group has been shown to control the polymerization of methyl methacrylate.[38] The monomer was incorporated into ligand **1.12e** via a polyethylene glycol spacer, and addition of an initiator solution caused polymerization on the interior of the complex. Polymerization is promoted by the proximity of the monomers, and no polymerization was observed when free monomer was combined with initiator. Polymer yield was dependent on the spacer length between the monomer and the ligand, and a 73% yield of polymer was observed with a tri(ethylene oxide) linker. This spacer length allows monomers to be close enough to promote polymerization but kept them far enough apart to avoid steric repulsion. This reaction proceeds under mild conditions and requires no additives which can disrupt the assembly.

A similar ligand could be prepared to give the cage a cationic interior.[39] A trimethylammonium group linked to the ligand (**1.12f**) allowed for the encapsulation of multiple anionic guests, and increasing the negative charge of the guest increased binding strength. Sodium *p*-styrenesulfonate could be bound inside $(\mathbf{1.12f})_{24}Pd_{12}$, and it was polymerized upon the addition of ammonium persulfate. Polymerization inside the complex proceeded faster than polymerization of the guest alone, and this is due to an increase in effective concentration upon encapsulation. The supramolecular environment controlled the extent of polymerization by limiting the number of monomers that were able to fit inside the cage.

These same nanospheres could also template inorganic nanoparticle synthesis. Incorporating glucose into a cage (ligand **1.12g**) allowed for binding of tetramethoxysilane, which forms silica nanoparticles upon heating.[40] Glucose was required for nanoparticles to form inside $(\mathbf{1.12g})_{24}Pd_{12}$, and reaction in the absence of cage resulted in the precipitation of silica gel rather than the formation of nanoparticles. The size of the nanoparticles was dependent on cage size, and larger nanoparticles could be synthesized by using extended ligands when synthesizing the cage. This process could also be used to synthesize core-shell nanoparticles (Figure 1.9b).[41] After the formation of the silica nanoparticles, Ti^{2+} could be added in the form $Ti(thd)_2(OiPr)_2$ (thd=2,2,6,6-tetramethyl-3,5-heptanedionate). The reaction proceeded over four days, and the resulting nanoparticles were found to contain a SiO_2/TiO_2 ratio of 100:18. The monodispersity of the original nanoparticles was retained, and formation of the shell was controlled by encapsulation. The shell-forming reaction could also proceed with zirconium.

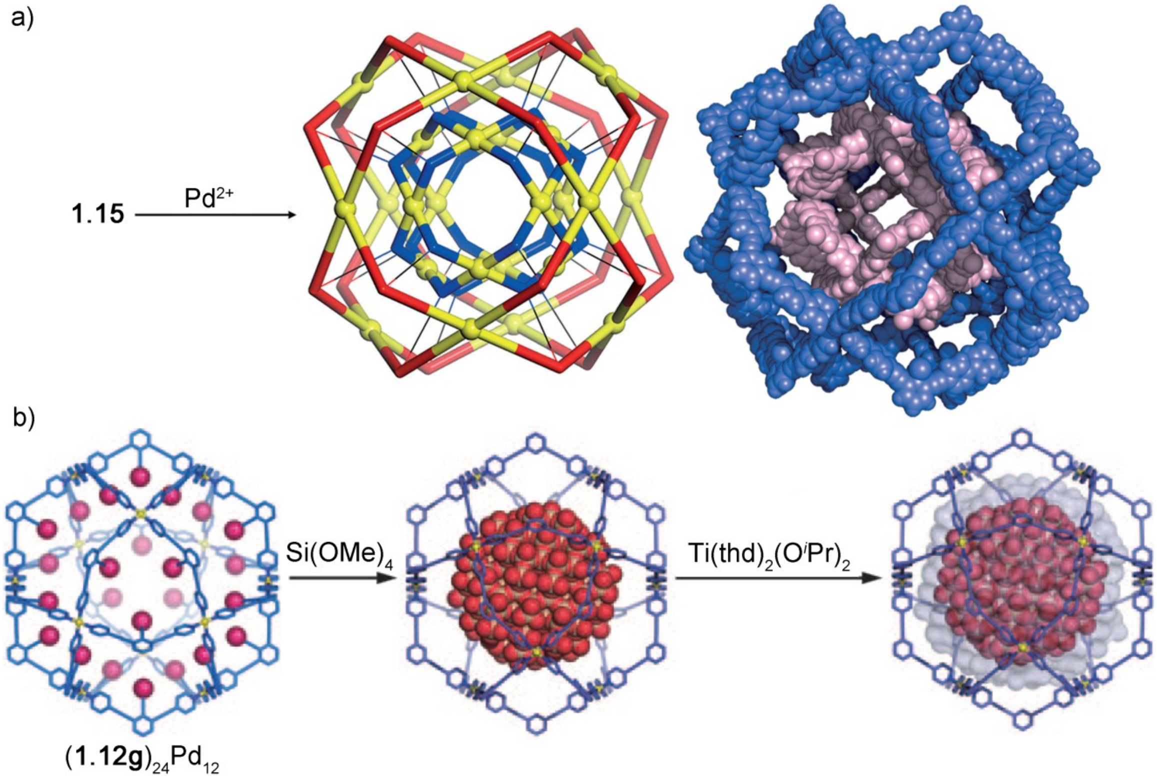

Figure 1.9: a) Cartoon and crystal structure of “cage within a cage” (**1.15**)$_{24}$Pd$_{24}$.; b) Nanoparticle synthesis and coating.

Titanium nanoparticles could also be templated by (**1.12g**)$_{24}$Pd$_{12}$.[42] Endohedral glucose was again required for titanium encapsulation, and a titanium dioxide suspension was formed in the absence of cage. The size of the nanoparticles was controlled by the rate of Ti(acac)$_2$(biphen) (acac=acetylacetonate, biphen=2,2’-biphenoxide) addition, and monodisperse nanoparticles resulted. Unlike the silica nanoparticles, the titanium nanoparticles could be removed from the cage through addition of a metal scavenger followed by precipitation.

An example of organic reactivity promoted by a cage is the previously-described (**1.17**)$_6$Fe$_4$ tetrahedron from the Nitschke group. The chiral alcohols can freely rotate and allows the groups to be exposed to a bound guest. When dichlorvos, an organophosphorus pesticide, was bound, its decomposition was catalyzed by (**1.17**)$_6$Fe$_4$, and 1% catalyst was effective. No acceleration of hydrolysis was observed in the presence of competitive guests or when individual components of the cage were present.

1.10 Outlook

While new self-assembled cage complexes continue to be synthesized and new routes to known types of cages are continually being discovered, supramolecular cage chemistry is moving toward the utility of cages rather than their synthesis. Numerous reactions can be promoted by encapsulation of reactants, but control of reactivity is only beginning to be explored. Reactivity inside complexes is inspired by biological systems, and supramolecular assemblies offer ways to access unique reactivity not observed in typical solution chemistry. Endohedral functionalization of cages offers the best possibility in using these systems for true biomimetic catalysis, and this chapter demonstrates how internal functional groups have already been shown to influence guest binding, stereocontrol, and reactivity. Functionalization of assemblies has great potential for selective recognition of guests and specialized reactivity, and endohedrally-functionalized assemblies may eventually be able to more accurately mimic the specificity and activity of enzymes.

1.11 References

1) a) Caulder, D. L.; Raymond, K. N. “Supermolecules by design.” *Acc. Chem. Res.* **1999**, *32*, 975-982.; b) Chakrabarthy, R., Mukherjee, P. S.; Stang, P. J. “Supramolecular coordination: Self-assembly of finite two- and three-dimensional ensembles.” *Chem. Rev,* **2011**, *111*, 6810-6918.; c) Fujita, M., Umemoto, K., Yoshizawa, M., Fujita, N., Kusukawa, T.; Biradha, K. “Molecular paneling *via* coordination.” *Chem. Commun.* **2001**, 509-518.; d) Smulders, M. M. J., Riddell, I. A., Browne, C.; Nitschke, J. R. “Building on architectural principles for three-dimensional metallosupramolecular construction.” *Chem. Soc. Rev.* **2013**, *42*, 1728-1754.

2) Hristova, Y. R.; Smulders, M. M. J.; Clegg, J. K.; Breiner, B.; Nitschke, J. R. “Selective anion binding by a “chameleon” capsule with a dynamically reconfigurable exterior.” *Chem. Sci.* **2011**, *2*, 638-641.

3) Fujita, M.; Oguro, D.; Miyazawa, M.; Oka, H.; Yamaguchi, K. Ogura, K. “Self-assembly of ten molecules into nanometre-sized organic host frameworks.” *Nature* **1995**, *378*, 469-471.

4) Wiester, M. J.; Ulmann, P. A.; Mirkin, C. A. “Enzyme mimics based upon supramolecular coordination chemistry.” *Angew.Chem., Int. Ed.* **2011**, *50*, 114-157.

5) a) Glasson, C. R. K.; Meehan, G. V.; Clegg, J. K.; Lindoy, L. F.; Turner, P.; Duriska, M. B.; Willis, R. “A new Fe^{II} quaterpyridyl M_4L_6 tetrahedron exhibiting selective anion binding.” *Chem. Commun.* **2008**, 1190-1192.; b) Custelcean, R. “Anion encapsulation and dynamics in self-assembled coordination cages.” *Chem. Soc. Rev.* **2014**, *43*, 1813-1824.; c) Frank, M.; Dieterich, J. M.; Freye, S.; Mata, R. A.; Clever, G. H. “Relative anion binding affinity in a series of interpenetrated coordination cages.” *Dalton Trans.* **2013**, *42*, 15906-15910.

6) a) Dong, V. M.; Fiedler, D.; Carl, B.; Bergman, R. G.; Raymond, K. N. “Molecular recognition and stabilization of iminium ions in water.” *J. Am. Chem. Soc.* **2006**, *128*, 14464-14465.; b) Parac, T. N.; Caulder, D. L.; Raymond, K. N. “Selective encapsulation of aqueous cationic guests into a supramolecular tetrahedral $[M_4L_6]^{12-}$ anionic host.” *J. Am. Chem. Soc.* **1998**, *120*, 8003-8004.

7) a) Mal, P.; Schultz, D.; Beyeh, K.; Rissanen, K.; Nitschke, J. R. “An unlockable-relockable iron cage by subcomponent self-assembly.” *Angew. Chem., Int. Ed.* **2008**, *47*, 8297-8301.; b) Biros, S. M.; Bergman, R. G.; Raymond, K. N. “The hydrophobic effect drives the recognition of hydrocarbons by an anionic metal-ligand cluster.” *J. Am. Chem. Soc.* **2007**, *129*, 12094-12095.; c) Ronson, T. K.; Giri, C.; Beyeh, N. K.; Minkkinen, A.; Topić, F.; Holstein, J. J.; Rissanen, K.; Nitschke, J. R. “Size-selective encapsulation of hydrophobic guests by self-assembled M_4L_6 cobalt and nickel cages.” *Chem. Eur. J.* **2013**, *19*, 3374-3382.; d) Turega, S.; Whitehead, M.; Hall, B. R.; Haddow, M. F.; Hunter, C. A.; Ward, M. D. “Selective guest recognition by a self-assembled paramagnetic cage complex.” *Chem. Commun.* **2012**, *48*, 2752-2754.; e) Takezawa, H.; Murase, T.; Fujita, M. “Temporary and permanent trapping of the metastable twisted conformer of an

overcrowded chromic alkene via encapsulation.” *J. Am. Chem. Soc.* **2012**, *134*, 17420-17423.

8) a) Wang, J. Z.; Brown, C. J.; Bergman, R. G.; Raymond, K. N; Toste, F. D. “Hydroalkoxylation catalyzed by a gold(I) complex encapsulated in a supramolecular host.” *J. Am. Chem. Soc.* **2011**, 133, 7358-7360.; b) Kohyama, Y.; Murase, T.; Fujita, M.; “Metal-organic proximity in a synthetic pocket.” *J. Am. Chem. Soc.* **2014**, *136*, 2966-2969.; c) Wang, Z. J.; Clary, K. N.; Bergman, R. G.; Raymond, K. N.; Toste, F. D. “A supramolecular approach to combining enzymatic and transition metal catalysis.” *Nat. Chem.* **2013**, *5*, 100-103.

9) a) Fiedler, D.; Bergman, R. G.; Raymond, K. N. “Stabilization of reactive organometallic intermediates inside a self-assembled nanoscale host.” *Angew. Chem., Int. Ed.*, **2006**, *45*, 745-748.; b) Kawano, M.; Kobayashi, Y.; Ozeki, T.; Fujita, M. “Direct crystallographic observation of a coordinatively unsaturated transition-metal complex in situ generated within a self-assembled cage.” *J. Am. Chem. Soc.* **2006**, *128*, 6558-6559.; c) Mal, P.; Breiner, B.; Rissanen, K.; Nitschke, J.R. “White phosphorus is air-stable within a self-assembled tetrahedral capsule.” *Science* **2009,** *324*, 1697-1699.; d) Brumaghim, J. L.; Michels, M.; Pagliero, D.; Raymond, K. N. “Encapsulation and stabilization of reactive aromatic diazonium ions and the tropylium ion within a supramolecular host.” *Eur. J. Org. Chem.* **2004**, 5115-5118.

10) Yoshizawa, M., Tamura, M.; Fujita, M. “Diels-alder in aqueous molecular hosts: Unusual regioselectivity and efficient catalysis.” *Science* **2006**, *312*, 251-254.

11) Horiuchi, S.; Murase, T.; Fujita, M. “Diels-alder reactions of inert aromatic compounds within a self-assembled coordination cage.” *Chem. Asian J.* **2011**, *6*, 1839-1847.

12) Fiedler, D.; Bergman, R.G.; Raymond, K.N. “Supramolecular catalysis of a unimolecular transformation: Aza-cope rearrangement within a self-assembled host.” *Angew. Chem., Int. Ed.* **2004**, *43*, 6748-6751.

13) Brown, C. J.; Bergman, R. G.; Raymond, K. N. "Enantioselective catalysis of the aza-cope rearrangement by a chiral supramolecular assembly." *J. Am. Chem. Soc.* **2009**, *131*, 17530-17531.

14) a) Hastings, C. J.; Bergman, R. G.; Raymond, K. N. "Enzymelike catalysis of the nazarov cyclization by supramolecular encapsulation" *J. Am. Chem. Soc.* **2010**, 132, 6938-6940.; b) Hastings, C. J.; Bergman, R. G.; Raymond, K. N. “Origins of large rate enhancements in the nazarov cyclization catalyzed by supramolecular encapsulation.” *Chem. Eur. J.* **2014**, *20*, 3966-3973.

15) a) Brown, C. J.; Miller, G. M.; Johnson, M. W.; Bergman, R. G.; Raymond, K. N. “High-turnover supramolecular catalysis by a protected ruthenium(II) complex in aqueous solution.” *J. Am. Chem. Soc.* **2011**, *133*, 11964-11966.; b) Leung, D. H.; Bergman, R. G.; Raymond, K. N. "Scope and mechanism of the C-H bond activation

reactivity within a supramolecular host by an iridium guest: A stepwise ion pair guest dissociation mechanism." *J. Am. Chem. Soc.* **2006** *128*, 9781-9797.

16) Lewis, J. E. M., Gavey, E. L., Cameron, S. A.; Crowley, J. D. “Stimuli-responsive Pd_2L_4 metallosupramolecular cages: Toward targeted cisplatin drug delivery.” *Chem. Sci.* **2012**, *3*, 778-784.

17) Harris, K., Sun, Q.-F., Sato, S.; Fujita, M. “$M_{12}L_{24}$ spheres with endo and exo coordination sites: Scaffolds for non-covalent functionalization.” *J. Am. Chem. Soc.* **2013**, *135*, 12497-12499.

18) Saalfrank, R. W., Seitz, V., Caulder, D. L, Raymond, K. N., Teichert, M.; Stalke, D. “Self-assembly of {2}-metallacryptands and {2}-metallacryptates.” *Eur. J. Inorg. Chem.* **1998**, 1313-1317.

19) Hiraoka, S., Kiyokawa, M., Hashida, S.; Shionoya, M. “Site-selective internal cross-linking between mercury(II)-centered vertices of an octahedral mercury(II) capsule by a rod-shaped ditopic ligand.” *Angew. Chem.*, *Int. Ed.* **2010**, *49*, 138-143.

20) Meng, W., Breiner, B., Rissanen, K., Thoburn, J. D., Clegg, J. K.; Nitschke, J. R. “A self-assembled M_8L_6 cubic cage that selectively encapsulates large aromatic guests.” *Angew. Chem., Int. Ed.* **2011**, *50*, 3479-3483.

21) Ramsay, W. J., Ronson, T. K., Clegg, J. K.; Nitschke, J. R. “Bidirectional regulation of halide binding in a heterometallic supramolecular cube.” *Angew. Chem., Int. Ed.* **2013**, *52*, 13439-13443.

22) Custelcean, R., Bosano, J., Bonnesen, P. V., Kertesz, V.; Hay, B. P. “Computer-aided design of a sulfate-encapsulating receptor.” *Angew. Chem., Int. Ed.* **2009**, *48*, 4025-4029.

23) Custelcean, R., Bonnesen, P. V., Duncan, N. C., Zhang, X., Watson, L. A., Van Berkel, G., Parson, W. B; Hay, B. P. “Urea-functionalized M_4L_6 cage receptors: Anion-templated self-assembly and selective guest exchange in aqueous solution.” *J. Am. Chem. Soc.* **2012**, *134*, 8525-8534.

24) Yi, S., Brega, V., Captain, B.; Kaifer, A. E. “Sulfate-templated self-assembly of new M_4L_6 tetrahedral metal organic cages.” *Chem. Commun.* **2012**, *48*, 10295-10297.

25) Wu, J.-Y., Zhong, M.-S., Chiang, M.-H., Tsai, M.-R.; Lai, L.-L. “Synthesis, characterization and structural transformation of a discrete tetragonal metalloprism.” *Dalton Trans.* **2012**, *41*, 156-164.

26) Suzuki, K., Iida, J., Sato, S., Kawano, M.; Fujita M. “Discrete and well-defined hydrophobic phases confined in self-assembled spherical complexes.” *Angew. Chem., Int. Ed.* **2008**, *47*, 5780-5782.

27) Suzuki, K., Takao, K., Sato, S.; Fujita, M. “Coronene nanophase within coordination spheres: Increased solubility of C_{60}.” *J. Am. Chem. Soc.* **2010**, *132*, 2544-2545.

28) Sato, S., Iida, J., Suzuki, K., Kawano, M., Ozeki, T.; Fujita, M. "Fluorous nanodroplets structurally confined in an organopalladium sphere." *Science* **2006**, *313*, 1273-1276.

29) Sun, Q.-F., Sato, S.; Fujita, M. "Self-assembled inverse dendrimer." *Chem. Lett.* **2011**, *40*, 726-727.

30) Suzuki, K.; Kawano, M.; Sato, S.; Fujita, M. "Endohedral peptide lining of a self-assembled molecular sphere to generate chirality-confined hollows." *J. Am. Chem. Soc.* **2007**, *129*, 10652-10653.

31) Fujita, D., Suzuki, K., Yagi-Utsumi, M., Yamaguchi, Y., Mizuno, N., Kumasaka, T., Takata, M., Noda, M., Uchiyama, S., Kato, K.; Fujita, M. "Protein encapsulation within synthetic molecular hosts." *Nat. Commun.* **2012**, *3*, 1093-1099.

32) Murase, T., Sato, S.; Fujita, M. "Switching the interior hydrophobicity of a self-assembled spherical complex through the photoisomerization of confined azobenzene chromophores." *Angew. Chem., Int. Ed.* **2007**, *46*, 5133-5136.

33) Freye, S., Hey, J., Torras-Galán, A., Stalke, D., Herbst-Irmer, R., John, M.; Clever, G. H. "Allosteric binding of halide anions by a new dimeric interpenetrated coordination cage." *Angew. Chem., Int. Ed.* **2012**, *51*, 2191-2194.

34) Freye, S., Michel, R., Stalke, D., Pawliczek, M., Frauendorf, H.; Clever, G. H. "Template control over dimerization and guest selectivity of interpenetrated coordination cages." *J. Am. Chem. Soc.* **2013**, *135*, 8476-8479.

35) Ousaka, N., Grunder, S., Castilla, A. M., Whalley, A. C., Stoddart, J. F.; Nitschke, J. R. "Efficient long-range stereochemical communication and cooperative effects in self-assembled Fe_4L_6 cages." *J. Am. Chem. Soc.* **2012**, *134*, 15528-15537.

36) Bolliger, J. L., Belenguer, A. M.; Nitschke, J. R. "Enantiopure water-soluble $[Fe_4L_6]$ cages: Host-guest chemistry and catalytic activity." *Angew. Chem., Int. Ed.* **2013**, *52*, 7958-7962.

37) Sun, Q.-F., Murase, T., Sato, S.; Fujita, M. "A sphere-in-sphere complex by orthogonal self-assembly." *Angew. Chem., Int. Ed.* **2011**, *50*, 10318-10321.

38) Murase, T., Sato, S.; Fujita, M. "Nanometer-sized shell molecules that confine endohedral polymerizing units." *Angew. Chem., Int. Ed.* **2007**, *46*, 1083-1085.

39) Kukuchi, T., Murase, T., Sato, S.; Fujita, M. "Polymerization of an anionic monomer in a self-assembled $M_{12}L_{24}$ coordination sphere with cationic interior." *Supramol. Chem.* **2008**, *20*, 81-94.

40) Suzuki, K., Sato, S.; Fujita, M. "Template synthesis of precisely monodisperse silica nanoparticles within self-assembled organometallic spheres." *Nat. Chem.* **2010**, *2*, 25-29.

41) Suzuki, K., Takao, K., Sato, S.; Fujita, M. “The precise synthesis and growth of core-shell nanoparticles within a self-assembled sphereical template.” *Angew. Chem., Int. Ed.* **2011**, *50*, 4858-4861.

42) Ichijo, T., Sato, S.; Fujita, M. “Size-, mass-, and density-controlled preparation of TiO_2 nanoparticles in a spherical coordination template.” *J. Am. Chem. Soc.* **2013**, *135*, 6786-6789.

Chapter Two: Self-Sorting in Aniline-Functionalized Paddle-Wheel Complexes

2.1 Introduction

As described in Chapter 1, there is precedent for palladium-pyridine interactions serving as the basis for self-assembled complexes. Taking into account rational design considerations, M_2L_4 paddle-wheel shaped complexes could be synthesized with square planar palladium(II) and v-shaped ligands.[1] Sonogashira coupling of 1,3-diethynylbenzene **2.1** and two equivalents of 3-bromopyridine **2.2** yielded *bis*-pyridyl ligand **2.3**. Upon addition of 0.5 eq palladium nitrate in DMSO, complexation occurred to give M_2L_4 paddlewheel [(**2.3**)$_4$Pd$_2$](NO$_3$)$_4$ (Figure 2.1). Complexes could also be formed from platinum(II). Other weak counterions such as triflate and tetraphenylborate were suitable for assembly as well.

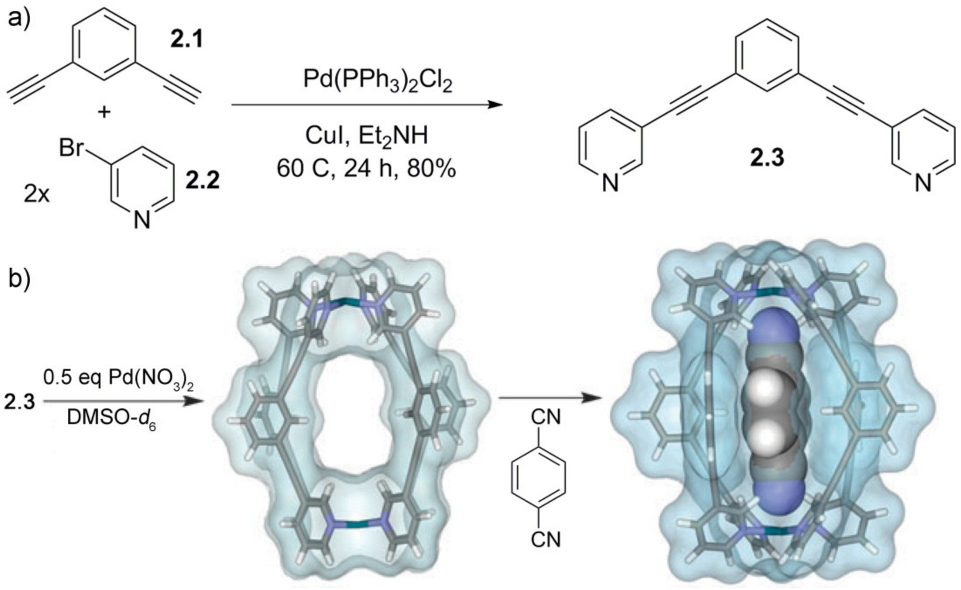

Figure 2.1: Formation of paddle-wheel complexes: a) synthesis of *bis*-pyridine ligand **2.3**; b) formation of M_2L_4 paddle-wheel complex [(**2.3**)$_4$Pd$_2$](NO$_3$)$_4$, and binding of terephthalonitrile (SPARTAN, AM1 forcefield).[1]

Because complex [(**2.3**)$_4$Pd$_2$](NO$_3$)$_2$ has a defined cavity, guest binding was explored. Suitably-sized hydrocarbons such as *p*-xylene and naphthalene were not bound, but terephthalonitrile was bound as shown in Figure 2.1. A two-component control of guest binding was observed. Guests were required to be the correct size and shape and also have a lone pair of electrons to donate to the cationic palladium. Other aromatic nitriles such as benzonitrile, 4-tolunitrile, and 4-chlorobenzonitrile were bound, as was 1,4-difluorobenzene. Binding constants ranged from 7.8 M^{-1} for 1,4-difluorobenzene to 12.4 M^{-1} for 4-chlorobenzonitrile. This weak binding was a result of competitive binding of both the DMSO solvent and the nitrate counterion.

2.2 Synthesis of Ligands with Endohedral Amines

The general structure of ligand **2.3** is compatible with the introduction of endohedral functionality. The edges of the ligands make up the walls of the complex and the bent shape forces functional groups to point inside the complex. Endohedral amines were targeted because they are small functional groups that have Lewis basicity and the potential to interact with encapsulated guests. They are also relatively easy to introduce from commercially available dihalides. Sonogashira coupling between functionalized 2,6-dihalides and 3-ethynylpyridine yielded ligands **2.6a-c** with endohedral anilines and **2.6d** with an endohedral pyridine in poor to moderate yield (Figure 2.2a). Figure 2.2b shows an alternative Sonogashira reaction which introduces functionality to the pyridine rings of the ligand. Reaction of 1,3-diethynylbenzene **2.1** and functionalized pyridines **2.7a-b** yielded **2.8a-b** in moderate yield. Ester ligand **2.8b** was hydrolyzed to acid ligand **2.8c** to increase solubility.[2]

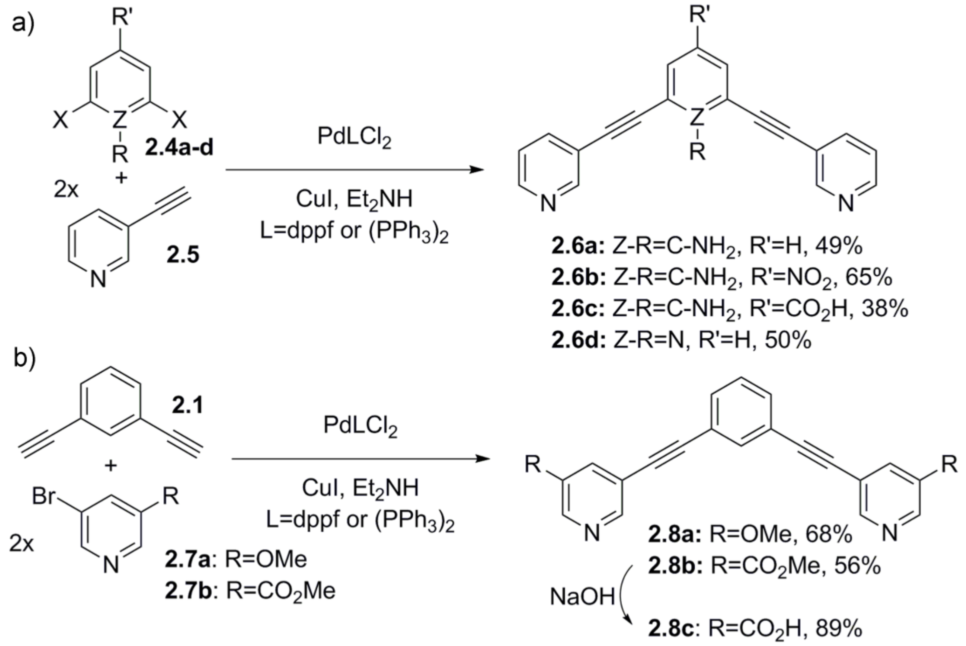

Figure 2.2: Synthesis of *bis*-pyridine ligands: a) ligands with endohedral amines or pyridine; b) ligands with pyridyl functionality.

Introduction of the amines required optimization of the reaction conditions because the amines can participate in Buchwald-Hartwig coupling[3] or react with the alkynes after the coupling is complete to form indoles.[4] Both of these reactions are also palladium catalyzed. Because of unwanted side reactions, yields were low, and extensive column chromatography was required for the isolation of pure ligand. Optimization of the catalyst was also required. While triphenylphosphine was a suitable ligand for the synthesis of **2.3**, higher yield and cleaner ligand were observed with 1,1'-*bis*(diphenylphosphino)ferrocene, and this ligand was required for synthesis of the endohedrally-functionalized **2.6a-d**.

2.3 Complex Formation

When palladium(II) nitrate was added to a solution of ligand in DMSO, the ^1H NMR spectrum showed at least a slight downfield shift in all of the peaks. This is indicative of complex formation due to the electron withdrawing effect of the pyridine-palladium interaction. The extent of the shift was dependent on proximity to the palladium center, and the protons closest to the coordinating nitrogen of the pyridine experienced the most downfield shifts (Figure 2.3). As the concentration of palladium increased, the peaks for the complex increased in intensity while the peaks for the ligand decreased in intensity. Complexation occurred rapidly (under 10 s) at ambient temperature and at millimolar concentrations, and most experiments were performed in an NMR tube. Peaks for ligand and complex were present during a ^1H NMR titration (Figure 2.3 b-c), but the exchange was too slow to be determined by 2D EXSY NMR. A single set of peaks was observed, indicating the formation of a single, symmetrical complex. Complete conversion to complex occurred after the addition of 0.5 mol. eq. palladium, and this 1:2 metal:ligand ratio fits with the predicted structure of an M_2L_4 complex.

Complexation was also possible with functionalized ligands **2.6a-d** and **2.8a,c**. NMR titrations were similar to that of ligand **2.3** for all ligands, and the presence of potentially coordinating amines, carboxylic acids, and pyridines in the core of the ligand had no effect on complex formation. Figure 2.4 shows representative ligand and complex spectra for functionalized ligands.

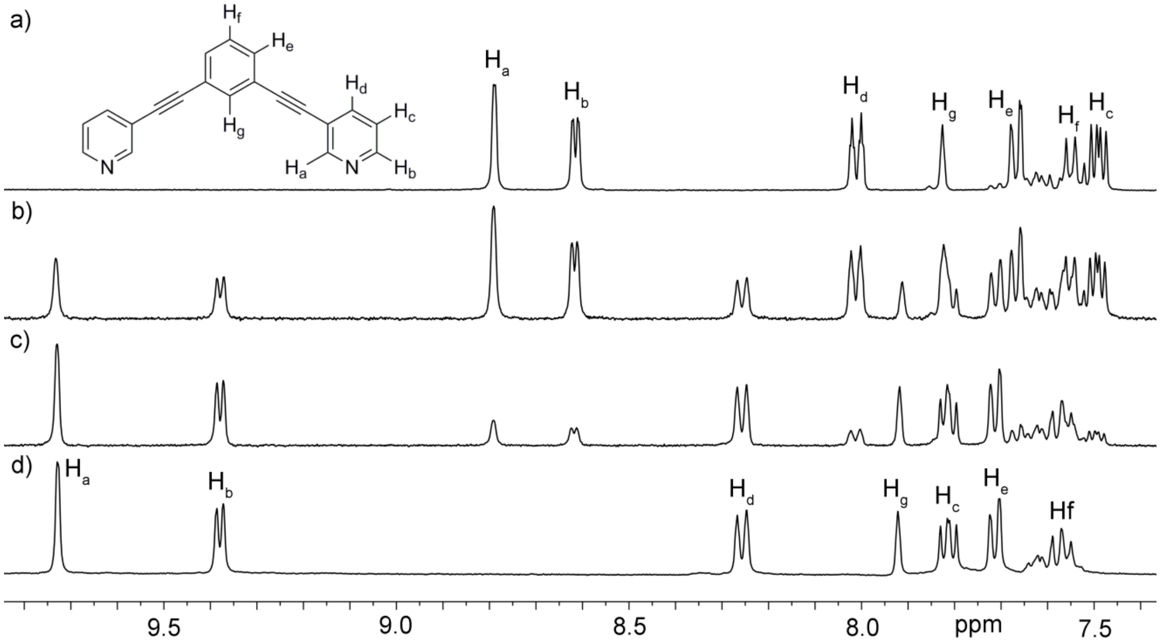

Figure 2.3: Titration of $Pd(NO_3)_2$ into **2.3**: a) 0 eq $Pd(NO_3)_2$; b) 0.16 eq; c) 0.32 eq; d) 0.5 eq (400 MHz, DMSO-d_6, 298 K).

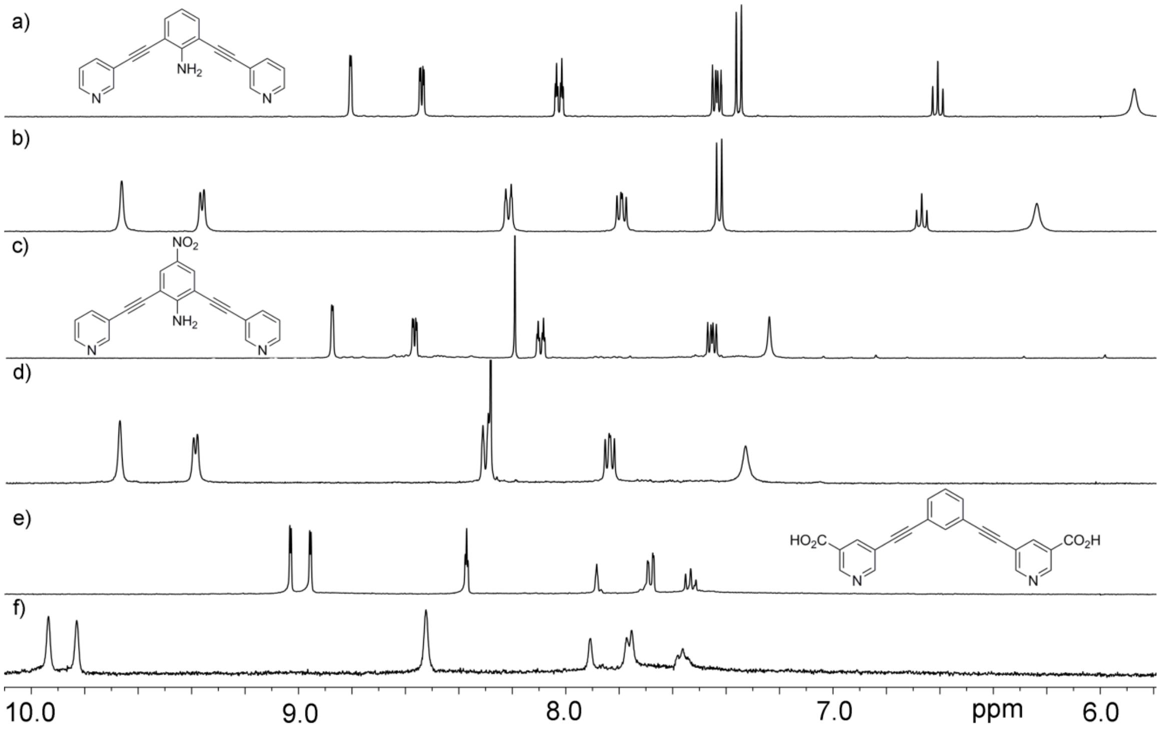

Figure 2.4: Representative ^{1}H NMR spectra of ligands and complexes: a) **2.6a**; b) $[(\textbf{2.6a})_4Pd_2](NO_3)_4$; c) **2.6b**; d) $[(\textbf{2.6b})_4Pd_2](NO_3)_4$; e) **2.8c**; f) $[(\textbf{2.8c})_4Pd_2](NO_3)_4$ (400 MHz, DMSO-d_6, 298 K).

Complexes were stable to air, water, and light in solution and in the solid state but were susceptible to competitive coordination. When triethylamine was added to $[(\mathbf{2.3})_4Pd_2](NO_3)_4$, very little ligand dissociation was observed, and only 13% ligand was observed after the addition of 1.5 eq triethylamine. Addition of anionic sodium hydroxide resulted in a brown solution, and no distinct ligand or complex peaks were observed, suggesting that ligand decomposition was occurring. The complexes were stable to 2% nitric acid, and no dissociation was observed, even in complexes with endohedral anilines. Complexes were soluble only in DMSO but remained in solution up to the addition of 20% water. No solubility was observed in other, less polar solvents, and complexes could be precipitated by the addition of acetone. Changing the nitrate counterion to triflate resulted in greater solubility, and complexes could be characterized in acetonitrile, nitromethane, and acetone. NMR behavior of the triflate complexes was similar to that of the nitrate complexes. Studies with the triflate complexes were limited to mass spectrometric analysis (where DMSO could not be utilized) because of the difficulty in preparing $Pd(OTf)_2$.

2.4 Diffusion NMR Spectroscopy

Diffusion NMR spectroscopy (DOSY) can differentiate compounds based on differences in diffusion coefficient, which is dependent on the size and shape of a molecule.[5] This technique was used to compare ligands and their corresponding complexes. Figure 2.5 shows the DOSY spectra for a mixture of ligand **2.6b** and complex $[(\mathbf{2.6b})_4Pd_2](NO_3)_4$. The smaller ligand diffused faster than the complex as expected ($2.60 \pm 0.05\text{x}10^{-10}$ m^2/s for **2.6b** vs $1.35 \pm 0.01\text{x}10^{-10}$ m^2/s for $[(\mathbf{2.6b})_4Pd_2](NO_3)_4$), but the small difference is surprising, since there is a very large difference between a single ligand and the tetracationic complex with four ligands and two metals. There was no measurable difference in diffusion coefficient between different ligands or between different complexes: when a mixture of complexes was analyzed, all complexes displayed the same diffusion coefficient. Functionalizing acid-containing ligand **2.6c** with a trityl group to increase the size of the ligand was unsuccessful, and the trityl ester was hydrolyzed in solution.

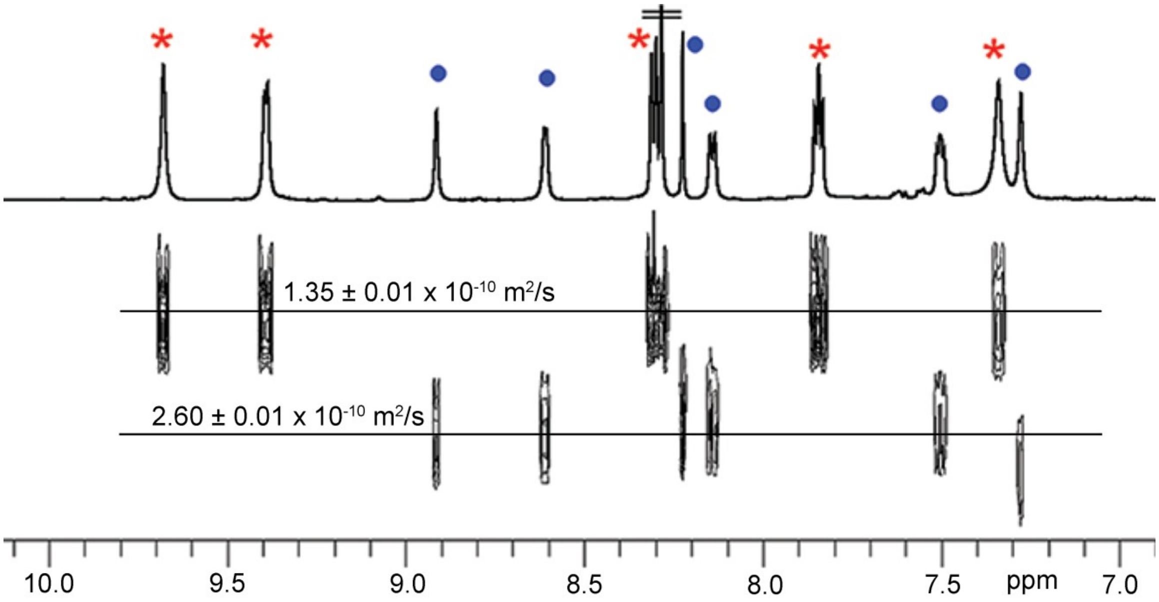

Figure 2.5: DOSY spectrum of a 1:1 mixture of **2.6b** and [(**2.6b**)$_4$Pd$_2$](NO$_3$)$_4$ (600 MHz, DMSO-*d*$_6$, 298 K, relaxation delay 2.5 s, Δ=200 ms, δ=2 ms). •=**2.6b** (blue), *=[(**2.6b**)$_4$Pd$_2$](NO$_3$)$_4$ (red).

2.5 Mass Spectrometric Analysis

Mass spectrometry was used to help confirm the M$_2$L$_4$ complex stoichiometry. Because the nitrate complexes were soluble only in DMSO, triflate complexes were used, and mass spectra were obtained from solutions of acetonitrile or nitromethane. The complexes were sensitive to standard ESI conditions, and a lowered skimmer voltage was required to preserve the assembly. All complexes were observed as the +1 ion with loss of one triflate counterion with the exception of [(**2.8c**)$_4$Pd$_2$](OTf)$_4$ which was not soluble enough to analyze. The experimental isotope patterns matched the predicted distributions as shown in Figure 2.6.

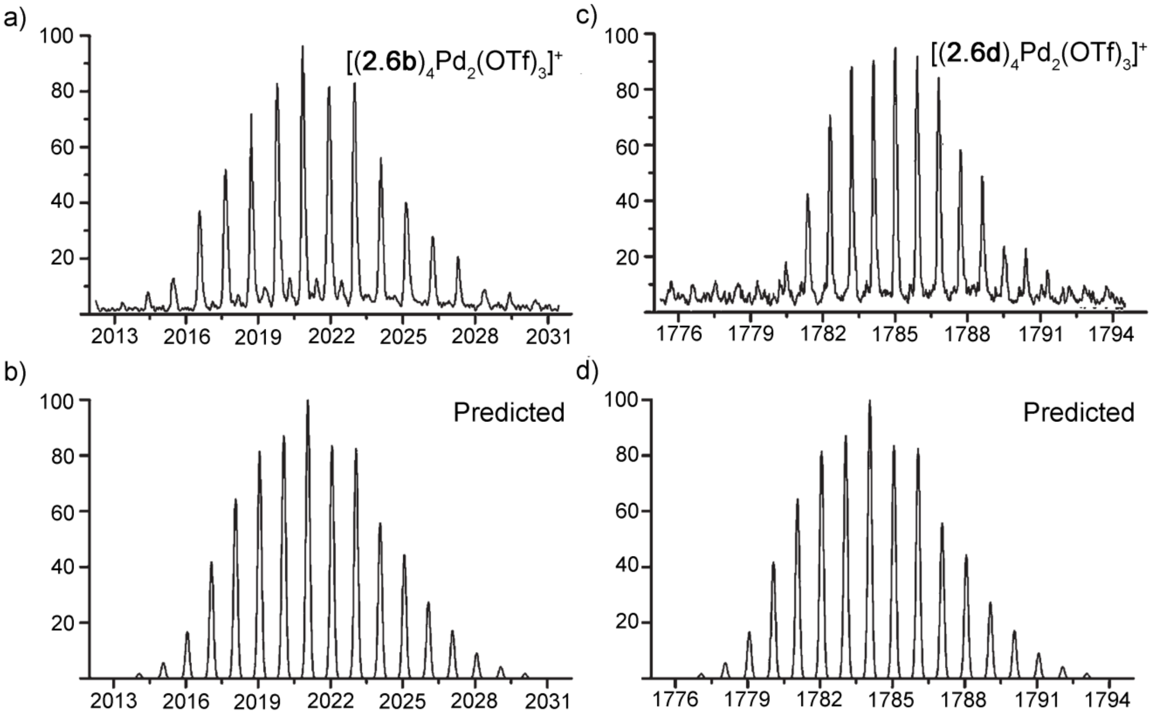

Figure 2.6: Experimental and predicted isotope patterns of [(**2.6b**)$_4$Pd$_2$](OTf)$_4$ and [(**2.6d**)$_4$Pd$_2$](OTf)$_4$.

2.6 X-ray Crystallographic Analysis

X-ray quality crystals of unfunctionalized complex [(**2.3**)$_4$Pd$_2$](OTf)$_4$ were obtained by slow evaporation from acetonitrile. The complex forms the predicted paddle-wheel shape (Figure 2.7a-b) with a clean “cross” formed at the palladium centers. The space group is C*m*, and disordered solvent molecules and triflate counterions are present in the spaces between the complexes. A disordered triflate anion is also present inside the complex, suggesting that these complexes may have potential for anion binding. The Pd atoms of neighboring complexes are 15.01 Å apart, and no π- π stacking or CH-π interactions are observed between complexes because the aromatic rings in different layers of complexes are offset.

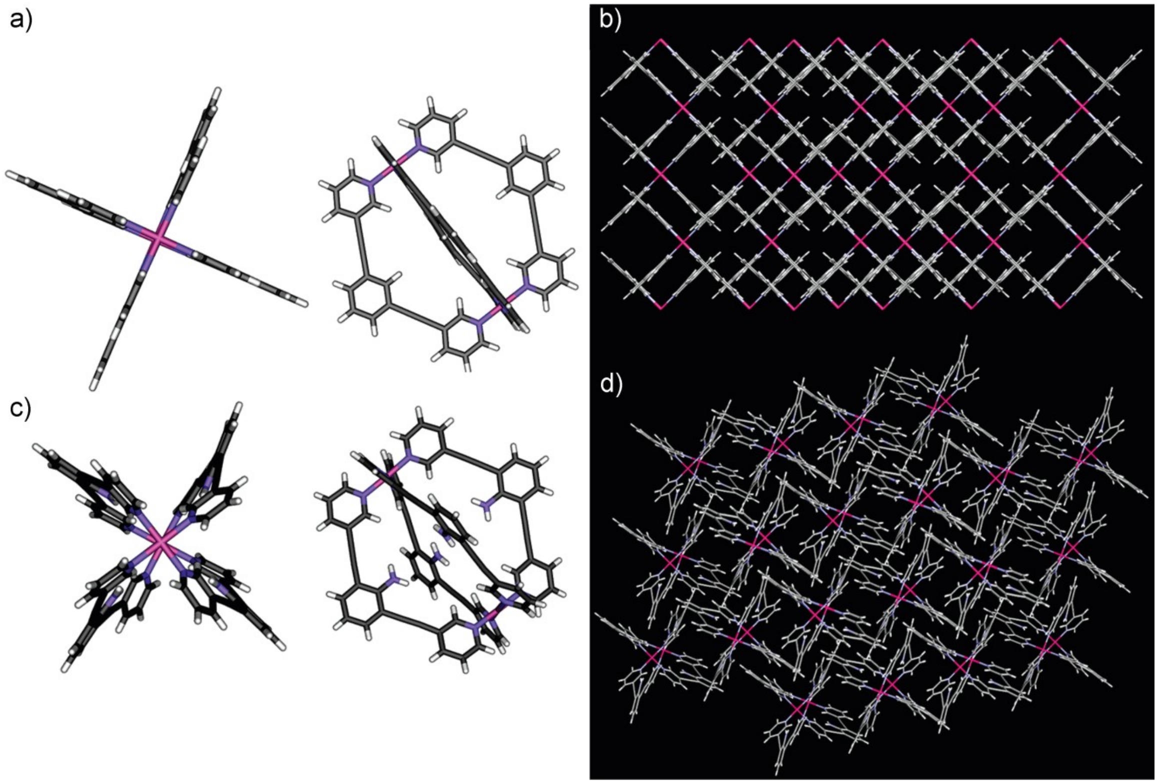

Figure 2.7: Comparision of the structures and unit cells of [(**2.3**)$_4$Pd$_2$](OTf)$_4$ and [(**2.6a**)$_4$Pd$_2$](OTf)$_4$.

Crystals of aniline complex [(**2.6a**)$_4$Pd$_2$](OTf)$_4$ were grown by slow evaporation of a 3:1 acetonitrile:toluene solution. Compared to unfunctionalized [(**2.3**)$_4$Pd$_2$](OTf)$_4$, the complex is far more twisted (Figure 2.7c). The only difference in complex structure is the presence of the endohedral amine, and the shape difference in the crystal is likely due to steric interactions between the amines and the encapsulated triflate anion. This complex also crystallizes in a different space group, $P\bar{1}$, and the palladium ions of neighboring complexes are closer together at 11.7 Å. Interactions between adjacent complexes are also observed, and π-π stacks between the central ring and alkyne and CH-π interactions between the central ring and H_d of the pyridine are present (Figure 2.8) Despite substantial efforts, aniline [(**2.6a**)$_4$Pd$_2$](OTf)$_4$ was the only functionalized complex that could be crystallized.

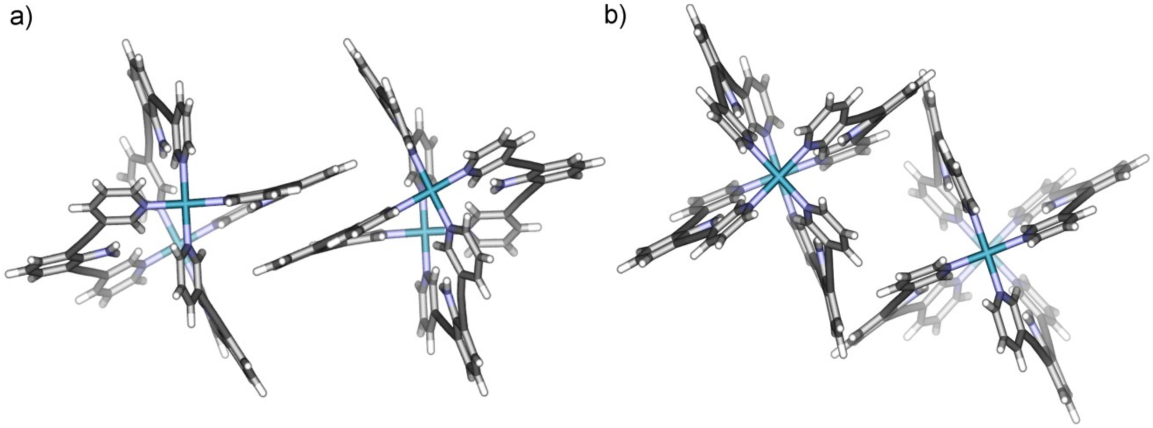

Figure 2.8: Interactions between neighboring [(**2.6a**)$_4$Pd$_2$](OTf)$_4$ complexes: a) π-π stacking; b) CH-π interactions.

2.7 Heterocomplex Formation

All of the paddle-wheel ligands synthesized have identical ligand geometry and metal coordinating groups. The main structural difference among them comes from the different functional groups that could be introduced (Figure 2.2). Because of these structural similarities, all of the ligands were predicted to have similar coordination properties, and analytical methods confirmed the M_2L_4 stoichiometry of all complexes. The different functional groups incorporated into the ligands have the potential to differentiate the ligands electronically, and mixtures of ligands were studied to determine the effects of these subtle ligand differences on self-assembly. Analysis was performed by ^{1}H NMR as spectra are sharp and ligands differentiable. Previous studies of different ligands in self-assembly relied on mass spectrometry as NMR spectra can often be broad or extremely complex.[6]

When $Pd(NO_3)_2$ was titrated into a mixture of **2.3** and **2.6a**, a very complicated NMR spectrum resulted (Figure 2.9) instead of the expected superposition of the two complexes [(**2.3**)$_4$Pd$_2$](NO_3)$_4$ and [(**2.6a**)$_4$Pd$_2$](NO_3)$_4$. The presence of many more peaks suggests that heterocomplexes, complexes made of more than one type of ligand, are being formed. The titration is similar to that of a single ligand: as the intensity of the ligand peaks decreases, the intensity of the complex peaks increases. Both ligands are incorporated into the mixture of complexes at the same rate, and no change in composition is observed over time.

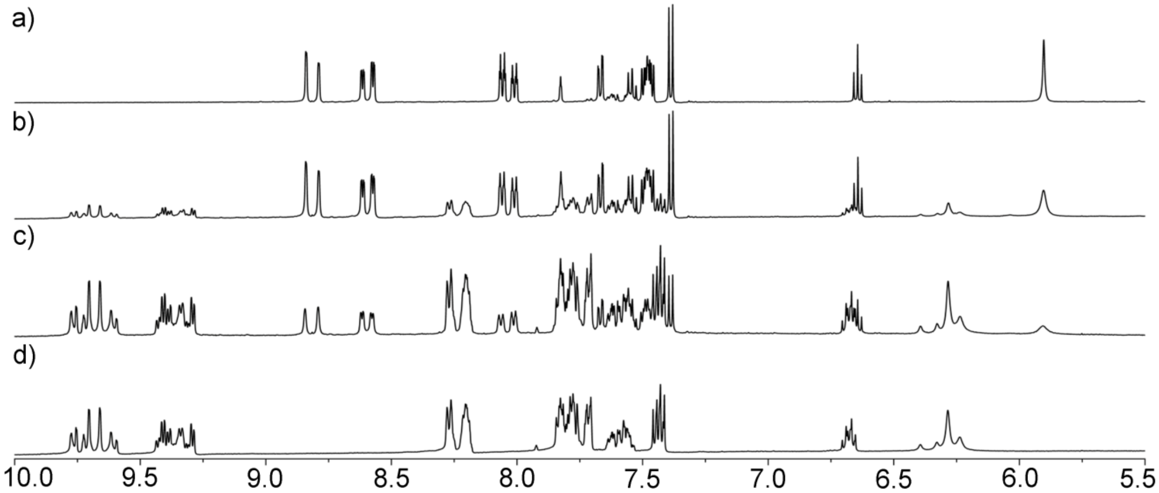

Figure 2.9: ^{1}H NMR spectra of the titration of $Pd(NO_3)_2$ into a 1:1 mixture of ligands **2.3** and **2.6a**. Molar equivalents $Pd(NO_3)_2$: a) 0; b) 0.16; c) 0.32; d) 0.50 (500 MHz, DMSO-d_6, 298 K).

Because the complexity of the NMR allowed only for partial assignment, mass spectrometry was used to identify which complexes were present. If two ligands, A and B, are mixed, six heterocomplexes can result: A_4B_0, A_3B_1, A_2B_2 (*cis*), A_2B_2 (*trans*), A_1B_3, and A_4B_0. As shown in Figure 2.10, all possible combinations form, but not in a statistical distribution. The peak for [(**2.3**)$_2$(**2.6a**)$_2$Pd$_2$](NO_3)$_4$ is the most intense because it represents indistinguishable *cis* and *trans* isomers, but [(**2.3**)$_3$(**2.6a**)$_1$Pd$_2$](NO_3)$_4$ appears to be the favored complex. Differences in favorability are the result of the slight differences in donor ability between ligands, and the distribution is similar to that observed in the NMR. When this mixture of complexes was analyzed by diffusion NMR, all complexes displayed the same diffusion coefficient.

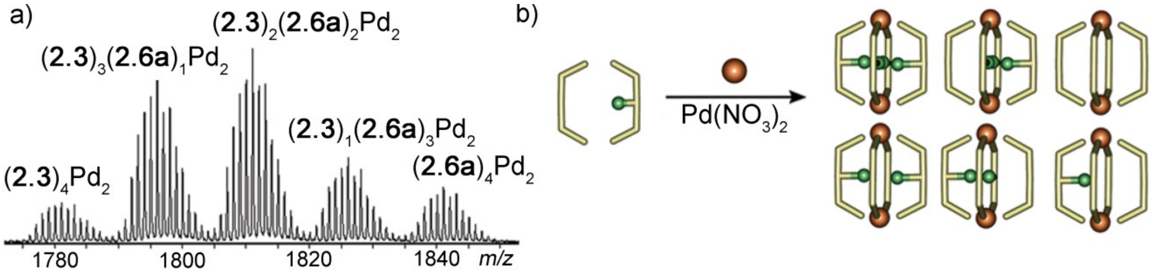

Figure 2.10: a) Mass spectrum of a 1:1 mixture of **2.3** and **2.6a** with 0.5 eq $Pd(NO_3)_2$ (complexes are singly charged with three triflate anions); b) cartoon representation of heterocomplex formation.

While the NMR spectrum is complex, peaks are sharp, and partial interpretation is possible. The most downfield peaks from 9.6-9.8 ppm were used in identification since this peak is well-separated and from the others, and the peaks within it are well defined. Comparison of the mixed spectrum to that of the corresponding homocomplexes allowed for identification of those peaks (Figure 2.11). Mixing ligands **2.3** and **2.6a** in a 3:1 ratio allowed for an enhancement of the corresponding 3:1 heterocomplex peaks (Figure 2.11 d-e). Multiple peaks are observed because of desymmetrization of the complex—**2.6a** next to **2.3** will appear different than **2.6a** across from **2.3**. The remaining peaks corresponded to the *cis* and *trans* 2:2 isomers, but differentiation between them was not possible.

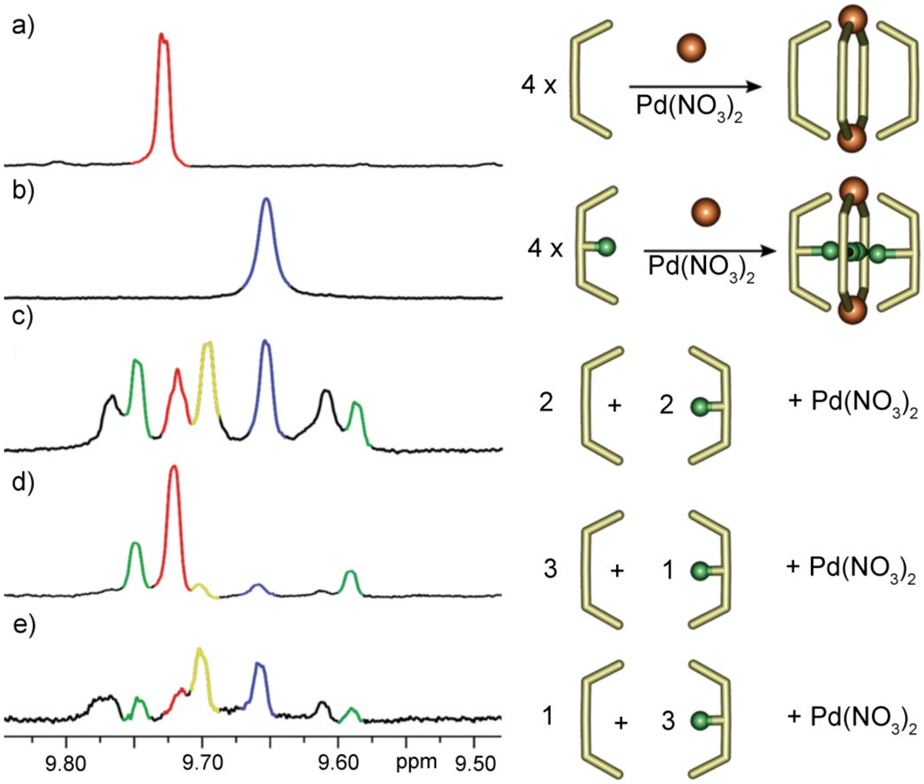

Figure 2.11: Identification of heterocomplex peaks (400 MHz, DMSO-d_6, 300 K). Red: [(**2.3**)$_4$Pd$_2$](NO$_3$)$_4$; blue: [(**2.6a**)$_4$Pd$_2$](NO$_3$)$_4$; green: [(**2.3**)$_3$(**2.6a**)$_1$Pd$_2$](NO$_3$)$_4$; yellow: [(**2.3**)$_1$(**2.6a**)$_3$Pd$_2$](NO$_3$)$_4$; peaks from [(**2.3**)$_2$(**2.6a**)$_2$Pd$_2$](NO$_3$)$_4$ overlap and are labeled in black.

2.8 Exchange Kinetics

Heterocomplexes could be formed in two different ways. The previous discussion showed that titration of metal into a mixture of ligands resulted in a heterocomplex mixture that is kinetically stable. Heterocomplexes could also be formed by adding ligand to a preformed complex. When aniline ligand **2.6a** was added to complex [(**2.3**)$_4$Pd$_2$](NO$_3$)$_4$, the products included both ligands **2.3** and **2.6a** and the previously described mixture of heterocomplexes. The displacement of ligand from the preformed complex and subsequent formation of heterocomplexes shows that ligands can exchange. Exchange was too slow to be monitored by 2D EXSY NMR on a mixture of ligand and corresponding homocomplex but could be monitored over several hours by observing the ratio of ligands and complexes present in a mixture of two different ligands (Figure 2.12).

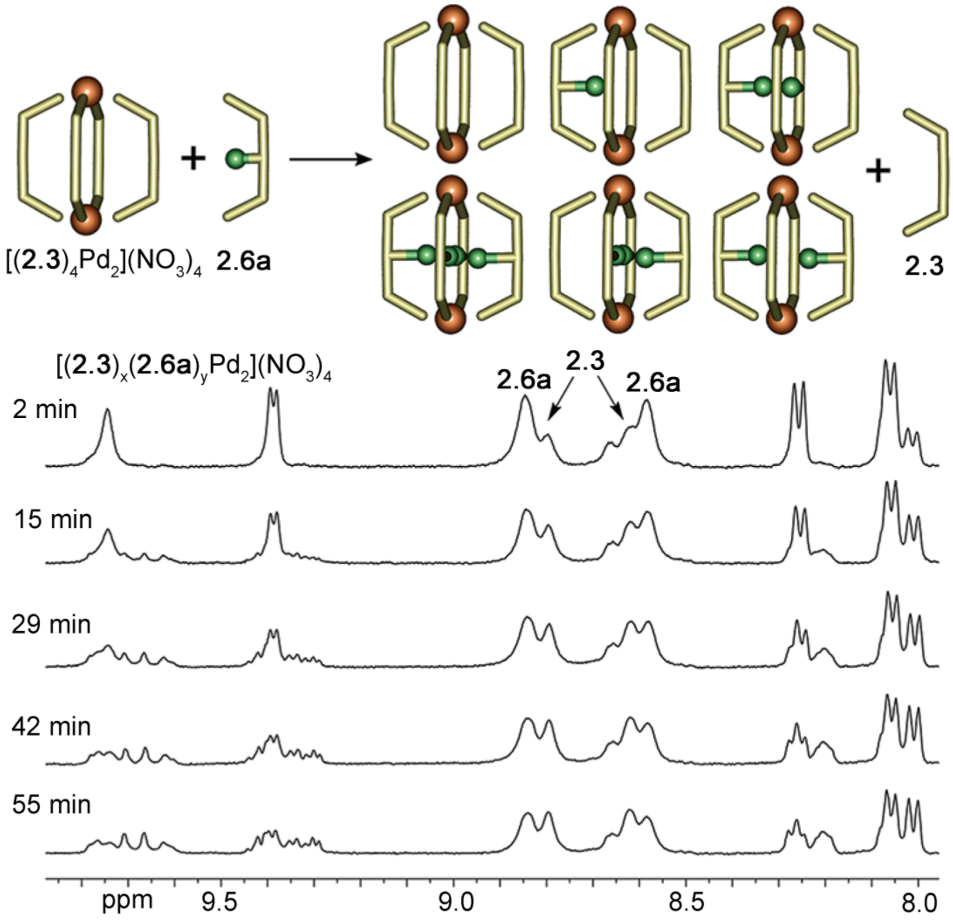

Figure 2.12: ^{1}H NMR spectra of the incorporation of ligand **2.6a** into complex $[(\mathbf{2.3})_4Pd_2](NO_3)_4$ (400 MHz, DMSO-d_6, 298 K).

Exchange begins immediately after mixing: at two minutes after the addition of **2.6a**, signals for **2.3** are already appearing. As time progresses, the concentrations of original ligand **2.6a** and original complex $[(\mathbf{2.3})_4Pd_2](NO_3)_4$ decrease while the concentration of **2.3** increases and **2.6a** is incorporated into heterocomplexes. The downfield portion of the NMR spectrum looks similar to the previous experiments suggesting that the proportions of the different heterocomplexes are the same. Initial rate calculations were performed, and the half life for exchange was 3.25 h. A second experiment was performed where **2.3** was incorporated into preformed $[(\mathbf{2.6d})_4Pd_2](NO_3)_4$, and the half life was 3.53 h. The small difference in the rate of incorporation of an electron rich and electron poor ligand shows that the exchange process is independent of the properties of the ligands.

2.9 Electronic Effects on Self-Sorting

Both electron rich and electron poor functional groups were incorporated into ligands to help determine what factors influence exchange and whether self-sorting of complexes can be controlled. Ligand **2.6a** has an electron-rich aniline, while ligands **2.6b-c** are slightly less electron-rich, as they contain an electron-withdrawing nitro or carboxylic acid, and ligand **2.6d** contains an electron-poor pyridine. Methoxy ligand **2.8a** and acid ligand **2.8c** contain functionality on the pyridine ring and were predicted to have a greater effect on assembly because the variations in electronics are closer to the coordinating group. Mixing experiments were performed on various combinations of electron rich and poor ligands, and Figure 2.13 shows a sample of the spectra that were obtained.

Heterocomplexes were observed in all mixtures, and varying amounts of assignment were possible depending on the extent of overlap. Sharp, separated peaks were present in most spectra with chemical shift depending on how electron rich or poor the ligands were. Figure 2.13a-c shows mixtures of unfunctionalized **2.3**, nitroaniline **2.6b**, and pyridine **2.6d**. The spectra in Figure 2.13d-j incorporate pyridine functionalized ligands **2.8a** and **2.8c** with the previously-mentioned ligands and include aniline **2.6a** as well. No general trend in heterocomplex formation was observed, and relatively statistical mixtures with only a slight preference for some complexes were observed.

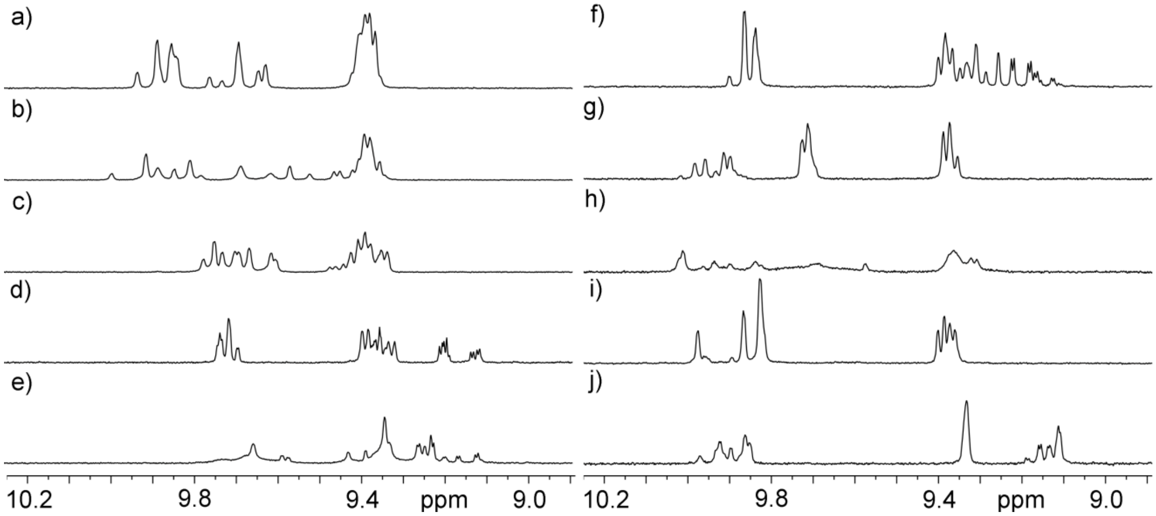

Figure 2.13: Downfield region of ^{1}H NMR spectra of mixing of ligands with different electronic properties: a) [(**2.3**)$_x$(**2.6d**)$_y$Pd$_2$](NO$_3$)$_4$; b) [(**2.6b**)$_x$(**2.6d**)$_y$Pd$_2$](NO$_3$)$_4$; c) [(**2.3**)$_x$(**2.6b**)$_y$Pd$_2$](NO$_3$)$_4$; d) [(**2.3**)$_x$(**2.8a**)$_y$Pd$_2$](NO$_3$)$_4$; e) [(**2.6a**)$_x$(**2.8a**)$_y$Pd$_2$](NO$_3$)$_4$; f) [(**2.6d**)$_x$(**2.8a**)$_y$Pd$_2$](NO$_3$)$_4$; g) [(**2.3**)$_x$(**2.8c**)$_y$Pd$_2$](NO$_3$)$_4$; h) [(**2.6b**)$_x$(**2.8c**)$_y$Pd$_2$](NO$_3$)$_4$; i) [(**2.6d**)$_x$(**2.8c**)$_y$Pd$_2$](NO$_3$)$_4$; j) [(**2.8a**)$_x$(**2.8c**)$_y$Pd$_2$](NO$_3$)$_4$ (400 MHz, DMSO-*d*$_6$, 298 K).

One combination was more amenable for study than the rest. The mixture of electron rich aniline **2.6a** and electron poor pyridine **2.6d** showed no formation of pyridine complex [(**2.8d**)$_4$Pd$_2$](NO$_3$)$_4$ by NMR or mass spectrometry. Aniline complex [(**2.6a**)$_4$Pd$_2$](NO$_3$)$_4$ was observed as were all possible heterocomplexes, and [(**2.6a**)$_1$(**2.6d**)$_3$Pd$_2$](NO$_3$)$_4$ was less intense than the other peaks (Figure 2.14a). This combination favors the electron rich **2.6a** although this is not a general trend as the electron rich methoxy in **2.8a** does not have a large effect on heterocomplex assembly.

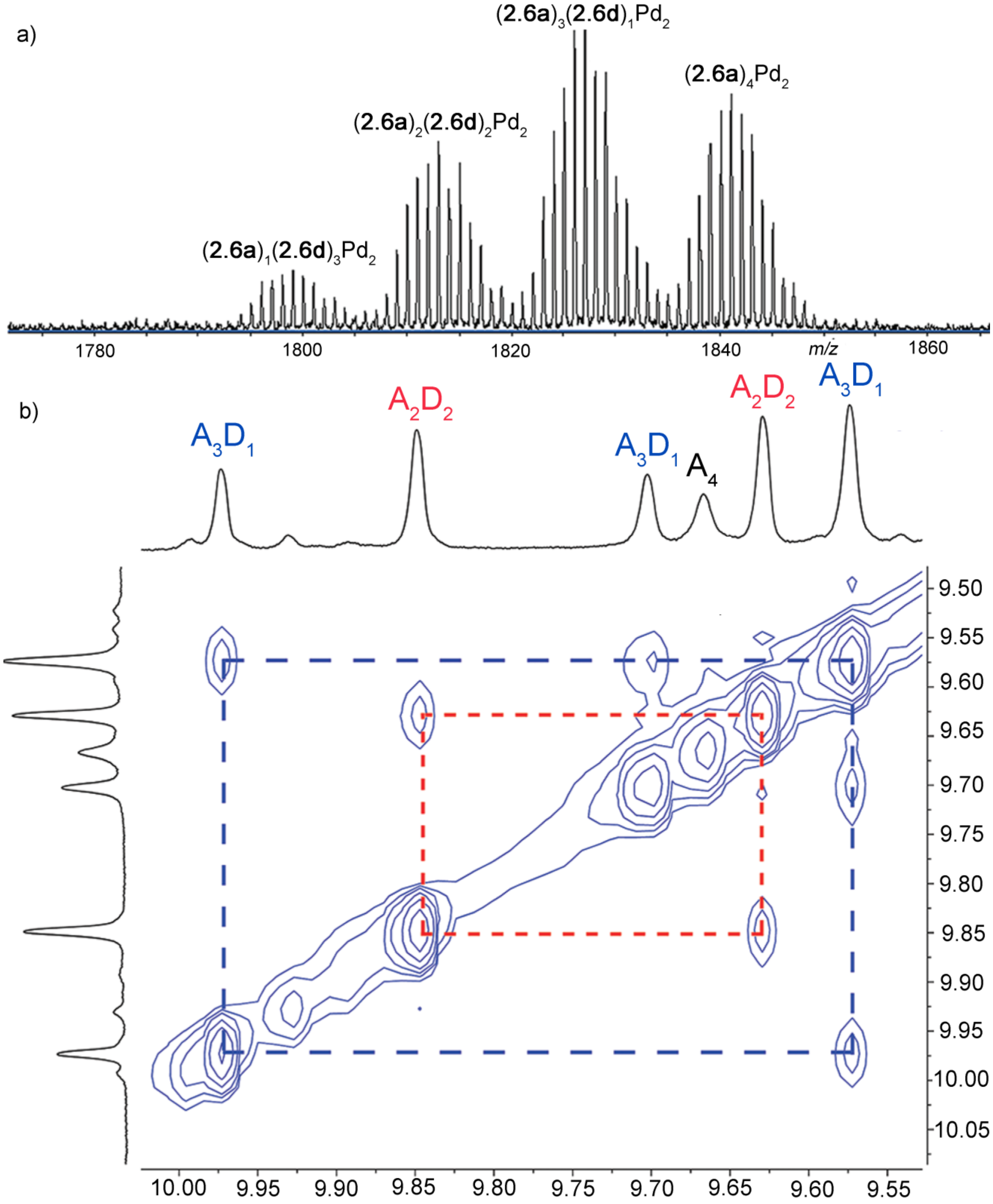

Figure 2.14: Analysis of the $[(\mathbf{2.6a})_x(\mathbf{2.6d})_y\mathrm{Pd}_2](\mathrm{NO}_3)_4$ heterocomplex system: a) ESI-MS spectrum of $[(\mathbf{2.6a})_x(\mathbf{2.6d})_y\mathrm{Pd}_2](\mathrm{NO}_3)_4$ (complexes are singly charged with three triflate anions); b) downfield region of the 2D NOESY spectrum of $[(\mathbf{2.6a})_x(\mathbf{2.6d})_y\mathrm{Pd}_2](\mathrm{NO}_3)_4$ indicating crosspeaks between H_a resonances on adjacent ligands (500 MHz, DMSO-d_6, 298 K).

This mixture was also amenable to 2D NOESY NMR analysis. Figure 2.14b shows the downfield region of the NMR spectrum of [(**2.6a**)$_x$(**2.6d**)$_y$Pd$_2$](NO$_3$)$_4$. The combination of electron rich and poor ligands allows for a range of chemical shifts and greater separation of heterocomplex peaks. Crosspeaks between adjacent ligands in heterocomplexes are observed and labeled in red ([(**2.6a**)$_2$(**2.6d**)$_2$Pd$_2$](NO$_3$)$_4$) and blue ([(**2.6a**)$_3$(**2.6d**)$_1$Pd$_2$](NO$_3$)$_4$). Aniline [(**2.6a**)4Pd$_2$](NO$_3$)$_4$ is present, but no crosspeaks are observed because all ligand peaks are equivalent in the homocomplex. The weak peaks downfield integrate in a 2:1:1 ratio and can be assigned as [(**2.6a**)$_1$(**2.6d**)$_3$Pd$_2$](NO$_3$)$_4$, and no peaks for pyridine complex [(**2.6d**)$_4$Pd$_2$](NO$_3$)$_4$ are observed. These results are consistent with what is observed by mass spectrometry.

2.10 Steric Effects on Self-Sorting

Aniline ligands were targeted as they contain functionality that is potentially reactive. As shown in the crystal structure comparison of [(**2.3**)$_4$Pd$_2$](NO$_3$)$_4$ and [(**2.6a**)$_4$Pd$_2$](NO$_3$)$_4$, the presence of even a small internal functional group can have a remarkable effect on self-assembly. This inspired an investigation of whether steric effects can be used to control heterocomplex formation.[7] Aniline ligand **2.6a** was derivatized as shown in Figure 2.15: reaction with trifluoroacetic anhydride formed a trifluoroacetamide (**2.9**), and reaction with phenyl isocyanate led to a phenylurea (**2.10**).

Self-sorting experiments showed that the small functional groups, a hydrogen in **2.3** and an aniline in **2.6a**, could form M$_2$L$_4$ complexes by themselves and with each other. A trifluoroacetamide is a medium-sized functional group and a phenylurea is a large group. Because of limited space inside the complex, ligands containing larger groups should not be able to assemble into M$_2$L$_4$ complexes. Molecular modeling suggests that one trifluoroacetamide **2.9** should be able to assemble with three smaller ligands and that phenylurea **2.10** is too large to fit in a heterocomplex.

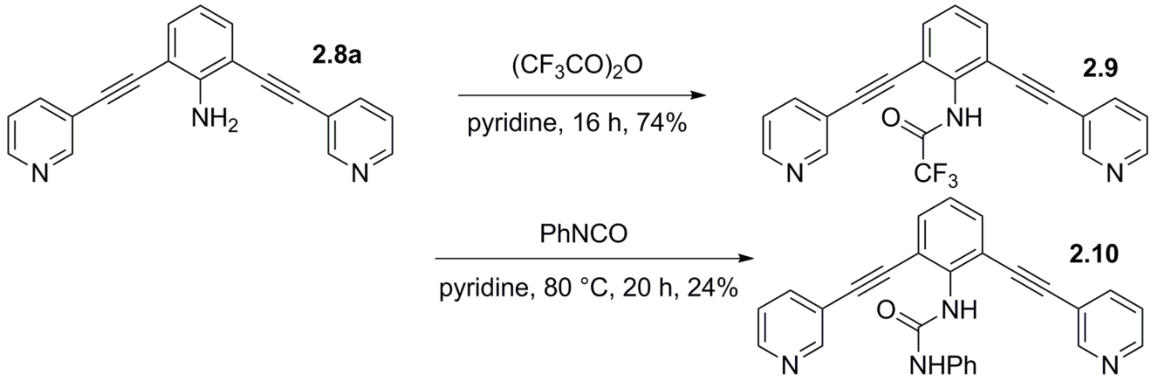

Figure 2.15: Synthesis of ligands for steric self-sorting.

When $Pd(NO_3)_2$ was added to a solution of **2.9**, a broad spectrum resulted (Figure 2.16b). No signals for ligand remained, indicating that complexation was occurring, but the spectrum was very different than the sharp NMRs of the complexes of the smaller ligands. Because four trifluoroacetamides cannot fit inside an M_2L_4 complex, undefined coordination polymers are being formed rather than discrete complexes. A similar spectrum was observed with large phenylurea ligand **2.10**.

When medium-sized **2.9** was mixed with small **2.3**, sharp peaks were observed in the ^1H NMR (Figure 2.16d). The spectrum was far simpler than those observed for previously-described mixing experiments (Figure 2.16c), and only four peaks were present in the downfield region of the spectrum. These correspond to the $[(\mathbf{2.3})_4Pd_2](NO_3)_4$ homocomplex and the $[(\mathbf{2.3})_3(\mathbf{2.9})_1Pd_2](NO_3)_4$ heterocomplex. Three peaks for $[(\mathbf{2.3})_3(\mathbf{2.9})_1Pd_2](NO_3)_4$ appear because of desymmetrization. One peak was also observed in the ^{19}F, NMR which indicates that only one complex containing **2.9** is present. These results were confirmed by mass spectrometry, where only the two complexes were observed (Figure 2.17a) with no other heterocomplexes or palladium aggregates. The incorporation of only one larger ligand shows that steric effects can control heterocomplex formation. NMR assignment was confirmed by 2D ROESY NMR (Figure 2.17d) where crosspeaks are observed between the interior H_a protons on adjacent ligands in the heterocomplex.

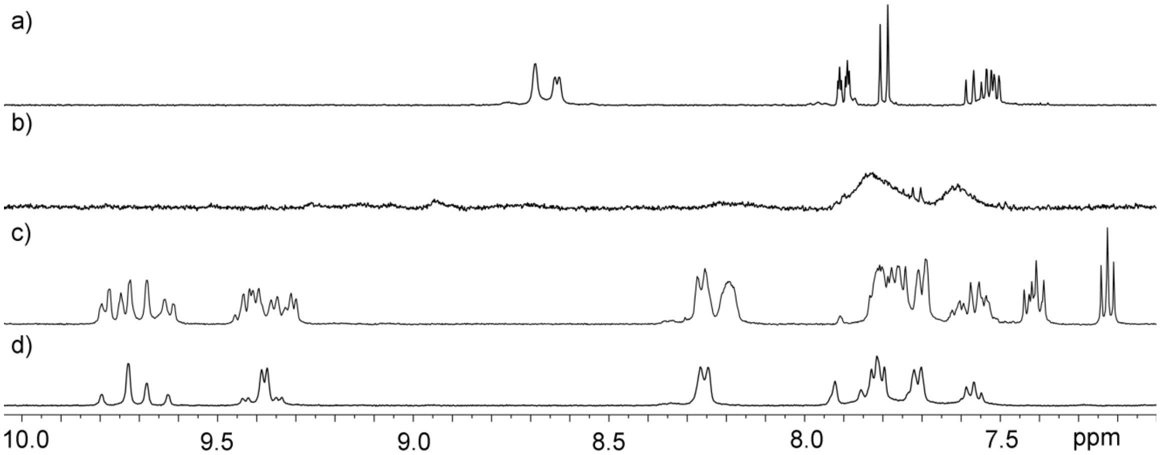

Figure 2.16: ^{1}H NMR spectra of steric control of assembly (4 mM, 400 MHz, DMSO-d_6): a) **2.9**; b) [(**2.9**)$_4$Pd$_2$](NO$_3$)$_4$; c) mixture of small complexes [(**2.3**)$_x$(**2.6a**)$_y$Pd$_2$](NO$_3$)$_4$; d) mixture of small and medium complexes [(**2.3**)$_4$Pd$_2$](NO$_3$)$_4$ and [(**2.3**)$_3$(**2.9**)$_1$Pd$_2$](NO$_3$)$_4$.

When aniline **2.6a** was mixed with trifluoroacetamide **2.9**, a broad spectrum similar to that of **2.9**+Pd(NO$_3$)$_2$ resulted. After one hour, however, peaks for homocomplex [(**2.6a**)$_4$Pd$_2$](NO$_3$)$_4$ grew in which shows that the aniline, while small, is large enough to disfavor heterocomplex formation. No other sharp peaks that could correspond to heterocomplexes were observed, which suggests that the smaller aniline complex is selected for while the larger **2.9** forms undefined palladium aggregates. Similar results were observed in mixing between **2.3** and **2.10**. Disordered aggregates were observed at first, but the [(**2.3**)$_4$Pd$_2$](NO$_3$)$_4$ homocomplex emerges after equilibration showing that the phenylurea is too large to be incorporated into a heterocomplex even with an unfunctionalized ligand. The selective incorporation of **2.9** with **2.3** but not **2.6a** highlights the sensitivity of this system to the size of endohedral functional groups.

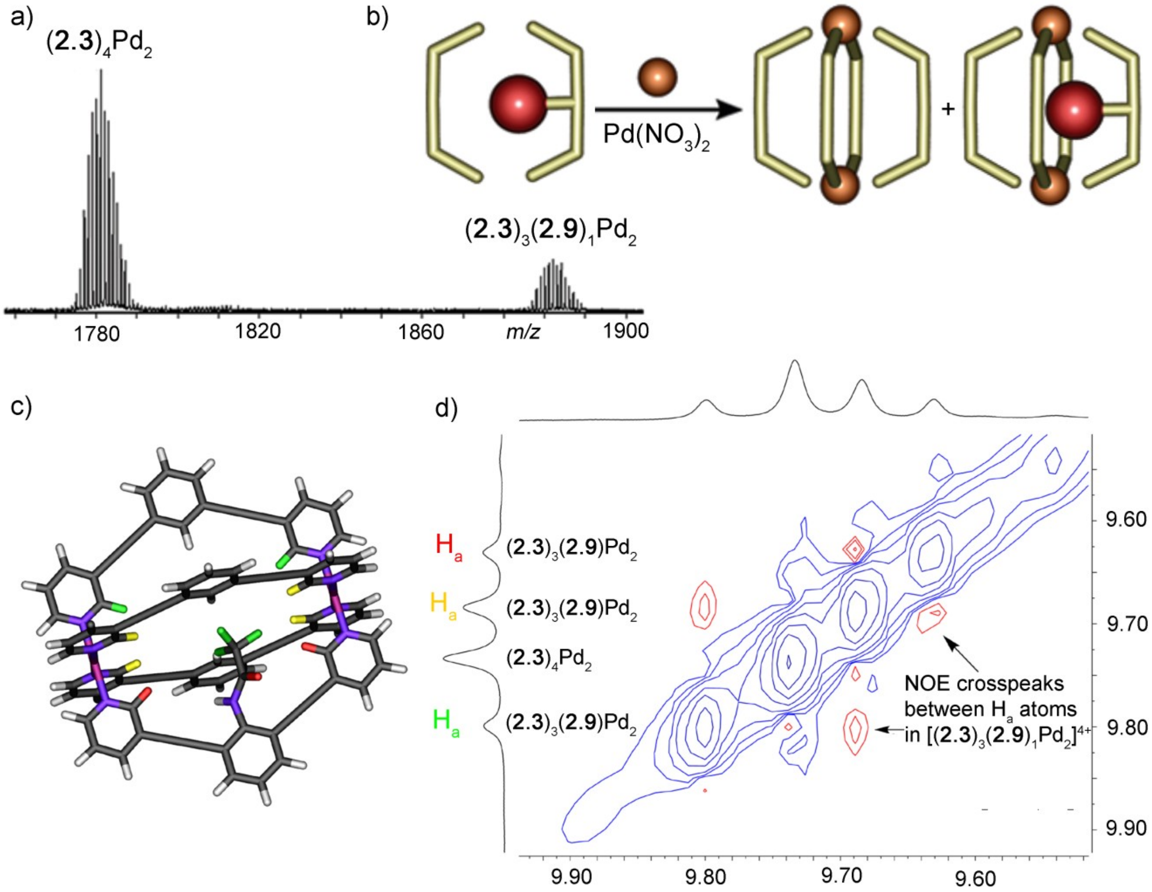

Figure 2.17: a) mass spectrum of [(**2.3**)$_4$Pd$_2$](NO$_3$)$_4$ and [(**2.3**)$_3$(**2.9**)$_1$Pd$_2$](NO$_3$)$_4$ (complexes are singly charged with three triflate anions); b) cartoon of steric self-assembly; c) model of [(**2.3**)$_3$(**2.9**)$_1$Pd$_2$](NO$_3$)$_4$ heterocomplex (SPARTAN, AM1 force field) with colored H$_a$ protons depicting NOE interactions; d) 2D ROESY NMR of [(**2.3**)$_4$Pd$_2$](NO$_3$)$_4$ and [(**2.3**)$_3$(**2.9**)$_1$Pd$_2$](NO$_3$)$_4$ (4 mM, 500 MHz, DMSO-*d*$_6$, 300 K, 500 ms mixing time).

2.11 Conclusion

This work has shown that endohedral functionality can be introduced into supramolecular metal-ligand complexes and that it can affect self-assembly. Complexes are tolerant to functional groups such as anilines and pyridines that could potentially compete for metal coordination. The palladium-pyridine contacts utilized in this system are indeed reversible, as shown by the ability of ligands to be incorporated into preformed complexes. Supramolecular self-sorting often relies on differences in size and shape of ligands[8] and heterocomplexes are observed in this series of ligands with identical size and coordination geometry. Electronic differences in ligand substitution showed only subtle effects on assembly, and no overall trend was observed which could be exploited for selective heterocomplex formation. Steric effects proved effective for controlling heterocomplex formation, and a single heterocomplex could be selectively assembled from ligands containing suitably-sized endohedral functionality despite having identical size, shape, and metal coordinator.

2.12 References

1) Liao, P.; Langloss, B. W.; Johnson, A. M.; Knudsen, E. R.; Tham, F. S.; Julian, R. R.; Hooley, R. J. "Two-component control of guest binding in a self-assembled cage molecule." *Chem. Commun.* **2010**, *46*, 4932-4934.

2) Johnson, A. M.; Moshe, O.; Gamboa, A. S.; Langloss, B. W.; Limtiaco, J. F. K.; Larive, C. K.; Hooley, R. J. "Synthesis and properties of metal—ligand complexes with endohedral amine functionality." *Inorg. Chem.* **2011**, *50*, 9430-9442.

3) Surry, D. S.; Buchwald, S. L. "Biaryl phosphane ligands in palladium-catalyzed amination." *Angew. Chem., Int. Ed.* **2008**, *47*, 6338-6361.

4) Iritani, K.; Matsubara, S.; Uchimoto, K. "Palladium catalyzed reaction of 2-alkynylanilines with allyl chlorides. Formation of 3-allylindoles." *Tetrahedron Lett.* **1988**, *29*, 1799-1802.

5) Sun, Q.-F.; Iwasa, J.; Ogawa, D.; Ishido, Y.; Sato, S.; Ozeki, T.; Sei, Y.; Yamaguchi, K.; Fujita, M. "Self-assembled $M_{24}L_{48}$ polyhedra and their sharp structural switch upon subtle ligand variation." *Science* **2010**, *328*, 1144-1147.

6) Zheng, Y.-R.; Stang, P. J. "Direct and quantitative characterization of dynamic ligand exchange between coordination-driven self-assembled supramolecular polygons." *J. Am. Chem. Soc.* **2009**, *131*, 3487-3489.

7) Johnson, A. M.; Hooley, R. J. "Steric effects control self-sorting in self-assembled clusters." *Inorg. Chem.* **2011**, *50*, 4671-4673.

8) a) Caulder, D. L.; Raymond, K. N. "Supramolecular self-recognition and self-assembly in gallium(III) catecholamide triple helices." *Angew. Chem. Int. Ed. Engl.* **1997**, *36*, 1440-1442.; b) Krämer, R.; Lehn, J.-M.; Marquis-Rigault, A. "Self-recognition in helicate self-assembly: Spontaneous formation of helical metal complexes from mixtures of ligands and metal ions." *Proc. Natl. Acad. Sci. USA* **1993**, *90*, 5394-5398.; c) Jiménez, A.; Bilbeisi, R. A.; Ronson, T. A.; Zarra, S.; Woodhead, C.; Nitschke, J. R. "Selective encapsulation and sequential release of guests within a self-sorting mixture of three tetrahedral cages." *Angew. Chem., Int. Ed.* **2014**, *53*, 4556-4560.

Chapter Three: Bidentate Hydroxamic Acid Ligands and Synthesis of Functionalized Ligand Cores

3.1 Introduction

The paddle wheel complexes described in Chapter 2 show that endohedral functionally can be incorporated into ligands, and that functional groups can have an impact on crystal packing and self-assembly. This work also exposed some limitations of the paddle-wheel system. While selective assembly was possible when incorporating a large endohedral functional group, this group filled the cavity and prevented further utilization of the cage. The unfunctionalized complex could bind a small molecule such as terephthalonitrile, but the endohedrally-functionalized aniline experienced distortion in the solid state when a triflate anion was bound. This small size of these complexes and sensitivity to sterics limits the possibilities of using these cages for guest binding and reactivity. The primary goal of introducing functionality to cages is to use them as synthetic hosts for reactivity, and larger cages must be synthesized to allow for larger or multiple guests to be bound. Extending the paddle-wheel ligands with additional aromatic rings and/or alkynes was not effective. The synthesis suffered from low yields, and endohedral functionality could not be introduced.[1]

An alternative strategy widely used in the literature is the formation of M_4L_6 tetrahedra from *bis*-bidentate ligands and octahedral metals.[2] A tetrahedral complex would possess a larger, more spherical cavity that can accommodate both guests and functional groups. The Raymond group has synthesized a small tetrahedral cage from ligands with hydroxamic acid chelators and Fe^{3+} or Ga^{3+} (Figure 3.1),[3] and this was the inspiration for extended ligands with hydroxamic acid chelators.

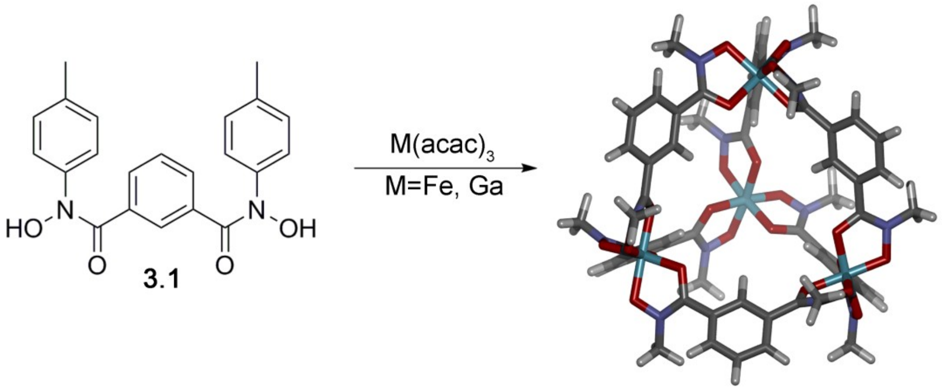

Figure 3.1: Formation of a M_4L_6 tetrahedron from a bis-hydroxamic acid ligand and $Fe(acac)_3$ or $Ga(acac)_3$. The tolyl groups have been omitted from the model for clarity.

3.2 Synthesis of Ligand Core and Reaction of *N*-Phenylhydroxylamine

To preserve the geometry of the ligand while making the ligand longer, a meta-terphenyl was used instead of a single aromatic ring. Figure 3.2 shows the synthesis of extended hydroxamic acid ligands. Suzuki coupling between 2,6-dibromobenzene and two equivalents of 4-ethoxycarbonylphenylboronic acid yielded terphenyl ester **3.4** which was hydrolyzed to diacid **3.5**. The acid could be converted to an acid chloride or other electrophilic species and reacted with *N*-Phenylhydroxylamine to form ligand **3.6**. *N*-Phenylhydroxylamine **3.8** was synthesized from nitrobenzene by reduction with zinc dust.[4]

Reduction proved difficult unless the literature procedure was followed exactly, and overreduction to aniline was a significant side reaction. Treatment of diacid **3.5** with oxalyl chloride to form an isolable acid chloride was unsuccessful, so other acid activation methods were attempted. Carbonyldiimidazole (CDI), isobutyl chloroformate, and dicyclohexylcarbodiimide (DCC) were all tested, but the peptide coupling reagent HCTU (*O*-(6-Chlorobenzotriazol-1-yl)-*N*,*N*,*N*',*N*'-tetramethyluronium hexafluorophosphate) proved to be the most effective. This was used in most of the subsequent C-N bond forming reactions.

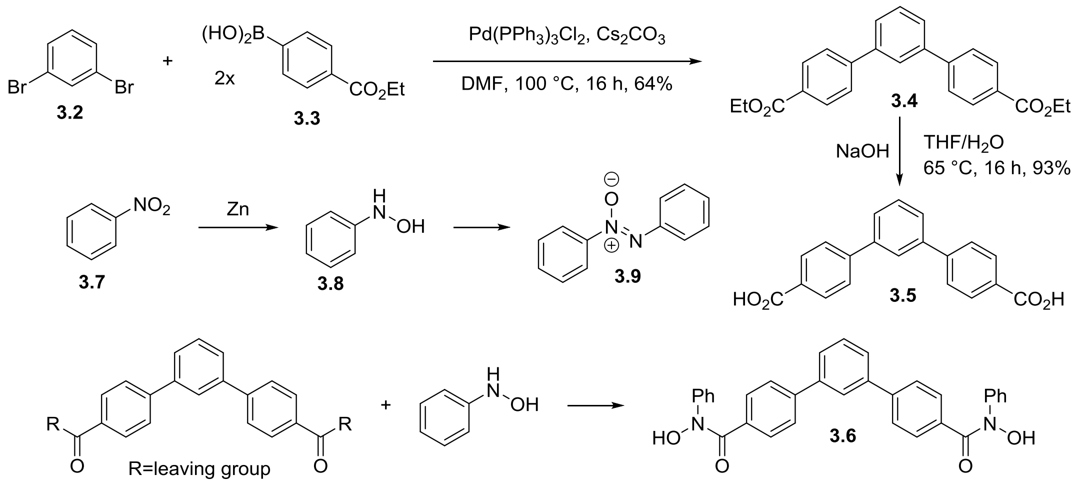

Figure 3.2: Synthesis of terphenyl ligand core, reduction of nitrobenzene to *N*-phenylhydroxylamine, and synthesis of terphenyl hydroxamic acid.

The desired hydroxamic acid product was never observed in reactions with *N*-phenylhydroxylamine, and a consistent product was observed by ^{1}H NMR despite varying reaction conditions. This was identified as azoxybenzene **3.9**, an oxidation product of *N*-phenylhydroxylamine.[5] Pure *N*-phenylhydroxylamine could be obtained by recrystallization from hexanes, but oxidation to **3.9** was observed even in a sealed vial under N_2 at –27 °C.

3.3 Reaction of *N*-Methylhydroxylamine

Because of the instability of *N*-phenylhydroxylamine, *N*-methylhydroxylamine was used instead. Acid chloride **3.10** was formed *in situ*, and reaction was observed with *N*-methylhydroxylamine. Two products were observed in most reactions, and they were assigned as the products of reactivity at both N and O as shown in Figure 3.3.

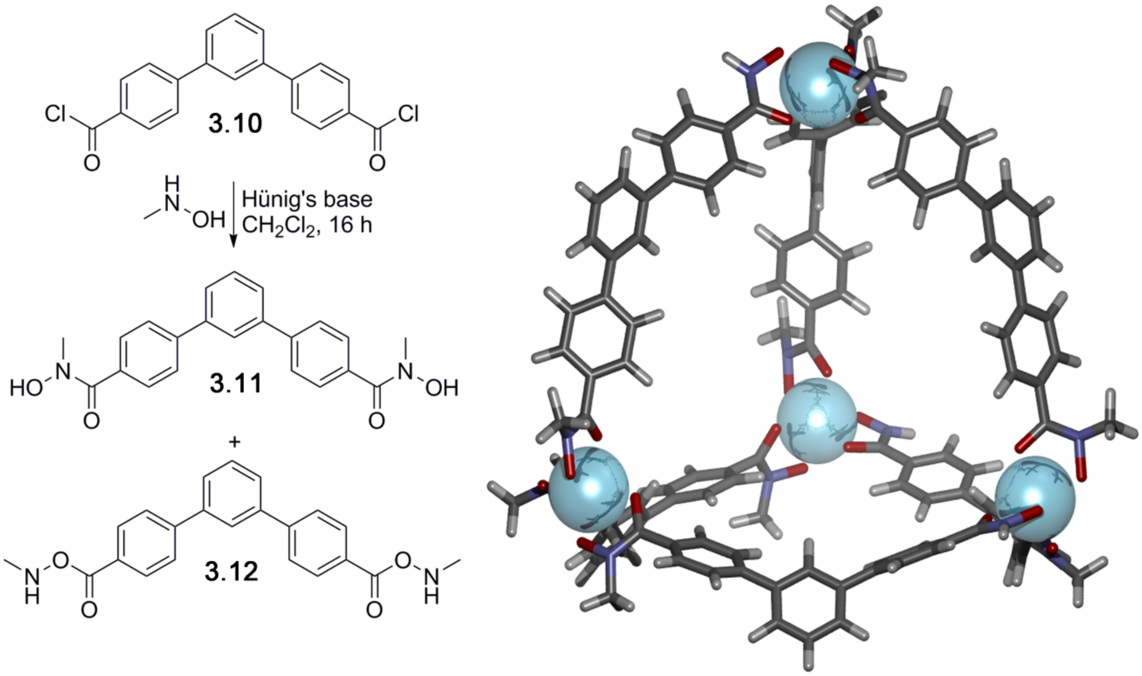

Figure 3.3: Competitive nucleophilicity of *N*-methylhydroxylamine and model of ($\mathbf{3.7}$)$_6$Ga$_4$ (SPARTAN, AM1 force field).

The two products were identified by comparing ^{1}H NMR shifts. The crude ^{1}H NMR spectrum showed only a slight preference for the *O*-substituted product, and it could be identified by comparison with ester **3.4**, which has a similar connectivity. The two products were unable to be separated by column chromatography, but recrystallization from acetone yielded pure **3.11** in 26% yield.

3.4 Complex Formation from *N*-Methyl Ligand

Complex formation with the *N*-methyl hydroxamic acid ligand was attempted via the literature procedure.[2b] Ligand **3.10** and 0.67 eq Ga(acac)$_3$ or Ga(NO$_3$)$_3$ were refluxed in methanol or acetone with a small amount of triethylamine. The resulting precipitate was added to a variety of NMR solvents (CDCl$_3$, D$_2$O, acetone-*d*$_6$, and DMSO-*d*$_6$) but was not soluble in any of them, even after heating. Complexation was also attempted with Fe(acac)$_2$ and Fe(acac)$_3$, but broad, unidentifiable NMRs resulted due to the paramagnetism of iron.

3.5 Introduction of Hexyl Chains

Due to the insolubility of the *N*-methyl complexes, methods of enhancing the solubility of the cages were investigated. It is synthetically more simple to introduce functionality on the hydroxylamine rather than the terphenyl, and alkyl chains were targeted. *N*-hexylhydroxylamine **3.14** was synthesized by condensation of hydroxylamine hydrochloride with hexanal followed by reduction with sodium cyanoborohydride. Activation of diacid **3.5** with HCTU followed by reaction with *N*-hexylhydroxylamine successfully produced ligand, but in poor yield. *N*- and *O*-substituted products were still observed, so methods to protect the oxygen were investigated.

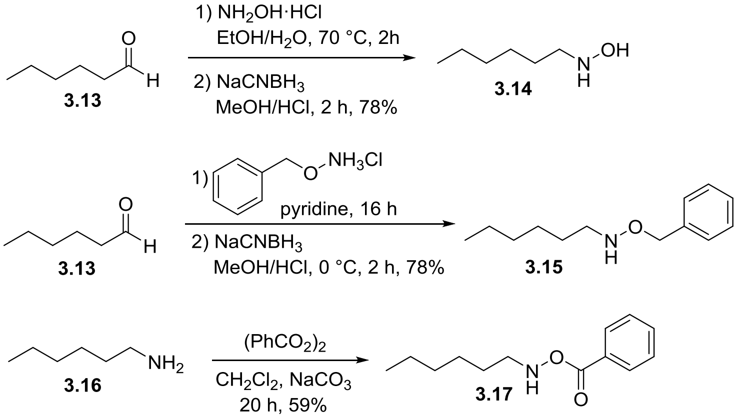

Figure 3.4: Synthesis of hexyl chains for increased solubility and *O*-protected hydroxylamines.

Benzyl-protected hydroxylamine **3.15** was synthesized in a similar manner as **3.14** using *O*-benzylhydroxylamine hydrochloride. Benzoyl-protected hydroxylamine **3.17** was synthesized from hexylamine and benzoyl peroxide. HCTU coupling between diacid **3.5** and the *O*-protected hydroxylamines produced protected hydroxamic acid ligands in both cases, but the reaction with the benzyl-protected hydroxylamine was far more effective (62% vs 25% with the benzoyl-protected). Figure 3.5 shows the synthesis of these *O*-protected ligands. Benzyl deprotection was achieved with boron tribromide to yield ligand **3.20** in 42% yield. Benzoyl deprotection was attempted with ammonium hydroxide in methanol,[6] but the hydroxamic acid was hydrolyzed.

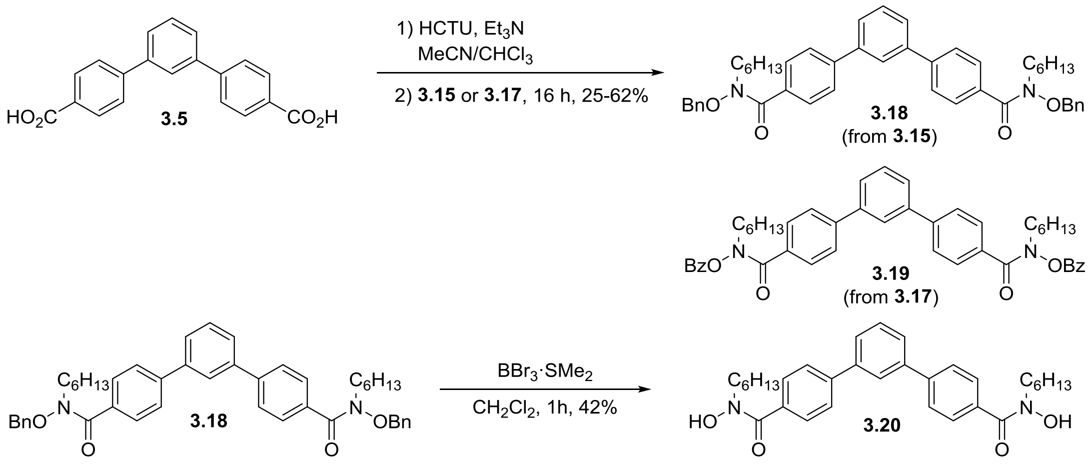

Figure 3.5: Synthesis of O-protected hydroxamic acid ligands and benzyl deprotection.

3.6 Complex Formation from *N*-Hexyl Ligand

Complexes of **3.20** were formed by mixing ligand, metal salt, and triethylamine in acetonitrile. The resulting precipitates were collected and analyzed by ^{1}H NMR in DMSO-d_6. Complexation was attempted with several metal ions and varied success in complexation was achieved. These spectra are shown in Figure 3.6. No complexation was observed with Ga^{3+}, even after heating overnight, and only partial complexation was observed with Ru^{3+}. The paramagnetism of Fe prevented ^{1}H NMR analysis, as peaks became broadened and unassignable. The best results were observed with Bi^{3+} and Pr^{3+}, and complexation required heating overnight. Complexation with Bi^{3+} resulted in a sharp spectrum, and a single set of peaks was observed. A more complex spectrum resulted from Pr^{3+}, and peaks were shifted out of the aromatic region. No scalar coupling was observed, but peaks were sharp and well-defined, unlike the spectra observed with paramagnetic Fe^{3+}. While the use of rare earth and main group metals allowed for facile ^1H NMR analysis, these complexes were only sparingly soluble in DMSO. No solubility was observed in other solvents, and this prevented mass spectrometric analysis. DMSO solubility also limited the techniques that could be used in crystal growing, and X-ray quality crystals were unable to be obtained. Aniline-functionalized ligands were synthesized by Suzuki coupling with 2,6-dibromoaniline or 2,6-diiodo-4-nitroaniline, but complexes from these ligands were even more insoluble than their unfunctionalized counterparts.

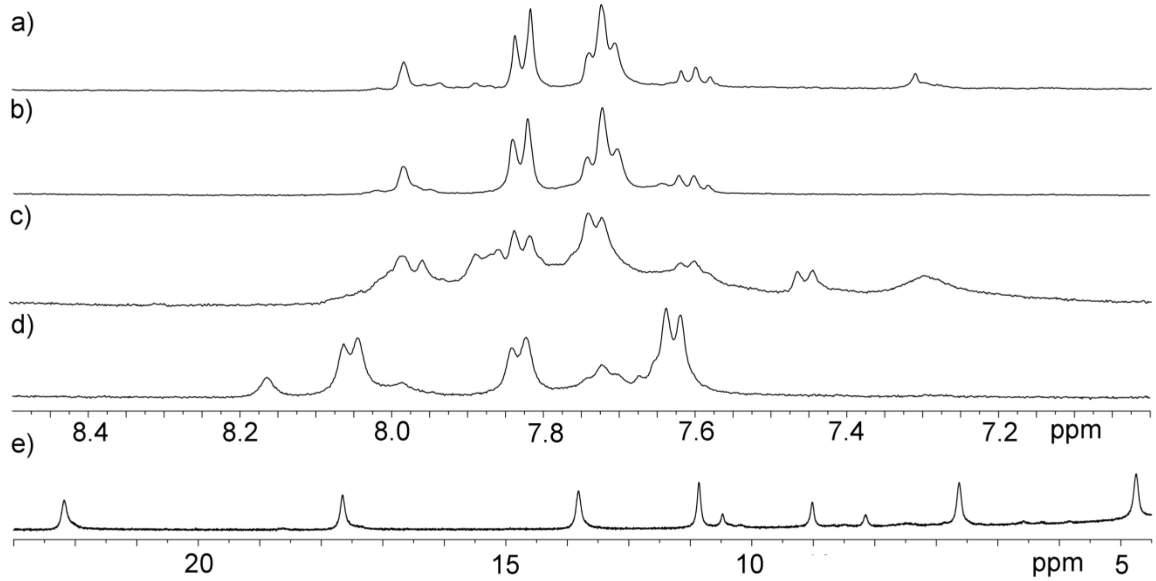

Figure 3.6: Complexation with ligand **3.20**: a) **3.20**; b) $Ga(OTf)_3$; c) $RuCl_3 \cdot xH_2O$; d) $Bi(OTf)_3$; e) $Pr(OTf)_3$ (400 MHz, DMSO-d_6, 298 K).

3.7 Synthesis of Functionalized Ligand Cores

A larger, tetrahedral complex allows for the introduction of larger, more reactive functional groups than simple anilines or pyridines. A benzyl amine would be more reactive than an aniline, and it was one of the first functional groups to be targeted.

Figure 3.7 shows the synthesis of a dibromo benzylamine. Bromination of methyl 3,5-dibromo-4-methylbenzoate **3.21** with NBS yielded bromide **3.22** in quantitative yield. This could be converted to azide **3.23** by reaction with sodium azide under phase transfer conditions. Several reduction methods were attempted, but none were able to successfully reduce the azide to the desired benzylamine **3.24**. Hydrogenation with Pd/C was unsuccessful when either H_2 or hydrazine was used as a hydrogen source. Lithium aluminium hydride successfully reduced the azide to an amine, but only one bromide was retained due to metal-halogen exchange. Staudinger reduction with triphenylphosphine successfully yielded the intermediate iminophosporane, but it was not able to be hydrolyzed. Palladium-catalyzed directed arylation from benzylamine was successful in directly synthesizing the terphenyl with a protected endohedral benzyl amine.[7] This reaction, however, suffered from low yield after extensive purification and was poorly reproducible.

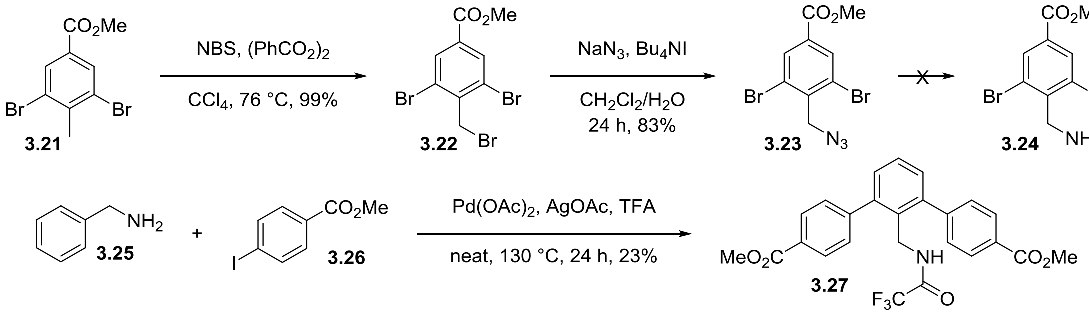

Figure 3.7: Synthesis of endohedral benzyl amines.

An endohedral carboxylic acid was also targeted, as it would present an acidic proton to the interior of a complex. Figure 3.8 shows the synthesis of endohedral acids. Direct oxidation of 2,6-dibromotoluene **3.28** to 2,6-dibromobenzoic acid **3.31** was unsuccessful, but **3.31** could be prepared stepwise. Bromination of **3.28** followed by displacement of the bromide with potassium hydroxide yielded alcohol **3.29**, and this could be more easily oxidized. Incorporation of the acid into the paddle-wheel ligands discussed in Chapter 2 was unsuccessful. Sonogashira coupling yielded only the monocoupled **3.33**, and reaction with an additional equivalent of 3-ethynylpyridine was also unsuccessful. This poor reactivity is likely due to a copper-catalyzed competitive cyclization between the acid and the alkyne.[8]

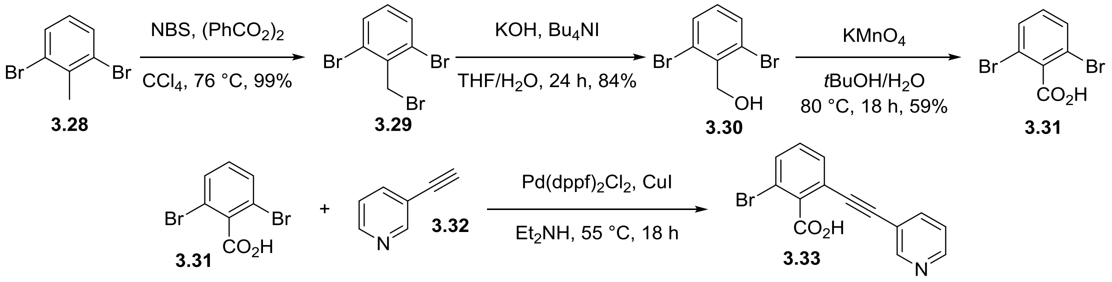

Figure 3.8: Synthesis of endohedral carboxylic acids.

A number of substituted 2,6-dihalophenols are commercially available, and these were useful starting points for the introduction of more complex endohedral functionality as shown in Figure 3.9. S_N2 reaction of **3.34** with 2 eq. ethyl bromoacetate followed by hydrolysis yielded diacid **3.35**. Suzuki reaction with 4-ethoxycarbonylphenylboronic acid yielded terphenyl **3.36** in good yield. This could be reacted with hydrazine to make precursors to the ligands discussed in Chapters 5 and 6, but the diacid resulted in the retention of hydrazine, and successful ligand synthesis could not be achieved.

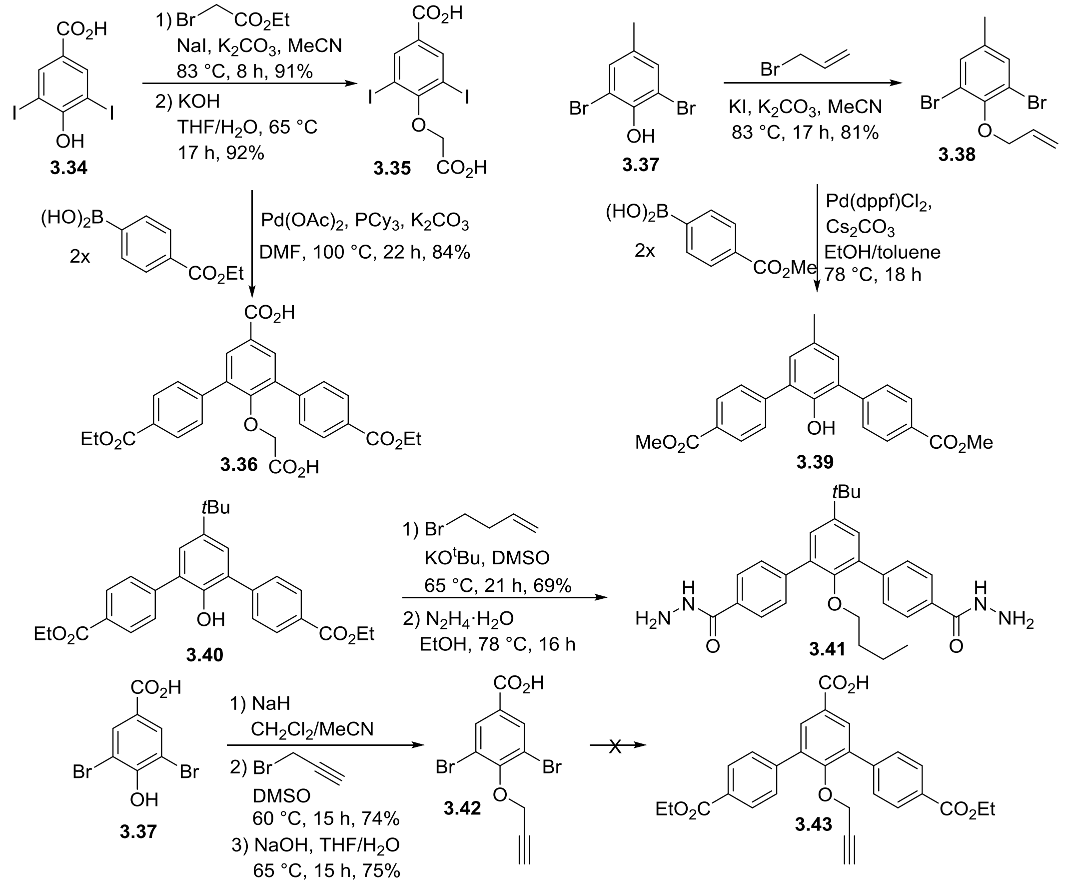

Figure 3.9: Endohedral functionality derived from phenols.

Endohedral alkenes or alkynes were targeted as substrates for thiol-ene or thiol-yne "click" reactions. These reactions proceed easily under mild conditions, making them suitable for reactivity in a supramolecular system.[9] S_N2 reaction of 2,6-dibromo-4-methylphenol **3.37** with allyl bromide yielded allyl ether **3.38**, but the allyl group was not tolerant to Suzuki coupling conditions. The allyl group could be introduced by S_N2 reaction from the terphenyl phenol, but it was not tolerant to the hydrazine required for the next step of ligand synthesis. Because of the instability of the allyl group, a homoallyl group was introduced instead. While the homoallyl-functionalized ester could be synthesized from terphenyl phenol **3.40**, it was also intolerant to hydrazine, and hydrogenation of the alkene resulted. A propargyl group could be introduced from the dibromide, and S_N2 reaction of propargyl bromide with **3.37** followed by hydrolysis yielded dibromide **3.42**. This was intolerant to Suzuki coupling conditions, and **3.43** could not be synthesized. Because of the precedent of instability in the allyl group, further optimization of reactions to introduce the propargyl group was not pursued.

Introduction of large, inert functional groups was more successful than attempts toward reactive functionality, as shown in Figure 3.10. Benzyl ether **3.45** was synthesized from 2,6-dibromophenol and benzyl bromide. Phenylurea **3.47** could be synthesized by derivatization of 2,6-dibromoaniline **3.46**. An adamantanamide could even be introduced, and this was synthesized from **3.46** and 1-adamantane carboxylic acid chloride **3.48**. All of these functional groups were tolerant to Suzuki coupling and the corresponding terphenyl diesters were obtained.

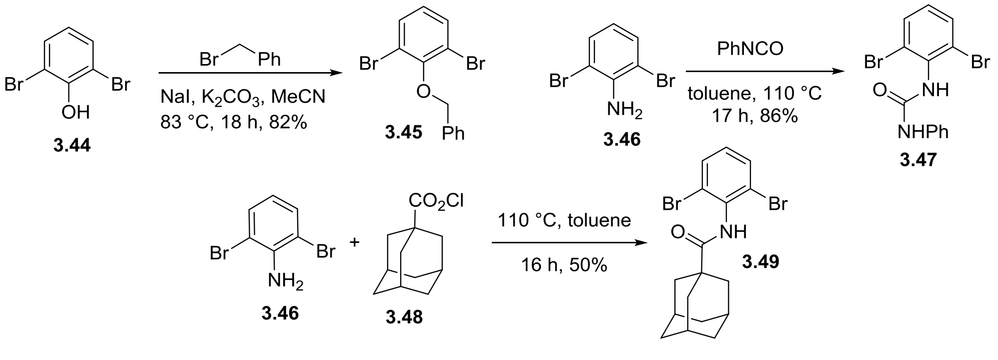

Figure 3.10: Synthesis of large endohedral functional groups.

3.8 Conclusion

This chapter has highlighted the synthesis of terphenyl-based ligands for the formation of tetrahedral M_4L_6 assemblies. Hydroxamic acid synthesis suffered from the instability of *N*-phenylhydroxylamine and competitive nucleophilicity of *N*-alkyl hydroxylamines. Benzyl protection of the hydroxylamine oxygen allowed for reactivity at the nitrogen, and *bis*-hydroxamic acid ligands could be synthesized. Complexation was successful with the nontransition metals Bi and Pr, but poor solubility limited characterization. Several routes to endohedral functionalization were attempted, and reactive functional groups could not be successfully introduced into the terphenyl ligand cores. Large, unreactive functional groups could be introduced and incorporated into ligands.

3.9 References

1) Johnson, A. M.; Moshe, O.; Gamboa, A. S.; Langloss, B. W.; Limtiaco, J. F. K.; Larive, C. K.; Hooley, R. J. “Synthesis and properties of metal-ligand complexes with endohedral amine functionality.” *Inorg. Chem.* **2011**, *50*, 9430-9442.

2) Chakrabarthy, R., Mukherjee, P. S.; Stang, P. J. “Supramolecular coordination: Self-assembly of finite two- and three-dimensional ensembles.” *Chem. Rev,* **2011**, *111*, 6810-6918.

3) a) Beissel, T.; Powers, R. E.; Raymond, K. N. “Symmetry-based metal complex cluster formation.” *Angew. Chem. Int. Ed. Engl.* **1996**, *35*, 1084-1086.; b) Beissel, T.; Powers, R. E.; Parac, T. N.; Raymond, K. N. “Dynamic isomerization of a supramolecular tetrahedral M_4L_6 cluster.” *J. Am. Chem. Soc.* **1999**, *121*, 4200-4206.

4) Evans, D. A.; Song, H.-J.; Fandrick, K. R. “Enantioselective nitrone cycloadditions of α,β-unsaturated 2-acyl imidazoles catalyzed by bis(oxazolinyl)pyridine-cerium(IV) triflate complexes.” *Org. Lett.* **2006**, *8*, 3351-3354.

5) White, R. C.; Selvam, T.; Ihmels, H.; Adam, W. “Photolysis of N-phenylhydroxylamine: A novel photochemical disproportionation reaction in N-O bond cleavage assisted by hydrogen bonding.” *J. Photochem. Photobiol., A.* **1999**, *122*, 7-10.

6) Nemchik, A.; Badescu, V.; Phanstiel, O., IV “*N*-(benzoyloxy)amines: An investigation of their thermal stability, synthesis, and incorporation into novel peptide constructs.” *Tetrahedron*, **2003**, *59*, 4315-4325.

7) Lazareva, A.; Dauglis, O. “Direct palladium-catalyzed *ortho*-arylation of benzylamines.” *Org. Lett.* **2006**, *8*, 5211-5213.

8) a) Castro, C. E.; Havlin, R.; Honwad, V. K.; Malte, A.; Moje, S. “Copper (I) substitutions. Scope and mechanism of cuprous acetylide substitutions.” *J. Am. Chem. Soc.* **1969**, *91*, 6464-6470.; b) Inack-Ngi, S.; Rahmani, R.; Commeiras, L.; Chouraqui, G.; Thibonnet, J.; Duchêne, A.; Abarbri, M.; Parrain, J.-L. “Copper-catalyzed preparation of γ-alkylidenebutenolides and isocoumarins under mild palladium-free conditions.” *Adv. Synth. Catal.* **2009**, *351*, 779-788.

9) Dondoni, A. “The emergence of thiol-ene coupling as a click process for materials and bioorganic chemistry.” *Angew. Chem., Int. Ed.* **2008**, *47*, 8995-8997.

Chapter Four: Tridentate Indazole Ligands

4.1 Introduction

The most common way to form supramolecular tetrahedra is with *bis*-bidentate ligands and octahedral transition metals as described in Chapter 3. An alternative strategy utilizes tridentate ligands and metals with nine coordination sites such as lanthanides. There are several lanthanide tetrahedra reported in the literature that form from *bis*-[1] or *tris*-tridentate[2] ligands. More information on self-assembled lanthanide complexes will be found in Chapter 6.

4.2 Ligand Synthesis

A similar synthetic strategy to the hydroxamic acids was used to synthesize tridentate ligands. The terphenyl acid described in Chapter 3 was activated with HCTU, and reaction with commercially available indazole-3-carboxylic acid yielded *bis*-tridentate ligand **4.3**. The coordination angle of this ligand is similar to that of the hydroxamic acids, and an analogous complex was predicted to form.

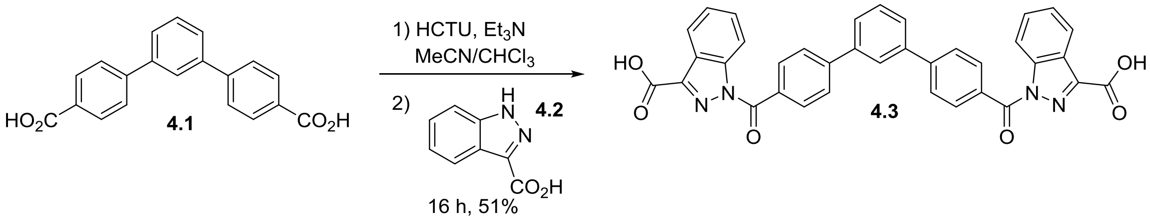

Figure 4.1: Synthesis of bis-tridentate ligand.

4.3 Metal Complexation

Complexation screens were performed by mixing metal and ligand in an NMR tube. Several solvents were tested, and **4.3** was soluble in DMSO, sparingly soluble in water, acetone, and acetonitrile, and insoluble in chloroform. No complexation with $Pr(NO_3)_3$ was observed with neutral **4.3** in any of the screens. When triethylamine was added, complexation was observed due to the stronger coordination ability of an anionic ligand. A discrete complex was formed in DMSO as shown in Figure 4.2. The ^1H NMR spectrum appeared similar to that of the hydroxamic acid-Pr complex described in Chapter 3. Peaks broadened and shifted, but not to as great an extent.

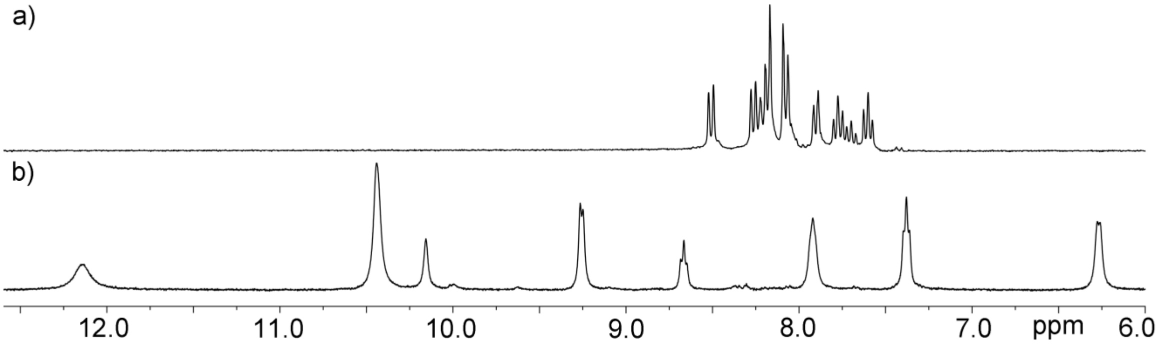

Figure 4.2: Complexation with $Pr(NO_3)_3$: a) **4.3**; b) **4.3** + $Pr(NO_3)_3$ + Et_3N (400 MHz, DMSO-d_6, 298 K).

4.4 Ligand Derivatization

Because diacid **4.3** was soluble only in DMSO, alkyl chains were added in an attempt to increase solubility in solvents that were more suitable for mass spectrometry and crystal growth. Two sites were available for derivatization—the exterior of the terphenyl core and the acid of the indazole chelator. Suzuki coupling between dibromide **4.4** and 4-methoxycarbonylphenylboronic acid yielded ester **4.6** with an external acid. A hexyl chain could be added after reaction with HCTU and *N*-hexylamine. Hydrolysis to acid **4.7** followed by HCTU coupling with indazole-3-carboxylic acid yielded ligand **4.8** which should show increased solubility in organic solvents.

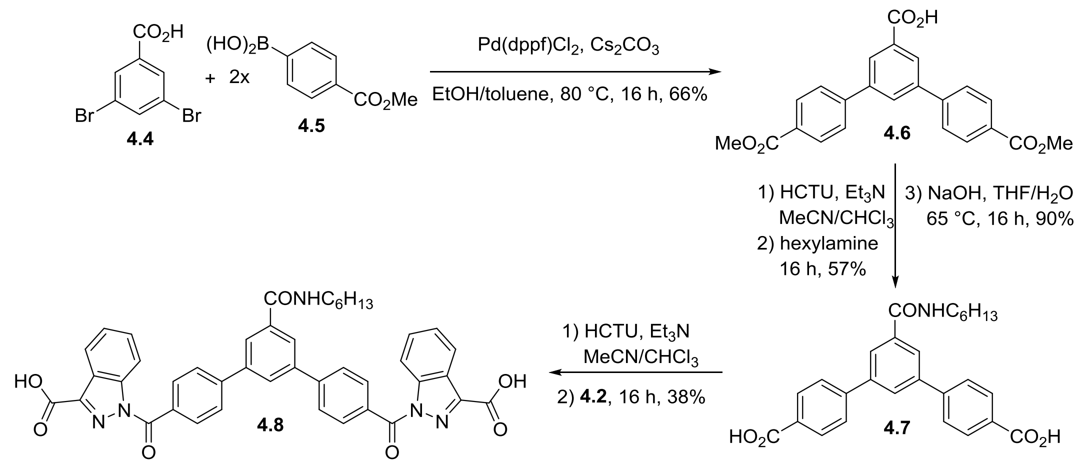

Figure 4.3: Addition of hexyl chains to terphenyl ligand core.

A different strategy was used to derivatize the indazole acid. Fischer esterification of indazole-3-carboxylic acid yielded ester **4.9** which could be converted to amide **4.10** after reaction with lithium dihexylamide. HCTU coupling between terphenyl acid **4.1** and the alkylated derivatives yielded ligands **4.11** and **4.12**.

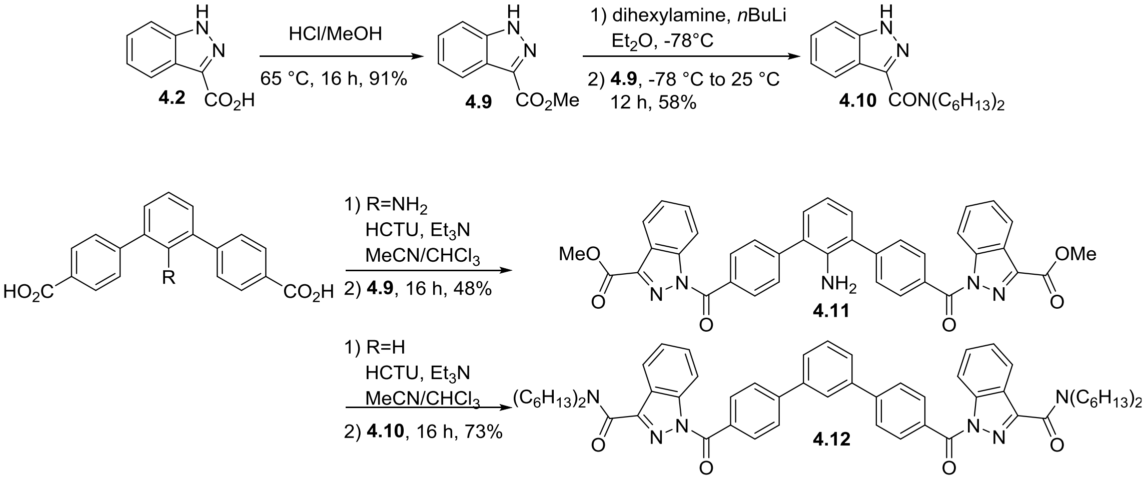

Figure 4.4: Indazole acid derivatization and synthesis of alkylated ligands.

4.5 Complexation of Alkylated Ligands

Complexation experiments similar to those of **4.3** were performed with hexyl-derivatized **4.8**. Complexation was similar to that of **4.3**, but no increase in solubility was observed. Compared to deprotonated acids **4.3** and **4.8**, the complexation ability of neutral **4.11** and **4.12** was significantly poorer. No complexation between ester **4.11** and $Pr(NO_3)_3$ was observed in chloroform, DMSO, water, or acetone, even after heating. NMR titration of $Sm(OTf)_3$ into amide **4.12** showed extremely weak binding as shown in Figure 4.5. Peaks shifted as metal was added, which is indicative of complexation, but an endpoint is not reached even after the addition of 5 eq. Sm.

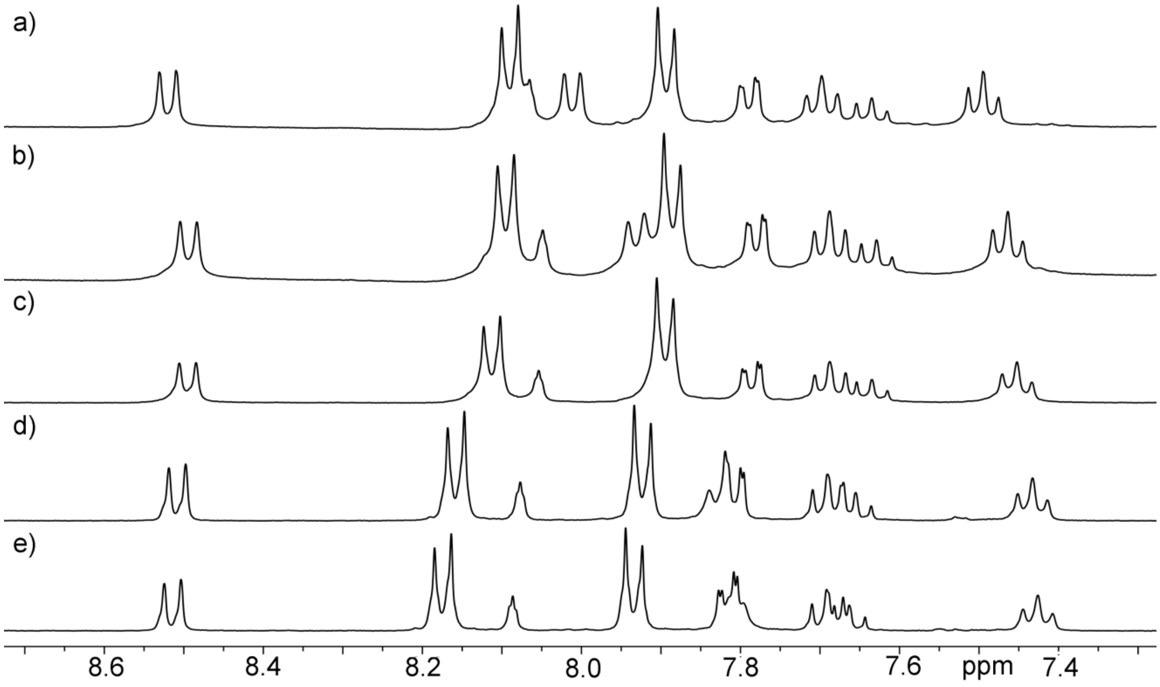

Figure 4.5: Titration of $Sm(OTf)_3$ into **4.12**: a) **4.12**; b) 0.5 eq.; c) 1 eq.; d) 3 eq.; e) 5 eq. (400 MHz, DMSO-d_6, 298 K).

This work has shown that it is possible to design ligands capable of binding lanthanides, but the solubility characteristics of this system are undesirable. Complexes were soluble only in DMSO which limits the potential for characterization by mass spectrometry. This also limits the methods available for crystal growth. Derivatization of the ligands to make neutral coordinators was effective in increasing the solubility of the ligands, but complexation was too weak to be effective for use in supramolecular self-assembly.

4.6 References

1) a) Liu, W.; Wu, X.; He, C.; Jiao, Y.; Duan, C. “Self-assembly of cerium-based metal-organic tetrahedrons for size-selectively luminescent sensing natural saccharides.” *Chem. Commun.* **2009**, 7554-7556.

2) a) Wang, J.; He, C.; Wu, P.; Wang, J.; Duan, C. “An amide-containing metal-organic tetrahedron responding to a spin-trapping reaction in a fluorescent enhancement manner for biological imagin of NO in living cells.” *J. Am. Chem. Soc.* **2011**, *133*, 12402-12405.; b) El Aroussi, B.; Guénée, L.; Pal, P.; Hamacek, J. “Lanthanide-mediated supramolecular cages and host-guest interactions.” *Inorg. Chem*. **2011**, *50*, 8588-8597.; c) Hamacek, J.; Poggiali, D.; Zebret, S.; El Aroussi, B.; Schneider, M. W.; Mastalerz, M. “Building large supramolecular nanocapsules with europium cations.” *Chem. Commun.* **2012**, *48*, 1281-1283.; d) Hamacek, J.; Bernardinelli, G.; Filinchuk, Y. “Tetrahedral assembly with lanthanides: Toward discrete polynuclear complexes.” *Eur. J. Inorg. Chem.* **2008**, 3419-3422.

Chapter Five: Variable Assembly in Bismuth Complexes

5.1 Introduction

Transition metals are most commonly utilized in supramolecular self-assembly because of their predictable geometry.[1] This is a powerful tool in rational design and allows for complementary ligands to be designed to form a complex of a desired shape. Lanthanides are becoming more popular when combined with tridentate ligands in self-assembled complexes[2] but still lack the popularity of transition metals due to challenges which will be discussed in Chapter 6. A relatively unexplored area in supramolecular self-assembly is the use of main group metal ions. A large advantage that main group metal ions have over those derived from transition metals is their diamagnetism. NMR spectroscopy is a powerful tool in the characterization of assemblies and can be used to monitor guest binding and reactivity inside the complex, in addition to determining information about the assembly itself. It also allows for real-time analysis of dynamic processes. Paramagnetic metal ions often hinder or prevent NMR characterization, which makes more expensive and less accessible techniques such as X-ray crystallography required for characterization. In addition to paramagnetism, transition metals ions can exhibit redox properties that can make assemblies sensitive to air and water, making them difficult to handle and characterize. Main group metal ions are diamagnetic and exhibit less variability in their oxidation states, allowing complexes to be easily handled and studied by NMR. They also have a more flexible coordination sphere and lack the predictable coordination geometry of transition metals. While this makes it more difficult to rationally design assemblies, it opens the possibility for accessing new types of supramolecular assemblies or switchable assemblies.

Complexes with aluminum and gallium ions are known[3] and form complexes analogous to those with transition metals, particularly iron. Their charge:size ratio makes them suited for coordination with hard, oxygen-containing ligands. Complexes with larger main group metals are far more rare, but self-assembled structures containing arsenic,[4] germanium,[5] tin,[6] lead,[7] and antimony[8] have been reported. Another underutilized metal in self-assembly is bismuth. Multiple coordination numbers of the metal are known,[9] and its flexible coordination sphere may allow for new advances in the construction of supramolecular cages. Self-assembled M_2L_3 bismuth-thiolate complexes have been reported along with arsenic and antimony analogues.[10] In this example, bismuth is tricoordinate. To access larger complexes with more predictable assembly properties, all nine coordination sites of bismuth must be exploited. A large number of coordination sites and a +3 charge state are similar to the lanthanides, and tridentate ligands should allow for complexes analogous to those formed with lanthanides. Additionally, bismuth is diamagnetic, and complexes will be amenable to NMR analysis.

5.2 Ligand Synthesis

Tridentate ligand **5.3** was synthesized as shown in Figure 5.1.[11] Diester **5.1** was treated with hydrazine hydrate in ethanol to yield dihydrazide **5.2**. This was reacted with 2-pyridinecarboxaldehyde and catalytic acetic acid to form ligand **5.3**. The carbonyl oxygen and imine and pyridine nitrogens have lone pairs available for coordination, and three of these ligands were predicted to assemble around 9-coordinate bismuth(III).

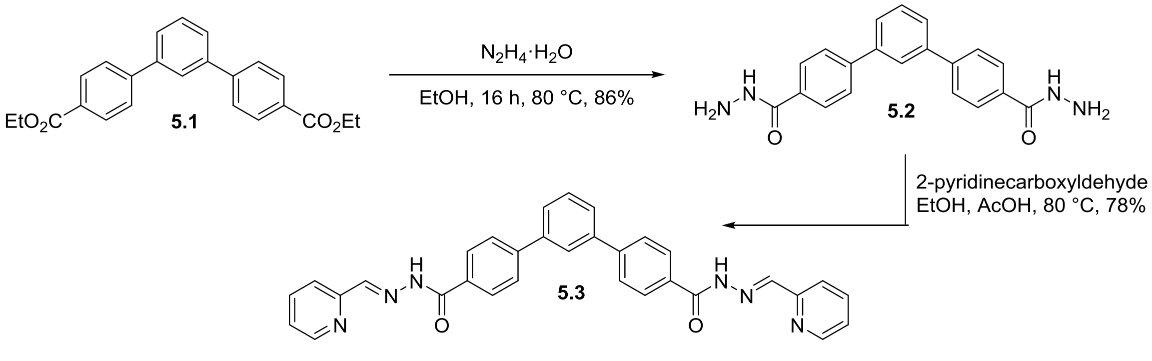

Figure 5.1: Synthesis of bis-pyridylhydrazone ligand **5.3**.

5.3 Metal Complexation

Self-assembly was studied by ^1H NMR in acetonitrile. Ligand **5.3** was only sparingly soluble, but rapid solubilization was observed upon the addition of $Bi(OTf)_3$. Figure 5.2 shows the downfield region of the ^1H NMR spectrum during a titration with $Bi(OTf)_3$. The *ortho*-pyridyl proton H_1 and imine proton H_2 were monitored during the titration as these peaks are well defined and separated from the rest of the spectrum. In contrast to the paddle-wheel complexes described in Chapter 2, signals for ligand and complex were not observed in the same spectrum, indicating that binding is weaker despite multidentate coordination. No complexation was observed in the competitively coordinating DMSO.

After addition of 0.5 eq $Bi(OTf)_3$, no signal for ligand remained and only one complex was observed in the ^1H NMR (Figure 5.2a). A second set of peaks began to grow in at 0.67 eq (Figure 5.2b) while the peaks for the first remained, and the peaks for the first complex went away after the addition of 1 eq $Bi(OTf)_3$ (Figure 5.2c). When 2 eq $Bi(OTf)_3$ were added, peaks for a third complex were observed (Figure 5.2d), and this was the dominant complex in the presence of excess $Bi(OTf)_3$ (Figure 5.2e).

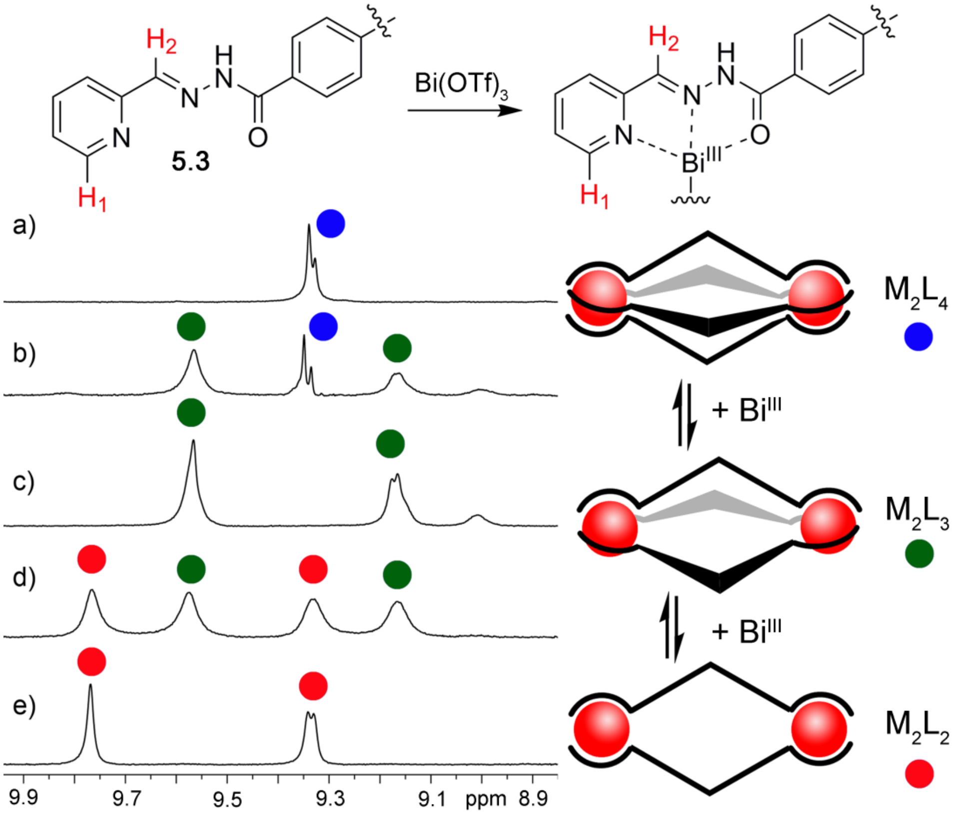

Figure 5.2: ^{1}H NMR titration of $Bi(OTf)_3$ into ligand **5.3**: a) 0.5eq.; b) 0.67 eq.; c) 1 eq.; d) 2 eq.; e) 3 eq. (400 MHz, CD_3CN, 298 K).

Based on the metal:ligand stoichiometry during the titration, the three complexes can be assigned as $[(\mathbf{5.3})_4Bi_2](OTf)_6$, $[(\mathbf{5.3})_3Bi_2](OTf)_6$, and $[(\mathbf{5.3})_2Bi_2](OTf)_6$. This highlights the versatility of bismuth in self-assembly, as transition metals do not exhibit this variable coordination, even with this same chelator.[12] The NH protons were retained in all complexes, suggesting that complexation is occurring with the neutral ligand and that positively-charged assemblies are forming.

5.4 Mass Spectrometric Analysis

Complexes $[(\mathbf{5.3})_4Bi_2](OTf)_6$, $[(\mathbf{5.3})_3Bi_2](OTf)_6$, and $[(\mathbf{5.3})_2Bi_2](OTf)_6$ were analyzed by ESI mass spectrometry. Analysis of the $[(\mathbf{5.3})_2Bi_2](OTf)_6$ complex (composition verified by NMR) led to the formation of all three complexes (Figure 5.3). Complexes were observed as the +2 cation, and the loss of triflic acid from the triflate counterions and four of the hydrazone NH protons accounts for the charge state. The +1 state with one triflate was also observed for the M_2L_2 complex. It may be possible to observe this for the larger complexes, but the mass of their +1 ions would exceed the detection limit for the spectrometer.

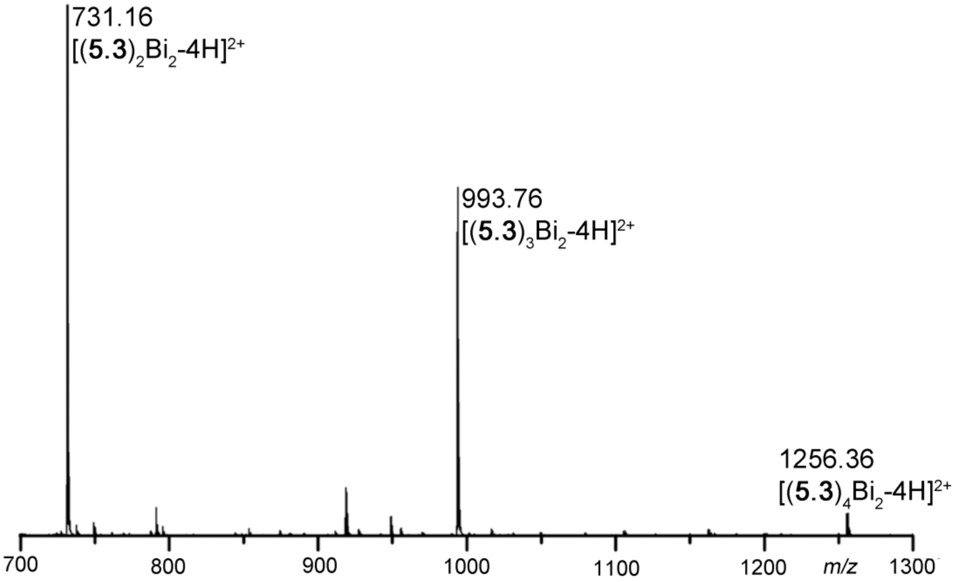

Figure 5.3: ESI-MS spectrum of **5.3** + $Bi(OTf)_3$ indicating formation of the M_2L_2, M_2L_3, and M_2L_4 complexes.

To favor the formation of the [(**5.3**)$_4$Bi$_2$](OTf)$_6$ and [(**5.3**)$_3$Bi$_2$](OTf)$_6$ complexes, samples containing 0.5 and 1 eq. Bi were prepared. All three complexes were again observed, and the [(**5.3**)$_4$Bi$_2$-4H]$^{2+}$ peak was enhanced in the sample containing 0.5 eq. Bi. The presence of three peaks and the intensity of [(**5.3**)$_2$Bi$_2$-4H]$^{2+}$ indicates fragmentation during ionization. Ligand **5.3** is neutral and does not change the charge of the complex if a ligand associates or dissociates during ionization.

5.5 Reversible Assembly

The presence of multiple species during the NMR titration and the necessity for excess Bi to drive formation of $[(\mathbf{5.3})_2Bi_2](OTf)_6$ suggests weak binding is occurring. While the equilibrium constants for the M_2L_4—M_2L_3 and M_2L_3—M_2L_2 conversions are linked, they can be calculated in the spectra where two species are observed (Figures 5.2b and 5.2d) assuming zero concentration for other species. The equilibrium constant for $[(\mathbf{5.3})_4Bi_2](OTf)_6$—$[(\mathbf{5.3})_3Bi_2](OTf)_6$ is 162 M^{-1} showing that $[(\mathbf{5.3})_3Bi_2](OTf)_6$ is strongly favored over $[(\mathbf{5.3})_4Bi_2](OTf)_6$. The equilibrium constant for $[(\mathbf{5.3})_3Bi_2](OTf)_6$—$[(\mathbf{5.3})_2Bi_2](OTf)_6$ is only 8 M^{-1}, showing a much similar favorability for these complexes. An equilibrium constant for the formation of $[(\mathbf{5.3})_4Bi_2](OTf)_6$ could not be calculated by NMR because undefined bismuth-ligand aggregates rather than discrete complexes are formed at low bismuth concentrations, and peaks for ligand and complex are not present at the same time for NMR integration.

The presence of multiple assemblies in the NMR titration and the magnitude of the equilibrium constants suggests that complexation is reversible. When ligand **5.3** was added to a solution of $[(\mathbf{5.3})_2Bi_2](OTf)_6$, peaks for $[(\mathbf{5.3})_3Bi_2](OTf)_6$ grew in and a mixture of $[(\mathbf{5.3})_2Bi_2](OTf)_6$ and $[(\mathbf{5.3})_3Bi_2](OTf)_6$ was observed (Figure 5.4). A similar pattern to the forward titration emerged, and $[(\mathbf{5.3})_3Bi_2](OTf)_6$ was the only complex observed with increasing ligand concentration (decreased relative bismuth concentration). A large amount of ligand was required to drive the titration backward. While peaks for $[(\mathbf{5.3})_4Bi_2](OTf)_6$ began to emerge, a clean spectrum could not be obtained and $[(\mathbf{5.3})_4Bi_2](OTf)_6$ was observed as a mixture with $[(\mathbf{5.3})_3Bi_2](OTf)_6$.

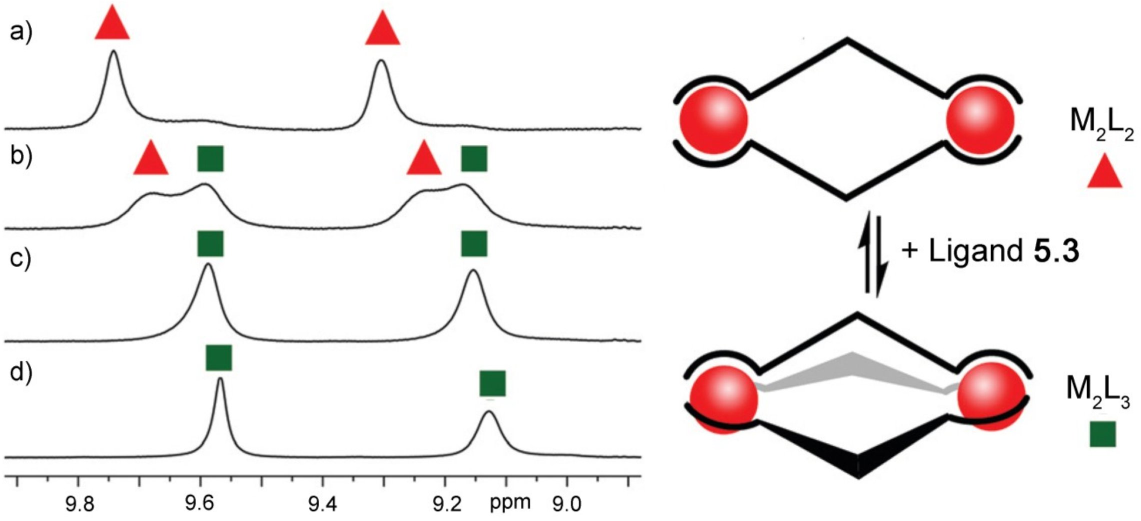

Figure 5.4: ^{1}H NMR titration of ligand **5.3** into preformed [(**5.3**)$_2$Bi$_2$](OTf)$_6$ complex: a) [(**5.3**)$_2$Bi$_2$](OTf)$_6$; b) 1.0 eq.; c) 1.8 eq.; d) 2.9 eq. (400 MHz, CD$_3$CN, 298 K).

5.6 X-Ray Crystallographic Analysis

Single crystals of [(**5.3**)$_2$Bi$_2$](OTf)$_6$ were obtained by diffusion of chloroform into a solution of complex in acetonitrile. Crystallization was attempted from samples containing different amounts of bismuth, but no other complexes crystallized. Figure 5.5a shows the crystal structure of [(**5.3**)$_2$Bi$_2$](OTf)$_6$.

In the solid state, [(**5.3**)$_2$Bi$_2$](OTf)$_6$ is a quasi-coordination polymer with each discrete M_2L_2 complex bridged by two triflates. Bismuth is nine-coordinate and six sites are occupied by two of the three tridentate ligands with the other three coordination sites occupied by triflates (Figure 5.5b). Two of the triflates are bridging and the third coordinates individually. Another uncoordinated triflate is present and balances the charge of the complex. Because three of the nine coordination sites in bismuth are occupied by labile triflates, it is likely that the structure of [(**5.3**)$_3$Bi$_2$](OTf)$_6$ is similar. Instead of three triflates coordinated to bismuth as observed in the crystal, these sites are instead occupied by a third ligand. Figure 5.5c shows the predicted structure of

$[(\mathbf{5.3})_3Bi_2](OTf)_6$, and this type of M_2L_3 helical structure is precedented for bent ligands and nine-coordinate lanthanides.[13]

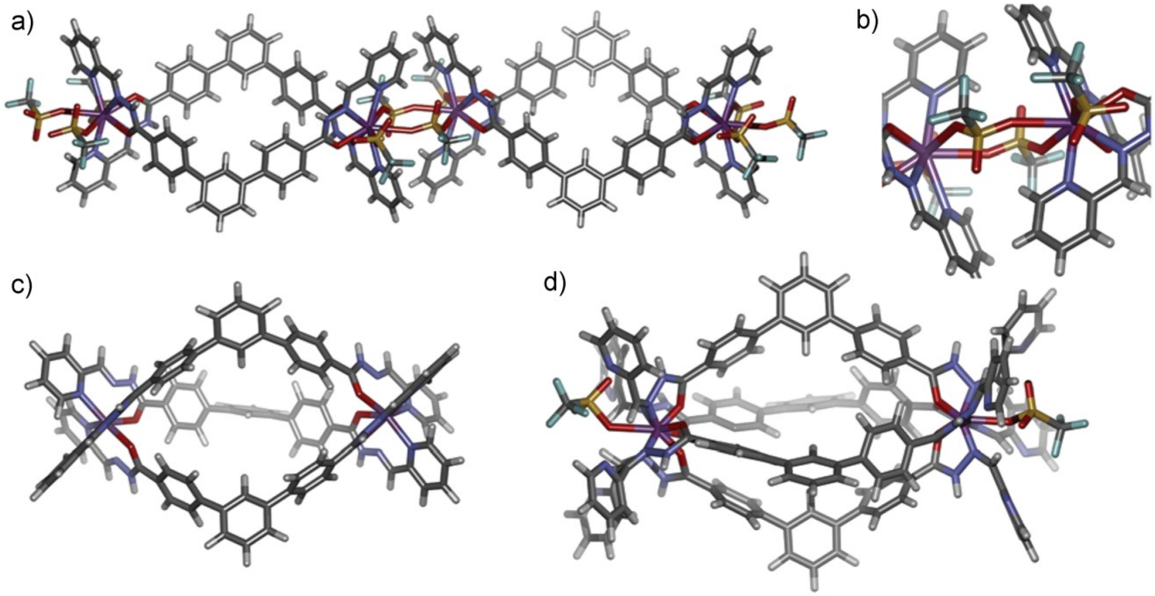

Figure 5.5: a) X-Ray diffraction structure of $[(\mathbf{5.3})_2Bi_2](OTf)_6$ in the solid state; b) expansion of the structure, indicating the coordination at bismuth; c) minimized structure of $[(\mathbf{5.3})_3Bi_2](OTf)_6$ (SPARTAN, AM1 force field); d) minimized structure of $[(\mathbf{5.3})_4Bi_2](OTf)_6$ (SPARTAN, AM1 force field).

The structure of $[(\mathbf{5.3})_4Bi_2](OTf)_6$ was more difficult to predict. Molecular minimization suggested that an M_2L_4 complex similar to the paddle-wheels discussed in Chapter 2 was possible if ligand **5.3** was acting as a bidentate rather than tridentate ligand. Figure 5.5d shows a minimized structure of this complex. Eight coordination sites on bismuth are occupied by ligands, and the ninth is occupied by a triflate. This is similar to the crystal of $[(\mathbf{5.3})_2Bi_2](OTf)_6$ where the sites unoccupied by ligand were filled by triflate. In contrast to the NMR spectra of $[(\mathbf{5.3})_2Bi_2](OTf)_6$ and $[(\mathbf{5.3})_3Bi_2](OTf)_6$, only one peak is shifted downfield. This corresponds to the imine proton rather than the *ortho*-pyridyl proton. A search of the Cambridge Crystallographic Database revealed that four N-O bidentate ligands can coordinate bismuth, providing precedent for the proposed structure.[14] Paddle-wheel ligand **2.3**, which only contains a pyridine for coordination, was also tested with bismuth. Downfield shifting of peaks was observed in the ^{1}H NMR titration (Figure 5.6), but H_c and H_d shifted the most instead of H_a and H_b, the protons next to the nitrogen of the pyridine. This gives further evidence that the pyridine does not participate in coordination.

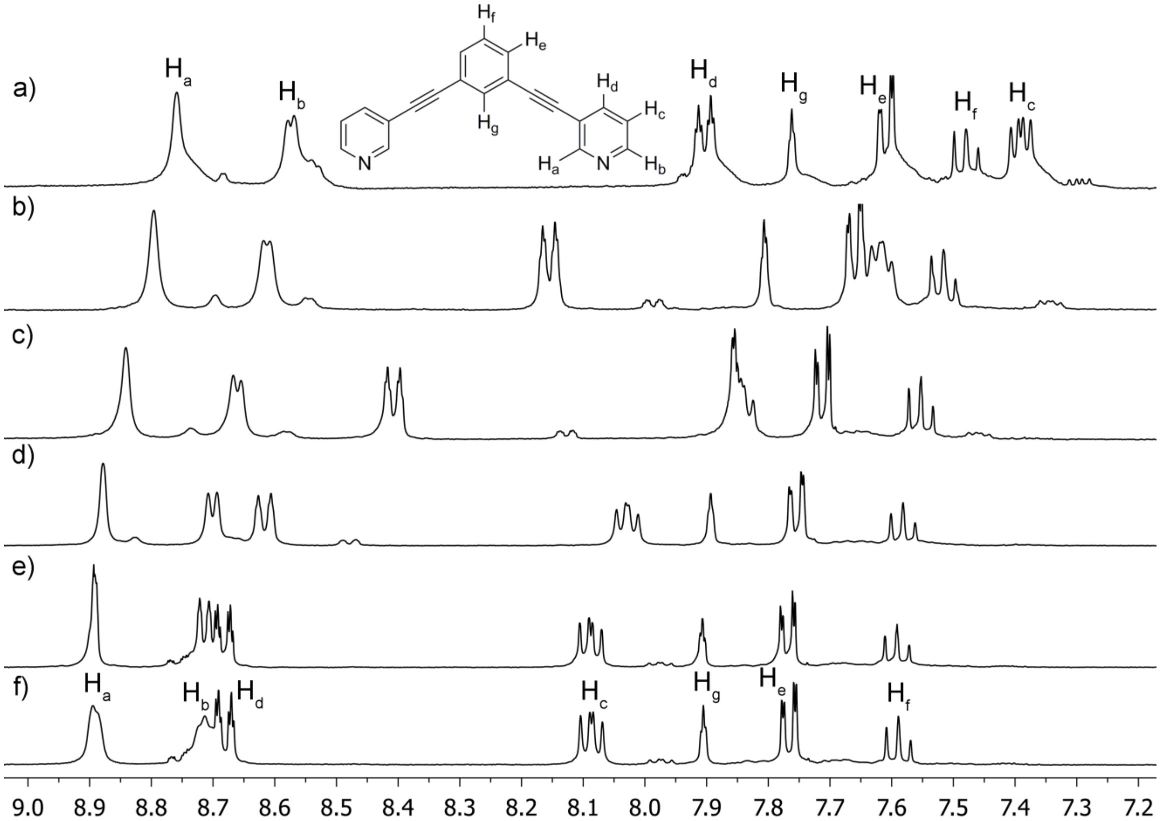

Figure 5.6: Bi titration into paddle wheel ligand **2.3**: a) **2.3**; b) 0.25 eq. $Bi(OTf)_3$; c) 0.5 eq.; d) 0.75 eq.; e) 1 eq.; f) 1.5 eq. (400 MHz, CD_3CN, 298 K).

5.7 Diffusion NMR Spectroscopy

Diffusion NMR was used to compare the relative size of the three complexes. Figure 5.7 shows the DOSY spectra of [(**5.3**)$_4$Bi$_2$](OTf)$_6$, [(**5.3**)$_3$Bi$_2$](OTf)$_6$, and [(**5.3**)$_2$Bi$_2$](OTf)$_6$. The diffusion coefficients for [(**5.3**)$_4$Bi$_2$](OTf)$_6$ and [(**5.3**)$_3$Bi$_2$](OTf)$_6$ are similar (6.32×10^{-10} m^2/s vs 4.34×10^{-10} m^2/s), indicating that the complexes are of a similar size and charge, which is what is expected from molecular modeling. The diffusion coefficient for [(**5.3**)$_4$Bi$_2$](OTf)$_6$ is also similar to the other complexes, indicating that it is likely existing as a discrete complex in solution and not a coordination polymer as observed by crystallographic analysis. These diffusion coefficients are similar to other discrete supramolecular complexes in CD$_3$CN that have been reported in the literature.[15]

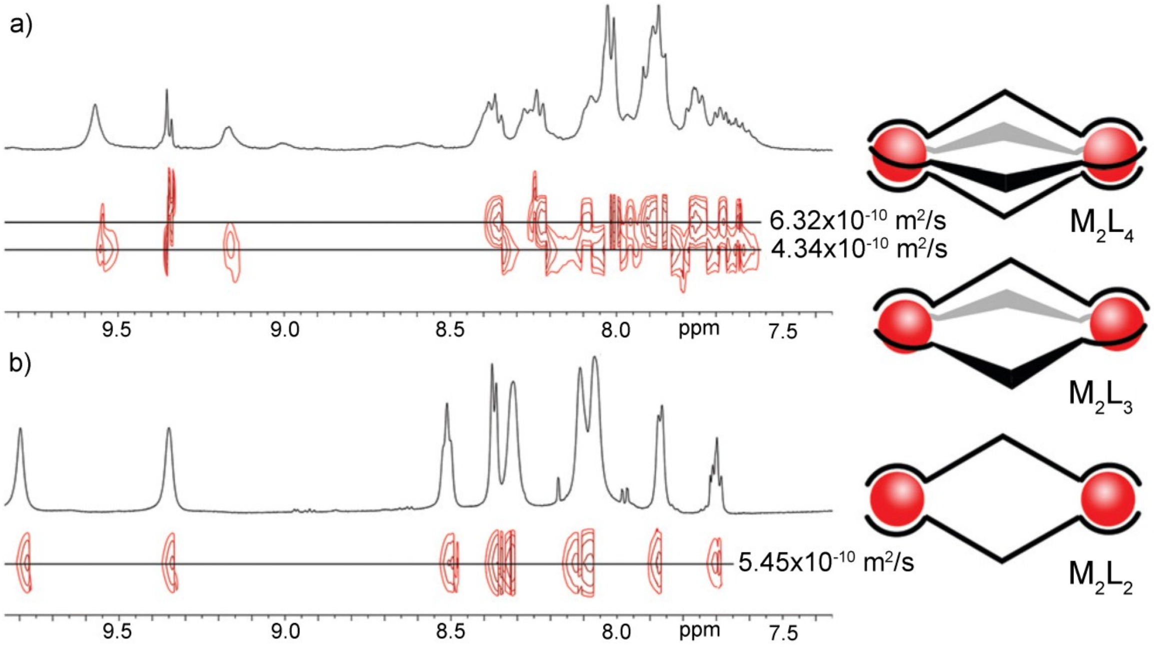

Figure 5.7: a) DOSY spectrum of **5.3** + 0.67 eq. Bi(OTf)$_3$ (CD$_3$CN, 600 MHz, 298 K, Δ=17.0 ms, δ=7000 μs, Diffusion coefficient=6.32×10^{-10} m^2/s for [(**5.3**)$_4$Bi$_2$](OTf)$_6$, 4.34×10^{-10} m^2/s for [(**5.3**)$_3$Bi$_2$](OTf)$_6$, and 3.06×10^{-9} m^2/s for CD$_3$CN); b) DOSY spectrum of **5.3** + 3 eq. Bi(OTf)$_3$ (CD$_3$CN, 600 MHz, 298 K, Δ=17.0 ms, δ=7000 μs, Diffusion coefficient=5.45×10^{-10} m^2/s for [(**5.3**)$_2$Bi$_2$](OTf)$_6$ and 3.80×10^{-9} m^2/s for CD$_3$CN).

5.8 Alternate Ligand Geometry

Experiments with a ligand of another geometry were also performed. Ligand **5.4** has the same chelator as **5.3** but is a linear, biphenyl ligand rather than a bent, terphenyl ligand. The linear geometry of **5.4** should prevent the formation of M$_2$L$_x$ complexes, and linear ligands are often used in the formation of M$_4$L$_6$ tetrahedra.[16] As with **5.3**, **5.4** was insoluble in acetonitrile until the addition of $Bi(OTf)_3$. Undefined coordination polymers were formed with less bismuth, highlighting the inability of **5.4** to form the M_2L_x complexes observed with **5.3**. After addition of 2 eq. $Bi(OTf)_3$, a discrete complex was observed in the NMR which could be assigned as an M_3L_3 triangle by mass spectrometry. Unfortunately, no crystals suitable for X-ray diffraction could be obtained to prove the structure unequivocally. Figure 5.8 shows the predicted structure of [(**5.4**)$_3$Bi$_3$](OTf)$_9$. The coordination geometry was modeled after [(**5.3**)$_2$Bi$_2$](OTf)$_6$ with six coordination sites filled by ligands and the other three by triflates. Analysis by diffusion NMR gave a similar diffusion coefficient to the complexes with **5.3** (4.88×10^{-10} m^2/s) suggesting that the charge and size properties are similar.

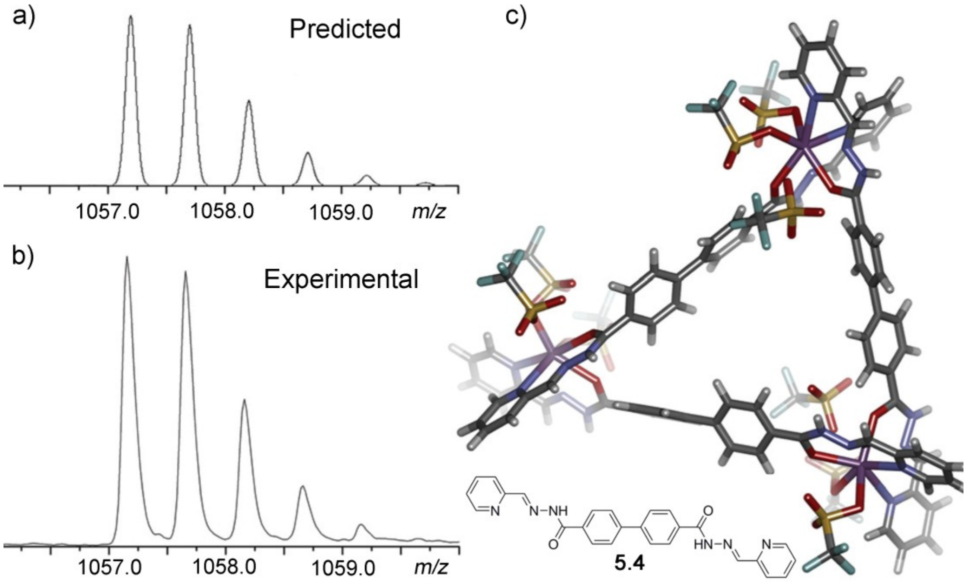

Figure 5.8: Formation of [(**5.4**)$_3$Bi$_3$](OTf)$_6$ triangle: a) predicted isotope pattern of [(**5.4**)$_3$Bi$_3$-6H(OTf)]$^{2+}$; b) experimental isotope pattern of [(**5.4**)$_3$Bi$_3$-6H(OTf)]$^{2+}$; c) minimized structure of [(**5.4**)$_3$Bi$_3$](OTf)$_9$ (SPARTAN, AM1 force field).

5.9 Other Effects on Assembly

Because of the coordinated triflates in the crystal structure of [(**5.3**)$_2$Bi$_2$](OTf)$_6$, the effects of triflate on solution assembly were studied. Bismuth(III) tetrafluoroborate, which contains more weakly coordinating counterions, was synthesized by mixing $BiBr_3$ and $AgBF_4$. After addition of 1 eq $Bi(BF_4)_3$ to **5.3**, a single complex with an NMR similar to $[(\mathbf{5.3})_4Bi_2](OTf)_6$ was obtained. Adding excess NaOTf to this assembly disrupted the complex, showing that triflate ions can competitively coordinate bismuth in the presence of weakly-coordinating ligands. Weak counterions on bismuth are required for assembly, and no assembly occurred with $BiBr_3$ because **5.3** is not a strong enough coordinator to displace the bromides.

Complexation with **5.3** is indeed relatively weak, and no coordination was observed when $Bi(OTf)_3$ was added to **5.3** in DMSO, a competitively coordinating solvent. When **5.3** was deprotonated with sodium hydride, the anionic ligand showed much stronger coordination, and complexes were able to be formed in DMSO. Variable coordination was observed in both acetonitrile and DMSO, and spectra were very similar to those of the protonated ligand. Assembly also occurred with $BiBr_3$. A complex spectrum was observed with low concentration of bismuth, but the NMR after addition of 1 eq. $BiBr_3$ looked similar to the spectrum of $[(\mathbf{5.3})_2Bi_2](OTf)_6$. The presence of this single complex suggests that the bromides cannot be displaced and only six coordination sites on bismuth are available for ligand coordination.

Endohedral functionality had no effect on assembly. The synthesis of phenylurea and adamantyl ligand cores is discussed in Chapter 3, and these were utilized to synthesize the corresponding tridentate ligands. A large functional group has the potential to change the variable assembly properties by disfavoring the more “cage-like” complexes, particularly the M_2L_4, through steric interactions among endohedral functional groups. Variable coordination similar to **5.3** was observed during titration of the phenylurea with $Bi(OTf)_3$, and molecular modeling suggested that the ligand was flexible enough to be oriented outside of the cage (Figure 5.9). Modeling also suggested similar flexibility with the adamantyl group. For endohedral functionality to be able to control assembly, it must be both large enough to prevent assembly of complexes and rigid enough to occupy the cavity.

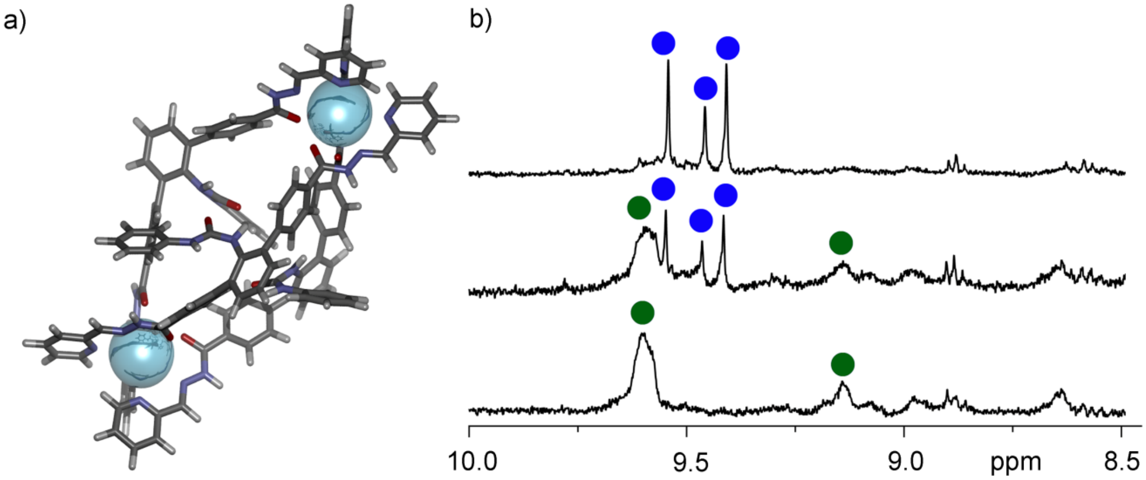

Figure 5.9: Assembly with an endohedral urea: a) model of M_2L_3 urea-functionalized complex with benzyl urea oriented outside of complex; b) portion of ^1H NMR titration showing variable coordination at 0.5, 0.67, and 1 eq. $Bi(OTf)_3$ (400 MHz, CD_3CN, 298K).

5.10 Lanthanide Complexation

Assembly of **5.3** with lanthanides was studied, since these metals also possess nine coordination sites. When an excess of $Y(OTf)_3$ was added to a solution of **5.3** in acetonitrile, peaks were shifted downfield, but a clean complex was not observed. Multiple species were present in solution but could not be identified. As with Bi, no coordination occurred in DMSO. Deprotonated **5.3** gave clean spectra when coordinated to lanthanides. Clean complexes of Y and La were obtained in DMSO, and titrations showed the same variable coordination as with Bi (Figure 5.10). A clean Sm complex could not be obtained, even after addition of 3 eq. $Sm(OTf)_3$. Complexation with paramagnetic Pr and Yb was also unsuccessful. These complexes could not be analyzed by mass spectrometry because DMSO was required for solubility.

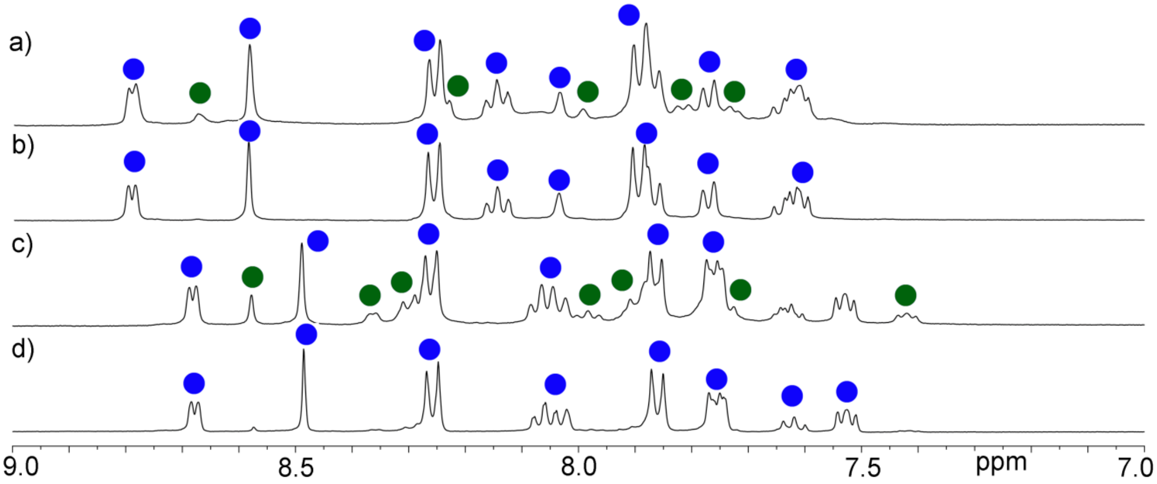

Figure 5.10: ^{1}H NMR spectra of variable coordination with lanthanides: a) **5.3** + 1.5 eq Y(OTf)$_3$; b) **5.3** + 3 eq Y(OTf)$_3$; c) **5.3** + 1.5 eq La(OTf)$_3$; d) **5.3** + 3 eq La(OTf)$_3$ (400 MHz, DMSO-*d*$_6$, 298 K).

5.11 Conclusion

This work has explored supramolecular assembly with bismuth, a main group metal that is relatively uncommon as a coordinating metal in self-assembled systems. While a bis-tridentate ligand was utilized, coordination was still relatively weak and reversible coordination was observed. Reversibility is uncommon in traditional transition metal based assemblies, and this weak, reversible coordination has the potential to be exploited in switchable assemblies. Lanthanide assemblies did not form cleanly with the protonated ligand, but similar assemblies to bismuth were observed with a more strongly coordinating, anionic ligand. This is interesting, as the crystal ionic radii of 8-coordinate bismuth and lanthanum differ by only 0.01 Å.[17] Assembly was also dependent on other factors such as the choice of counterion and ligand geometry.

5.12 References

1) a) Caulder, D. L.; Raymond, K. N. “Supermolecules by design.” *Acc. Chem. Res.* **1999**, *32*, 975-982.; b) Chakrabarthy, R., Mukherjee, P. S.; Stang, P. J. “Supramolecular coordination: Self-assembly of finite two- and three-dimensional ensembles.” *Chem. Rev,* **2011**, *111*, 6810-6918.; c) Fujita, M., Umemoto, K., Yoshizawa, M., Fujita, N., Kusukawa, T.; Biradha, K. “Molecular paneling via coordination.” *Chem. Commun.* **2001**, 509-518.; d) Smulders, M. M. J., Riddell, I. A., Browne, C.; Nitschke, J. R. “Building on architectural principles for three-dimensional metallosupramolecular construction.” *Chem. Soc. Rev.* **2013**, *42*, 1728-1754.

2) a) Jensen, T. B.; Scopelliti, R.; Bünzli, J.-C. G. “Tuning the self-assembly of lanthanide triple stranded heterobimetallic helicates by ligand design.” *Dalton Trans.* **2008**, 1027-1036.; b) Hamacek, J.; Poggiali, D.; Zebret, S.; El Aroussi, B.; Schneider, M. W.; Mastalerz, M. “Building large supramolecular nanocapsules with europium cations.” *Chem. Commun.* **2012**, *48*, 1281-1283.; c) Chen, X.-Y.; Bretonnière, Y.; Pécaut, J.; Imbert, D.; Bünzli, J.-C.; Mazzanti, M. “Selective self-assembly of hexameric homo- and heteropolymetallic lanthanide wheels: Synthesis, structure, and photophysical studies.” *Inorg. Chem.* **2007**, *46*, 625-637.

3) a) Caulder, D. L.; Raymond, K. N. “Supramolecular self-recognition and self-assembly in gallium(III) catecholamide triple helices.” *Angew. Chem. Int. Ed. Engl.* **1997**, *36,* 1439-1442.; b) Scherer, M.; Caulder, D. L.; Johnson, D. W.; Raymond, K. N. “Triple helicate—tetrahedral cluster interconversion controlled by host-guest interactions.” *Angew. Chem. Int. Ed. Engl.* **1999**, *38*, 1588-1592.; c) Wang, M.; Vajpayee, V.; Shanmugaraju, S.; Zheng, Y.-R.; Zhao, Z.; Kim, H.; Mukherjee, P. S.; Chi, K.-W.; Stang, P. J. “Coordination-driven self-assembly of M_3L_2 trigonal cages from preorganized metalloligands incorporating octahedral metal centers and fluorescent detection of nitroaromatics.” *Inorg. Chem.* **2011**, *50*, 1506-1512.;

4) a) Vickaryous, W. J.; Healy, E. R.; Berryman, O. B.; Johnson, D. W. “Synthesis and characterization of two isomeric, self-assembled arsenic-thiolate macrocycles.” *Inorg. Chem.* **2005**, *44*, 9247-9252.; b) Cangelosi, V. M.; Zakharov, L. N.; Fontenot, S. A.; Pitt, M. A.; Johnson, D. W. “Host-guest interactions in a series of self-assembled $As_2L_2Cl_2$ macrocycles.” *Dalton Trans.* **2008**, 3447-3453.; c) Pitt, M. A.; Zakharov, L. N.; Vanka, K.; Thompson, W. H.; Laird, B. B.; Johnson, D. W. “Multiple weak supramolecular interactions stabilize a surprisingly ‘twisted’ As_2L_3 assembly.” *Chem. Commun.* **2008**, *33*, 3936-3938.; d) Zukerman-Schpector, J. Otero-de-la-Roza, A.; Luaña, V.; Tiekink, E. R. T. “Supramolecular architectures based on As(lone pair)···π(aryl) interactions.” *Chem. Commun.* **2011**, *47*, 7608-7610.

5) Mugridge, J. S.; Fiedler, D.; Raymond, K. N. “A ferrocene-based catecholamide ligand: The consequences of ligand swivel for directed supramolecular self-assembly.” *J. Coord. Chem.* **2010**, *63*, 2779-2789.

6) García-Zarracino, R.; Höpfl, H. “Self-assembly of diorganotin(IV) moieties (R = Me, nBu, Ph) and 2,5-pyridinedicarboxylic acid to polymeric and trinuclear macrocyclic

hybrids with porous solid state structures – influence of substituents and solvent on the supramolecular structure." *J. Am. Chem. Soc.* **2005**, *127*, 3120-3130.

7) a) Onions, S. T.; Frankin, A. M.; Horton, P. N.; Hursthouse, M. B.; Matthews, C. J. "Self-assembly of a unique hexadecanuclear [4x(2x2)]-Pb_{16} 'grid of grids' type structure." *Chem. Commun.* **2003**, 2864-2865.; b) Najjari, B.; Le Gac, S.; Roisnel, T.; Dorcet, V.; Boitrel, B. "Metal migration processes in homo- and heterobimetallic bismuth(III)-lead(II) porphyrin complexes: Emergence of allosteric newton's cradle-like devices." *J. Am. Chem. Soc.* **2012**, *134*, 16017-16032.

8) a) Fontenot, S. A.; Cangelosi, V. M.; Pitt, M. A. W.; Sather, A. C.; Zakharov, L. N.; Berryman, O. B.; Johnson, D. W. "Design, synthesis and characterization of self-assembled As_2L_3 and Sb_2L_3 cryptands." *Dalton Trans.* **2011**, *40*, 12125-12131.; b) Pitt, M.; Johnson, D. W. "Main group supramolecular chemistry." *Chem. Soc. Rev.* **2007**, *36*, 1441-1453.

9) a) Summers, S. P.; Abboud, K. A.; Farrah, S. R.; Palenik, G. J. "Syntheses and structures of bismuth(III) complexes with nitrilotriacetic acid, ethylenediaminetetraacetic acid, and diethylenetriaminepentaacetic acid." *Inorg. Chem.* **1994**, *33*, 88-92.; b) Tran, D. T.; Chu, D.; Oliver, A. G.; Oliver, S. R. J. "A 3-D bismuth-organic framework containing 1-D cationic inorganic $[Bi_2O_2]^{2+}$ chains." *Inorg. Chem. Commun.* **2009**, *12*, 1081-1084.; c) Mendoza-Espinosa, D.; Rheingold, A. L.; Hanna, T. A. "Synthesis of bismuth and antimony complexes of the "larger" calix[*n*]arenes (n=6-8); from mononuclear to tetranuclear complexes." *Dalton Trans.* **2009**, 5226-5238.; d) Schilt, A. A.; Taylor, R. C. "Infra-red spectra of 1:10-phenanthroline metal complexes in the rock salt region below 2000 cm^{-1}." *J. Inorg. Nucl. Chem.* **1959,** *9*, 211-221.; e) Tan, R.; Yin, S.; Li, Y.; Qiu, R.; Meng, Z.; Song, X.; Luo, S.; Au, C.-T.; Wong, W.-Y. "Synthesis and structure of an air-stable organobismuth triflate complex and its use as a high-efficiency catalyst for the ring opening of epoxides in aqueous media with aromatic amines." *J. Organomet. Chem.* **2011**, *696*, 1579-1583.; f) Roggan, S.; Limberg, C.; Ziemer, B.; Brandt, M. "Intramolecular C-H activation in complexes with Mo-Bi metal bonds." *Angew. Chem., Int. Ed.* **2004**, *43*, 2846-2849.

10) Cangelosi, V. M.; Zakharov, L. N.; Johnson, D. W. "Supramolecular transmetallation leads to an unusual self-assembled P_2L_3 cryptand." *Angew. Chem., Int. Ed.* **2010**, *49*, 1248-1251.

11) Johnson, A. M.; Young, M. C.; Hooley, R. J. "Reversible multicomponent self-assembly mediated by bismuth ions." *Dalton Trans.* **2013**, *42*, 8394-8401.

12) a) Wang, J.; Wu, H.; He, C.; Zhao, L.; Duan, C. "Metal-organic cyclohelicates as optical receptors for glutathione: Syntheses, structures, and host-guest behaviors." *Chem. Asian J.* **2011**, *6*, 1225-1233.; b) Wu, H.; He, C.; Lin, Z.; Liu, Y.; Duan, C. "Metallohelical triangles for selective detection of adenosine triphosphate in aqueous media." *Inorg. Chem.* **2009**, *48*, 408-410.

13) a) Ryan, P. E.; Guénée, L.; Piguet, C. "Monitoring helical twists and effective molarities in dinuclear triple-stranded lanthanide helicates." *Dalton Trans.* **2013**, *42*, 11047-11055.; b) Piguet, C.; Bünzli, J.-C. G. "Self-assembled lanthanide helicates: From

basic thermodynamics to applications." In *Handbook on the Physics and Chemistry of Rare Earths*; Gschneider, K. A., Jr.; Bünzli, J.-C. G.; Pecharsky, V. K., Eds.; Elsevier: Amsterdam, The Netherlands, 2010; Vol. *40*, pp 301-553.; c) Shi, J.; Hou, Y.; Chu, W.; Shi, X.; Gu, H.; Wang, B.; Sun, Z. "Crystal structure and highly luminescent properties studies of bis-β-diketonate lanthanide complexes." *Inorg. Chem.* **2013**, *52*, 5013-5022.

14) Anjaneyulu, O.; Maddileti, D.; Kumara Swamy, K. C. "Structural motifs in phenylbismuth heterocyclic carboxylates—secondary interactions leading to oligomers." *Dalton Trans.* **2012**, *41*, 1004-1012.

51) a) Bunzen, J.; Iwasa, J.; Bonakdarzadeh, P.; Numata, E.; Rissanen, K.; Sato, S.; Fujita, M. "Self-assembly of $M_{24}L_{48}$ polyhedra based on empirical prediction." *Angew. Chem., Int. Ed.* **2011**, *51*, 3161-3163.; b) Li, W.; Chung, H.; Daeffler, C.; Johnson, J. A.; Grubbs, R. H. "Application of ^{1}H DOSY for facile measurements of polymer molecular weights." *Macromolecules* **2012**, *45*, 9595-9603.

16) a) Caulder, D. L.; Brückner, C.; Powers, R. E.; König, S.; Parac. T. N.; Leary, J. A.; Raymond, K. N. "Design, formation and properties of tetrahedral M_4L_4 and M_4L_6 supramolecular clusters." *J. Am. Chem. Soc.* **2001**, *123*, 8923-8938.; b) Clegg, J. K.; Cremers, J.; Hogben, A. J.; Breiner, B.; Smulders, M. M. J.; Thoburn, J. D.; Nitschke, J. R. "A stimuli responsive system of self-assembling anionbinding Fe_4L_6 cages." *Chem. Sci.* **2013**, *4*, 68-76.

17) CRC Handbook of Chemistry and Physics, 87th ed.; Lide, D. R., Ed.; CRC Press: Boca Raton, FL, 2006; Sect. 12, p11.

Chapter Six: Cooperative Thermodynamic Control of Selectivity in the Self-Assembly of Rare Earth Metal-Ligand Helices

6.1 Introduction

As described in previous chapters, transition metals are frequently used in supramolecular self-assembly. Their predictable coordination geometries make them useful when rationally designing complexes, but they may suffer from oxidative instability and paramagnetism, both of which present additional challenges to characterization. A less explored area, but one that is increasing in popularity, is lanthanide-based assemblies. Lanthanides possess a stable +3 oxidation state, and some members of the series are diamagnetic or only weakly paramagnetic, allowing for facile NMR analysis. One of the challenges in using lanthanides as structural elements in supramolecular complexes is their variable coordination geometry. Tridentate ligands can be used (rather than the typical mono- or bidentate ligands used with transition metals) to fill nine coordination sites of the metal. Lanthanides have been used most often in the synthesis of M_2L_3 helices,[1] although tetrahedra[2] and other structures[3] have been reported.

Members of the lanthanide series display similar physical properties, and little regard is given to the choice of a particular metal in an assembly. In some examples, analogous assemblies are formed with all metals in the series (with the exception of radioactive promethium).[4] The main difference between lanthanides is their size, although size differences are small. The difference in effective ionic radius (EIR) between La^{3+} and Lu^{3+} is only 0.21 Å,[5] and adjacent metals are exceptionally close in size. This makes selective binding and extraction of lanthanides quite challenging, and this is an active area of research in nuclear waste remediation.[6]

6.2 Ligand Synthesis

Tridentate salicylhydrazone-based ligands were synthesized as shown in Figure 6.1. Reaction of known[7] hydrazide **6.1** with salicylaldehyde and catalytic acetic acid yielded bis-tridentate ligand **6.2**. This was exhaustively deprotonated with sodium hydride to yield tetraanionic **6.3** which is able to assemble into M_2L_3 helical complexes when combined with lanthanide salts in DMSO. Ligand **6.4**, containing only one chelator, acts as a control and can coordinate only a single metal. This was synthesized in two steps from ethyl 4-bromobenzoate in a similar manner to **6.2**.

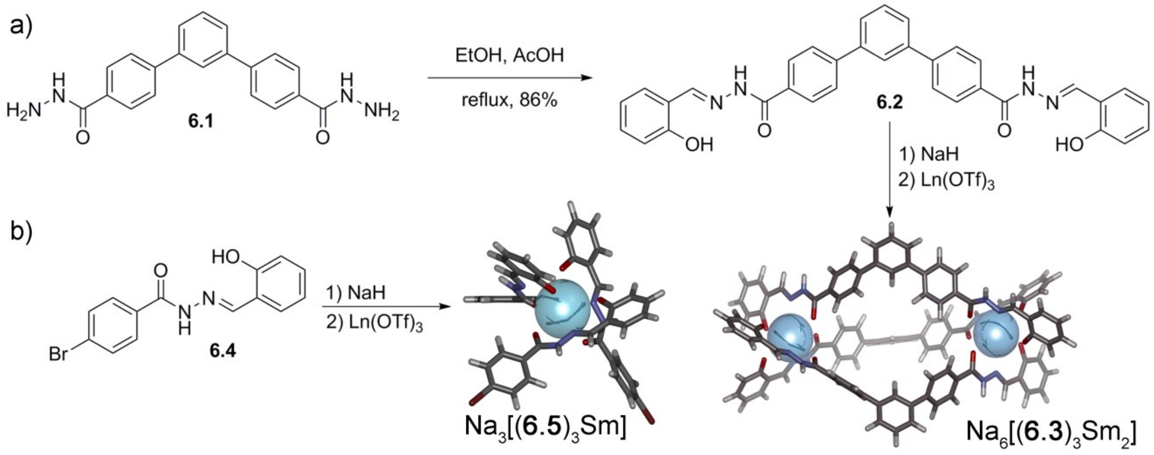

Figure 6.1: Synthesis of tridentate salicylhydrazone ligands for lanthanide assembly: a) Synthesis of bis tridentate ligand **6.2** and model of $Na_6[(\mathbf{6.3})_3Sm_2]$ (SPARTAN, AM1 force field); b) synthesis of control ligand **6.4** and model of monometallic complex $Na_3[(\mathbf{6.5})Sm]$ (SPARTAN, AM1 force field).

6.3 Metal Complexation

Metal complexation was studied with various lanthanide salts.[8] Triflates, nitrates, and chlorides were available, but triflates were preferred, as they are weakly coordinating, and most members of the series are commercially available. Weak coordination in DMSO was observed with **6.2**, but anionic **6.3** showed increased affinity for lanthanide triflates. Complexation studies were monitored by ^1H NMR, and complexation was observed after mixing ligand and metal in an NMR tube. Figure 6.2 shows the ^{1}H NMR spectra of complexes of various lanthanides. These metals (La, Pr, Sm, Yb, and lanthanide surrogate Y) are spread across the series and provide a range of ionic radii (Y is similar in size to Ho). Highly paramagnetic metals were avoided to allow for ^{1}H NMR analysis. Diamagnetic Y and La and weakly paramagnetic Sm have chemical shifts in the aromatic region, as expected, while paramagnetic Pr and Yb shift the spectrum downfield and upfield respectively. While the metals are paramagnetic and no coupling was observed, the spectra of the Pr and Yb complexes exhibited sharp, integrable signals that could be monitored in various NMR experiments. Complexes could also be formed with Nd, Eu, Dy, and Er, although these were not as extensively studied. The Nd complex appeared similar to that of Pr, although broader, and Eu produced a sharp spectrum, but some peaks overlapped with water present in the DMSO solvent. ^{1}H NMR spectra of Dy and Er could be obtained, but the quality of these spectra was poor due to the very high magnetic moments of these metal ions.

Stoichiometry of the complexes was determined by ^{1}H NMR titration. When a solution of $Sm(OTf)_3$ was titrated into a solution of **6.3**, a single, discrete complex was observed at 0.67 eq. metal, and no peaks for ligand were retained. No variable coordination was observed as described with Bi in Chapter 5, and the spectrum stayed constant, even after the addition of excess metal. This data fits with the stoichiometry of a M_2L_3 helical complex, and this type of complex is precedented for bent, *bis*-tridentate ligands and lanthanide ions.[1] The minimized structure of $Na_6[(\mathbf{6.3})_3Sm_2]$ is shown in Figure 6.1. Titration data was consistent for all the larger metals (La, Pr, Sm, and Y), but complete complexation was observed after 1 eq. for Yb. This indicates that the smaller coordination sphere of Yb cannot accommodate three tridentate ligands and an M_2L_2

complex is being formed instead. This complex is analogous to the M_2L_2 bismuth complex described in Chapter 5.

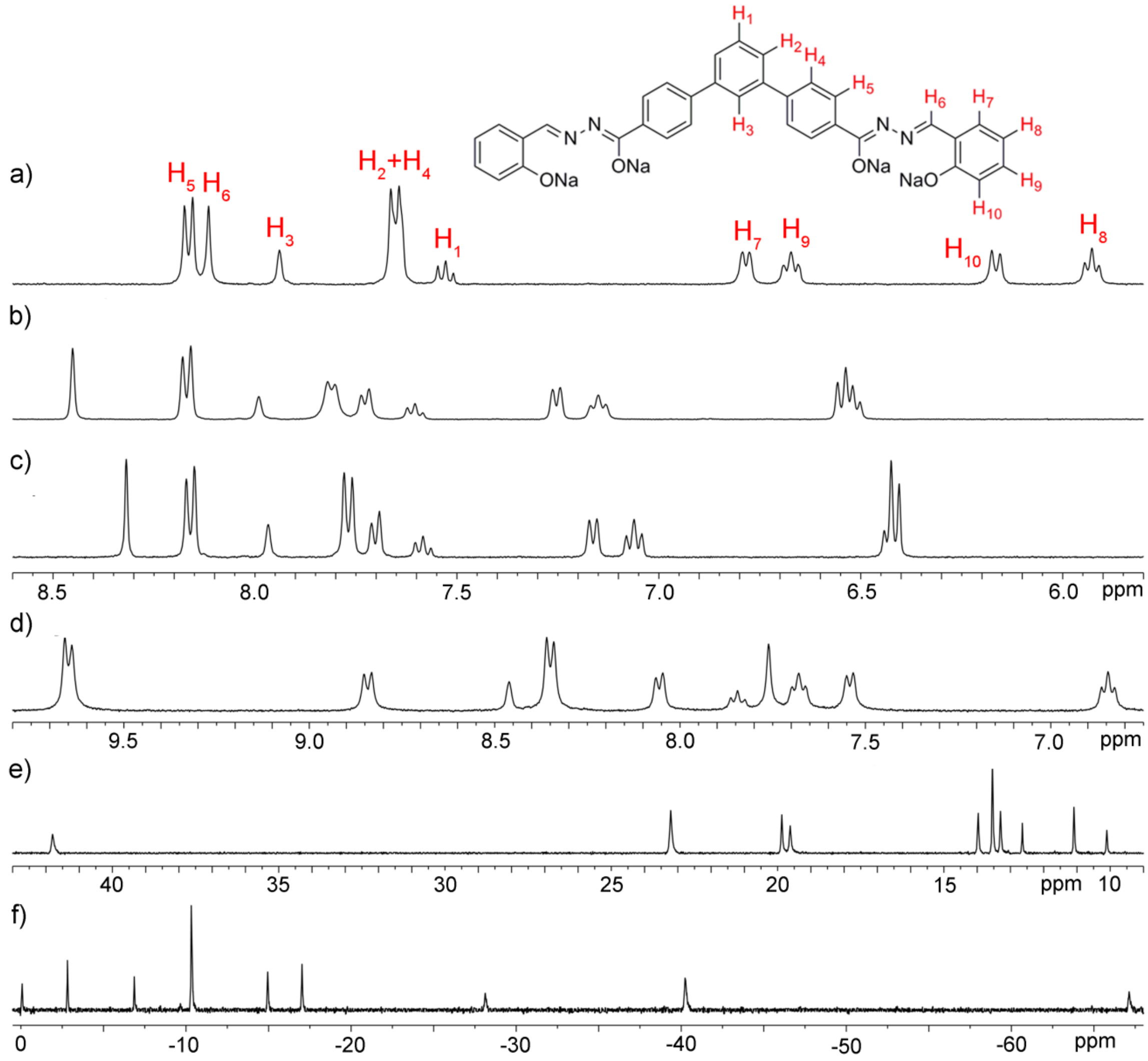

Figure 6.2: ^{1}H NMR spectra of self-assembled lanthanide helical complexes (400 MHz, DMSO-*d*$_6$, 298 K): a) **6.3**; b) $Na_6[(\mathbf{6.3})_3Y_2]$; c) $Na_6[(\mathbf{6.3})_3La_2]$; d) $Na_6[(\mathbf{6.3})_3Sm_2]$; e) $Na_6[(\mathbf{6.3})_3Pr_2]$; f) $Na_6[(\mathbf{6.3})_3Yb_2]$.

When complexation was attempted with different lanthanide sources such as nitrates, the ^{1}H NMR spectra were identical to those of the complexes with the lanthanide triflates. Lack of participation of the anion indicates that the lanthanide centers are saturated by the ligands. Complexes were also characterized by diffusion

NMR. The diffusion coefficient for $Na_6[(\mathbf{6.3})_3Y_2]$ was 7.24 x 10^{-11} m^2/s, and the diffusion coefficient for $Na_6[(\mathbf{6.3})_3Sm_2]$ was 8.13 x 10^{-11} m^2/s. The similarity between diffusion coefficients suggests that the complexes have a very similar size and shape. Diffusion analysis was attempted for $Na_6[(\mathbf{6.3})_2Yb_2]$ to compare complexes of different stoichiometry, but the paramagnetism of Yb prevented acquision of a spectrum.

Despite many attempts, X-ray quality crystals could not be obtained. Complexes were tolerant to other solvents, but required DMSO for initial dissolution. This prevented crystallization by slow evaporation, the method used to crystallize the complexes described in Chapters 2 and 5. The anionic complexes were also susceptible to protonation with water in the solvent and noncrystalline powders resulted. Complexes could be solubilized in THF under the proper conditions, but metal triflates were preferentially crystallized.

6.4 Mass Spectrometric Analysis

The complexes resulting from deprotonation of **6.2** with sodium hydride were soluble only in DMSO, but deprotonation with potassium *tert*-butoxide yielded complexes that were soluble in THF. The assemblies were amenable to ESI mass spectral analysis in positive ion mode, and Figure 6.3 shows the spectra and minimized structures of $[(\mathbf{6.2})_3Y_2\text{-}6H]$ and $[(\mathbf{6.2})_2Yb_2\text{-}4H](OTf)_2$.

While an anionic ligand was employed for complexation, the acidic ionization conditions caused protonation of the ligands and $[(\mathbf{6.2})_3Ln_2\text{-}4H]^{2+}$ parent ions were observed. These ions were observed in all M_2L_3 lanthanide complexes, but were susceptible to fragmentation. Loss of ligand was the most significant fragmentation, and $[(\mathbf{6.2})_2Ln_2\text{-}5H]^+$ and $[(\mathbf{6.2})_2Ln_2\text{-}4H]^{2+}$ ions were also present. The $[(\mathbf{6.2})_3Ln_2\text{-}4H]^{2+}$ ions were subjected to MS/MS analysis, and fragmentation resulted in the singly and doubly charged M_2L_2 cations. This suggests that the M_2L_2 complexes observed are a result of ligand loss under ionizing conditions and not from incomplete assembly. Compared to the M_2L_3 complexes of the larger lanthanides, the spectrum of [(**6.2**)$_2$Yb$_2$-4H](OTf)$_2$ exhibited only one major peak, the M_2L_2 ion [(**6.2**)$_2$Yb$_2$-4H]$^{2+}$. The absence of peaks from a M_2L_3 complex matches the NMR titration results, and confirms that the Yb complex is of a M_2L_2 stoichiometry. The isotope distributions matched those predicted for all complexes, and no complexes of another stoichiometry were observed such as M_2L_4 or M_4L_6.

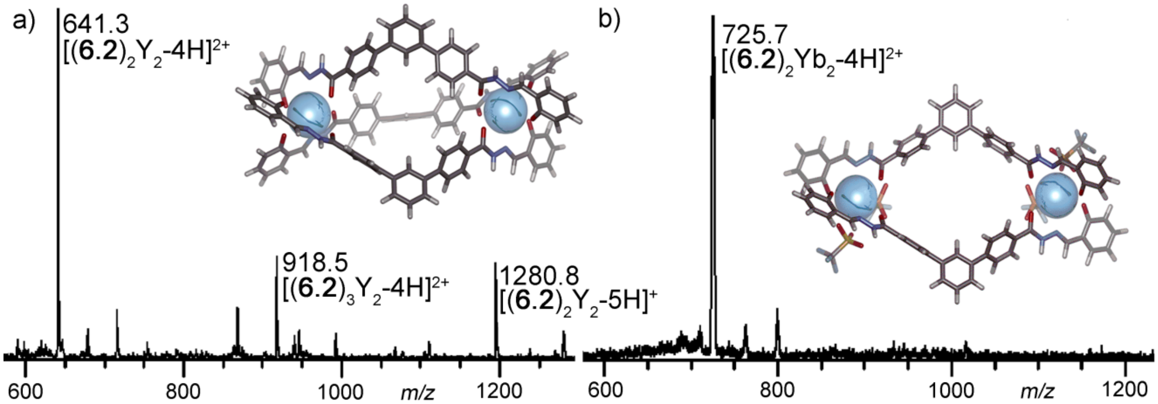

Figure 6.3: Mass spectra and minimized structures (SPARTAN, AM1 force field) of a) [(**6.2**)$_3$Y$_2$-6H] and b) [(**6.2**)$_2$Yb$_2$-4H](OTf)$_2$.

6.5 Kinetic Displacement Experiments

While all of the metals tested were capable of forming complexes, significant differences were observed in experiments with different metals. Both initial kinetic favorability and thermodynamic preference after equilibration were tested. Kinetic displacement was tested by titrating a solution of Ln^A(OTf)$_3$ into a solution of preformed Na$_6$[(**6.3**)$_3$Ln^B]. The extent of displacement could be determined by integration of the ^{1}H

NMR spectrum. Various combinations of Y, La, Pr, Sm, and Yb were tested, and a clear correlation was observed between the effective ionic radius of the metal and its preference for displacement where smaller metals were able to displace larger ones. A slight favorability for Nd over Pr was even observed, and the neighboring metals differ in ionic radius by only 0.02 Å. ^{1}H NMR spectra and graphs for these experiments can be found in Chapter 8. Almost absolute selectivity was observed in Y^{3+}/La^{3+} experiments, as shown by the partial ^{1}H NMR spectra in Figure 6.4. When $Y(OTf)_3$ was titrated into $Na_6[(\mathbf{6.3})_3La_2]$, complete displacement of La^{3+} by Y^{3+} was observed, and the spectrum resembled that of $Na_6[(\mathbf{6.3})Y_2]$ (Figure 6.4a). When the larger La^{3+} was added to a solution of $Na_6[(\mathbf{6.3})_3Y_2]$, almost no displacement was observed and the spectrum was still that of $Na_6[(\mathbf{6.3})_3Y_2]$ (Figure 6.4b).

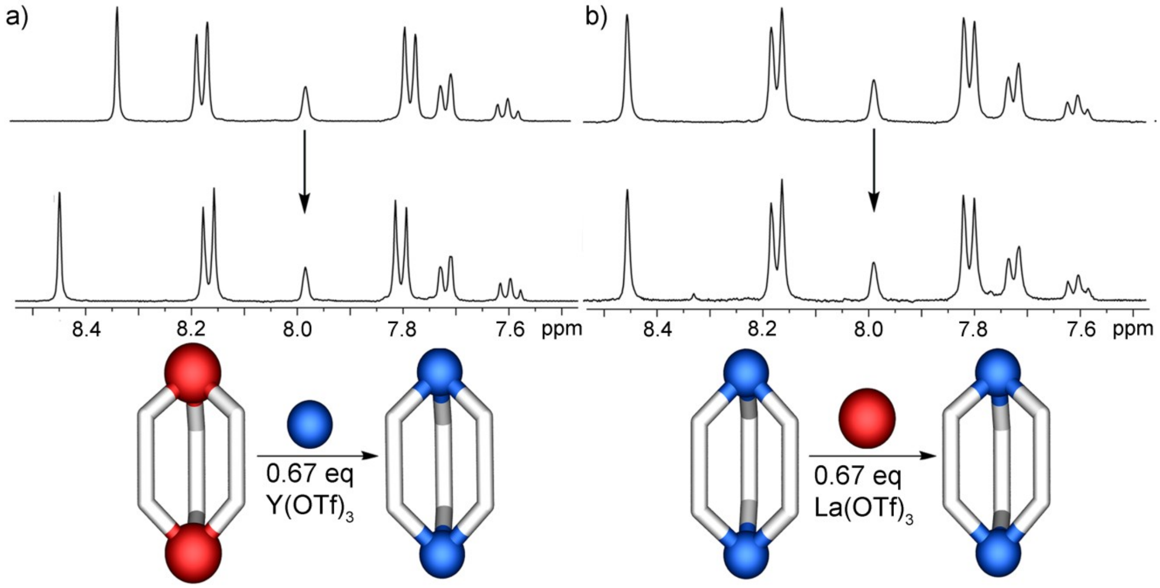

Figure 6.4: Displacement of La by Y: a) addition of $Y(OTf)_3$ to $Na_6[(\mathbf{6.3})_3La_2]$; b) addition of $La(OTf)_3$ to $Na_6[(\mathbf{6.3})_3Y_2]$ (400 MHz, DMSO-d_6, 298K).

Only the Y^{3+}/La^{3+} combination, having the greatest ΔEIR, exhibited complete selectivity, and combinations of metals with smaller ΔEIR values showed lower selectivity. Heterometallic complexes also formed. Overlapping signals made the analysis of mixtures of diamagnetic metals challenging, but paramagnetic Pr and Yb acted as shift reagents, separating the signals and allowing for identification of the heterometallic complexes. Figure 6.5 shows the identification of Pr and Sm complexes and a table of displacement results.

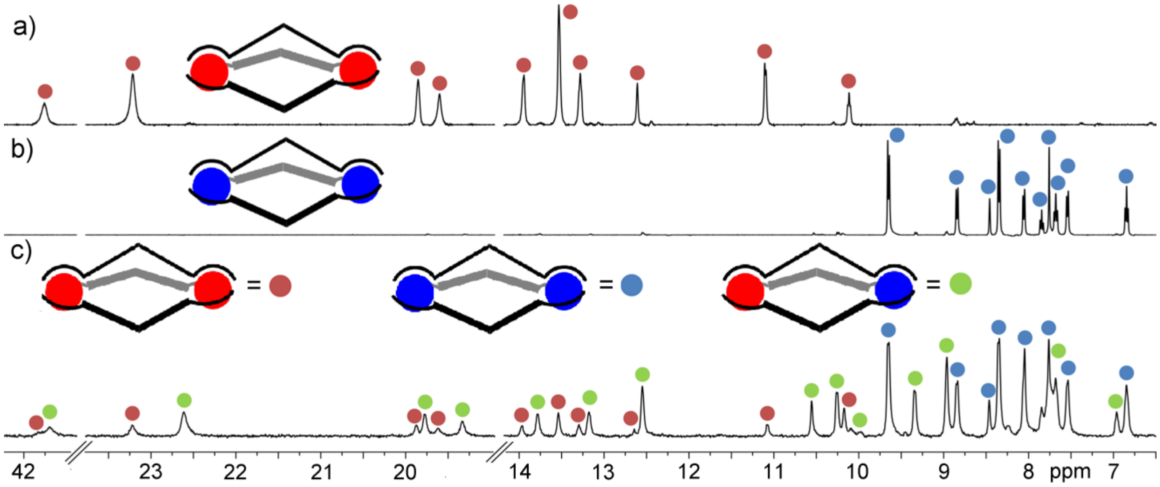

Figure 6.5: Identification of heterometallic complexes: a) $Na_6[(\mathbf{6.3})_3Pr_2]$; b) $Na_6[(\mathbf{6.3})_3Sm_2]$; c) mixture of $Na_6[(\mathbf{6.3})_3Pr_2]$ (red), $Na_6[(\mathbf{6.3})_3Sm_2]$ (blue), and $Na_6[(\mathbf{6.3})_3PrSm]$ (green) (400 MHz, DMSO-d_6, 298K).

Metals	**%A$_2$**	**%B$_2$**	**%AB**	**Ln^{3+}**	**EIR (Å)**[5]
Y:La	97	3	0	**La**	1.18
Y:Pr	70	15	15	**Pr**	1.14
Y:Yb	5	55	40	**Sm**	1.09
La:Sm	10	57	33	**Y**	1.02
Pr:Sm	7	57	36	**Yb**	0.98

Table 6.1: Percentage of complexes after displacement titrations and effective ionic radii of Ln^{3+} ions.

To help determine the limits of selectivity and the influence of the increase in charge:size ratio during the lanthanide contraction, complexation of Ce^{+4} and Th^{+4} was studied. Ce^{+4} is similar in size to Lu^{3+}, and Th^{4+}, an actinide, is similar to Gd^{3+}. Titration experiments with Ce were not as clean as with the +3 lanthanides. While complete complexation was observed after addition of 1 eq. $Ce(OTf)_4$, as would be expected for a complex of a smaller lanthanide, one set of peaks was not observed, even after addition of excess Ce (Figure 6.6a). Displacement experiments with the larger Y and slightly larger Yb did not show the usual selectivity for the smaller metal, and Ce was displaced in each experiment. Because Ce^{4+} can be used as an oxidant, it might be possible that the poor quality of the NMR could be attributed to ligand oxidation, but this seems unlikely as clean spectra of $Na_6[(\mathbf{6.3})_3Y_2]$ or $Na_2[(\mathbf{6.3})_3Yb_2]$ result when Ce is displaced as shown in Figure 6.6c.

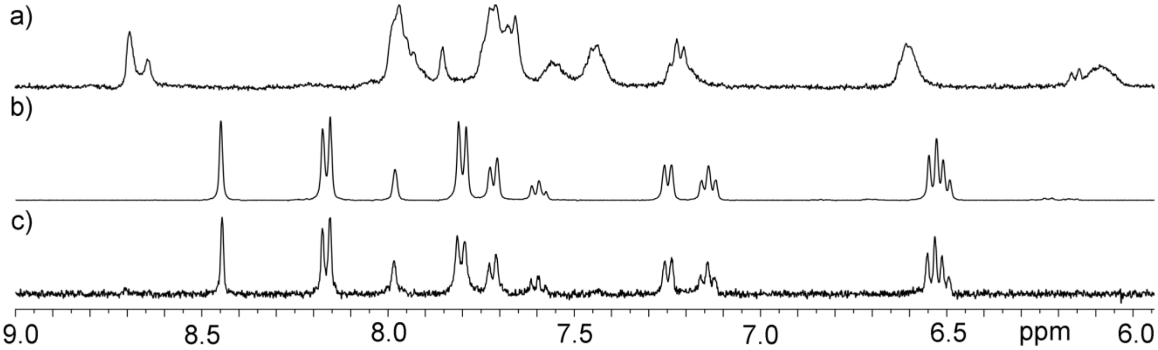

Figure 6.6: Displacement experiments with $Ce(OTf)_4$: a) **6.3** + 1 eq. $Ce(OTf)_4$; b) $Na_6[(\mathbf{6.3})_3Y_2]$; c) $Na_x[(\mathbf{6.3})_yCe_2]$ + 0.67 eq $Y(OTf)_3$ (400 MHz, DMSO-d_6, 298K).

When displacement between Ce and Th was tested, Th was favored, which shows that this ligand may have potential for selective actinide extraction. Experiments with the larger Sm and smaller Y also supported this, as Th was selected for in each case. If charge:size ratio is the determining factor in selectivity, the more highly charged +4 ions should be selected for, and these experiments show that charge:size ratio alone is not the only determining factor in selectivity. Titrations with $Th(NO_3)_4 \cdot xH_2O$ showed peaks for a discrete complex after the addition of 0.67 eq. metal, which was similar to what was observed with the +3 lanthanides. It is likely that a similar helical complex is being formed, and there is literature precedent for the use of Th in self-assembled helices.[9] Unfortunately, the complexes could not be characterized by mass spectrometry due to the radioactivity of Th. Interestingly, the Th complex was more soluble than the complexes formed from lanthanide triflates and could be studied in a 2:1 mixture of MeCN:H_2O.

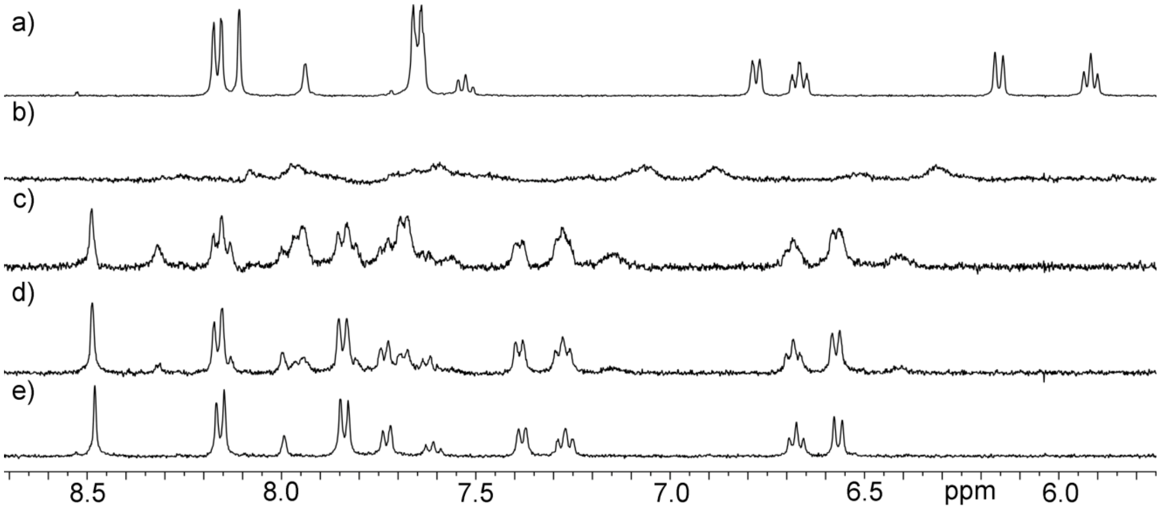

Figure 6.7: ^1H NMR titration of $Th(NO_3)_4 \cdot xH_2O$ into ligand **6.3**: a) **6.3**; b) 0.33 eq.; c) 0.67 eq.; d) 1 eq.; e) 3 eq. (400 MHz, DMSO-d_6, 298K).

6.6 Comparison with Control Ligand

To determine whether selectivity was based on supramolecular coordination effects, the same experiments were repeated with control ligand **6.5**, which can coordinate only one metal. The NMR behavior of **6.5** was the same as **6.3**. After addition of 0.33 eq. $Ln(OTf)_3$, clean $Na_3[(\mathbf{6.5})_3Ln]$ complexes were formed. As with ligand **6.3**, control ligand **6.5** coordinated all of the lanthanides tested. Mass spectral behavior was also similar to **6.3**. The $[(\mathbf{6.4})_3Ln\text{-}2H]^{2+}$ parent ion was observed along with fragmentation into $[(\mathbf{6.4})_2\text{Ln-2H}]^+$, and MS/MS analysis showed that the $[(\mathbf{6.4})_2\text{Ln-2H}]^+$ ion resulted from fragmentation of $[(\mathbf{6.4})_3\text{Ln-2H}]^{2+}$.

Kinetic displacement experiments yielded the same results as **6.3**, and metals with smaller ionic radii were preferentially incorporated into complexes. A strong correlation between the extent of displacement and ΔEIR was again observed, showing that charge plays an important role in the kinetic selectivity for smaller metals. As the metal EIR decreases, the charge:size ratio increases, as does the affinity of the anionic ligand for the smaller metal.

6.7 Equilibration Experiments

In addition to kinetic displacement, thermodynamic equilibration was measured. To test equilibration, an equimolar solution of metals was added to a solution of ligand and ^{1}H NMR spectra were periodically acquired over 30 h. Figure 6.8 shows the percentage of complexes versus time with mixtures of Y^{3+}, La^{3+}, and Sm^{3+} and either ligand **6.3** or **6.5**.

The complex of the smaller metal is initially preferred in all samples. Over time, however, the selection preference inverts and the complex of the larger metal ion is observed. Equilibration is complete after 24 hours and in the Y^{3+}/La^{3+} mixture, only the larger $Na_6[(\mathbf{6.3})_3La_2]$ is present (Figure 6.8a). The initial 96:4:0 ratio of $Na_6[(\mathbf{6.3})_3Y_2]$:$Na_6[(\mathbf{6.3})_3La_2]$:$Na_6[(\mathbf{6.3})_3YLa]$ almost completely inverts to 6:94:0 $Na_6[(\mathbf{6.3})_3Y_2]$:$Na_6[(\mathbf{6.3})_3La_2]$:$Na_6[(\mathbf{6.3})_3YLa]$. The Y^{3+}/Sm^{3+} mixture (Figure 6.8b), which has a smaller ΔEIR, initially shows a ratio of 50:9:4 $Na_6[(\mathbf{6.3})_3Y_2]$:$Na_6[(\mathbf{6.3})_3Sm_2]$:$Na_6[(\mathbf{6.3})_3YSm]$ which equilibrates to 17:37:46

$Na_6[(\mathbf{6.3})_3Y_2]$:$Na_6[(\mathbf{6.3})_3Sm_2]$:$Na_6[(\mathbf{6.3})_3YSm]$. As in the displacement experiments, heterometallic complexes are present.

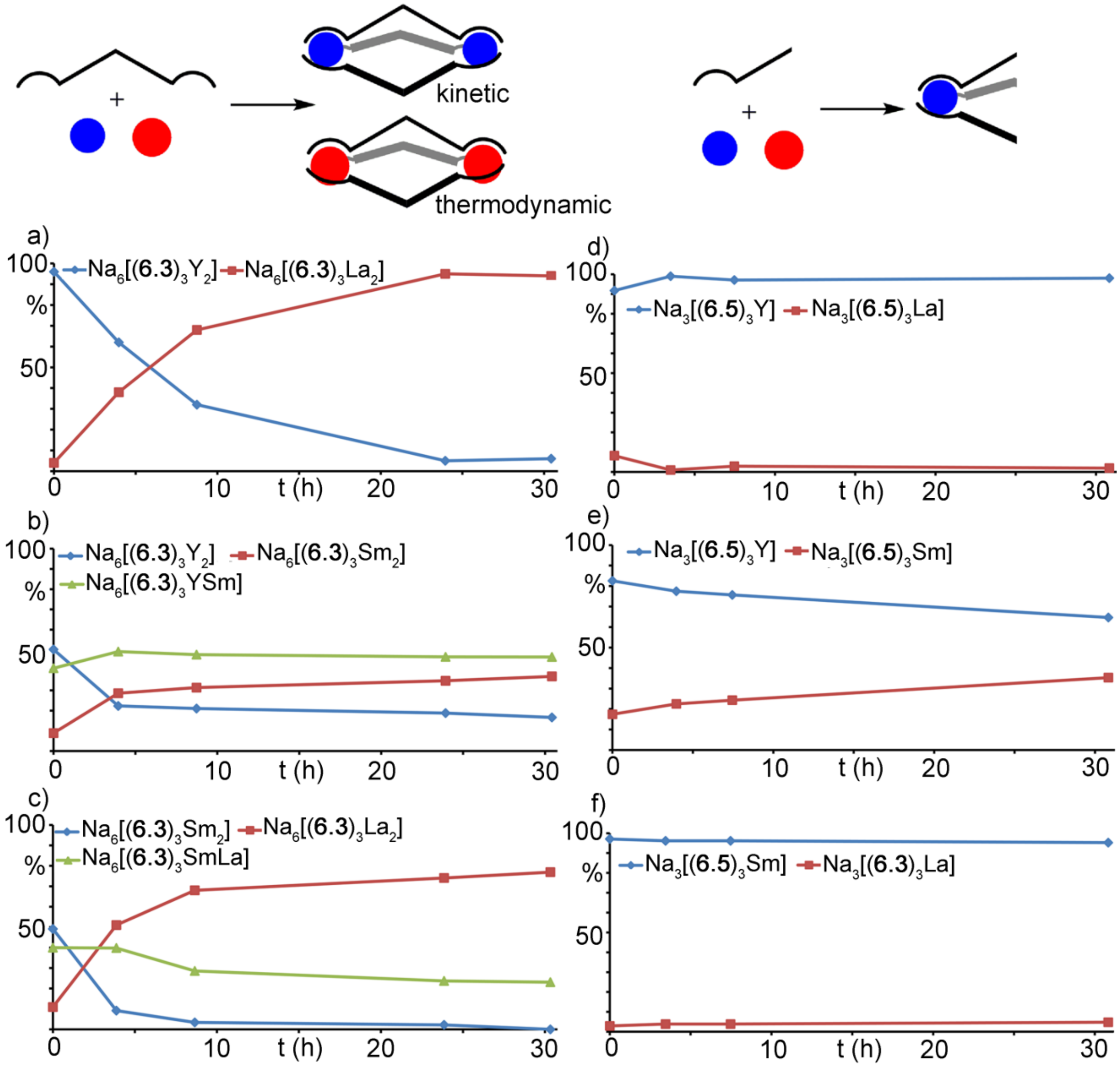

Figure 6.8: Equilibration of lanthanide complexes: a) $Na_6[(\mathbf{6.3})_3Y_2]$ vs $Na_6[(\mathbf{6.3})_3La_2]$; b) $Na_6[(\mathbf{6.3})_3Y_2]$ vs $Na_6[(\mathbf{6.3})_3Sm_2]$; c) $Na_6[(\mathbf{6.3})_3Sm_2]$ vs $Na_6[(\mathbf{6.3})_3La_2]$; d) $Na_3[(\mathbf{6.5})_3Y]$ vs $Na_3[(\mathbf{6.5})_3La]$; e) $Na_3[(\mathbf{6.5})_3Y]$ vs $Na_3[(\mathbf{6.5})_3Sm]$; f) $Na_3[(\mathbf{6.5})_3Sm]$ vs $Na_3[(\mathbf{6.5})_3La]$ (DMSO-d_6, 298 K).

The selectivity after equilibration also showed a linear correlation with ΔEIR. As ΔEIR increased, so did the percentage of the larger metal ion after equilibration. The

Y^{3+}/La^{3+} combination has the largest ΔEIR (0.16 Å) and was almost completely selective for the larger $Na_6[(\mathbf{6.3})_3La_2]$. A smaller ΔEIR resulted in the formation of heterometallic complexes as seen in the Y^{3+}/La^{3+} and La^{3+}/Sm^{3+} mixtures, and the concentration of these was also size-dependent. The closer in size the metals, the greater the propensity for heterometallic complex formation. The selectivity of rigid, anionic **6.3** is much greater than literature reports with flexible, neutral bis-tridentate ligands.[10] In that example, very similar amounts of $(Ln^A)_2$, $(Ln^B)_2$, and (Ln^{AB}) complexes were formed after addition of an equimolar mix of metals.

When equilibration was measured with control **6.5**, the results were different. Only a small amount of equilibration was observed, even after 30 hours, as shown in Figure 6.8d-f. The differences in kinetic and thermodynamic selectivity between bis-tridentate **6.3** and control **6.5** show that selectivity is a supramolecular effect. With the presence of the second chelator in **6.3**, charge is not as strong of a factor in selectivity. Lanthanides have flexible coordination spheres, and this allows ligands to shift into more favorable conformations to minimize steric interactions.[4] The metals in the helical complexes of **6.3** are connected by rigid aromatic rings, which restricts the conformational flexibility of the ligands and add strain to the complex. Larger metals provide more space for ligands to reach a favorable conformation, and they are preferentially coordinated after equilibration. The use of rigid ligands to control assembly is precedented for transition metal complexes[11] but is rare in complexes of metals with less defined coordination geometries. Ligand **6.3** is a departure from the common lanthanide-coordinating ligands that contain flexible methylene spacers. These ligands usually show no selectivity between metals unless different chelators are present to take advantage of small differences among lanthanides.[12]

6.8 Effects of Water on Equilibration

The presence of water in the sample has a large effect on equilibration. Water is known to coordinate lanthanides and is correlated to the contrast and relaxivity in Gd-based MRI contrast agents.[13] In the helical $Na_6[(\mathbf{6.3})_3Ln_2]$ complexes, increasing the water concentration causes faster equilibration to the thermodynamic product, the complex of the larger metal ion. This is most noticeable in the Y^{3+}/La^{3+} combination. Figure 6.9a shows the percentage of $Na_6[(\mathbf{6.3})_3Y_2]$ and $Na_6[(\mathbf{6.3})_3La_2]$ versus time with varying amounts of water.

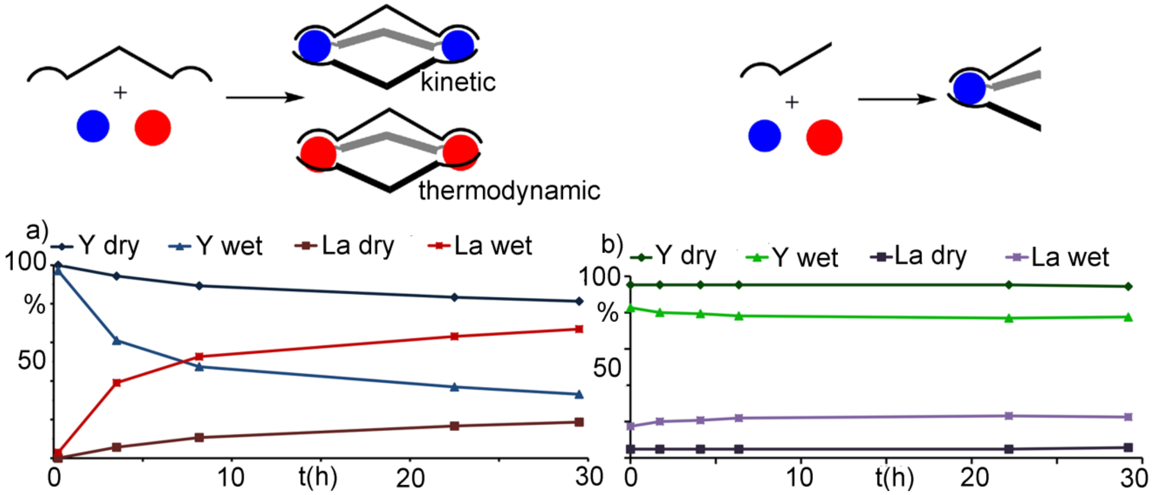

Figure 6.9: Plots of percent complex vs time: a) $Na_6[(\mathbf{6.3})_3Y_2]$ and $Na_6[(\mathbf{6.3})_3La_2]$ in samples containing 50 mM water (dry) and 150 mM water (wet); b) $Na_3[(\mathbf{6.5})_3Y]$ and $Na_3[(\mathbf{6.5})_3La]$ in samples containing 100 mM water (dry) and 300 mM water (wet).

In samples containing 50 mM water, very slow equilibration occurred, and conversion to $Na_6[(\mathbf{6.3})_3La_2]$ did not occur even after several days. Much faster equilibration was observed in samples containing 150 mM water, and the graph looks similar to that in Figure 6.8a. The concentration of water in all equilibration experiments in Figure 6.8 was identical. The monometallic control complex, in comparison, exhibits almost no equilibration, even in the presence of additional water. The proportion of complexes during initial selectivity changes slightly, but no significant equilibration is observed. This difference lends additional evidence for supramolecular cooperativity. The reversible coordination of water speeds up the equilibration process by allowing faster exchange between ligands. This has no effect in the nonequilibrating control complex, but plays an important role in cooperative equilibration in the helical $Na_6[(\mathbf{6.3})_3Ln_2]$ complexes.

6.9 Bismuth Complexation

Complexation was studied with Bi to compare the coordinative ability of ligands **6.3** and **5.3** described in Chapter 5. Both ligands have the same core structure and a similar coordination geometry, but they have slightly different coordination angles and a different charge when deprotonated. Titration of $Bi(OTf)_3$ into **6.3** showed the formation of a single complex rather than the variable coordination discussed in Chapter 5. Displacement experiments with Y and La showed complete selectivity for Y over Bi. Experiments with La, which is almost identical in size to Bi,[14] showed formation of the Bi complex after the addition of excess metal (Figure 6.10a), but La was selected for after equilibration (Figure 6.10b). Equilibration experiments were also selective for the lanthanide, and this is likely due to the high oxophilicity of Ln ions. ^{1}H NMR spectra of these experiments are shown in Figure 6.10.

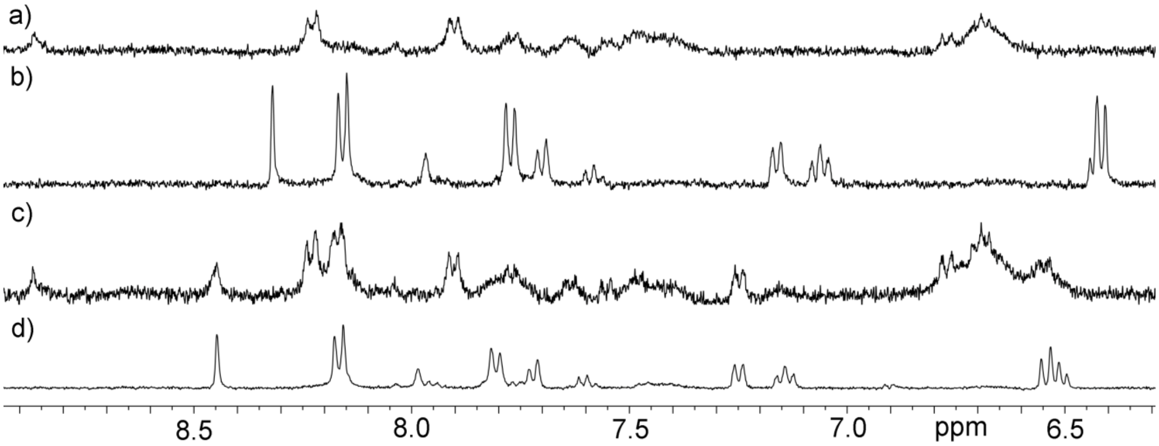

Figure 6.10: Displacement and equilibration experiments with Y, La, and Bi: a) $Na_6[(\mathbf{6.3})_3La_2]$ + 1.5 eq $Bi(OTf)_3$; b) 18 h equilibration; c) **6.3** + 1.5 eq $Y(OTf)_3$+1.5 eq $Bi(OTf)_3$; d) 18 h equilibration.

6.10 Conclusion

This chapter has described the synthesis and characterization of a series of lanthanide-based M_2L_3 helical complexes. Complexes were formed from both large and small lanthanides, lanthanide surrogate Y, and actinide Th. Remarkable discrimination between metals was achieved despite identical ligand coordination environment and extremely small size differences in metal ionic radius. A kinetic preference for smaller metals and a thermodynamic preference for larger metals was observed, and there is a correlation between distribution of complex and size difference of metals. Equilibration is a cooperative effect which requires the participation of two metal coordination sites. A control ligand with only one coordination site showed no equilibration. Equilibration was also dependent on the concentration of water in the sample, and increased water concentration resulted in faster equilibration.

6.11 References

1) a) Jensen, T. B.; Scopelliti, R.; Bünzli, J.-C. G. "Tuning the self-assembly of lanthanide triple stranded heterobimetallic helicates by ligand design." *Dalton Trans.* **2008**, 1027-1036.; b) Piguet, C.; Bernardinelli, G.; Hopfgartners, G. "Helicates as versatile supramolecular complexes." *Chem. Rev.* **1997**, *97*, 2005-2062.; c) Stomeo, F.; Lincheneau, C.; Leonard, J. P.; O'Brien, J. E.; Peacock, R. D.; McCoy, C. P.; Gunnlaugsson, T. "Metal-directed synthesis of enantiomerially pure dimetallic lanthanide luminescent triple-stranded helicates." *J. Am. Chem. Soc.* **2009**, *131*, 9636-9637.; d) Wang, B.; Zang, Z.; Wang, H.; Dou, W.; Tang, X.; Liu, W.; Shao, Y.; Ma, J.; Li, Y.; Zhou, J. "Multiple lanthanide helicate clusters and the effects of anions on their configuration." *Angew. Chem.*, *Int. Ed.* **2013**, *52*, 3756-3759.; e) Shi, J.; Hou, Y.; Chu, W.; Shi, X.; Gu, H.; Wang, B.; Sun, Z. "Crystal structure and highly luminescent properties studies of bis-β-diketonate lanthanide complexes." *Inorg. Chem.* **2013**, *52*, 5013-5022.; f) Jensen, T. B.; Scopelliti, R.; Bünzli, J.-C. G. "Thermodynamic parameters governing the self-assembly of head-head-head lanthanide bimetallic helicates." *Chem. Eur. J.* **2007**, *13*, 8404-8410.; g) Piguet, C.; Bünzli, J.-C. G. "Self-assembled lanthanide helicates: From basic thermodynamics to applications" In *Handbook on the Physics and Chemistry of Rare Earths*; Gschneider, K. A., Jr.; Bünzli, J.-C. G.; Pecharsky, V. K., Eds.; Elsevier: Amsterdam, The Netherlands, 2010; Vol. *40*, pp 301-553; h) Albrecht, M.; Osetska, O.; Frölich, R.; Bünzli, J.-C. G.; Aebischer, A.; Gumy, F.; Hamacek, J. "Highly efficient near-IR emitting Yb/Yb and Yb/Al helicates." *J. Am. Chem. Soc.* **2007**, *129*, 14178-14179.; i) Ryan, P. E.; Guénée, L.; Piguet, C. "Monitoring helical twists and effective molarities in dinuclear triple-stranded lanthanide helicates." *Dalton Trans.* **2013**, *42*, 11047-11055.

2) a) Wang, J.; He, C.; Wu, P.; Wang, J.; Duan, C. "An amide-containing metal-organic tetrahedron responding to a spin-trapping reaction in a fluorescent enhancement manner for biological imagin of NO in living cells." *J. Am. Chem. Soc.* **2011**, *133*, 12402-12405.; b) Liu, W.; Wu, X.; He, C.; Jiao, Y.; Duan, C. "Self-assembly of cerium-based metal-organic tetrahedrons for size-selectively luminescent sensing natural saccharides." *Chem. Commun.* **2009**, 7554-7556.; c) El Aroussi, B.; Guénée, L.; Pal, P.; Hamacek, J. "Lanthanide-mediated supramolecular cages and host-guest interactions." *Inorg. Chem.* **2011**, *50*, 8588-8597.; d) Hamacek, J.; Poggiali, D.; Zebret, S.; El Aroussi, B.; Schneider, M. W.; Mastalerz, M. "Building large supramolecular nanocapsules with europium cations." *Chem. Commun.* **2012**, *48*, 1281-1283.

3) a) Chen, X.-Y.; Bretonnière, Y.; Pécaut, J.; Imbert, D.; Bünzli, J.-C.; Mazzanti, M. "Selective self-assembly of hexameric homo- and heteropolymetallic lanthanide wheels: Synthesis, structure, and photophysical studies." *Inorg. Chem.* **2007**, *46*, 625-637.; b) El Aroussi, B.; Zebret, S.; Besnard, C.; Perrottet, P.; Hamacek, J. "Rational design of a ternary supramolecular system: Self-assembly of pentanuclear lanthanide helicates." *J. Am. Chem. Soc.* **2011**, *133*, 10764-10767.; c) Jeong, K. S.; Kim, Y. S.; Kim, Y. J.; Lee, E.; Yoon, J. H.; Park, W. H.; Park, Y. W.; Jeon, S.-J.; Kim, Z. H.; Kim, J.; Jeong, N. "Lanthanitin: A chiral nanoball encapsulating 18 lanthanum ions by ferritin-like assembly." *Angew. Chem., Int. Ed.* **2006**, *45*, 8134-8138.

4) a) Petoud, S.; Bünzli, J.-C. G.; Renaud, F.; Piguet, C.; Schenk, K. J.; Hopfgartner, G. "Stability and size-discriminating effects in mononuclear lanthanide triple-helical building

blocks with tridentate aromatic ligands." *Inorg. Chem.* **1997**, *36*, 5750-5760.; b) Le Borgne, T.; Bénech, J.-M.; Floquet, S.; Bernardinelli, G.; Aliprandini, C.; Bettens, P.; Piguet, C. "Monometallic lanthanide complexes with tridentate 2,6-dicarboxamidopyridine ligands. Influence of peripheral substitutions on steric congestion and antenna effect." *Dalton Trans.* **2003**, 3856-3868.

5) CRC Handbook of Chemistry and Physics, 87th ed.; Lide, D. R., Ed.; CRC Press: Boca Raton, FL, 2006; Sect. 4, p132.

6) a) Gorden, A. E. V.; DeVore, II, M. A.; Maynard, B. A. "Coordination chemistry with f-element complexes for an improved understanding of factors that contribute to extraction selectivity." *Inorg. Chem.* **2013**, *52*, 3445-3458.; b) Lewis, F. W.; Hudson, M. J.; Harwood, L. M. "Development of highly selective ligands for separations of actinides from lanthanides in the nuclear fuel cycle." *Synlett*, **2011**, *18*, 2609-2632.; c) Paiva, A. P.; Malik, P. "Recent advances on the chemistry of solvent extraction applied to the reprocessing of spent nuclear fuels and radioactive wastes." *J. Radioanal. Nucl. Chem.* **2004**, *261*, 485-496.; d) Panak, P. J.; Geist, A. "Complexation and extraction of trivalent actinides and lanthanides by triazinylpyridine N-donor ligands." *Chem. Rev.* **2013**, *113*, 1199-1236.

7) Johnson, A. M.; Young, M. C.; Hooley, R. J. "Reversible multicomponent self-assembly mediated by bismuth ions." *Dalton Trans.* **2013**, *42*, 8394-8401.

8) Johnson, A. M., Young, M. C.; Zhang, X.; Julian, R. R.; Hooley, R. J. "Cooperative thermodynamic control of selectivity in the self-assembly of rare earth metal-ligand helices." *J. Am. Chem. Soc.* **2013**, *135*, 17723-17726.

9) Xu, J.; Raymond, K. N. "Structurally characterized quadruple-stranded bisbidentate helicates." *Angew. Chem., Int. Ed.* **2006**, *45*, 6480-6485.

10) Piguet, C.; Bünzli, J.-C. G.; Bernardinelli, G.; Hopfgartner, G.; Williams, A. F. "Self-assembly and photophysical properties of lanthanide dinuclear triple-helical complexes." *J. Am. Chem. Soc.* **1993**, *115*, 8197-8206.

11) a) Young, M. C.; Johnson, A. M.; Gamboa, A. S.; Hooley, R. J. "Achiral endohedral functionality provides stereochemical control in Fe(II)-based self-assemblies." *Chem. Commun.* **2013**, *49*, 1627-1629.; b) Ousaka, N.; Grunder, S.; Castilla, A. M.; Whalley, A. C.; Stoddart, J. F.; Nitschke, J. R. "Efficient long-range stereochemical communication and cooperative effects in self-assembled Fe_4L_6 cages." *J. Am. Chem. Soc.* **2012**, *134*, 15528-15537.

12) a) Sorgho-Aboshyan, L.; Nozary, H.; Aebischer, A.; Bünzli, J.-C. G.; Morgantini, P.-Y.; Kittilstved, K. R. "Optimizing millisecond time scale near-infrared emission in polynuclear chrome(III)-lanthanide(III) complexes." *J. Am. Chem. Soc.* **2012**, *134*, 12675-12684.; b) Albrecht, M.; Osetska, O.; Bünzli, J.-C. G.; Gumy, F.; Fröhlich, R. "Homo- and heterodinuclear helicates of lanthanide(III), zinc(II) and aluminum(III) based on 8-hydroxyquinoline ligands." *Chem. Eur. J.* **2009**, *15*, 8791-8799.; c) Zeckert, K.; Hamacek, J.; Rivera, J.-P.; Floquet, S.; Pinto, A.; Borkovec, M.; Piguet, C. "A simple thermodynamic

model for rationalizing the formation of self-assembled multimetallic edifices: applications to triple-stranded helicates." *J. Am. Chem. Soc.* **2004**, *126*, 11589-11601.; d) Riis-Johannessen, T.; Bernardinelli, G.; Filinchuk, Y.; Clifford, S.; Favera, N. D.; Piguet, C. "Self-assembly of the first discrete 3d-4f-4f triple-stranded helicate." *Inorg. Chem.* **2009**, *48*, 5512-5525.

13) Caravan, P.; Ellison, J. J.; McMurry, T. J.; Lauffer, R. B. "Gadolinium(III) chelates as MRI contrast agents: Structure, dynamics, and applications." *Chem. Rev.* **1999**, *99*, 2293-2352.

14) CRC Handbook of Chemistry and Physics, 87th ed.; Lide, D. R., Ed.; CRC Press: Boca Raton, FL, 2006; Sect. 12, p11.

Chapter Seven: Narcissistic Self-Sorting in Fluorene-Based Lanthanide Assemblies

7.1 Introduction

Controlled assembly is vital to the successful formation of macromolecular systems in nature. Self-complementary motifs are often found, and a notable example of these are the hydrogen bonds present in nucleotide assemblies. Molecular recognition during the self-assembly process is enhanced with these self-complementary motifs, and this has been used to great effect in the sorting of synthetic hydrogen-bonded assemblies.[1]

Self-sorting is also an area of interest in assemblies based on metal-ligand interactions. Controlled assembly in these systems is more challenging, but sorting has been observed in a variety of complexes.[2] There are two types of self-sorting possible upon multicomponent self assembly: narcissistic[3] and social.[4] In narcissistic self-sorting, discrimination among components is achieved and the components form assemblies with themselves. In social self-sorting, no self-recognition occurs and mixed assemblies are formed. The heterocomplexes in Chapter 2 and the heterometallic complexes in Chapter 6 are examples of social self-sorting systems.

Different types of sorting can be favored by tuning structural differences in ligands such as size, shape, coordination angle, and coordination denticity. As ligands decrease in similarity, sorting becomes easier. In complexes with different coordination motifs, it can be predicted that only components that are meant to assemble actually do. In a study by the Isaacs group, a mixture of ten components narcissistically self-sorts despite the fact that all of them assemble via hydrogen bonding.[5] Although hydrogen bonding motifs are present in all of the components, different types of self-complementary motifs are able to recognize each other, which leads to narcissistic self-sorting. In ligands with similar coordination motifs, discrimination becomes significantly more difficult, and structural differences are often built in to favor selectivity. Narcissistic self-sorting has been observed in ligands with identical coordination type, most notably between *bis*-catecholate or *bis*-bipyridine ligands of varying lengths.[6] Differences in coordination angle[7] and stereoinduction[8] are also methods to differentiate between identical coordination motifs, as is steric hindrance in the interior of the complex as discussed in Chapter 2.[9]

Because of the difficulty in discriminating among similar ligands in the self-assembly process, it is interesting to determine how similar components can be while allowing for narcissistic self-sorting. While structural differences can be built into ligands to influence differentiation, mixing is still most often observed in complexes of the same geometry with the same coordination motif.[10] As described in Chapter 6, selectivity between lanthanide ions was observed with a symmetrical ligand despite very small differences in the size of the metals.[11] Self-sorting in lanthanide helices has primarily focused on selectivity among metals,[12] but the results described in Chapter 6 suggest that ligand-based sorting may be possible in similar systems.

7.2 Ligand Synthesis

Fluorene-based ligands with salicylhydrazone chelators were synthesized as shown in Figure 7.1. Activation of 9-fluorenone-2,7-dicarboxylic acid **7.1** with HCTU followed by reaction with hydrazine yielded fluorenone dihydrazide **7.2** which could then be reacted with salicylaldehyde to form fluorenone ligand **L7.3**. Derivatization of the central ketone in **7.1** allowed for the introduction of endohedral functionality. Reaction with hydroxylamine hydrochloride or *O*-benzylhydroxylamine hydrochloride allowed for the introduction of an oxime or benzyl oxime (**L7.5a** and **L7.5b**). The ketone could be reduced via a Wolff-Kischner reduction, and fluorene ligand **L7.8** could be obtained after conversion to the hydrazide and reaction with salicylaldehyde.

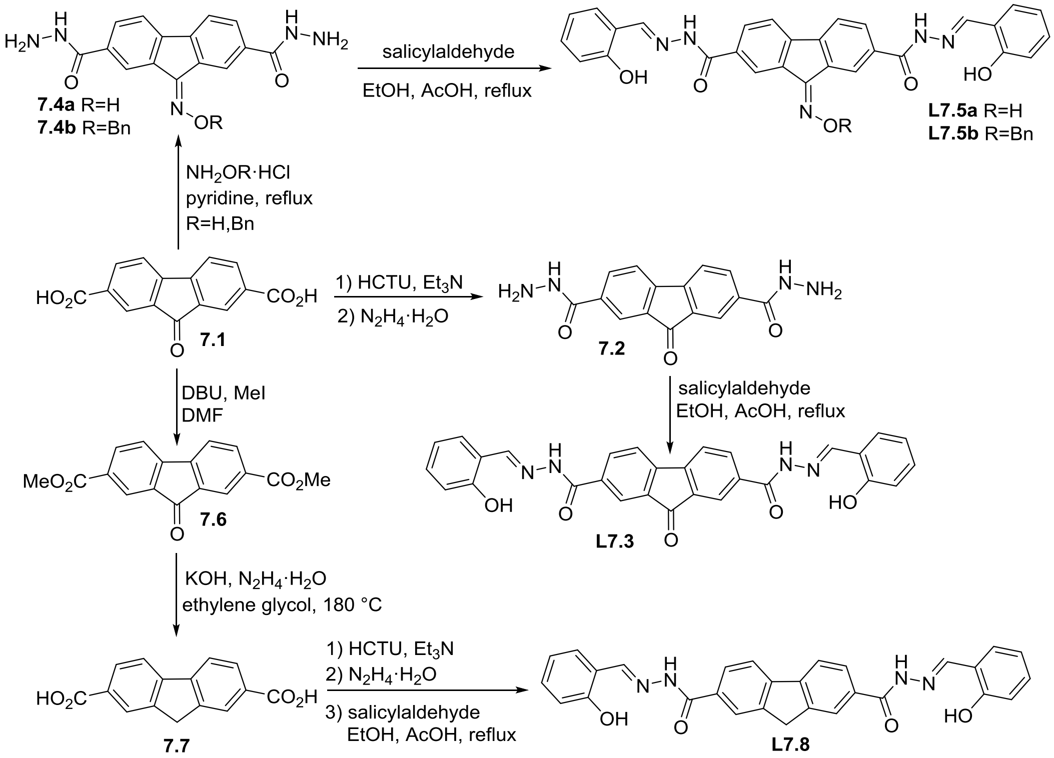

Figure 7.1: Synthesis of ligands for narcissistic self-sorting in lanthanide assemblies.

7.3 Metal Complexation

For coordination to lanthanides, ligands were exhaustively deprotonated with sodium hydride to yield more strongly coordinating anionic ligands **7.3**, **7.5a-b**, and **7.8**. As with the terphenyl salicylhydrazone ligands described in Chapter 6, assembly was studied by ^{1}H NMR in DMSO. Addition of a lanthanide triflate to a solution of ligand resulted in the formation of a single, discrete complex. While complexes could be assembled from several lanthanides, assembly was primarily studied with diamagnetic lanthanum and yttrium for ease of NMR analysis. These metals represent variation in the lanthanide series (Y is similar in size to Ho) and should provide representative data for both larger and smaller metals. Figure 7.2 shows the Y and La spectra of the fluorene-based complexes. Based on previous results with *bis*-tridentate salicylhydrazone ligands, helical M_2L_3 assemblies or tetrahedral M_4L_6 assemblies were expected to form. NMR titrations were expected to show an endpoint after the addition of 0.67 eq. metal triflate, but a clean assembly did not appear until the addition of 1 eq. metal triflate. This may possibly be due to the insolubility of the complexes during the intermediate points of the titration, and determining stoichiometry by NMR was deemed inconclusive.

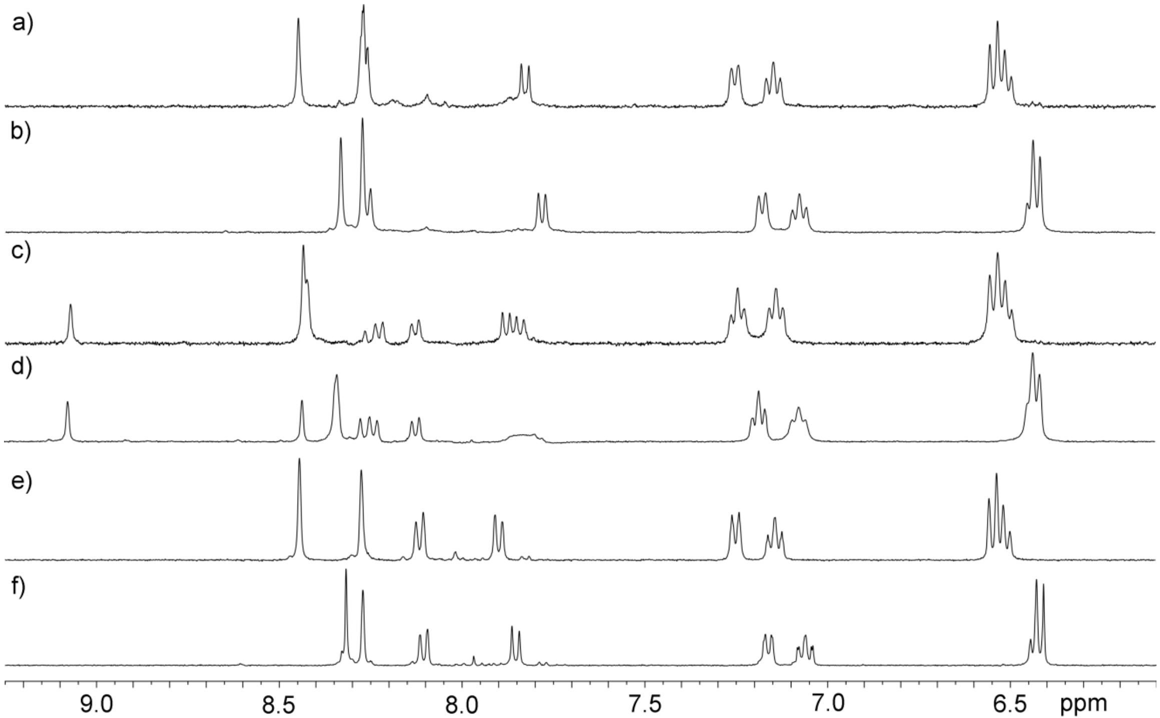

Figure 7.2: ^{1}H NMR spectra of fluorene-based lanthanide complexes: a) $Na_6[(\mathbf{7.3})_3Y_2]$; b) $Na_6[(\mathbf{7.3})_3La_2]$; c) $Na_6[(\mathbf{7.5a})_3Y_2]$; d) $Na_6[(\mathbf{7.5a})_3La_2]$; e) $Na_6[(\mathbf{7.8})_3Y_2]$; f) $Na_6[(\mathbf{7.8})_3La_2]$ (400 MHz, DMSO-d_6, 298K).

Diffusion NMR spectra were acquired for $Na_6[(\mathbf{7.3})_3La_2]$ and $Na_6[(\mathbf{7.5a})_3La_2]$. The diffusion coefficient for $Na_6[(\mathbf{7.3})_3La_2]$ was 8.11×10^{-11} m^2/s, and the diffusion coefficient for $Na_6[(\mathbf{7.5a})_3La_2]$ was 4.75x10^{-11} m^2/s. These similar values suggest that the complexes are of a similar size and forming a similar type of assembly. These are also similar to the diffusion coefficients observed for the M_2L_3 terphenyl-based lanthanide assemblies described in Chapter 6.

7.4 Mass Spectrometric Analysis

Mass spectrometry was used to confirm the stoichiometry of the complexes. Compared to the bent geometry of the previously described terphenyl ligands, the fluorene core imparts an almost linear geometry. Based on literature precedent for linear ligands,[13] it is possible that an M_4L_6 tetrahedron could be forming. Figure 7.3 shows the minimized structures of the possible helix or tetrahedron structures.

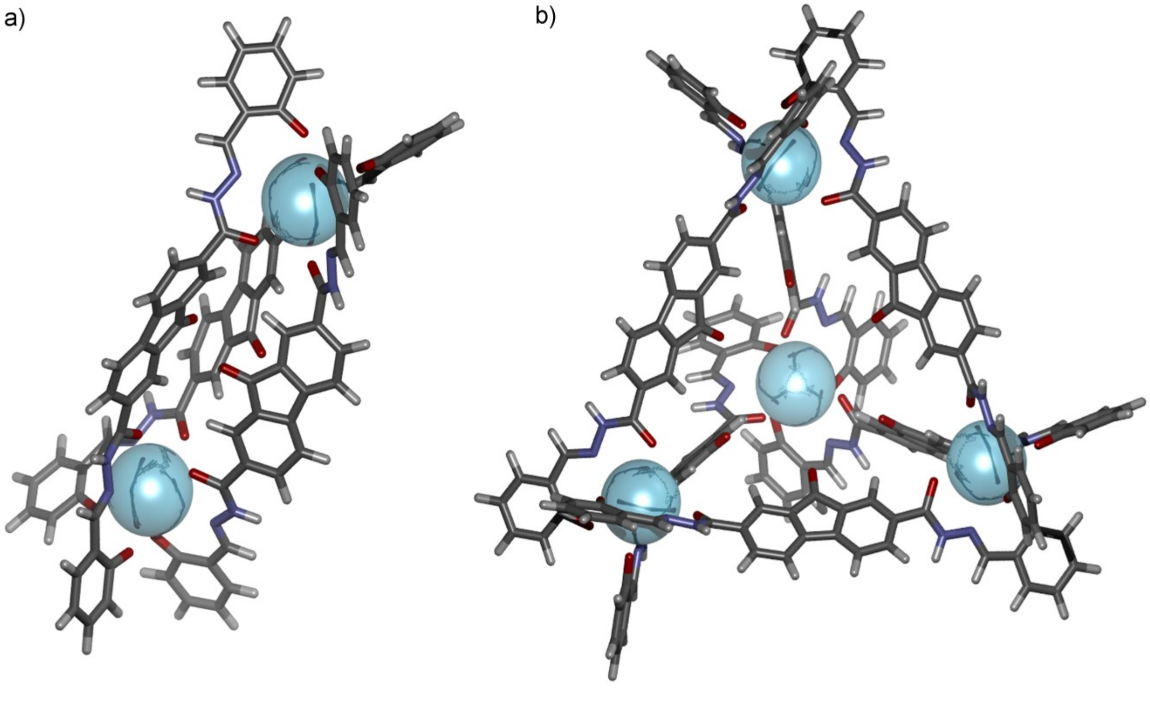

Figure 7.3: Minimized structures of possible complexes: a) $Na_6[(\mathbf{7.3})_3Y_2]$ helix; b) $Na_6[(\mathbf{7.3})_4Y_6]$ tetrahedron (SPARTAN, AM1 force field).

When subjected to mass spectrometric analysis, the $[M_2L_3\text{-}4H]^{2+}$ ion was observed. Ligand and $[M_2L_2\text{-}4H]^{2+}$ were also observed, and MS/MS analysis showed these to be fragmentations of the M_2L_3 complex. No signals that could correspond to the larger M_4L_6 assembly were observed, and the isotope patterns matched those predicted for the M_2L_3 assemblies. These results are analogous to those for the terphenyl complexes in Chapter 6.

7.5 Displacement and Equilibration

Displacement and equilibration were tested with Y, La, and Sm complexes of fluorenone **7.3**. Displacement followed the expected trend, where smaller metals were able to displace larger metals. When equilibration was tested, very little equilibration was observed, which contrasts with the inversion of selectivity described in Chapter 6. Interestingly, water had only a minor effect on equilibration. Full tabulation of this data can be found in Chapter 8.

7.6 Narcissistic Self-Sorting

The fluorene-based ligands have the same coordination geometry and metal chelator and differ only in endohedral functionality. This series of ligands is similar to the paddle-wheel ligands described in Chapter 2, and mixtures of ligands were studied to determine whether narcissistic or social self-sorting was observed. Sorting was studied with varying levels of ligand similarity as shown in Figure 7.4. Fluorenone **7.3** and oxime **7.5a** have medium-sized endohedral functional groups. Benzyl oxime **7.5b** is larger, but the flexibility of the benzyl group prevents inhibition of assembly through steric effects. Fluorene **7.8** is small and provides more space on the interior of the complex. Fluorene ligands were also mixed with terphenyl **7.9**, biphenyl **7.10**, and control **7.11a** to determine the effects of ligand size and shape on assembly.

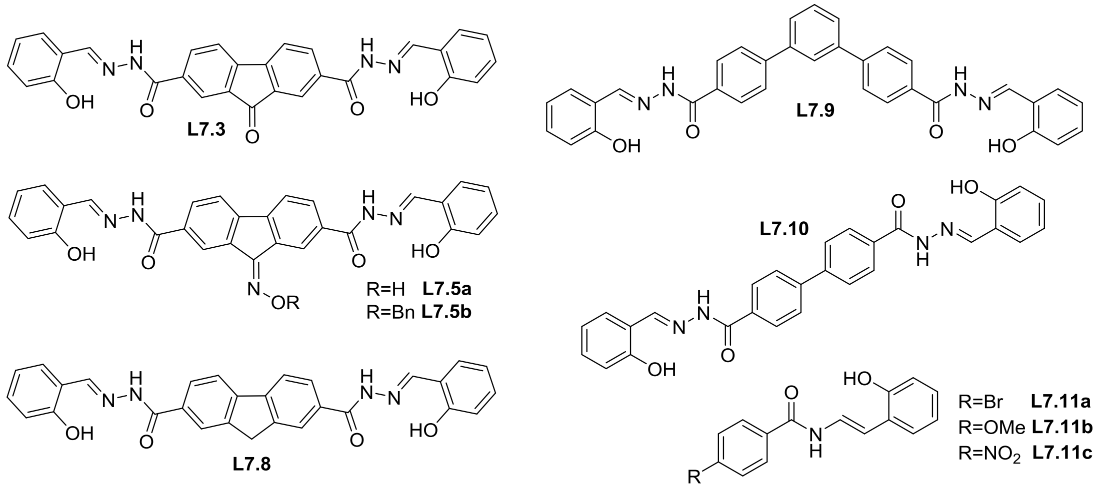

Figure 7.4: Salicylhydrazone ligands used in self-sorting experiments.

A common way to induce narcissistic self-sorting is by combining ligands of differing size and shape. Nearly linear fluorenone **7.3** was mixed with both bent **7.9** and linear **7.10**. Unsurprisingly, complete discrimination was observed upon addition of metal to a mixture of ligands. The ^{1}H NMR spectra obtained from the mixing experiments (Figure 7.5d-f) appeared as a superposition of the spectra of the individual complexes (Figure 7.5a-c). Sorting with control ligand **7.11a**, which can only form ML_3 complexes, was also investigated. Complete discrimination was again observed, and supramolecular assemblies were favored over the possible oligomers that could be imagined if **7.11a** was partially incorporated into the assemblies. This supports the literature where differences in size and shape are effective methods of discrimination in systems with identical coordination motif.

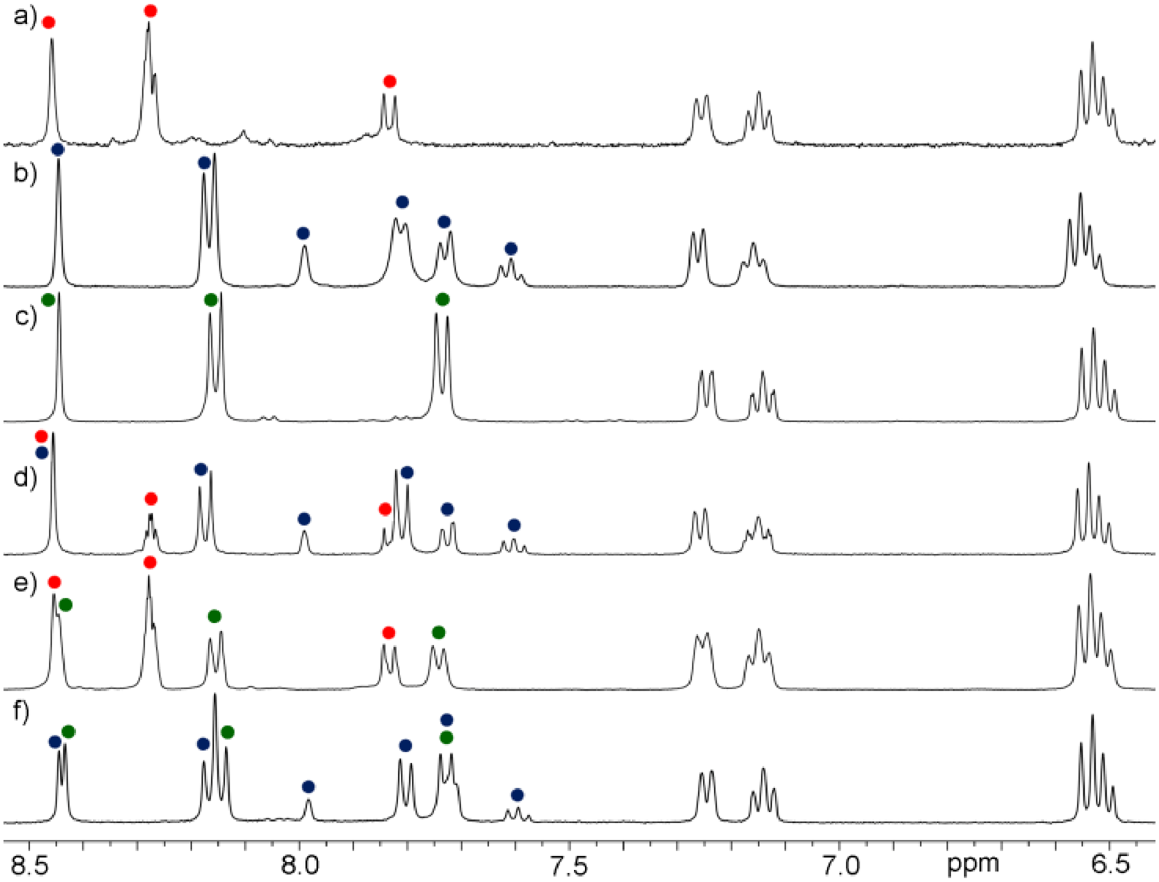

Figure 7.5: Narcissistic self-sorting in ligands of different geometry: a) Na$_6$[(**7.3**)$_3$Y$_2$]; b) Na$_6$[(**7.9**)$_3$Y$_2$]; c) Na$_{12}$[(**7.10**)$_6$Y$_4$]; d) **7.3** + **7.9** + Y(OTf)$_3$; e) **7.3** + **7.10** + Y(OTf)$_3$; f) **7.9** + **7.10** + Y(OTf)$_3$ (400 MHz, DMSO-*d*$_6$, 298 K).

Selective assembly becomes more challenging as components increase in similarity. When fluorene ligands **7.3**, **7.5a-b**, and **7.8** were mixed, narcissistic self-sorting was again observed. This is remarkable because the ligands differ only in endohedral functionalization. Self-sorting is kinetically controlled, and complete discrimination was observed immediately after addition of metal to the mixture of ligands. No exchange occurred, even after heating overnight. Figure 7.6 shows the ^{1}H NMR spectra of the oxime **7.5a** and benzyl oxime **7.5b** combination. The spectrum of the mixture (Figure 7.6d) again appears as a superposition of the two component complexes. Of particular note are the singlets near 9.0 and 5.5 ppm. If mixed complexes were forming, multiplicity would be observed in these peaks.

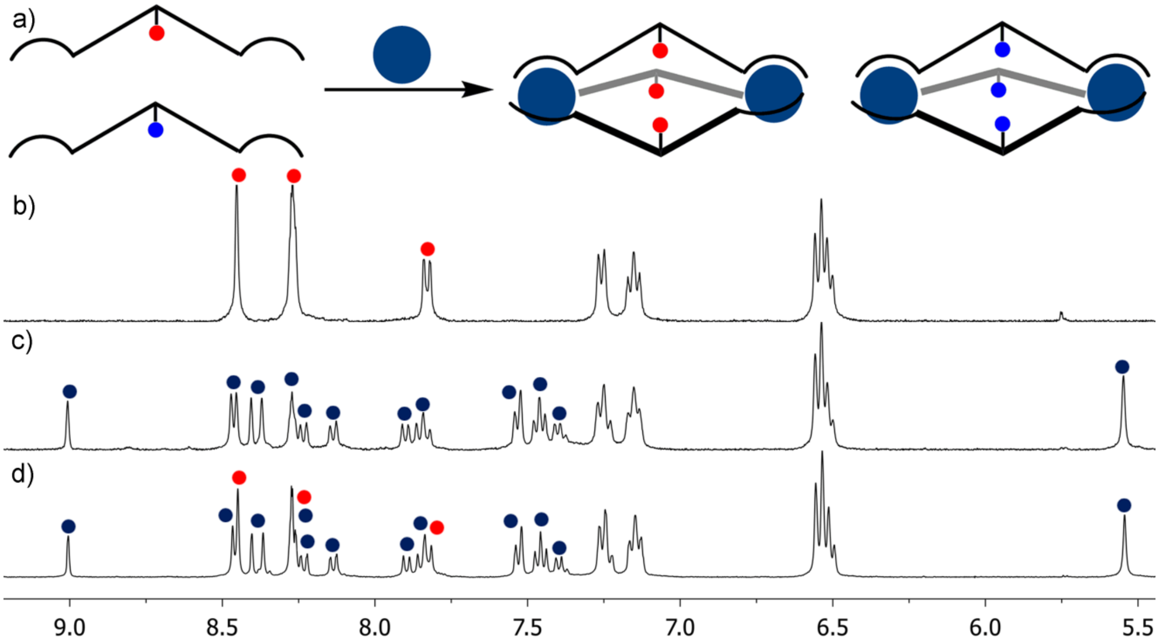

Figure 7.6: Narcissistic self-sorting in oxime ligands: a) cartoon of narcissistic self-sorting; b) $Na_6[(\mathbf{7.5a})_3Y_2]$ c) $Na_6[(\mathbf{7.5b})_3Y_2]$; d) **7.5a** + **7.5b** + $Y(OTf)_3$; (400 MHz, DMSO-d_6, 298 K).

Narcissistic self-sorting was even observed in ligands with similarly sized endohedral functionality. Figure 7.7 shows the ^{1}H NMR spectra of mixtures of fluorenone **7.3**, oxime **7.5a**, and fluorene **7.8**. The individual complexes can again be identified, even in the extremely close fluorenone/oxime pairing (Figure 7.7b).

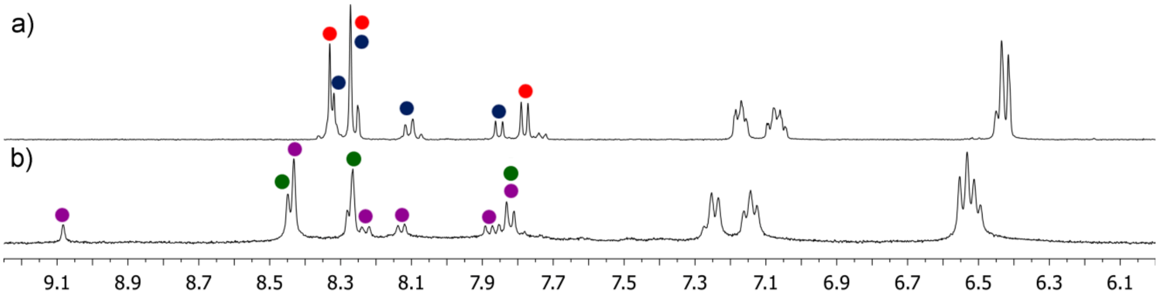

Figure 7.7: Narcissistic self-sorting in ligands with similarly-sized endohedral functionality: a) **7.3** + **7.8** + $La(OTf)_3$; b) **7.3** + **7.5a** + $Y(OTf)_3$ (400 MHz, DMSO-d_6, 298K). Red=$Na_6[(\mathbf{7.3})_3La_2]$, blue=$Na_6[(\mathbf{7.8})_3La_2]$, green=$Na_6[(\mathbf{7.3})_3Y_2]$, purple=$Na_6[(\mathbf{7.5a})_3Y_2]$.

7.7 Mixing in Control Complexes

To determine whether narcissistic self-sorting in this system was a supramolecular effect, mixing experiments were performed with control ligands **7.11a-7.11c**. These ligands contain only one metal-coordinating group and form monometallic ML_3 complexes rather than supramolecular helices. Figure 7.7 shows the spectra of mixing experiments between bromo control **7.11a** and methoxy control **7.11b**.

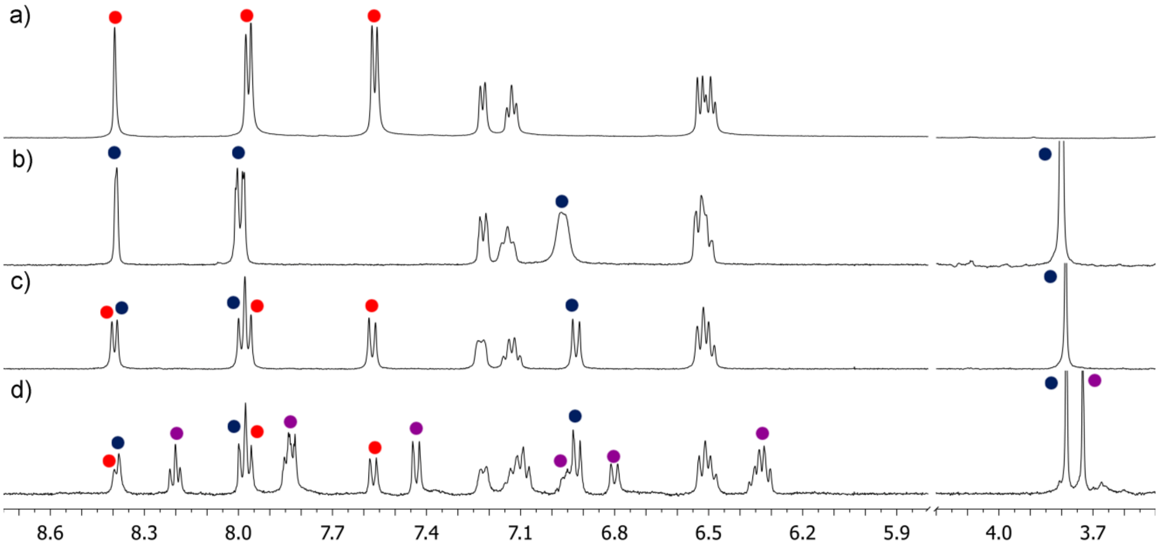

Figure 7.8: Formation of heterocomplexes in control ligands: a) $Na_3[(\mathbf{7.11a})_3Y]$; b) $Na_3[(\mathbf{7.11b})_3Y]$; c) $Na_3[(\mathbf{7.11a})_x(\mathbf{7.11b})_yY]$; d) $Na_3[(\mathbf{7.11a})_x(\mathbf{7.11b})_yY]$ at 60 °C overnight (400 MHz, DMSO-d_6, 298 K). Red=$Na_3[(\mathbf{7.11a})_3Y]$, blue=$Na_3[(\mathbf{7.11b})_3Y]$, purple=heterocomplexes.

Upon initial mixing, self-sorting is observed as in the *bis*-tridentate ligands. After heating, however, new signals appear in the spectrum which can be assigned as heterocomplexes $Na_3[(\mathbf{7.11a})_1(\mathbf{7.11b})_2Y]$ and $Na_3[(\mathbf{7.11a})_2(\mathbf{7.11b})_1Y]$. This result was confirmed by mass spectrometry where the heterocomplex $[(\mathbf{L7.11a})_1(\mathbf{L7.11b})_2\text{-H}]^{2+}$ ion was observed. Mixing was also observed in the control complexes of La which shows that narcissistic self-sorting in this system is a supramolecular effect.

7.8 Conclusion

This work has described narcissistic self-sorting in a series of salicylhydrazone-lanthanide complexes. Complete discrimination was predicted with ligands of differing size and shape, and this was observed. Remarkably, narcissistic self-sorting was also observed in ligands with the same size, shape, and metal coordinator that differed only in endohedral functionality. The sorting ability of the system was retained even when ligands became extremely similar such as between a ketone and an oxime. Narcissistic self-sorting is a supramolecular effect, and heterocomplexes were observed in mixtures of monometallic control ligands.

7.9 References

1 a) Singh, A. S.; Sun, S.-S. “Narcissistic self-sorting of hydrogen-bonded dimeric capsules formed through self-assembly of flexible tripodal receptors in polar solvents.” *Chem. Commun.* **2012**, *48*, 7392-7394.; b) Acharyya, K.; Mukherjee, P. S. “Hydrogen-bond-driven controlled molecular marriage in covalent cages.” *Chem. Eur. J.* **2014**, *20*, 1646-1657.; c) Ghosh, S.; Wu, A.; Fettinger, J. C.; Zavalij, P. Y.; Isaacs, L. “Self-sorting molecular clips.” *J. Org. Chem.* **2008**, *73*, 5915-5925.; d) Barrett, E. S.; Dale, T. J.; Rebek, J., Jr. “Stability, dynamics, and selectivity in the assembly of hydrogen-bonded hexameric capsules.” *J. Am. Chem. Soc.* **2008**, *130*, 2344-2350.; e) Shi, Q.; Bergquist, K.-E.; Huo, R.; Li, J.; Lund, M.; Vácha, R.; Sundin, A.; Butkus, E.; Orentas, E.; Wärnmark, K. “Composition- and size-controlled cyclic self-assembly by solvent- an C_{60}-responsive self-sorting.” *J. Am. Chem. Soc.* **2013**, *135*, 15263-15268.; f) Pellizzaro, M. L.; Houton, K. A.; Wilson, A. J. “Sequential and phototriggered supramolecular self-sorting cascades using hydrogen-bonded motifs.” *Chem. Sci.* **2013**, *4*, 1825-1829.

2 a) Safont-Sempere, M. M.; Fernández, G.; Würther, F. “Self-sorting phenomena in complex supramolecular systems.” *Chem. Rev.* **2011**, *111*, 5784-5814.; b) Ward, M. D.; Raithby, P. R. “Functional behavior from controlled self-assembly: Challenges and prospects.” *Chem. Soc. Rev.* **2013**, *42*, 1619-1636.; c) Saha, M. L.; Schmittel, M. “Degree of molecular self-sorting in multicomponent systems.” *Org. Biomol. Chem.* **2012**, *10*, 4651-4684; d) Hamacek, J.; Borkovec, M.; Piguet, C. “Simple thermodynamics for unravelling sophisticate self-assembly processes.” *Dalton Trans.* **2006**, 1473-1490.; e) Saha, M. L.; De, S.; Pramanik, S.; Schmittel, M. “Orthogonality in discrete self-assembly—survey of current concepts.” *Chem. Soc. Rev.* **2013**, *42*, 6860-6909.

3 a) Northrop, B. H.; Yang, H.-B.; Stang, P. J. “Second-order self-organization in coordination-driven self-assembly: Exploring the limits of self-selection.” *Inorg. Chem.* **2008**, *47*, 11257-11268.; b) Kamada, T.; Aratani, N.; Ikeda, T.; Shibata, N.; Higuchi, Y.; Wakamiya, A.; Yamaguchi, S.; Kim, K. S.; Yoon, Z. S.; Dongho, K.; Osuka, A. “High fidelity self-sorting assembling of *meso*-cinchomeronimide appended *meso-meso* linked Zn(II) diporphyrins.” *J. Am. Chem. Soc.* **2006**, *128*, 7670-7678.; c) Acharyya, K.; Mukherjee, S.; Mukherjee, P. S. “Molecular marriage through partner preferences in covalent cage formation and cage-to-cage transformation.” *J. Am. Chem. Soc.* **2013**, *135*, 554-557.

4 a) Yamanaka, M.; Yamada, Y.; Sei, Y.; Yamaguchi, K.; Kobayashi, K. “Selective formation of a self-assembling homo or hetero cavitand cage via metal coordination based on thermodynamic or kinetic control.” *J. Am. Chem. Soc.* **2006**, *128*, 1531-1539.; b) Mukhopadhyay, P.; Wu, A.; Isaacs, L. “Social self-sorting in aqueous solution.” *J. Org. Chem.* **2004**, *69*, 6157-6164.; c) Le, L.; Zhang, H.-Y.; Zhao, J.; Li, N.; Liu, Y. “Self-sorting of four organic molecules into a heterowheel polypseudorotaxane.” *Chem. Eur. J.* **2013**, *19*, 6498-6506.; d) Saha, M. L.; Schmittel, M. “From 3-fold completive self-sorting of a nine-component library to a seven-component scalene quadrilateral.” *J. Am. Chem. Soc.* **2013**, *135*, 17743-17746.; e) Smulers, M. M. J.; Jiménez, A.; Nitschke, J. R. “Integrative self-sorting synthesis of a $Fe_8Pt_6L_{24}$ cubic cage.” *Angew. Chem., Int. Ed.* **2012**, *51*, 6681-6685.; f) Saha, M. L.; Pramanik, S.; Schmittel, M. “Spontaneous and catalytic fusion of supramolecules.” *Chem. Commun.* **2012**, *48*, 9459-9461.; g) Cao, L.-P.; Wang, J.-G.;

Ding, J.-Y.; Wu, A.-X.; Isaacs, L. “Reassembly self-sorting triggered by heterodimerization.” *Chem. Commun.* **2011**, *47*, 8548-8550.

5) Wu, A.; Isaacs, L. “Self-sorting: the exception or the rule?” *J. Am. Chem. Soc.* **2003**, *125*, 4831-4835.

6 a) Caulder, D. L.; Raymond, K. N. “Superamolecular self-recognition and self-assembly in gallium(III) catecholamide triple helices.” *Angew. Chem. Int. Ed. Engl.* **1997**, *36*, 1440-1442.; b) Krämer, R.; Lehn, J.-M.; Marquis-Rigault, A. “Self-recognition in helicate self-assembly: Spontaneous formation of helical metal complexes from mixtures of ligands and metal ions.” *Proc. Natl. Acad. Sci. USA* **1993**, *90*, 5394-5398.; c) Albrecht, M.; Schneider, M.; Röttele, H. “Template-directed self-recognition of alkyl-bridged bis(catechol) ligands in the formation of helicate-type complexes.” *Angew. Chem., Int. Ed.* **1999**, *38*, 557-559.

7 a) Sun, Q.-F.; Iwasa, J.; Ogawa, D.; Ishido, Y.; Sato, S.; Ozeki, T.; Sei, Y.; Yamaguchi, K.; Fujita, M. “Self-assembled $M_{2}4L_{48}$ polyhedra and their sharp structural switch upon subtle ligand variation.” *Science* **2010**, *328*, 1144-1147.; b) Pinalli, R.; Cristini, V.; Sottili, V.; Geremia, S.; Campagnolo, M.; Caneschi, A.; Dalcanale, E. “Cavitand-based nanoscale coordination cages.” *J. Am. Chem. Soc.* **2004**, *126*, 6516-6517.; c) Jiménez, A.; Bilbeisi, R. A.; Ronson, T. A.; Zarra, S.; Woodhead, C.; Nitschke, J. R. “Selective encapsulation and sequential release of guests within a self-sorting mixture of three tetrahedral cages.” *Angew. Chem., Int. Ed.* **2014**, *53*, 4556-4560.

8 a) Gütz, C.; Hovorka, R.; Schnakenburg, G.; Lützen, A. “Homochiral supramolecular M_2L_4 cages by high-fidelity self-sorting of chiral ligands.” *Chem. Eur. J.* **2013**, *19*, 10890-10894.; b) Helmich, F.; Smulders, M. M. J.; Lee, C. C.; Schenning, A. P. H. J.; Meijer, E. W. “Effect of stereogenic centers on the self-sorting, depolymerization, and atropisomerization kinetics of porphyrin-based aggregates.” *J. Am. Chem. Soc.* **2011**, *133*, 12238-12246.; c) Sisco, S. W.; Moore, J. S. “Homochiral self-sorting of BINOL macrocycles.” *Chem. Sci.* **2014**, *5*, 81-85.

9) Johnson, A. M.; Hooley, R. J. “Steric effects control self-sorting in self-assembled clusters.” *Inorg. Chem.* **2011**, *50*, 4671-4673.

10 a) Johnson, A. M.; Moshe, O.; Gamboa, A. S.; Langloss, B. W.; Limtiaco, J. F. K.; Larive, C. K.; Hooley, R. J. “Synthesis and properties of metal-ligand complexes with endohedral amine functionality.” *Inorg. Chem.* **2011**, *50*, 9430-9442.; b) Frank, M.; Krause, L.; Herbst-Irmer, R.; Stalke, D.; Clever, G. H. “Narcissistic self-sorting *vs.* statistic ligand shuffling within a series of phenothiazine-based coordination cages.” *Dalton Trans.* **2014**, *43*, 4587-4592.; c) Bilbeisi, R. A.; Clegg, J. K.; Elgrishi, R.; de Hatten, X.; Devillard, M.; Breiner, B.; Mal, P.; Nitschke, J. R. “Subcomponent self-assembly and guest-binding properties of face-capped $Fe_4L_4^{8+}$ capsules.” *J. Am. Chem. Soc.* **2012**, *134*, 5110-5119.

11) Johnson, A. M., Young, M. C.; Zhang, X.; Julian, R. R.; Hooley, R. J. “Cooperative thermodynamic control of selectivity in the self-assembly of rare earth metal-ligand helices.” *J. Am. Chem. Soc.* **2013**, *135*, 17723-17726.

12 a) Jensen, T. B.; Scopelliti, R.; Bünzli, J.-C. G. “Tuning the self-assembly of lanthanide triple stranded heterobimetallic helicates by ligand design.” *Dalton Trans*. **2008**, 1027-1036.; b) Jensen, T. B.; Scopelliti, R.; Bünzli, J.-C. G. “Thermodynamic parameters governing the self-assembly of head-head-head lanthanide bimetallic helicates.” *Chem. Eur. J.* **2007**, *13*, 8404-8410.; c) Sorgho-Aboshyan, L.; Nozary, H.; Aebischer, A.; Bünzli, J.-C. G.; Morgantini, P.-Y.; Kittilstved, K. R. “Optimizing millisecond time scale near-infrared emission in polynuclear chrome(III)-lanthanide(III) complexes.” *J. Am. Chem. Soc.* **2012**, *134*, 12675-12684.; d) Albrecht, M.; Osetska, O.; Bünzli, J.-C. G.; Gumy, F.; Fröhlich, R. “Homo- and heterodinuclear helicates of lanthanide(III), zinc(II) an aluminum(III) based on 8-hydroxyquinoline ligands.” *Chem. Eur. J.* **2009**, *15*, 8791-8799.; e) Riis-Johannessen, T.; Bernardinelli, G.; Filinchuk, Y.; Clifford, S.; Favera, N. D.; Piguet, C. “Self-assembly of the first discrete 3d-4f-4f triple-stranded helicate.” *Inorg. Chem.* **2009**, *48*, 5512-5525.

13 a) Caulder, D. L.; Brückner, C.; Powers, R. E.; König, S.; Parac. T. N.; Leary, J. A.; Raymond, K. N. “Design, formation and properties of tetrahedral M_4L_4 and M_4L_6 supramolecular clusters.” *J. Am. Chem. Soc.* **2001**, *123*, 8923-8938.; b) Clegg, J. K.; Cremers, J.; Hogben, A. J.; Breiner, B.; Smulders, M. M. J.; Thoburn, J. D.; Nitschke, J. R. “A stimuli responsive system of self-assembling anionbinding Fe_4L_6 cages.” *Chem. Sci.* **2013**, *4*, 68-76.

Chapter Eight: Experimental

8.1 General Information

^{1}H and ^{13}C spectra were recorded on a Varian Inova 300,Varian Inova 400, Varian Inova 500, or Bruker Avance 600 spectrometer. Proton (^{1}H) chemical shifts are reported in parts per million (δ) with respect to tetramethylsilane (TMS, δ=0), and referenced internally with respect to the protio solvent impurity. Deuterated NMR solvents were obtained from Cambridge Isotope Laboratories, Inc., Andover, MA, and used without further purification. Mass spectra were recorded on a LCQ Deca XP Plus mass spectrometer (Thermo Fisher Scientific, San Jose, CA) using electrospray ionization and processed with Thermos Xcalibur 2.0 software (Chapters 2, 3, and 5), or an Agilent 6210 LC TOF mass spectrometer using electrospray ionization and processed with an Agilent MassHunter Operating System (Chapters 6 and 7). Gentle source conditions were employed to keep the metal-ligand complexes intact (Chapter 2). This was achieved by lowering voltages in the capillary/skimmer interface region. Mass spectra for Chapter 6 were acquired under the following conditions: 4 kV ion spray voltage, 29 V capilary voltage, 160 V tube lens offset. X-ray intensity data were collected at 100(2) K on a Bruker APEX2 platform-CCD X-ray diffractometer system. All other materials were obtained from Aldrich Chemical Company, St. Louis, MO or Combi-Blocks, San Diego, CA and were used as received. Solvents were dried through a commercial solvent purification system (Pure Process Technologies, Inc.). Molecular modeling (semi-empirical calculations) was performed using the AM1 force field in SPARTAN.[1]

8.2 Chapter Two Experimental

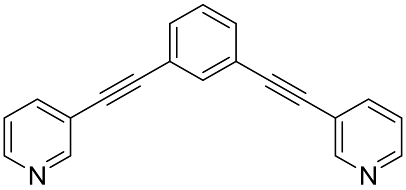

1,3-bis(pyridin-3-ylethynyl)benzene (2.3): To a 10 mL round bottom flask equipped with stir bar and reflux condenser was added 1,3-diethynyl benzene (150 mg, 1.19 mmol), 3-bromopyridine (2.85 mmol), 1,1'-bis(diphenylphosphino)ferrocene palladium(II) dichloride (50 mg, 0.06 mmol), and copper(I) iodide (13 mg, 0.07 mmol). The mixture was placed under nitrogen, and diisopropylamine (5 mL) was added. The reaction was stirred under nitrogen at 80 ˚C for 40 h. Ethyl acetate (5 mL) was added and the reaction was filtered through celite topped with a thin layer of silica gel. The filtrate was evaporated under reduced pressure, and the residue was purified by column chromatography on silica gel (ethyl acetate) to yield a tan solid (306 mg, 92%). ^{1}H NMR (400 MHz, DMSO-d_6) δ 8.78 (d, J=1.6 Hz, 2H); 8.61 (dd, J=1.6, 4.9 Hz, 2H); 8.00 (dt, J=1.6, 7.9 Hz, 2H); 7.81 (br s, 1H); 7.66 (dd, J=1.6, 7.7 Hz, 2H); 7.53 (t, J=7.7, 2H); 7.48 (dd, J=4.9, 7.9 Hz, 2H); ^{13}C (100 MHz, DMSO-d_6) δ 87.7, 91.8, 119.8, 123.1, 124.3, 130.2, 132.7, 134.9, 139.3, 149.9, 152.4; HRMS (ESI) *m/z*: calcd for $C_{20}H_{13}N_2$ $(M+H)^+$ 281.1079; found 281.1080.

Complex $[(2.3)_4Pd_2](NO_3)_4$: ^{1}H NMR (400 MHz, DMSO-d_6) δ 9.73 (d, J=1.6 Hz, 8H); 9.38 (dd, J=1.6, 5.6 Hz, 8H); 8.26 (d, J=8.2 Hz, 8H); 7.92 (br s, 4H); 7.82 (dd, J=5.6, 8.2 Hz, 8H); 7.71 (dd, J=8.2, 1.2 Hz, 8H); 7.57 (t, J=8.2 Hz, 8H); ^{13}C NMR (100 MHz, DMSO-d_6) δ 85.8, 94.4, 122.4, 122.9, 128.0, 130.7, 134.0, 134.6, 143.5, 151.3, 153.5;

HRMS (ESI) *m/z*: calcd for $C_{80}H_{48}N_{11}O_9{}^{106}Pd{}^{108}Pd$ (M+3 NO_3^-)$^+$ 1520.1705; found 1520.1696.

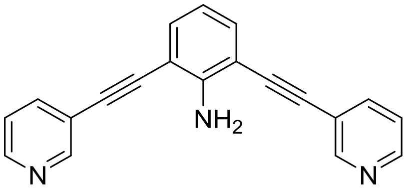

2,6-Bis(pyridin-3-ylethynyl)aniline (2.6a): To a 10 mL round bottom flask equipped with stir bar and reflux condenser was added 2,6-dibromoaniline (130 mg, 0.52 mmol), 3-ethynylpyridine (129 mg, 1.25 mmol), 1,10-*bis*(diphenylphosphino)ferrocene palladium(II) dichloride (22 mg, 0.03 mmol), and copper(I) iodide (6 mg, 0.03 mmol). The mixture was placed under nitrogen and dry, degassed tetrahydrofuran (2 mL) and degassed diisopropylamine (2 mL) were added. The reaction was heated at 80 °C for 48 h. Ethyl acetate (10 mL) was added, the reaction was filtered, and the filtrate was washed with water (3x20 mL) and brine (20 mL). The organic layer was dried over magnesium sulfate and evaporated under reduced pressure. The crude solid was recrystallized from ethyl acetate to yield a brown solid (74.3 mg, 49%). ^{1}H NMR (400 MHz, DMSO-d_6) δ 8.84 (s, 2H); 8.58 (d, J=4.0 Hz, 2H); 8.06 (td, J=4.0, 8.0 Hz, 2H); 7.47 (dd, J=8.0, 8.0 Hz, 2H); 7.39 (d, J=8.0 Hz, 2H); 6.64 (t, J=8.0 Hz, 1H); 5.91 (s, 1H); ^{13}C NMR (100 MHz, DMSO-d_6) δ 152.8; 150.1; 142.5; 133.9; 133.3; 129.2; 127.3; 122.3; 121.2; 93.7; 85.1. HRMS (ESI) *m/z*: calcd for $C_{20}H_{13}N_3$ (M+H)$^+$ 296.1182; found 296.1118.

Complex [(2.6a)$_4$Pd$_2$](NO$_3$)$_4$: ^{1}H NMR (400 MHz, DMSO-d_6) δ 9.66 (s, 2H); 9.36 (d, J=8.0 Hz, 2H); 8.21 (d, J=8.0 Hz, 2H); 7.79 (dd, J=8.0, 8.0 Hz, 2H); 7.43 (d, J=8.0 Hz, 2H); 6.67 (t, J=8.0 Hz, 1H); 6.24 (s, 2H); ^{13}C NMR (100 MHz, DMSO-d_6) δ 152.6; 150.5;

149.9; 142.0; 134.8; 127.2; 122.9; 116.9; 105.1; 92.4; 89.6. HRMS (ESI) *m/z*: calcd for $C_{83}H_{52}N_{12}O_9F_9S_3{}^{106}Pd{}^{108}Pd$ (M-OTf$^-$)$^+$ 1841.1067; found 1841.1054.

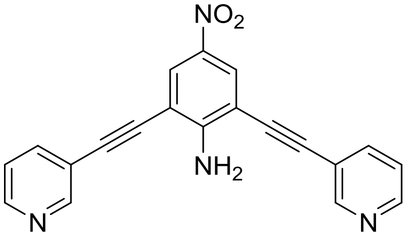

2,6-Bis(pyridylethynyl)-4-nitroaniline (2.6b): To an oven-dried 25 mL round bottom flask equipped with stir bar and reflux condenser was added 2,6-diiodonitroaniline (390 mg, 1.00 mmol), 3-ethynylpyridine (250 mg, 2.40 mmol), bis(triphenylphosphine)palladium(II) dichloride (20 mg, 0.03 mmol), and triphenylphosphine (20 mg, 0.08 mmol). The mixture was placed under nitrogen and degassed diethylamine (5 mL) was added. The reaction was heated to 70 °C for 18 h. Ethyl Acetate (50 mL) was added to the reaction, and the mixture was filtered. Water (50 mL) was added and the reaction was extracted with ethyl acetate (3x30 mL), dried over anhydrous magnesium sulfate, and evaporated under reduced pressure. The residue was purified by flash column chromatography on silica gel (chloroform, 2% methanol/chloroform, 4% methanol/chloroform) to yield a yellow solid (220 mg, 65%). ^{1}H NMR (400 MHz, DMSO-*d*$_6$) δ 8.92 (d, J=1.9 Hz, 2H); 8.61 (dd, J=1.6, 4.8 Hz, 2H); 8.24 (s, 2H); 8.14 (dt, J=1.8, 7.9 Hz, 2H); 7.50 (dd, J=5.0, 8.0 Hz, 2H); 7.28 (s, 2H). ^{13}C NMR (100 MHz, DMSO-*d*$_6$) δ 154.6; 152.1; 149.2; 138.9; 135.9; 129.1; 123.5; 119.2; 105.5; 92.6; 86.8. HRMS (ESI) *m/z*: calcd for $C_{20}H_{12}N_4O_2$ (M+H)$^+$ 341.1033; found 341.1009.

Complex [(2.6b)$_4$Pd$_2$](NO$_3$)$_4$: ^{1}H NMR (400 MHz, DMSO-*d*$_6$) δ 9.68 (s, 2H); 9.40 (d, J=4.0 Hz, 2H); 8.31 (d, J=8.0 Hz, 2H); 8.29 (s, 2H); 7.85 (dd, J=6.0, 8.0 Hz, 2H); 7.34 (s, 2H); ^{13}C NMR (125 MHz, DMSO-d_6) δ 154.5; 152.8; 150.5; 142.5; 136.5; 130.2; 127.3; 122.3; 105.1; 90.5; 89.9. HRMS (ESI) *m/z*: calcd for $C_{83}H_{48}N_{16}O_{17}F_9S_3{}^{106}Pd^{108}Pd$ (M-OTf$^-$)$^+$ 2021.0470; found 2021.0531.

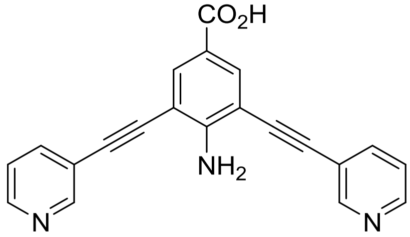

4-Amino-3,5-bis(pyridin-3-ylethynyl)benzoic Acid (2.6c): To an oven dried 25 mL round bottom flask equipped with stir bar and reflux condenser was added 4-amino-3,5-diiodobenzoic acid (195 mg, 0.50 mmol), 3-ethynylpyridine (130 mg, 1.26 mmol), bis(triphenylphosphine) palladium(II) dichloride (15 mg, 0.02 mmol), and triphenylphosphine (9 mg, 0.03 mmol). The mixture was placed under nitrogen, and dry, degassed tetrahydrofuran (4 mL), and degassed triethylamine (4 mL) were added. The reaction was heated at 50 °C for 16 h. Tetrahydrofuran was added (20 mL), and the reaction was filtered. The filtrate was evaporated under reduced pressure, and the residue was purified by column chromatography on silica gel (4% methanol/chloroform to 10% methanol/chloroform) to yield a yellow solid (65 mg, 38%). ^{1}H NMR (400 MHz, DMSO-d_6) δ 12.64 (br s, 1H); 8.89 (d, J=1.2 Hz, 2H); 8.59 (dd, J=1.6, 4.8 Hz, 2H); 8.11 (td, J=2.0, 8.0 Hz, 2H); 7.91 (s, 2H); 7.48 (dd, J=4.8, 8.0 Hz, 2H); 6.64 (s, 2H); ^{13}C NMR (100 MHz, DMSO-d_6) δ 165.9; 152.9; 151.9; 148.9; 138.7; 134.7; 123.4; 119.6; 118.1; 105.4; 91.7; 88.0; HRMS (ESI) *m/z*: calcd for $C_{21}H_{13}N_3O_2$ (M+H)$^+$ 340.1081; found 340.1073.

Complex $[(\mathbf{2.6c})_4\mathbf{Pd}_2](\mathbf{NO}_3)_4$: ^{1}H NMR (400 MHz, DMSO-d_6) δ 9.68 (s, 2H); 9.37 (d, J=5.2 Hz, 2H); 8.29 (d, J=8.0 Hz, 2H); 7.96 (s, 2H); 7.81 (dd, J=6.0, 7.6 Hz, 2H); 6.83 (s, 2H); HRMS (ESI) *m/z*: calcd for $C_{87}H_{52}N_{12}O_{17}F_9S_3{}^{106}Pd^{108}Pd$ $(M\text{-}OTf^-)^+$ 2017.0660; found 2017.0727. Note: this complex was too insoluble to obtain a ^{13}C NMR spectrum in any reasonable amount of time.

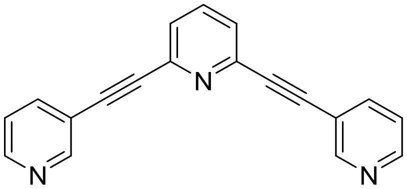

2,6-Bis(pyridin-3-ylethynyl)pyridine (2.6d): To an oven dried 25 mL round bottom flask equipped with stir bar and reflux condenser was added 2,6-dibromopyridine (58 mg, 0.24 mmol), 3-ethynylpyridine (61 mg, 0.59 mmol), bis(triphenylphosphine)palladium(II) dichloride (9 mg, 0.01 mmol), triphenylphosphine (7 mg, 0.03 mmol) and copper(I) iodide (3 mg, 0.02 mmol). The mixture was placed under nitrogen and degassed diethylamine (3 mL) was added. The reaction was heated to 60 ^{o}C under nitrogen for 16 h. Ethyl acetate (10 mL) was added and the reaction was filtered. The residue was evaporated under reduced pressure, and the crude product was purified by column chromatography on silica gel (ethyl acetate) to yield an orange solid (55 mg, 80%). ^{1}H NMR (400 MHz, DMSO-d_6) δ 8.85 (s, 2H); 8.66 (d, J=3.6 Hz, 2H); 8.08 (dt, J=1.8, 7.9 Hz, 2H); 7.98 (t, J=7.8 Hz, 2H); 7.74 (d, J=7.8 Hz, 2H); 7.52 (dd, J=4.9, 7.9 Hz, 2H). ^{13}C NMR (100 MHz, DMSO-d_6) δ 152.0; 149.8; 142.3; 139.1; 137.9; 127.4; 123.8; 118.3; 90.9; 85.8. HRMS (ESI) *m/z*: calcd for $C_{19}H_{11}N_3$ $(M+H)^+$ 282.1026; found 282.1002.

Complex $[(\mathbf{2.6d})_4Pd_2](NO_3)_4$: ^{1}H NMR (400 MHz, DMSO-d_6) δ 9.88 (s, 2H); 9.41 (d, J=5.3 Hz, 2H); 8.32 (d, J=8.0 Hz, 2H); 7.97 (t, J=7.8Hz, 2H); 7.84 (dd, J=5.9, 7.9 Hz, 2H); 7.75 (d, J=7.8 Hz, 2H); ^{13}C NMR (100 MHz, DMSO-d_6) δ 153.5; 151.0; 143.3; 141.9; 138.0; 128.6; 127.3; 121.6; 93.3; 83.3. HRMS (ESI) *m/z*: calcd for $C_{79}H_{44}N_{12}O_9F_9S_3{}^{106}Pd^{108}Pd$ (M-OTf$^-$)$^+$ 1785.0441; found 1785.0473.

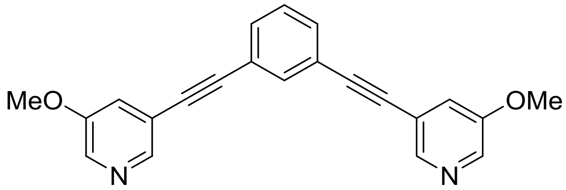

1,3-Bis((5-methoxypyridin-3-yl)ethynyl)benzene (2.8a): To a 10 mL round bottom flask equipped with stir bar and reflux condenser was added 1,3-diethynylbenzene (48 mg, 0.38 mmol), 3-bromo-5-methoxypyridine (178 mg, 0.95 mmol), 1,10 bis(diphenylphosphino)ferrocene palladium(II) dichloride (15 mg, 0.02 mmol), and copper(I) iodide (4 mg, 0.02 mmol). The mixture was placed under nitrogen, and degassed diisopropylamine (1 mL) was added. The reaction was heated at 80 °C for 22 h. Ethyl acetate (10 mL) was added, the reaction was filtered, and the filtrate was evaporated under reduced pressure. The crude product was recrystallized from ethyl acetate to yield a brown solid (87 mg, 68%). ^{1}H NMR (400 MHz, DMSO-d_6) δ 8.37 (s, 2H); 8.33 (d, J=2.0 Hz, 2H); 7.81 (s, 1H); 7.66 (dd, J=1.2, 8.4 Hz, 2H); 7.60 (dd, J=2.0, 2.8 Hz; 2H); 7.54 (t, J=7.7 Hz, 1H); 3.87 (s, 6H); ^{13}C NMR (100 MHz, DMSO-d_6) δ 154.9; 143.8; 138.15; 134.3; 132.0; 129.6; 122.4; 122.1; 119.4; 90.9; 87.0; 55.7; HRMS (ESI) *m/z*: calcd for $C_{22}H_{17}N_2O_2$ (M+H)$^+$ 341.1285; found 341.1295.

Complex $[(2.8a)_4Pd_2](NO_3)_4$: ^{1}H NMR (400 MHz, DMSO-*d*$_6$) δ 9.36 (s, 2H); 9.13 (d, J=2.4 Hz, 2H); 7.92 (s, 1H); 7.91 (s, 2H); 7.70 (d, J=8.4 Hz, 2H); 7.59 (t, J=7.6 Hz, 1H); 3.97 (s, 6H); ^{13}C NMR (100 MHz, DMSO-*d*$_6$) δ 156.7; 144.4; 139.3; 134.2; 133.3; 130.0; 126.7; 122.3; 121.7; 93.5; 85.0; 56.8; HRMS (ESI) *m/z*: calcd for $C_{91}H_{64}N_{12}O_9F_9S_3$ $^{106}Pd^{108}Pd$ $(M\text{-}OTf^-)^+$ 2021.1476; found 2021.1514.

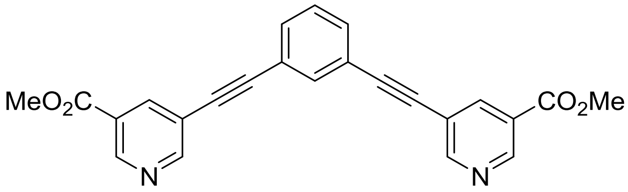

Dimethyl 5,5'-(1,3-phenylenebis(ethyne-2,1-diyl))dinicotinate (2.8b): To a 10 mL round bottom flask equipped with stir bar and reflux condenser was added 1,3-diethynylbenzene (25 mg, 0.20 mmol), methyl 5-bromonicotinate (87 mg, 0.40 mmol), and 1,10-bis(diphenylphosphino) ferrocene palladium(II) dichloride (8 mg, 0.01 mmol). The mixture was placed under nitrogen and anhydrous N,N'-dimethylformamide (1 mL), and degassed triethylamine (0.5 mL) were added. The reaction was heated at 80 °C for 16 h. Water (10 mL) was added, and the resulting precipitate was filtered. The crude product was purified by column chromatography on silica gel (methylene chloride) to yield a tan solid (44 mg, 56%). ^{1}H NMR (400 MHz, $CDCl_3$) δ 9.15 (d, J=1.6 Hz, 2H); 8.90 (d, J=1.6 Hz, 2H); 8.41 (t, J=2.0 Hz, 2H); 7.76 (s, 1H); 7.56 (dd, J=1.6, 7.6 Hz, 2H); 7.40 (t, J=7.6 Hz, 1H); 3.98 (s, 6H); ^{13}C NMR (100 MHz, $CDCl_3$) δ 165.22 155.6; 149.7; 139.5; 135.0; 132.3; 128.9; 125.8; 122.9; 120.3; 92.6; 85.9; 52.8; HRMS (ESI) *m/z*: calcd for $C_{24}H_{17}N_2O_4$ $(M+H)^+$ 397.1183; found 397.1154.

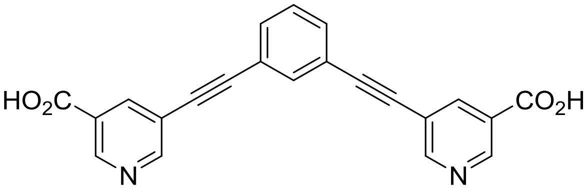

5,5’-(1,3-Phenylenebis(ethyne-2,1-diyl))dinicotinic acid (2.8c): To a 10 mL round bottom flask equipped with stir bar and reflux condenser was added dimethyl 5,5’-(1,3-phenylenebis(ethyne-2,1-diyl))dinicotinate (64 mg, 0.16 mmol), sodium hydroxide (53 mg, 1.32 mmol), tetrahydrofuran (0.8 mL), and water (0.2 mL). The reaction was heated at 65 °C for 16 h. The reaction was allowed to cool, and 10% aq. HCl was added until acidic. The resulting precipitate was filtered to yield a tan solid (53 mg, 89%). ^{1}H NMR (400 MHz, DMSO-d_6) δ 13.68 (br s, 2H); 9.06 (d, J=2.0 Hz, 2H); 8.99 (d, J=1.6 Hz, 2H); 8.40 (t, J=2.0 Hz, 2H); 7.91 (s, 1H); 7.71 (dd, J=1.2, 7.6 Hz, 2H); 7.56 (t, J=7.6 Hz, 1H); ^{13}C NMR (100 MHz, DMSO-d_6) δ 165.5; 154.9; 149.5; 139.1; 134.6; 132.3; 129.6; 126.5; 122.2; 119.2; 92.0; 86.1; HRMS (ESI) *m/z*: calcd for $C_{22}H_{13}N_2O_4$ $(M+H)^+$ 369.0870; found 369.0861.

Complex [(2.8c)$_4$Pd$_2$](NO$_3$)$_4$: ^{1}H NMR (400 MHz, DMSO-d_6) δ 9.98 (d, J=1.2 Hz, 2H); 9.87 (d, J=1.6 Hz, 2H); 8.56 (s, 2H); 7.94 (s, 1H); 7.80 (dd, J=1.2, 8.0 Hz, 2H); 7.60 (t, J=8.0 Hz, 1H); ^{13}C NMR (100 MHz, DMSO-d_6) δ 163.8; 155.8; 151.3; 142.5; 134.1; 133.7; 130.1; 128.5; 122.4; 121.7; 94.5; 84.9. HRMS data could not be obtained due to insolubility.

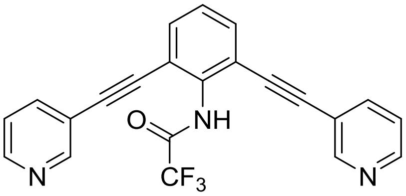

N-(2,6-bis(pyridin-3-ylethynyl)phenyl)-2,2,2-trifluoroacetamide (2.9): To a 10 mL round bottom flask equipped with stir bar was added 2,6-bis(pyridylethynyl)aniline (23 mg, 0.08 mmol), trifluoroacetic anhydride (54 µL, 0.39 mmol), and 1 mL dry pyridine. The mixture was stirred at room temperature for 16 h. Water (10 mL) was added and the mixture was extracted with ethyl acetate (3 x 10 mL). The combined organic layers were dried over magnesium sulfate and evaporated under reduced pressure to yield an orange solid (22 mg, 74 %). ^{1}H NMR (400 MHz, DMSO-d_6) δ 11.75 (s, 1H); 8.69 (s, 2H); 8.63 (d, J=4.0 Hz, 2H); 7.90 (dt, J=2.0, 8.0 Hz, 2H); 7.80 (d, J=8.0 Hz, 2H); 7.57 (t, J=8.0 Hz, 1H); 7.52 (dd, J=4.8, 8.0 Hz, 2H); ^{13}C (100 MHz, CDCl$_3$) δ 152.2; 150.7; 149.3; 145.9; 138.9; 136.4; 133.5; 128.4; 123.5; 121.6; 118.7 (q, J=287 Hz); 92.5; 87.8. HRMS (ESI) *m/z*: calcd for $C_{22}H_{13}N_3OF_3$ (M+H$^+$) 392.1005; found 392.1009.

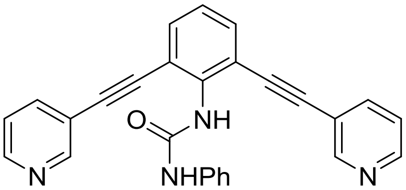

1-(2,6-Bis(pyridin-3-ylethynyl)phenyl)-3-phenylurea (2.10): To a sealed tube equipped with stir bar was added 2,6-bis(pyridylethynyl)aniline (25 mg, 0.08 mmol), phenyl isocyanate (47 µL, 0.43 mmol), and 0.5 mL dry pyridine. The reaction was stirred at 80 ˚C for 20 h. Water (10 mL) was added, and the precipitate was filtered and washed with chloroform (10 mL). The filtrate was extracted with chloroform (3 x 10 mL), washed with brine (10 mL), dried over magnesium sulfate, and evaporated under reduced pressure. The residue was purified by column chromatography (92:7:1 chlorofrom:methanol:triethylamine) to yield a yellow solid (9 mg, 24 %). Complete conversion was not possible, and a small amount of inseparable starting material was present in the sample. ^{1}H NMR (300 MHz, $CDCl_3$) δ 8.97 (s, 1H); 8.92 (s, 1H); 8.70 (d, J=3.0 Hz, 2H); 8.54 (d, J=3.0 Hz, 2H); 7.77 (d, J=9.0 Hz, 2H); 7.71 (dt, J=3.0, 9.0 Hz, 2H); 7.57 (t, J=6.0 Hz, 1H); 7.42 (dd, J=3.0, 6.0 Hz, 2H); 7.30 (tt, J=3.0, 9.0 Hz, 2H); 7.22 (dd, J=6.0, 6.0 Hz, 2H); 7.11 (tt, J=3.0, 6.0 Hz, 1H); ^{13}C NMR (100 MHz, $CDCl_3$) δ 152.9; 152.5; 149.5; 139.0; 137.2; 133.6; 130.1; 129.3; 129.3; 125.0; 123.3; 121.2; 120.9; 119.4; 92.9; 86.9; HRMS (ESI) *m/z*: calcd for $C_{27}H_{19}N_4O$ $(M+H)^+$ 415.1553; found 415.1557.

Procedure for Complex Formation: Ligand (7 μmol) was dissolved in DMSO-d_6 (0.5 mL) and added to an NMR tube. A solution of $Pd(NO_3)_2{\cdot}xH_2O$ was added (3.5 μmol), and the sample was shaken for 10 s for quantitative formation of complex.

Procedure for Kinetics Measurements:

Addition of Ligand 2.6d to Complex $[(2.3)_4Pd_2](NO_3)_4$: Ligand **2.3** was dissolved in DMSO-d_6 to make a 14 mM solution, and a 152 mM solution of $Pd(NO_3)_2$ was titrated in until complex formation was almost complete. A portion of this solution was added to an equal volume 28 mM solution of ligand **2.6d**. After mixing, spectra were periodically acquired (3 s delay, 32 scans). Concentrations of ligands and complexes were measured by integrating the peaks at 8.78, 8.85, and 9.94-9.61.

Exchange of [(2.3)$_4$Pd$_2$](NO$_3$)$_4$ and 2.6a:

[**2.6a**]$_0$=0.00532 M
Observed rate (loss of free ligand **2.6a**) = 5.92x10^{-5} s^{-1} t$_{1/2}$= 3.25 h

Time (s)	[**2.6a**] (M)	ln([**2.6a**]$_0$/[**2.6a**]$_t$)
120	0.00532	0.0008
300	0.00516	0.0030
480	0.00533	-0.0024
600	0.00500	0.0660
780	0.00506	0.0492
960	0.00506	0.0492
1080	0.00500	0.0628

Table 8.1: Exchange of [(**2.3**)$_4$Pd$_2$](NO$_3$)$_4$ and **2.6a**.

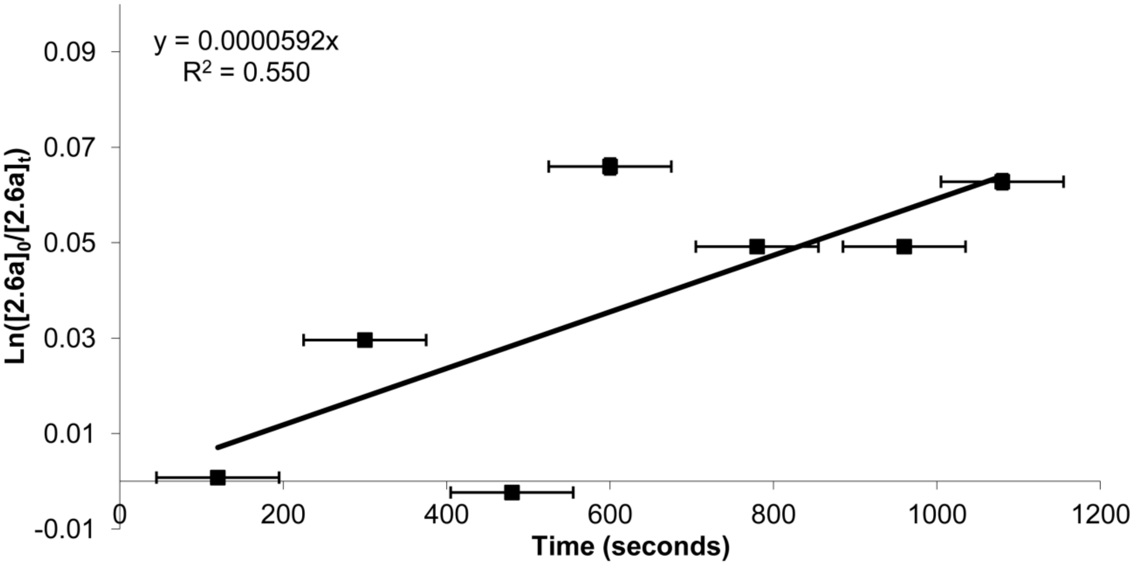

Figure 8.1: Graph of **2.6a** concentration vs time in Exchange of [(**2.3**)$_4$Pd$_2$](NO$_3$)$_4$ and **2.6a**.

Addition of Ligand 2.6a to Complex [(2.3)$_4$Pd$_2$](NO$_3$)$_4$: Ligand **2.3** was dissolved in DMSO-*d*$_6$ to make a 14 mM solution, and a 152 mM solution of Pd(NO$_3$)$_2$ was titrated in until complex formation was complete. A portion of this solution was added to an equal volume 28 mM solution of ligand **2.6a**. After mixing, spectra were periodically acquired (3 s delay, 32 scans).Concentrations of ligands and complex were measured by integrating the peaks at 8.00, 8.06, and 9.59-9.80 ppm.

Exchange of $[(2.3)_4Pd_2](NO_3)_4$ and 2.6d:

[**2.6d**]$_0$=0.00532 M
Observed rate (loss of free ligand **2.6d**) = 5.45x10^{-5} s^{-1} t$_{1/2}$= 3.53 h

Time (s)	[**2.6d**] (M)	ln([**2.6d**]$_0$/[**2.6d**]$_t$)
120	0.00321	0.0051
300	0.00320	0.0083
480	0.00313	0.0300
600	0.00314	0.0272
780	0.00292	0.1013
960	0.00329	-0.0175
1080	0.00297	0.0824

Table 8.2: Exchange of [(**2.3**)$_4$Pd$_2$](NO$_3$)$_4$ and **2.6d**.

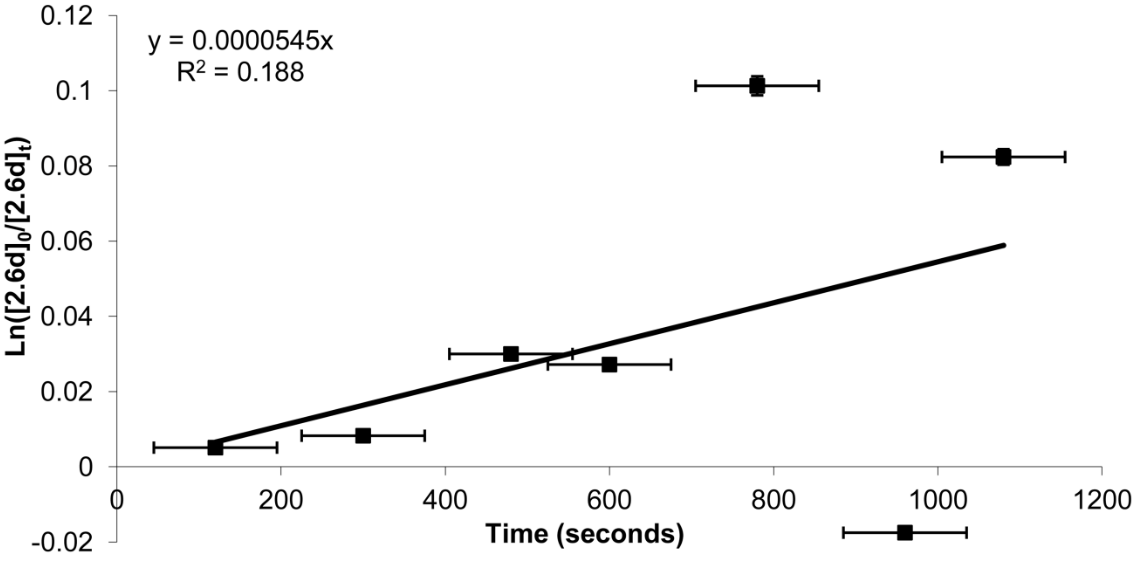

Figure 8.2: Graph of **2.6d** concentration vs time in Exchange of [(**2.3**)$_4$Pd$_2$](NO$_3$)$_4$ and **2.6d**.

Procedure for Diffusion Experiments: Diffusion experiments were performed using a Bruker Avance 600 MHz NMR spectrometer equipped with a broadband inverse probe with x-, y-, and z-gradients. Chemical shifts were referenced to the dimethyl sulfoxide-d_5 resonance (2.504) ppm. Diffusion data sets were acquired using the stimulated echo experiment with bipolar gradients (stebpgp1s) included with the Topspin release version 1.3. Gradient amplitudes were incremented as a square dependence from 5% to 95% into 22 gradient increments. A spoil gradient pulse of length 1 ms and amplitude of -17.13% was used to effectively remove transverse magnetization following the encode period of the pulse program. Spectra were acquired with 128 transients coadded and 28,672 data points per transient for each of the 22 increments. Diffusion (Δ) and gradient pulse times (δ) were optimized using a one-dimensional version of the stimulated echo pulse sequence, stebpgp1s1d to give values of 2.0 and 200 ms, respectively. Following acquisition, the FIDs were apodized by multiplication with an exponential function equivalent to 1 Hz line broadening prior to processing in Topspin to obtain pseudo-2D DOSY plots. Diffusion coefficients were calculated using the DOSY Toolbox software.[2] To simplify analysis of the diffusion coefficients, processing was carried out on individual spectral regions corresponding to the resonances at 9.679, 9.391, 8.914, and 8.609 ppm. Analysis of the diffusion coefficients was carried out on individual spectral regions corresponding to the resonances at 9.679, 9.391, 8.914, and 8.609 ppm. The data was fit using a standard monoexponential decay with a diffusion resolution of 256 points. Fitting statistics for the pure exponential fitting to the Stejskal-Tanner equation for the diffusion coefficients and fitting errors were determined and displayed following DOSY processing.

8.3 Chapter Three Experimental

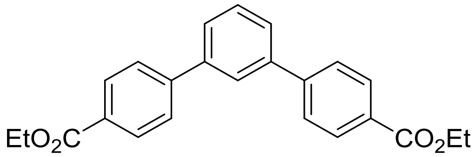

Diethyl [1,1':3',1''-terphenyl]-4,4''-dicarboxylate (3.4): To a round bottom flask equipped with stir bar and reflux condenser was added 1,3-dibromobenzene (600 mg, 2.54 mmol), 4-ethoxycarbonylphenylboronic acid (1.23 g, 6.35 mmol), bis(triphenylphosphine)palladium(II) chloride (90 mg, 0.13 mmol), and cesium carbonate (2.49 g, 7.65 mmol). The mixture was placed under nitrogen and anhydrous N,N-dimethylformamide (10 mL) was added. The reaction was heated under nitrogen at 100 ˚C for 16 h. Methanol (20 mL) was added and the reaction was filtered. The filtrate was allowed to cool in an ice bath, and the resulting precipitate was filtered. The crude product was dissolved in methylene chlordie (5 mL) and filtered through a celite plug topped with a thin layer of silica gel. The filtrate was evaporated under reduced pressure to yield a white solid (610 mg, 64%). ^{1}H NMR (400 MHz, $CDCl_3$) δ 8.14 (d, J=8.4 Hz, 4H); 7.85 (t, J=2.0 Hz, 1H); 7.71 (d, J=8.4 Hz, 4H); 7.65 (dd, J=1.6, 6.8 Hz, 2H); 7.57 (dd, J=6.8, 8.4 Hz, 1H); 4.42 (q, J=7.1 Hz, 4H); 1.43 (t, J=7.1 Hz, 6H); ^{13}C NMR (100 MHz, $CDCl_3$) δ 166.6; 145.3; 141.0; 130.3; 129.70; 129.65; 127.3; 127.2; 126.4; 61.2; 14.5; HRMS (ESI) m/z calcd for $C_{24}H_{23}O_4$ $(M+H)^+$ 375.1591; found 375.1601.

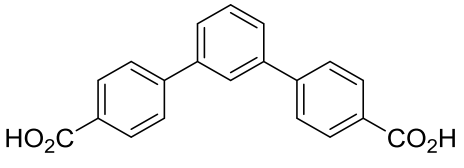

[1,1':3',1''-terphenyl]-4,4''-dicarboxylic acid (3.5): To a round bottom flask equipped with stir bar and reflux condenser was added diethyl [1,1':3',1''-terphenyl]-4,4''-

dicarboxylate (203 mg, 0.54 mmol), sodium hydroxide (181 mg, 4.53 mmol), tetrahydrofuran (4 mL), and water (1 mL). The reaction was heated at 65 ˚C for 16 h. The reaction was cooled and 10% aq. HCl was added until the aqueous layer was acidic. The resulting precipitate was filtered to yield a white solid (161 mg, 93%). ^{1}H NMR (400 MHz, DMSO-d_6) δ 8.05 (d, J=8.3 Hz, 4H); 8.05 (s, 1H); 7.93 (d, J=8.4 Hz, 4H); 7.79 (dd, J=2.0, 10.0 Hz, 2H); 7.64 (t, J=9.6 Hz, 1H); ^{13}C NMR (125 MHz, DMSO-d_6) δ 167.2; 144.1; 140.0; 130.0; 129.9; 127.2; 127.1; 126.9; 125.7.

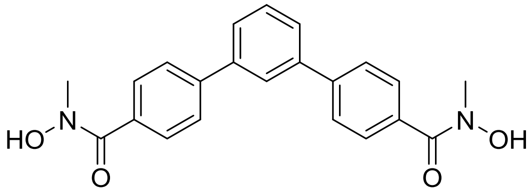

N^4,$N^{4''}$-dihydroxy-N^4,$N^{4''}$-dimethyl-[1,1’:3’,1”-terphenyl]-4,4”-dicarboxamide (3.11): To a round bottom flask equipped with stir bar and reflux condenser was added [1,1’:3’,1”-terphenyl]-4,4”-dicarboxylic acid (43 mg, 0.13 mmol), oxalyl chloride (0.5 mL), and one drop N,N’-dimethylformamide. The mixture was refluxed for 4 h, the solvent was evaporated, and the resulting solid was cooled to 0 ˚C. A solution of *N*-Methyl hydroxylamine (84 mg, 1.06 mmol) and Hünig’s base (370 µL, 2.12 mmol) in 2 mL methylene chloride was added dropwise. The reaction was warmed to room temperature and stirred for 16 h. The solvent was evaporated under reduced pressure and the crude mixture was stirred in conc. NH_4OH for 1 h. The precipitate was collected and stirred with 10% aq. HCl for 1 h. The precipitate was collected and recrystallized from acetone to yield a white solid (13 mg, 26%). ^{1}H NMR (300 MHz, $CDCl_3$) δ 7.81 (s, 1H); 7.73 (d, J=8.3 Hz, 4H); 7.66 (d, J=8.3 Hz, 4H); 7.62 (m, 1H); 7.61 (d, J=8.2 Hz, 2H); 3.48 (s, 6H).

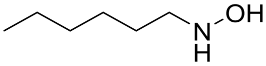

***N*-Hexylhydroxylamine (3.14):** To a round bottom flask equipped with stir bar and reflux condenser was added hydroxylamine hydrochloride (3.47 g, 50.0 mmol) and 5 mL water. Hexanal (1.23 mL, 10 mmol) was added in ethanol (5 mL), and 10% aq. NaOH was added until cloudiness persisted. The reaction was stirred at 70 ˚C for 2 h, and the ethanol was evaporated under reduced pressure. The remaining water was extracted with diethyl ether (3 x 15 mL), dried over magnesium sulfate, and evaporated under reduced pressure to yield a clear oil. This was suspended in methanol(10 mL) and cooled to -78 ˚C. Solutions of sodium cyanoborohydride (821 mg, 13.1 mmol) in methanol (10 mL) and 1:1 6 M HCl:methanol (10 mL) were added simultaneously at -78 ˚C. The reaction was warmed to -15 ˚C and stirred for 2 h. Cold brine (15 mL) was added, and the pH was adjusted to 10 with cold 10% aq. NaOH. The reaction was extracted with cold diethyl ether (3 x 25 mL), dried over magnesium sulfate, and evaporated under reduced pressure to yield a white solid (911 mg, 78%). ^{1}H NMR (300 MHz, $CDCl_3$) δ 5.80 (br s, 1H); 2.93 (t, J=7.1 Hz, 2H); 1.52 (p, J=7.0 Hz, 2H); 1.37-1.30 (m, 6H); 0.89 (t, J=6.9 Hz, 3H).

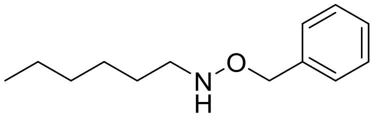

***O*-benzyl-*N*-hexylhydroxylamine (3.15):** To a round bottom flask equipped with stir bar was added hexanal (1.00 g, 10.00 mmol), *O*-benzylhydroxylamine hydrochloride (1.59 g, 9.98 mmol), and pyridine (6 mL). The reaction was stirred for 16 h. Water (20 mL) was added and the reaction was extracted with diethyl ether (3 x 20 mL), washed with brine, and dried over anhydrous magnesium sulfate. The solvent was removed under reduced pressure to yield a clear oil which was dissolved in methanol (5 mL) and cooled to 0 ˚C. Sodium cyanoborohydride (816 mg, 12.98 mmol) in methanol (10 mL) and 1:1 6 M HCl:water (10 mL) were added simultaneously and the reaction was stirred at 0 ˚C for 2 h. Brine (20 mL) was added and the reaction was basified with 10% aq. NaOH, extracted with diethyl ether (3 x 20 mL), washed with brine, dried over magnesium sulfate, and the solvent was evaporated under reduced pressure. The crude product was purified by column chromatography on silica gel (10% ethyl acetate/hexanes) to yield a light yellow oil (1.64 g, 79%). ^{1}H NMR (300 MHz, $CDCl_3$) δ 7.38-7.29 (m, 5H); 5.32 (br s, 1H); 4.71 (s, 2H); 2.93 (t, J=7.2 Hz, 2H); 1.51 (p, J=7.1 Hz, 2H); 1.37-1.26 (m, 6H); 0.89 (t, J=6.9 Hz, 3H).

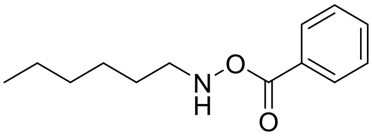

***O*-benzoyl-*N*-hexylhydroxylamine (3.17):** To a round bottom flask equipped with stir bar was added N-hexylamine (1.30 mL, 9.84 mmol), benzoyl peroxide, 2.62 g, 10.84 mmol), methylene chlordie (50 mL), and pH 10.5 sodium carbonate buffer (50 mL). The reaction was stirred vigorously for 20 h and the layers were separated. The aqueous layer was extracted with methylene chloride (3 x 50 mL), washed with brine, and dried over anhydrous magnesium sulfate. The solvent was removed under reduced pressure, and the residue was purified by column chromatography on silica gel (25% ethyl acetate/hexanes) to yield a clear oil (1.28 g, 59%). ^{1}H NMR (300 MHz, $CDCl_3$) δ 8.02 (d, J=7.2 Hz, 2H); 7.58 (t, J=7.3 Hz, 1H); 7.46 (t, J=7.7 Hz, 2H); 3.14 (t, J=7.1 Hz, 2H); 1.62 (p, J=7.2 Hz, 2H); 1.45-1.25 (m, 6H); 0.89 (t, J=6.9 Hz, 3H).

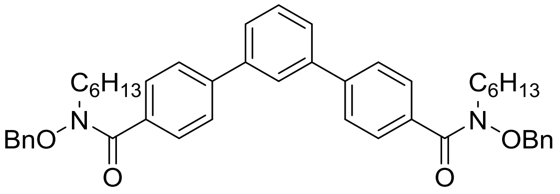

N^4,$N^{4''}$-bis(benzyloxy)-N^4,$N^{4''}$-dihexyl-[1,1':3',1''-terphenyl]-4',4''-dicarboxamide (3.18): To a round bottom flask equipped with stir bar was added [1,1':3',1''-terphenyl]-4,4''-dicarboxylic acid (204 mg, 0.64 mmol), 2-(6-Chloro-1H-benzotriazole-1-yl)-1,1,3,3-tetramethylaminium hexafluorophosphate (HCTU) (582 mg, 1.41 mmol), acetonitrile (3 mL), chloroform (3 mL), and triethylamine (357 µL, 2.56 mmol). The reaction was stirred for 2 h, and *O*-benzyl-*N*-hexylhydroxylamine (398 mg, 1.92 mmol) and triethylamine (535 µL, 3.84 mmol) were added. The reaction was stirred an additional 16 h and the solvent was evaporated. Saturated aq. sodium bicarbonate was added, the mixture was extracted with diethyl ether, washed with 10% aq. HCl, washed with brine, and dried over magnesium sulfate. The solvent was evaporated under reduced pressure to yield an oil which was purified by column chromatography on silica gel (25% ethyl acetate/hexanes) to yield a clear oil (278 mg, 62%). ^{1}H NMR (400 MHz, $CDCl_3$) δ 7.85 (s, 1H); 7.75 (d, J=8.0 Hz, 4H); 7.68 (d, J=8.3 Hz, 4H); 7.65 (d, J=8.3 Hz, 2H); 7.58 (t, J=8.7 Hz, 1H); 7.31-7.28 (m, 6H); 7.12 (d, J=7.7 Hz, 4H); 4.70 (s, 4H); 3.77 (t, J=7.2 Hz, 4H); 1.77 (p, J=7.3 Hz, 4H); 1.40-1.29 (m, 12H); 0.89 (t, J=7.1 Hz, 6H); ^{13}C NMR (100 MHz, $CDCl_3$) δ 169.8; 143.0; 141.3; 134.5; 133.9; 129.6; 129.6; 129.1; 129.0; 128.6; 126.9; 126.8; 126.3; 76.6; 47.3; 31.6; 27.4; 26.5; 22.7; 14.2.

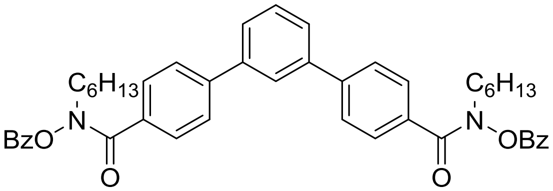

N^4,$N^{4''}$-bis(benzoyloxy)-N^4,$N^{4''}$-dihexyl-[1,1':3',1''-terphenyl]-4',4''-dicarboxamide (3.19): To a round bottom flask equipped with stir bar was added [1,1':3',1''-terphenyl]-4,4''-dicarboxylic acid (108 mg, 0.34 mmol), 2-(6-Chloro-1H-benzotriazole-1-yl)-1,1,3,3-tetramethylaminium hexafluorophosphate (HCTU) (309 mg, 0.75 mmol), triethylamine (190 µL, 1.36 mmol), acetonitrile (5 mL), and chloroform (5 mL). The reaction was stirred for 1.75 h and *O*-benzoyl-*N*-hexylhydroxylamine (188 mg, 0.85 mmol) and triethylamine (237 µL, 1.70 mmol) were added. The reaction was then stirred at 50 ˚C for 22 h. The solvents were evaporated and saturated aq. sodium bicarbonate was added. The mixture was extracted with diethyl ether, washed with 10% aq. HCl, washed with brine, and dried over magnesium sulfate. The solvent was evaporated under reduced pressure to yield an oil which was purified by column chromatography on silica gel (25% ethyl acetate/hexanes) to yield a clear oil (62 mg, 25%). ^{1}H NMR (300 MHz, $CDCl_3$) δ 8.05 (d, J=8.4 Hz, 4H); 7.79 (s, 1H); 7.70 (d, J=8.6 Hz, 4H); 7.71-7.63 (m, 6H); 7.58 (dd, J=5.9, 9.0 Hz, 1H); 7.41-7.33 (m, 6H); 3.90 (t, J=7.2 Hz, 4H); 1.77 (p, J=7.4 Hz, 4H); 1.46-1.26 (m, 12H); 0.89 (t, J=6.8 Hz, 6H).

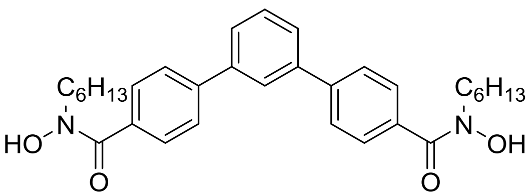

N^4,$N^{4''}$-dihexyl-N^4,$N^{4''}$-dihydroxy-[1,1':3',1''-terphenyl]-4',4''-dicarboxamide (3.20): To a round bottom flask equipped with stir bar was added N^4,$N^{4''}$-bis(benzyloxy)-N^4,$N^{4''}$-

dihexyl-[1,1':3',1''-terphenyl]-4',4''-dicarboxamide (158 mg, 0.23 mmol) and anhydrous methylene chloride (2 mL). Boron tribromide dimethyl sulfide complex (518 mg, 1.66 mmol) in anhydrous methylene chloride (8 mL) was added dropwise. The reaction was stirred for 1 h and water was added. The reaction was stirred 16 h and extracted with methylene chloride. The combined organics were washed with brine and dried over magnesium sulfate. Solvents were removed under reduced pressure to yield an oil which was purified by column chromatography on iron-free silica gel (5% methanol/methylene chloride) to yield a white solid (50 mg, 42%). ^{1}H NMR (400 MHz, $CDCl_3$) δ 8.57 (br s, 2H); 7.81 (t, J=2.2 Hz, 1H); 7.71 (d, J=7.9 Hz, 4H); 7.62 (m, 6H); 7.6 (dd, J=2.4, 6.4 Hz, 1H); 3.70 (t, J=7.0 Hz, 4H); 1.77 (q, J=7.0 Hz, 4H); 1.25 (m, 12H); 0.86 (t, J=6.7 Hz, 6H); ^{13}C NMR (100 MHz, $CDCl_3$) δ 166.8; 143.5; 140.9; 131.6; 129.8; 128.6; 127.5; 127.0; 126.3; 51.1; 31.4; 27.6; 26.2; 22.7; 14.1; HRMS (ESI) m/z calcd for $C_{32}H_{40}NaN_2O_4$ $(M+Na)^+$ 539.2880; found 539.2874.

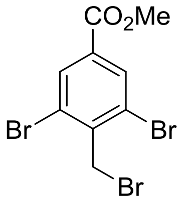

Methyl 3,5-dibromo-4-(bromomethyl)benzoate (3.22): To a round bottom flask equipped with stir bar and reflux condenser was added methyl 3,5-dibromo-4-methylbenzoate (256 mg, 0.83 mmol), N-bromosuccinimide (165 mg, 0.93 mmol), benzoyl peroxide (22 mg, 0.09 mmol), and carbon tetrachloride (3 mL). The reaction was refluxed for 16 h and filtered. The filtrate was evaporated under reduced pressure to yield a white solid (320 mg, 99%). ^{1}H NMR (400 MHz, $CDCl_3$) δ 8.20 (s, 2H); 4.82 (s, 2H); 3.94 (s, 3H); ^{13}C NMR (100MHz, $CDCl_3$) δ 164.2; 140.9; 133.6; 132.4; 125.6; 53.0; 33.1.

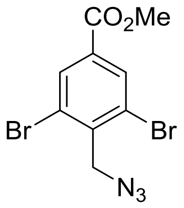

Methyl 4-(azidomethyl)-3,5-dibromobenzoate (3.23): To a round bottom flask equipped with stir bar was added methyl 3,5-dibromo-4-(bromomethyl)benzoate (259 mg, 0.67 mmol), sodium azide (51 mg, 0.78 mmol), tetrabutylammonium iodide (27 mg, 0.07 mmol), methylene chloride (1 mL), and water (1 mL). The reaction was stirred at room temperature for 16 h. Water (10 mL) was added and the aqueous layer was extracted with methylene chloride (3 x 10 mL). The combined organic layers were washed with brine (20 mL), dried over anhydrous magnesium sulfate, and evaporated under reduced pressure to yield an orange solid. The crude product was purified by column chromatography on silica gel (50% ethyl acetate/hexanes) to yield a white solid (194 mg, 83%). ^{1}H NMR (400 MHz, $CDCl_3$) δ 8.23 (s, 2H); 4.78 (s, 2H); 3.94 (s, 3H); ^{13}C NMR (100 MHz, $CDCl_3$) δ 164.2; 139.0; 133.6; 132.9; 126.2; 54.3; 53.0.

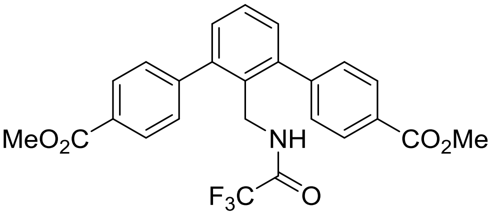

Dimethyl 2'-((2,2,2-trifluoroacetamido)methyl)-[1,1':3',1''-terphenyl]-4,4''-dicarboxylate (3.27): To a sealed tube equipped with stir bar was added benzylamine (26 mg, 0.24 mmol), methyl 4-iodobenzoate (314 mg, 1.20 mmol), palladium(II) acetate (3 mg, 0.01 mmol), silver acetate (95 mg, 0.57 mmol), and trifluoroacetic acid (92 µL, 1.20 mmol). The reaction was placed under nitrogen and heated at 130 °C for 24 h. The mixture was cooled, diluted with toluene, filtered, and the filtrate was evaporated under reduced pressure. The residue was dissolved in anhydrous pyridine (0.5 mL), and trifluoroacetic anhydride (165 μL, 1.19 mmol) was added. This was stirred for 16 h, water was added, and the resulting precipitate was filtered. This was purified by column chromatography on silica gel (methylene chloride, 5% methanol/methylene chloride) to yield a brown solid (26 mg, 23%). ^{1}H NMR (300 MHz, $CDCl_3$) δ 8.14 (d, J=8.1 Hz, 4H); 7.48 (t, J=8.2 Hz, 1H); 7.43 (d, J=8.2 Hz, 4H); 7.32 (d, J=7.7 Hz, 2H); 5.77 (br s, 1H); 4.44 (d, J=5.3 Hz, 2H); 3.95 (s, 6H).

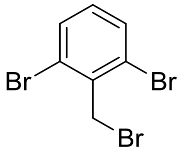

1,3-dibromo-2-(bromomethyl)benzene (3.29): To a round bottom flask equipped with stir bar and reflux condenser was added 2,6-dibromotoluene (512 mg, 2.05 mmol), N-bromosuccinimide (365 mg, 2.05 mmol), benzoyl peroxide (50 mg, 0.21 mmol), and carbon tetrachloride (5 mL). The reaction was refluxed for 16 h and filtered. The filtrate was evaporated under reduced pressure to yield a white solid (670 mg, 99%). ^{1}H NMR (300 MHz, $CDCl_3$) δ 7.55 (d, J=8.0 Hz, 2H), 7.02 (t, J=8.1 Hz, 1H), 4.83 (s, 2H).

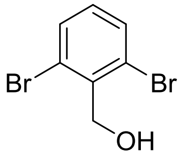

(2,6-dibromophenyl)methanol (3.30): To a round bottom flask equipped with stir bar and reflux condenser was added 1,3-dibromo-2-(bromomethyl)benzene (100 mg, 0.30 mmol), potassium hydroxide (198 mg, 3.53 mmol), iodine (8 mg, 0.03 mmol), tetrahydrofuran (5 mL), and water (0.25 mL). The reaction was refluxed for 18 h, acidified with 10% aq. HCl, extracted with ethyl acetate, washed with sodium thiosulfate, and dried over magnesium sulfate. The solvent was removed under reduced pressure to yield a yellow solid (75 mg, 93%). ^{1}H NMR (300 MHz, $CDCl_3$) δ 7.55 (d, J=8.0 Hz, 2H), 7.03 (t, J=8.0 Hz, 1H), 5.01 (s, 2H).

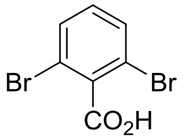

2,6-dibromobenzoic acid (3.31): To a round bottom flask equipped with stir bar and reflux condenser was added (2,6-dibromophenyl)methanol (95 mg, 0.36 mmol), potassium permanganate (567 mg, 3.59 mmol), water (6 mL), and t-butanol (3 mL). The reaction was stirred at 80 °C for 18 h, cooled to room temperature, and filtered. Saturated aq. sodium bicarbonate was added to the filtrate, and it was extracted with methylene chloride. The aqueous layer was acidified with 10% aq. HCl and extracted with methylene chloride. The organic layer was dried over magnesium sulfate, and the solvent was evaporated under reduced pressure to yield a white solid (59 mg, 59%). ^{1}H NMR (300 MHz, $CDCl_3$) δ 7.56 (d, J=8.1 Hz, 2H), 7.16 (t, J=8.1 Hz, 1H).

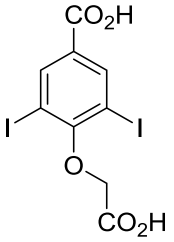

4-(carboxymethoxy)-3,5-diiodobenzoic acid (3.35): To a round bottom flask equipped with stir bar and reflux condenser was added 3,5-diiodo-4-hydroxybenzoic acid (543 mg, 1.39 mmol), ethyl bromoacetate (340 µL, 3.07 mmol), sodium iodide (27 mg, 0.18 mmol), potassium carbonate (479 mg, 3.47 mmol), and acetonitrile (8 mL). The reaction was refluxed 17 h, water was added, and the resulting precipitate was filtered to yield 2-

ethoxy-2-oxoethyl 4-(2-ethoxy-2-oxoethoxy)-3,5-diiodobenzoate as a white solid (708 mg, 90%). ^{1}H NMR (400 MHz, $CDCl_3$) δ 8.48 (s, 2H); 4.82 (s, 2H); 4.62 (s, 2H); 4.35 (q, J=7.1 Hz, 2H); 4.26 (q, J=7.1 Hz, 2H); 1.35 (t, J=7.2 Hz, 3H); 1.30 (t, J=7.1 Hz, 3H); ^{13}C NMR (100 MHz, $CDCl_3$) δ 167.5; 167.3; 162.8; 160.9; 141.8; 129.1; 90.2; 68.9; 61.9; 61.8; 61.7; 14.4; 14.3. This ester (298 mg, 0.53 mmol) was added to a round bottom flask with sodium hydroxide (340 mg, 8.50 mmol), tetrahydrofuran (4 mL), and water (1 mL). The reaction was heated at 65 °C 17 h, acidified with 10% aq. HCl, and the resulting precipitate was filtered to yield a white solid (218 mg, 92%). ^{1}H NMR (400 MHz, $CDCl_3$) δ 8.28 (s, 2H); 4.49 (s, 2H); ^{13}C NMR (100 MHz, $CDCl_3$) δ 168.3; 164.3; 159.9; 140.4; 130.6; 91.7; 68.4.

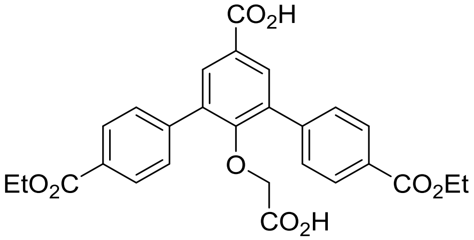

2’-(carboxymethoxy)-4,4’’-bis(ethoxycarbonyl)-[1,1’:3’,1’’-terphenyl]-5’-carboxylic acid (3.36): To a round bottom flask equipped with stir bar and reflux condenser was added 4-(carboxymethoxy)-3,5-diiodobenzoic acid (153 mg, 0.34 mmol), 4-ethoxycarbonylphenylboronic acid (168 mg, 0.87 mmol), palladium(II) acetate (4 mg, 0.02 mmol), tricyclohexylphosphine (10 mg, 0.04 mmol), N,N’-dimethylformamide (0.5 mL), and 2 M aq. potassium carbonate (0.5 mL). The reaction was placed under nitrogen and stirred at 100 °C for 17 h. The reaction was acidified with 10% aq. HCl, extracted with ethyl acetate, and dried over magnesium sulfate. The solvent was evaporated under reduced pressure to yield a white solid (141 mg, 84%). ^{1}H NMR (300 MHz, $CDCl_3$) δ

8.15 (d, J=8.6 Hz, 4H); 8.14 (s, 2H); 7.70 (d, J=8.5 Hz, 4H); 4.41 (q, J=7.1 Hz, 4H); 3.90 (s, 2H); 1.42 (t, J=7.1 Hz, 6H).

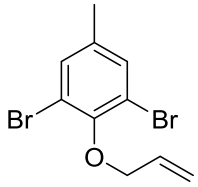

2-(allyloxy)-1,3-dibromo-5-methylbenzene (3.38): To a round bottom flask equipped with stir bar and reflux condenser was added 2,6-dibromo-4-methyl phenol (540 mg, 2.03 mmol), potassium iodide (39 mg, 0.23 mmol), potassium carbonate (420 mg, 3.04 mmol), allyl bromide (195 µL, 2.25 mmol), and acetonitrile (5 mL). The reaction was refluxed 16 h and water was added. The mixture was extracted with ethyl acetate, washed with brine, dried over magnesium sulfate, and the solvent was evaporated under reduced pressure to yield an orange oil (504 mg, 81%). ^{1}H NMR (300 MHz, $CDCl_3$) δ 7.31 (s, 2H); 6.17 (dq, J=5.8, 10.4 Hz, 1H); 5.45 (td, J=1.5, 17.2 Hz); 5.29 (d, J=10.3 Hz, 1H); 4.51 (dd, J = 1.1, 5.9 Hz, 2H); 2.27 (s, 3H).

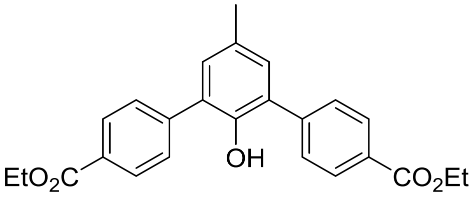

Diethyl 2’-hydroxy-5’-methyl-[1,1’:3’,1’’-terphenyl]-4,4’’-dicarboxylate (3.39): To a round bottom flask equipped with stir bar was added 2,6-dibromo-4-methyl phenol (523 mg, 1.97 mmol), 4-methoxycarbonylphenylboronic acid (881 mg, 4.89 mmol), 1,10-*bis*(diphenylphosphino)ferrocene palladium(II) dichloride (83 mg, 0.10 mmol), toluene (2.5 mL), ethanol (2.5 mL), and 2 M aq. potassium carbonate. The reaction was placed under nitrogen and refluxed 15 h. The mixture was acidified with 10% aq. HCl, extracted with ethyl acetate, dried over magnesium sulfate, and the solvent was evaporated under reduced pressure. The residue was recrystallized from ethanol to yield a brown solid (263 mg, 36%). ^{1}H NMR (300 MHz, $CDCl_3$) δ 8.14 (d, J=8.1 Hz, 4H); 7.63 (d, J=8.1 Hz, 4H); 7.13 (s, 2H); 5.16 (s, 1H); 3.95 (s, 6H); 2.37 (s, 3H).

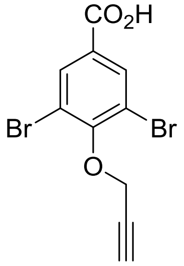

3,5-dibromo-4-(prop-2-yn-1-yloxy)benzoic acid (3.42): To a round bottom flask equipped with stir bar was added 3,5-diiodo-4-hydroxybenzoic acid (126 mg, 0.32 mmol), sodium hydride (31 mg, 0.78 mmol, 60% suspension in mineral oil), anhydrous CH_2Cl_2 (0.5 mL), and anhydrous acetonitrile (0.5 mL). The reaction was stirred 10 min and the solvents were removed under reduced pressure. To this residue was added dimethyl sulfoxide (0.75 mL) and propargyl bromide (77 µL, 0.71 mmol, 9.2 M solution in toluene). The reaction was stirred at 60 °C for 15 h. Water was added, and the resulting precipitate was filtered to yield prop-2-yn-1-yl 3,5-dibromo-4-(prop-2-yn-1-yloxy)benzoate as a tan solid (111 mg, 74%). ^{1}H NMR (400 MHz, $CDCl_3$) δ 8.46 (s, 2H); 4.91 (d, J=2.3 Hz, 2H); 4.79 (d, J=2.3 Hz, 2H); 2.58 (t, J=2.3 Hz, 1H); 2.54 (t, J=2.2 Hz, 1H);); ^{13}C NMR (100 MHz, $CDCl_3$) δ 162.6; 160.9; 141.8; 141.5; 129.1; 91.0; 77.3; 77.1; 75.7; 60.8; 53.2. This ester (388 mg, 0.833 mmol) was added to a round bottom flask with sodium hydroxide (375 mg, 9.38 mmol), tetrahydrofuran (4 mL), and water (1 mL). The reaction was stirred at 65 °C for 15 h, 10% aq. HCl was added, and the resulting precipitate was filtered to yield a white solid (267 mg, 75%). ^{1}H NMR (400 MHz, $CDCl_3$) δ 8.49 (s, 2H); 4.81 (d, J=2.4 Hz, 2H); 2.59 (t, J=2.4 Hz, 1H).

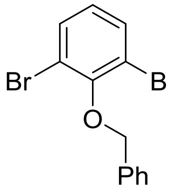

2-(benzyloxy)-1,3-dibromobenzene (3.45): To a round bottom flask equipped with stir bar and reflux condenser was added 2,6-dibromophenol (580 mg, 2.30 mmol), benzyl bromide (274 µL, 2.30 mmol), potassium carbonate (479 mg, 3.47 mmol), sodium iodide (33 mg, 0.22 mmol), and acetonitrile (7 mL). The reaction was refluxed 16 h and cooled. Water was added and the reaction was extracted with diethyl ether, washed with brine, dried over magnesium sulfate, and the solvent was evaporated under reduced pressure. The crude product was purified by filtration through a silica plug with hexanes to yield a white solid (645 mg, 82%). ^{1}H NMR (400 MHz, $CDCl_3$) δ 7.61 (d, J=7.2 Hz, 2H); 7.54 (d, J=8.0 Hz, 2H); 7.44-7.35 (m, 3H); 6.90 (t, J=8.0 Hz, 1H); 5.04 (s, 2H); ^{13}C NMR (100 MHz, $CDCl_3$) δ 153.0; 136.4; 132.9; 128.6; 128.5; 126.6; 118.9; 74.7; HRMS (ESI) m/z calcd for $C_{13}H_{14}Br_2NO$ $(M+NH_4)^+$ 359.9417; found 359.9432.

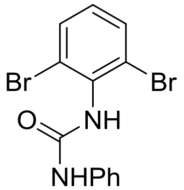

1-(2,6-dibromophenyl)-3-phenylurea (3.47): To a round bottom flask equipped with stir bar and reflux condenser was placed 2,6-dibromoaniline (2.07 g, 8.26 mmol), phenyl isocyanate (900 µL, 8.28 mmol), and anhydrous toluene (10 mL). The reaction was placed under nitrogen and refluxed for 16 h. The mixture was filtered and washed with toluene to yield a white solid (2.64 g, 86%). ^{1}H NMR (300 MHz, DMSO-d_6) δ 8.91 (s, 1H); 8.17 (s, 1H); 7.72 (dd, J=0.8, 8.1 Hz, 2H); 7.45 (dd, J=0.8, 7.8 Hz, 2H); 7.26 (t, J=7.6 Hz, 2H); 7.16 (t, J=8.1 Hz, 1H); 6.96 (td, J=1.0, 7.4 Hz, 1H); ^{13}C NMR (125 MHz, DMSO-d_6) δ 152.2; 139.8; 135.8; 132.2; 129.5; 128.8; 124.9; 121.8; 118.0; HRMS (ESI) m/z calcd for $C_{13}H_{11}Br_2N_2O$ $(M+H)^+$ 368.9233; found 368.9225.

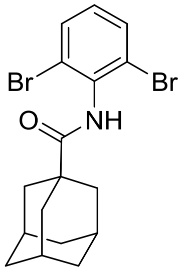

(3*r*,5*r*,7*r*)-*N*-(2,6-dibromophenyl)adamantane-1-carboxamide (3.49): To a round bottom flask equipped with stir bar was added 2,6-dibromoaniline (161 mg, 0.64 mmol) and 1-adamantane carboxylic acid chloride (128 mg, 0.64 mmol). The reaction was placed under nitrogen and anhydrous toluene (2 mL) was added. After refluxing 16 h, the solvent was evaporated and the residue was recrystallized from ethanol to yield a white solid (133 mg, 50%). ^{1}H NMR (300 MHz, $CDCl_3$) δ 7.57 (d, J=8.0 Hz, 2H); 7.15 (br s, 1H); 7.01 (t, J=8.1 Hz, 1H); 2.12 (s, 3H); 2.05 (s, 6H); 1.78 (s, 6H).

Procedure for Complex Formation: To a round bottom flask equipped with reflux condenser was added **3.20** (10 mg, 0.019 mmol), metal salt (0.015 mmol), acetonitrile (0.5 mL), and triethylamine (2 drops). The reaction was refluxed 16 h and the resulting precipitate was collected and analyzed by ^{1}H NMR in DMSO-d_6.

8.4 Chapter Four Experimental

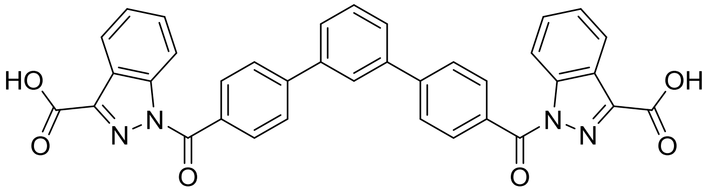

1,1'-([1,1':3',1''-terphenyl]4,4''-dicarbonyl)bis(1 *H*-indazole-3-carboxylic acid) (4.3): To a round bottom flask equipped with stir bar was added [1,1':3',1''-terphenyl]-4,4''-dicarboxylic acid (48 mg, 0.15 mmol), 2-(6-Chloro-1H-benzotriazole-1-yl)-1,1,3,3-tetramethylaminium hexafluorophosphate (136 mg, 0.33 mmol), triethylamine (84 μL, 0.60 mmol), and acetonitrile (5 mL). The reaction was stirred 1.5 h and indazole-3-carboxylic acid (55 mg, (0.34 mmol) and triethylamine (142 μL, 1.02 mmol) were added. The reaction was stirred an additional 16 h and the solvent evaporated under reduced pressure. 10% HCl was added and the resultant precipitate filtered to yield the crude product which was recrystallized from acetone to yield a white solid (46 mg, 51%). ^{1}H NMR (300 MHz, DMSO-d_6) δ 13.78 (br s, 2H); 8.51 (d, J=8.5 Hz, 2H); 8.26 (d, J=8.1 Hz, 2H); 8.22 (s, 1H); 8.18 (d, J=8.3 Hz, 4H); 8.08 (d, J=8.4 Hz, 4H); 7.90 (d, J=7.7 Hz, 2H); 7.77 (t, J=7.8 Hz, 2H); 7.70 (t, J=7.9 Hz, 1H); 7.60 (t, J = 7.6 Hz, 1H).

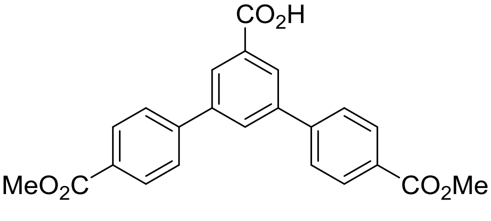

4,4''-bis(methoxycarbonyl)-[1,1':3',1''-terphenyl]-5'-carboxylic acid (4.6): To a round bottom flask equipped with stir bar and reflux condenser was added 3,5-dibromobenzoic acid (213 mg, 0.76 mmol), 4-methoxycarbonylphenylboronic acid (343 mg, 1.91 mmol), 1,1'-bis(diphenylphosphino)ferrocene palladium(II) dichloride (33 mg, 0.04 mmol), cesium carbonate (749 mg, 2.30 mmol), anhydrous toluene (2 mL), and anhydrous ethanol (2 mL). The reaction was degassed, placed under nitrogen, and stirred at 80 ˚C for 16 h. The reaction was cooled, 10% aq. HCl added, and the resulting precipitate was filtered and recrystallized from ethyl acetate to yield a gray solid (197 mg, 66%). ^{1}H NMR (300 MHz, $CDCl_3$) δ 8.37 (s, 2H); 8.17 (d, J=8.3 Hz, 4H); 8.08 (s, 1H); 7.76 (d, J=6.7 Hz, 4H); 3.97 (s, 6H).

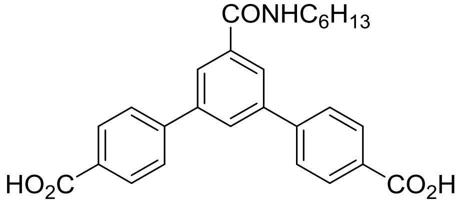

5’-(hexylcarbamoyl)-[1,1’:3’,1’’-terphenyl]-4,4’’-dicarboxylic acid (4.7): To a round bottom flask equipped with stir bar was added 4,4’’-bis(methoxycarbonyl)-[1,1’:3’,1’’-terphenyl]-5’-carboxylic acid (457 mg, 1.17 mmol), 2-(6-Chloro-1H-benzotriazole-1-yl)-1,1,3,3-tetramethylaminium hexafluorophosphate (532 mg, 1.29 mmol), triethylamine (326 µL, 2.34 mmol), and acetonitrile (16 mL). The reaction was stirred 1.5 h and *N*-hexylamine (464 µL, 3.51 mmol) was added. The reaction was allowed to stir an additional 16 h and the resulting precipitate was filtered to yield a white solid (317 mg, 57%). ^{1}H NMR (400 MHz, $CDCl_3$) δ 8.15 (d, J=7.8 Hz, 4H); 8.00 (s, 2H); 7.95 (s, 1H); 7.73 (d, J = 7.8 Hz, 4H); 6.23 (t, J=3.4 Hz, 1H); 3.96 (s, 6H); 3.51 (q, J=6.3 Hz, 2H); 1.66 (p, J=6.9 Hz, 2H); 1.43 (p, J=6.7 Hz, 2H); 1.34 (s, 4H); 0.90 (s, 3H). ^{13}C NMR (100 MHz, $CDCl_3$) δ 167.1; 166.9; 144.5; 141.5; 136.7; 130.4; 129.8; 129.1; 127.4; 125.5; 52.4; 40.5; 31.7; 29.8; 26.9; 23.5; 22.7. This ester was then added to a round bottom flask with sodium hydroxide (325 mg, 8.13 mmol), tetrahydrofuran (4 mL), and water (1 mL). The reaction was refluxed overnight and 10% aq. HCl was added until the aqueous layer was acidic. The mixture was extracted with ethyl acetate (3 x 10 mL), washed with brine (15 mL), dried over magnesium sulfate, and the solvent was evaporated under reduced pressure to yield an off-white solid (159 mg, 90%). ^{1}H NMR (300 MHz, D_2O) δ 7.74 (d, J=7.6 Hz, 4H); 7.45 (s, 1H); 7.36 (s, 2H); 7.24 (d, J=7.6 Hz, 4H); 3.04 (t, J=7.0 Hz, 2H); 1.34 (p, J=6.2 Hz, 2H); 1.12 (s, 6H); 0.75 (t, J=6.8 Hz, 3H).

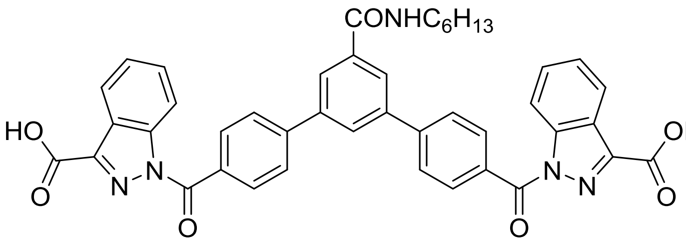

1,1'-(5'(hexylcarbamoyl)-[1,1':3',1''-terphenyl]-4,4''-dicarbonyl)bis(1 *H*-indazole-3-carboxylic acid) (4.8): To a round bottom flask equipped with stir bar was added 5'-(hexylcarbamoyl)-[1,1':3',1''-terphenyl]-4,4''-dicarboxylic acid (103 mg, 0.23 mmol), 2-(6-Chloro-1H-benzotriazole-1-yl)-1,1,3,3-tetramethylaminium hexafluorophosphate (211 mg, 0.51 mmol), acetonitrile (10 mL), and triethylamine (129 μL, 0.93 mmol). The reaction was stirred 1.5 h and methyl 1*H*-indazole-3-carboxylate (84 mg, 0.52 mmol) and triethylamine (218 μL, 1.56 mmol) were added. The reaction was stirred an additional 16 h and the solvent was evaporated. Saturated aq. sodium bicarbonate was added and the resulting precipitate filtered and stirred with 10% aq. HCl. The solid was filtered and recrystallized from ethyl acetate to yield a tan solid (64 mg, 38%). ^{1}H NMR (400 MHz, DMSO-d_6) δ 8.77 (t, J=5.7 Hz, 1H); 8.50 (d, J=8.6 Hz, 2H); 8.35 (s, 1H); 8.32 (s, 2H); 8.26 (d, J=8.0 Hz, 2H); 8.20 (d, J=8.3 Hz, 4H); 8.12 (d, J=8.3 Hz, 4H); 7.77 (t, J=7.8 Hz, 2H); 7.60 (t, J=7.6 Hz, 2H); 1.59 (p, J=7.0 Hz, 2H); 1.34 (m, 2H); 1.32 (m, 4H); 0.88 (t, J=6.8 Hz, 3H); ^{13}C NMR (100 MHz, DMSO-d_6) δ 167.7; 165.4; 162.7; 143.4; 141.6;

140.8; 139.9; 136.2; 131.9; 131.5; 130.0; 128.3; 126.8; 126.1; 125.8; 124.3; 122.3; 115.3; 31.1; 29.1; 26.3; 22.1; 14.0.

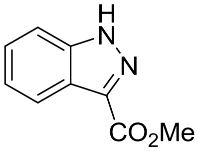

Methyl 1*H*-indazole-3-carboxylate (4.9): To a round bottom flask equipped with stir bar and reflux condenser was added indazole-3-carboxylic acid (1.00 g, 6.17 mmol) and methanol (20 mL). Concentrated HCl (20 drops) was added and the reaction refluxed overnight. The solvent was evaporated under reduced pressure until a precipitate formed. Water (30 mL) was added and the reaction was filtered to yield a white solid (984 mg, 91%). ^{1}H NMR (400 MHz, $CDCl_3$) δ 13.92 (s, 1H); 8.08 (d, J=8.2 Hz, 1H); 7.66 (d, J=8.2 Hz, 1H); 7.45 (t, J=7.6 Hz, 1H); 7.32 (t, J=7.9 Hz, 1H); 3.93 (s, 3H).

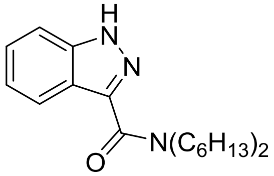

***N*,*N*-dihexyl-1*H*-indazole-3-carboxamide (4.10):** To a two-neck flask equipped with stir bar and septum was added dihexylamine (1.53 mL, 6.52 mmol). This was placed under nitrogen and anhydrous diethyl ether (5 mL) was added. The reaction was cooled to -78 ˚C and *n*-butyllithium (4.00 mL, 6.40 mmol, 1.6 M solution in hexanes) was added. The mixture was allowed to warm until unfrozen and after 5 min, was added to a solution of methyl 1*H*-indazole-3-carboxylate (521 mg, 2.96 mmol) in anhydrous diethyl ether (5 mL) at -78 ˚C. The reaction was warmed to room temperature, stirred for 12 h, quenched with saturated aq. ammonium chloride, extracted with ethyl acetate, washed with brine, and dried over magnesium sulfate. The solvents were removed under reduced pressure and the crude product was purified by column chromatography on silica gel (50% ethyl acetate/hexanes) to yield a white solid (561 mg, 58%). ^{1}H NMR (300 MHz, $CDCl_3$) δ 10.4 (s, 1H); 8.14 (d, J=8.2 Hz, 1H); 7.47 (d, J=8.3 Hz, 1H); 7.39 (t, J=6.8 Hz, 1H); 7.25 (t, J=7.4 Hz, 1H); 3.75 (t, J=7.7 Hz, 2H); 3.56 (t, J=7.6 Hz, 2H); 1.71-1.64 (m, 4H); 1.41-1.35 (m, 6H); 1.22-1.20 (m, 6H); 0.93-0.89 (m, 3H); 0.82-0.79 (m, 3H).

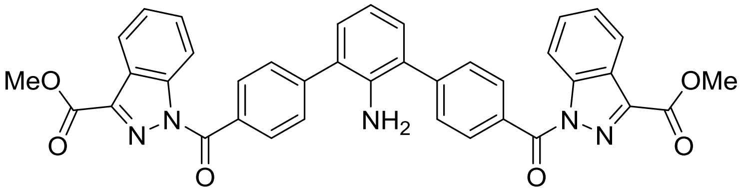

Dimethyl 1,1'-(2'-amino-[1,1':3',1''-terphenyl]-4,4''-dicarbonyl)bis(1 *H*-indazole-3-carboxylate) (4.11): To a round bottom flask equipped with stir bar was added 2'-amino-[1,1':3',1''-terphenyl]-4,4''-dicarboxylic acid (39 mg, 0.12 mmol), 2-(6-Chloro-1H-benzotriazole-1-yl)-1,1,3,3-tetramethylaminium hexafluorophosphate (HCTU) (107 mg, 0.26 mmol), acetonitrile (3.5 mL), and triethylamine (66 µL, 0.47 mmol). The reaction was stirred 1.5 h and Methyl 1*H*-indazole-3-carboxylate (46 mg, 0.26 mmol) and triethylamine (110 µL, 0.79 mmol) were added. The reaction was stirred an additional 16 h and the solvents were evaporated. The residue was dissolved in saturated aq. ammonium chloride, extracted with methylene chloride, dried over magnesium sulfate, and the solvent was removed under reduced pressure. The crude product was recrystallized from acetone to yield a white solid (37 mg, 48%). ^{1}H NMR (300 MHz, $CDCl_3$) δ 8.60 (d, J=8.5 Hz, 2H); 8.32 (d, J=8.5 Hz, 2H); 8.27 (d, J=8.2 Hz, 4H); 7.73 (d, J=8.2 Hz, 4H; 7.68 (d, J=8.2 Hz, 2H); 7.54 (t, J=7.6 Hz, 2H); 7.22 (d, J=7.5 Hz, 2H); 6.96 (t, J=7.6 Hz, 1H); 4.07 (s, 6H).

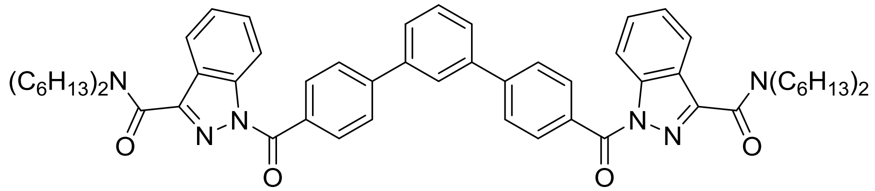

1,1'-([1,1':3',1''-terphenyl]-4,4''-dicarbonyl)bis(*N*,*N*-dihexyl-1 *H*-indazole-3-carboxamide) (4.12): To a round bottom flask equipped with stir bar was added [1,1':3',1''-terphenyl]-4,4''-dicarboxylic acid (106 mg, 0.33 mmol), 2-(6-Chloro-1H-benzotriazole-1-yl)-1,1,3,3-tetramethylaminium hexafluorophosphate (305 mg, 0.74 mmol), triethylamine (186 µL, 1.33 mmol), acetonitrile (3 mL), and chloroform (3 mL). The reaction was stirred 1.5 h and *N*,*N*-dihexyl-1H-indazole-3-carboxamide (241 mg, 0.73 mmol) and triethylamine (204 µL, 1.46 mmol) were added. The reaction was stirred an additional 16 h and the solvents were evaporated. Saturated aq. sodium bicarbonate was added and the reaction was extracted with methylene chloride. The combined organics were washed with brine, dried over magnesium sulfate, and the solvent was evaporated under reduced pressure. The crude product was purified by column chromatography on silica gel (35% ethyl acetate/hexanes) to yield a yellow oil (230 mg, 73%). ^{1}H NMR (300 MHz, $CDCl_3$) δ 8.57 (d, J=8.4 Hz, 2H); 8.17 (d, J=8.4 Hz, 4H); 8.12 (d, J=8.0 Hz, 2H); 7.93 (s, 1H); 7.80 (d, J=8.4 Hz, 4H); 7.72-7.44 (m, 5H); 7.47 (t, J=7.8 Hz, 2H); 3.56-3.45 (m, 8H); 1.75-1.68 (m, 4H); 1.60-1.52 (m, 4H); 1.41-1.31 (m, 16H); 0.97-0.88 (m, 14H); 0.64 (t, J=7.1Hz, 3H).

Complex Formation: Ligand (5 mg), metal salt (0.75 eq), and triethylamine (1 drop) were combined in an NMR tube with DMSO-*d*$_6$ (0.5 mL). ^{1}H NMR spectra were acquired after mixing and after heating overnight at 60 °C.

8.5 Chapter Five Experimental

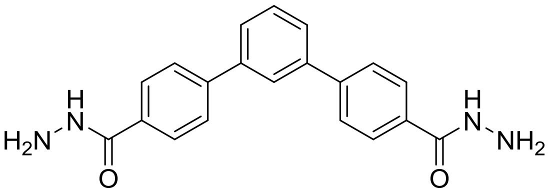

[1,1’:3’,1”-terphenyl]-4,4”-dicarbohydrazide (5.2): To a round bottom flask equipped with stir bar and reflux condenser was added diethyl [1,1’:3’,1”-terphenyl]-4,4”-dicarboxylate (254 mg, 0.68 mmol) and hydrazine (3 mL). The reaction was stirred at 85 ˚C for 18 h before water (5 mL) was added and the precipitate was filtered to yield a white solid (203 mg, 86%). ^{1}H NMR (400 MHz, DMSO-d_6) δ 9.86 (s, 2 H); 8.02 (s, 1H); 7.76 (d, J=8.2 Hz, 4H); 7.88 (d, J=8.3 Hz, 4H); 7.75 (d, J=7.7 Hz, 2H); 7.60 (t, J=7.8 Hz, 1H); 4.54 (br s, 4H); ^{13}C NMR (100 MHz, DMSO-d_6) δ 165.6; 142.5; 140.0; 132.3; 129.8; 127.6; 126.9; 126.6; 125.5; HRMS (ESI) m/z calcd for $C_{20}H_{19}N_4O_2$ $(M+H)^+$ 347.1503; found 347.1536.

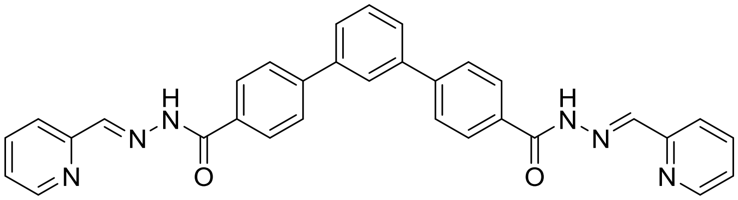

[1,1’:3’,1”-terpheny]l-4,4”-dicarboxylic acid, bis-(2-pyridinylmethylene)-hydrazide (5.3): To a round bottom flask equipped with stir bar and reflux condenser was added [1,1’:3’,1”-terphenyl]-4,4”-dicarbohydrazide (176 mg, 0.51 mmol), 2-pyridinecarboxaldehyde (112 µL, 1.27 mmol), ethanol (5 mL), and acetic acid (2 drops). The reaction was refluxed for 16 h, cooled in an ice bath, and washed with cold ethanol to yield a white solid (208 mg, 78%). ^{1}H NMR (400 MHz, DMSO-d_6) δ 12.17 (s, 2H); 8.62 (d, J=4.8 Hz, 2H); 8.52 (s, 2H); 8.08 (m, 5H); 8.03 (d, J=8.0 Hz, 2H); 7.98 (d, J=7.7 Hz, 4H); 7.90 (t, J=7.6 Hz, 2H); 7.81 (d, J=7.6 Hz, 2H); 7.64 (t, J=7.8 Hz, 1H); 7.43 (t, J=6.3 Hz, 2H); ^{13}C NMR (100 MHz, DMSO-d_6) δ 163.3; 153.4; 149.7; 148.2; 143.5; 140.1; 137.1; 132.2; 130.0; 128.6; 127.2; 127.0; 125.7; 124.6; 120.2; HRMS (ESI) m/z calcd for $C_{32}H_{25}N_6O_2$ $(M+H)^+$ 525.2034; found 525.1983.

Complex [(5.3)$_2$Bi$_2$](OTf)$_6$: Ligand **5.3** (5.0 mg, 0.01 mmol) and Bi(OTf)$_3$ (18.8 mg, 0.03 mmol) were combined in an NMR tube with 0.5 mL CD_3CN. The mixture was shaken for 10 s for quantitative formation of [(5.3)$_2$Bi$_2$](OTf)$_6$. ^{1}H NMR (400 MHz, CD_3CN) δ 9.77 (s, 2H); 9.34 (s, 2H); 8.49 (t, J=7.8 Hz, 2H); 8.35 (d, J=7.6 Hz, 2H); 8.31 (d, J=8.0 Hz, 4H); 8.14 (s, 1H); 8.08 (m, 6H); 7.87 (d, J=8.0 Hz, 2H); 7.70 (t, J=7.8 Hz, 1H); ^{13}C NMR (100 MHz, CD_3CN) δ 169.0; 154.1; 153.0; 148.4; 144.1; 140.7; 131.4; 131.1; 131.0; 129.2; 128.9; 127.5; 126.7; 122.8; 119.6. HRMS (ESI) m/z calcd for $C_{78}H_{54}Bi_3N_{18}O_6$ $(M-4(TfOH)-2(OTf))^{2+}$ 731.1602; found 655.1290.

NMR Titration Procedure: Ligand **5.3** (4.4 mg, 0.008 mmol) and 0.5 mL CD_3CN were combined in an NMR tube, and a solution of Bi(OTf)$_3$ was added at 0.25, 0.33, 0.50, 0.67, 0.75 1, 1.5, and 2 eq with shaking to mix at each addition.

Procedure for Diffusion Experiments: Diffusion experiments were performed using a Bruker Avance 600 MHz NMR spectrometer equipped with a broadband inverse probe with *x*-, *y*-, and *z*-gradients. Chemical shifts were referenced to the acetonitrile-*d(2)* resonance (1.94) ppm. Diffusion datasets were acquired using the stimulated echo experiment with bipolar gradients (stebpgp1s) included with the Topspin release version 1.3. Gradient amplitudes were incremented as a square dependence from 5% to 95%

into 64 or 96 gradient increments. A spoil gradient pulse of length 1 ms and amplitude of -17.13% was used to effectively remove transverse magnetization following the encode period of the pulse program. Spectra were acquired with 128 transients coadded and 28,672 data points per transient for each of the 64 or 96 increments. Diffusion (Δ) and gradient pulse times (δ) were optimized using a one-dimensional version of the stimulated echo pulse sequence, stebpgp1s1d to give values of 17 and 7 ms, respectively. Diffusion coefficients were calculated using the processing features in Topspin by Bruker.

Calculation of Equilibrium Constants:

[(5.3)$_4$Bi$_2$](OTf)$_6$ and [(5.3)$_3$Bi$_2$](OTf)$_6$: Only complexes [(**5.3**)Bi$_2$](OTf)$_6$ and [(**5.3**)$_2$Bi$_2$](OTf)$_6$ were observed at equilibrium, so contributions from **5.3** and [(**5.3**)$_2$Bi$_2$](OTf)$_6$ were assumed to be negligible. Concentrations of each complex from a mixture of 9.91x10^{-3} mmol **5.3**, 7.42x10^{-3} mmol Bi(OTf)$_3$, and 0.545 mL DMSO were determined by integrating the ^{1}H NMR from 9.60-9.48 ppm and 9.38-9.31 ppm.

[(**5.3**)$_4$Bi$_2$](OTf)$_6$=2.72x10^{-3} M; [(**5.3**)$_3$Bi$_2$](OTf)$_6$=2.44x10^{-3} M; [Bi]=3.30x10^{-3}M

$3\ M_2L_4 + 2\ M \rightarrow 4\ M_2L_3$

$$K_1 = \frac{[\mathbf{M_2L_3}]^4}{[\mathbf{M_2L_4}]^3[\mathbf{M}]^2} = 162 \pm 16\ \ M^{-1}$$

[(5.3)$_3$Bi$_2$](OTf)$_6$ and [(5.3)$_2$Bi$_2$](OTf)$_6$: Only complexes [(**5.3**)$_3$Bi$_2$](OTf)$_6$ and [(**5.3**)$_2$Bi$_2$](OTf)$_6$ were observed at equilibrium, so contributions from **5.3** and [(**5.3**)$_4$Bi$_2$](OTf)$_6$ were assumed to be negligible. Concentrations of each complex from a mixture of 9.91x10^{-3} mmol **5.3**, 1.98x10^{-2} mmol Bi(OTf)$_3$, and 0.620 mL DMSO were determined by integrating the ^{1}H NMR from 9.78-9.65 ppm and 9.65-9.51 ppm.

$[(\mathbf{5.3})_3Bi_2](OTf)_6 = 3.27\times10^{-3}$ M; $[(\mathbf{5.3})_2Bi_2](OTf)_6 = 3.1\times10^{-3}$ M; [Bi]=1.92×10^{-2}M

$2\ M_2L_3 + 2\ M \rightarrow 3\ M_2L_2$

$$K_2 = \frac{[\mathbf{M_2L_2}]^3}{[\mathbf{M_2L_3}]^2[\mathbf{M}]^2} = 8 \pm 1\ \ M^{-1}$$

8.6 Chapter Six Experimental

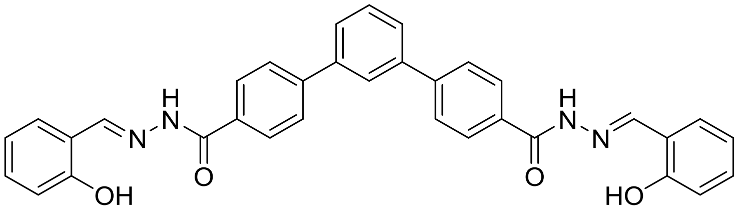

***N*,*N*-bis((E)-2-hydroxybenzylidene)-[1,1’:3’,1’’-terphenyl]-4,4’’-dicarbohydrazide (6.2):** To a round bottom flask equipped with stir bar and reflux condenser was added 1,1’:3’,1’’-Terphenyl-4,4’’-dicarbohydrazide (190 mg, 0.55 mmol), salicylaldehyde (231 µL, 2.19 mmol), ethanol (2.5 mL), and acetic acid (2 drops). The reaction was refluxed 18 h, cooled, and washed with cold ethanol to yield a yellow solid (262 mg, 86%). ^{1}H NMR (400 MHz, DMSO-d_6) δ 12.20 (s, 2H); 11.32 (s, 2H); 8.68 (s, 2H); 8.09 (s, 1H); 8.08 (d, J=8.6 Hz, 4H); 7.99 (d, J=8.1 Hz, 4H); 7.82 (d, J=8.0 Hz, 2H); 7.66 (t, J=7.7 Hz, 1H); 7.57 (d, J=7.5 Hz, 2H); 7.32 (t, J=7.8 Hz, 2H); 6.98 (m, 4H); ^{13}C NMR (125 MHz, DMSO-d_6) δ 162.4; 157.5; 148.3; 143.3; 139.9; 131.7; 131.4; 129.8; 129.5; 128.3; 127.1; 126.8; 125.6; 119.4; 118.7; 116.4; MS (ESI) *m/z* calcd for $C_{34}H_{27}N_4O_4$ $(M+H)^+$ 555.20; found 555.33.; mp 298 °C dec.

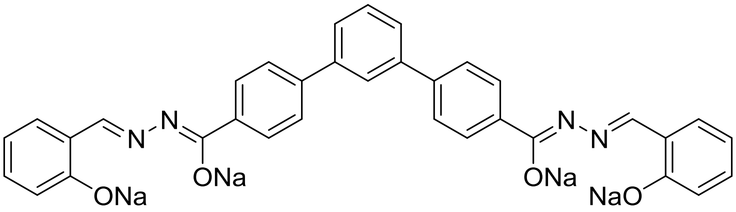

Ligand 6.3: Ligand **6.2** was suspended in anhydrous methylene chloride (2 mL) and an excess of sodium hydride was added. The mixture was allowed to stir 1 h, quenched with nonanhydrous methylene chloride and hexanes, and stirred an additional 30 min. The deprotonated ligand was collected by centrifugation and dried to yield a light yellow solid in quantitative yield. ^{1}H NMR (400 MHz, DMSO-d_6) δ 8.18 (d, J=7.9 Hz, 4H); 8.13 (s, 2H); 7.94 (s, 1H); 7.66 (d, J=7.3 Hz, 6H); 7.53 (t, J=7.7 Hz, 1H) 6.80 (d, J=7.8 Hz, 2H); 6.69 (t, J=8.8 Hz, 2H); 6.20 (d, J=8.3 Hz, 2H); 5.95 (t, J=7.1 Hz, 2H); ^{13}C NMR (100 MHz, DMSO-d_6) δ 171.3; 167.3; 151.9; 141.6; 141.2; 138.8; 133.0; 129.4; 128.1; 128.0; 125.3; 125.3; 124.6; 124.0; 121.8; 106.7.; mp >300 °C dec.

Complex formation: Ligand **6.3** and metal triflate (0.67 or 1 eq) were combined in an NMR tube with 0.5 mL DMSO-d_6. The sample was shaken for 10 s for quantitative formation of $Na_x[(\mathbf{6.3})_yLn_2]$.

NMR titrations: Ligand **6.3** was dissolved in 0.5 mL DMSO-d_6 and a solution of metal triflate was slowly added with shaking to mix after each addition.

Complex $Na_6[(6.3)_3Y_2]$: ^{1}H NMR (400 MHz, DMSO-d_6) δ 8.45 (s, 2H); 8.17 (d, J=7.9 Hz, 4H); 7.98 (s, 1H); 7.80 (d, J=7.9 Hz, 4H); 7.72 (d, J=7.7 Hz, 2H); 7.60 (t, J=7.6 Hz, 1H); 7.25 (d, J=7.5 Hz, 2H); 7.14 (t, J=7.8 Hz, 2H); 6.55-6.50 (m, 4H); ^{13}C NMR (125 MHz, DMSO-d_6) δ 168.7; 165.3; 156.3; 141.1; 140.7; 135.6; 133.6; 132.4; 129.9; 128.4; 126.5;

126.1; 125.0; 121.9; 119.6; 114.1; MS (ESI) *m/z* calcd for $C_{102}H_{74}N_{12}O_{12}Y_2$ $[Y_2L_3\text{-}4H]^{2+}$ calcd 918.2; found 918.5.; mp >300 °C dec.

Complex $Na_6[(6.3)_3La_2]$: ^{1}H NMR (400 MHz, DMSO-d_6) δ 8.33 (s, 2H); 8.17 (d, J=8.0 Hz, 4H); 7.97 (s, 1H); 7.77 (d, J=8.0 Hz, 4H); 7.71 (d, J=7.7 Hz, 2H); 7.59 (t, J=7.7 Hz, 1H); 7.17 (d, J=7.4 Hz, 2H); 7.07 (t, J=8.3 Hz, 2H); 6.45-6.41 (m, 4H); ^{13}C NMR (125 MHz, DMSO-d_6) δ 168.4; 165.9; 154.9; 140.8; 140.6; 136.9; 133.7; 131.6; 129.8; 128.4; 126.3; 125.9; 124.9; 122.8; 119.5; 113.2; MS (ESI) *m/z* calcd for $C_{102}H_{74}La_2N_{12}O_{12}$ $[La_21_3\text{-}4H]^{2+}$ calcd 968.2; found 968.5.; mp >300 °C dec.

Complex $Na_6[(6.3)_3Pr_2]$: ^{1}H NMR (400 MHz, DMSO-d_6) δ 41.80 (s, 2H), 23.22 (s, 4H); 19.87 (s, 2H); 19.62 (s, 2H); 13.97 (s, 2H); 13.54 (s, 4H); 13.30 (s, 2H); 12.64 (s, 1H); 11.09 (s, 2H); 10.10 (s, 1H); MS (ESI) *m/z* calcd for $C_{102}H_{74}N_{12}O_{12}Pr_2$ $[Pr_21_3\text{-}4H]^{2+}$ 970.2; found 970.6. ^{13}C data could not be obtained due to signal broadening from the paramagnetic metal.; mp >300 °C dec.

Complex $Na_6[(6.3)_3Sm_2]$: ^{1}H NMR (400 MHz, DMSO-d_6) δ 9.65 (d, J=7.8 Hz, 4H); 8.84 (d, J=8.1 Hz, 2H); 8.46 (s, 1H); 8.35 (d, J=7.8 Hz, 4H); 8.06 (d, J=7.6 Hz, 2H); 7.85 (t, J=7.6 Hz, 1H); 7.76 (s, 2H); 7.68 (t, J=7.8 Hz, 2H); 7.54 (d, J=7.5 Hz, 2H); 6.85 (t, J=7.2 Hz, 2H); ^{13}C NMR (125 MHz, DMSO-d_6) δ 177.5; 171.0; 153.5; 141.3; 141.2; 135.1; 134.4; 132.0; 130.1; 129.5; 127.0; 126.3; 125.4; 123.3; 118.8; 113.8; HRMS (ESI) *m/z* calcd for $C_{102}H_{74}N_{12}O_{12}Sm_2$ $[Sm_2L_3\text{-}4H]^{2+}$ calcd 981.2; found 980.5.; mp >300 °C dec.

Complex $Na_2[(6.3)_2Yb_2]$: ^{1}H NMR (400 MHz, DMSO-d_6) δ -0.08 (s, 1H); -2.82 (s, 2H); -6.87 (s, 1H); -10.32 (s, 6H); -14.95 (s, 2H); -17.03 (s, 2H); -28.13 (s, 2H); -40.23 (s, 4H); -67.13 (s, 2H); HRMS (ESI) *m/z* calcd for $C_{68}H_{48}N_8O_8Yb_2$ $[Yb_21_2\text{-}4H]^{2+}$ 726.1; found 725.7. ^{13}C data could not be obtained due to signal broadening from the paramagnetic metal.; mp >300 °C dec.

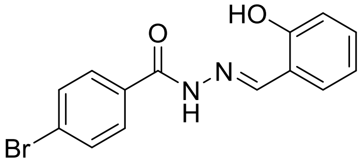

(*E*)-4-bromo-*N*'-(2-hydroxybenzylidene)benzohydrazide (6.4): Ethyl 4-bromobenzoate (350 µL, 2.14 mmol) was added to a round-bottomed flask with 0.5 mL each ethanol and hydrazine hydrate. The reaction was stirred 1 h and the precipitate was filtered and washed with cold ethanol to yield a white solid. This was added to a round-bottomed flask with salicylaldehyde (226 µL, 2.15 mmol), ethanol (2.5 mL), and acetic acid (3 drops), and the reaction was refluxed for 18 h. The resulting precipitate was filtered and washed with cold ethanol to yield a white solid (266 mg, 39%). ^{1}H NMR (300 MHz, DMSO-d_6) δ 12.16 (s, 1H); 11.21 (s, 1H); 8.64 (s, 1H); 7.89 (d, J=8.1 Hz, 2H); 7.77 (d, J=8.1 Hz, 2H); 7.56 (d, J=7.7 Hz, 1H); 7.31 (t, J=7.7 Hz, 1H); 6.95-6.90 (m, 2H); ^{13}C NMR (125 MHz, DMSO-d_6) δ 161.9; 157.5; 148.4; 131.9; 131.6; 131.5; 129.7; 129.4; 125.8; 119.4; 118.7; 116.4; HRMS (ESI) m/z calcd for $C_{14}H_{12}BrN_2O_2$ $(M+H)^+$ 319.0077; found 319.0120.

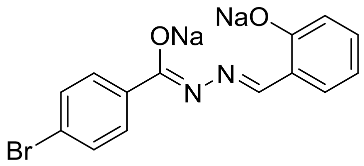

Ligand 6.5: Ligand **6.4** was suspended in anhydrous methylene chloride (2 mL) and an excess of sodium hydride was added. The mixture was allowed to stir 1 h, quenched with nonanhydrous methylene chloride and hexanes, and stirred an additional 30 min. The deprotonated ligand was collected by centrifugation and dried to yield a light yellow solid in quantitative yield. ^{1}H NMR (500 MHz, DMSO-d_6) δ 8.09 (s, 1H); 8.00 (d, J=8.1 Hz, 2H); 7.40 (d, J=8.1 Hz, 2H); 6.79 (d, J=7.7 Hz, 1H); 6.69 (t, J=8.6 Hz, 1H); 6.22 (d, J=8.2 Hz, 1H); 5.96 (t, J=7.1 Hz, 1H); ^{13}C NMR (125 MHz, DMSO-d_6) δ 171.2; 166.6; 152.5; 141.5; 133.1; 129.7; 129.6; 128.3; 123.7; 121.9; 120.6; 107.1.

Complex $Na_3[(6.5)_3Y]$: ^{1}H NMR (500 MHz, DMSO-d_6) δ 8.39 (s, 1H); 7.97 (d, J=8.1 Hz, 2H); 7.57 (d, J=8.1 Hz, 2H); 7.22 (d, J=7.6 Hz, 1H); 7.13 (t, J=7.7 Hz, 1H); 6.54-6.48 (m, 2H); ^{13}C NMR (125 MHz, DMSO-d_6) δ 167.9; 165.3; 156.5; 135.6; 133.6; 132.4; 130.9; 129.7; 123.1; 121.8; 119.6; 114.0.

Complex $Na_3[(6.5)_3La]$: ^{1}H NMR (500 MHz, DMSO-d_6) δ 8.28 (s, 1H); 7.97 (d, J=8.3 Hz, 2H); 7.54 (d, J=8.4 Hz, 2H); 7.14 (d, J=6.3 Hz, 1H); 7.06 (t, J=7.6 Hz, 1H); 6.43-6.40 (m, 2H); ^{13}C NMR (125 MHz, DMSO-d_6) δ 167.6; 165.9; 155.2; 136.9; 133.7; 131.6; 130.7; 129.8; 129.7; 122.6; 122.5; 113.1; MS (ESI) *m/z* calcd for $C_{42}H_{31}Br_3LaN_6O_6$ 1094.9; found 1094.5.

Complex $Na_3[(6.5)_3Pr]$: ^1H NMR (400 MHz, DMSO-d_6) δ 41.39 (s, 1H); 21.67 (s, 2H); 19.83 (s, 1H); 19.62 (s, 1H); 14.07 (s, 1H); 13.32 (s, 1H); 11.96 (s, 2H). ^{13}C data could not be obtained due to signal broadening from the paramagnetic metal.

Complex $Na_3[(6.5)_3Sm]$: ^1H NMR (500 MHz, DMSO-d_6) δ 9.36 (d, J=8.0 Hz, 2H); 8.80 (d, J=8.1 Hz, 1H); 7.99 (d, J=7.9 Hz, 2H); 7.70 (s, 1H); 7.66 (t, J=7.6 Hz, 1H); 7.51 (d, J=7.2 Hz, 1H); 6.82 (t, J=7.2 Hz, 1H); ^{13}C NMR (125 MHz, DMSO-d_6) δ 176.4; 171.0; 153.8; 135.1; 134.4; 132.0; 131.3; 130.8; 123.2; 123.1; 118.7; 113.8.

Complex $Na[(6.5)_2Yb]$: ^1H NMR (400 MHz, DMSO-d_6) δ -6.83 (s, 2H); -10.02 (s, 1H); -14.34 (s, 1H); -16.63 (s, 1H); -26.74 (s, 1H); -37.58 (s, 2H); -66.12 (s, 1H); MS (ESI) *m/z* calcd for $C_{28}H_{20}Br_2N_4O_4Yb$ 809.9; found 810.1. ^{13}C data could not be obtained due to signal broadening from the paramagnetic metal.

General procedure for displacement experiments: To a solution of **6.3** (3.5 mg, 5.45 µmol) in 0.5 mL DMSO-d_6 was added 7.24 µmol lanthanide triflate in 40 µL DMSO-d_6 and a ^1H NMR spectrum was acquired. An equimolar solution of the second lanthanide triflate was added in two portions with a spectrum acquired after each addition. The same procedure was used for **6.5** using half the amount of metal. Integration of the signals corresponding to each complex allowed for determination of the ratio of complexes.

General procedure for equilibrium experiments: To a solution of **6.3** (4 mg, 6.23 µmol) in 0.42 mL DMSO-d_6 was added 8.28 µmol each of two lanthanide triflates in 80 μL DMSO-d_6. ^{1}H NMR spectra were acquired after the first addition and periodically over approximately 30 h. The same procedure was used for **6.5** using half the amount of metal.

General procedure for experiments with varying amounts of water: Two samples were prepared according to the procedure for equilibrium experiments with 25 μL water added to one of the samples. The amount of water in the sample was determined by integrating and comparing the intensity for the signals corresponding to water and the complex.

8.7 Chapter Seven Experimental

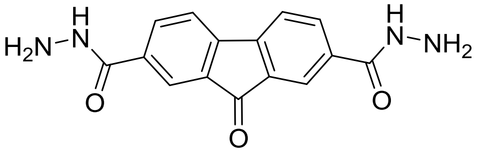

9-oxo-9*H*-fluorene-2,7-dicarbohydrazide (7.2): To a round-bottomed flask equipped with stir bar was added 9-oxo-9*H*-fluorene-2,7-dicarboxylic acid (510 mg, 1.90 mmol), 2-(6-Chloro-1H-benzotriazole-1-yl)-1,1,3,3-tetramethylaminium hexafluoro-phosphate (HCTU) (1.73 g, 4.18 mmol), triethylamine (1.06 mL, 7.61 mmol), acetonitrile (5 mL), and chloroform (5 mL). The reaction was stirred for 1.5 h and hydrazine hydrate (181 μL, 3.71 mmol) and triethylamine (1.03 mL, 7.39 mmol) were added. Stirring was continued for 19 h and the reaction was filtered. The solid was suspended in saturated aqueous sodium bicarbonate, filtered, and washed with water to yield a yellow solid (450 mg, 80%). ^{1}H NMR (300 MHz, DMSO-d_6) δ 9.99 (s, 2H); 8.12 (dd, J=1.6, 7.7 Hz, 2H); 8.07

(d, J=1.4 Hz, 2H); 7.97 (d, J=7.8 Hz, 2H); 4.59 (s, 4H); ^{13}C NMR (125 MHz, DMSO-d_6) δ 191.8; 164.4; 145.3; 134.7; 134.3; 133.9; 122.4; 121.8.

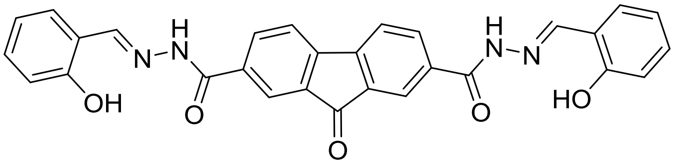

***N'*^{2},*N'*^{7}-bis((E)-2-hydroxybenzylidene)-9-oxo-9*H*-fluorene-2,7-dicarbohydrazide (L7.3):** To a round-bottomed flask equipped with stir bar and reflux condenser was added 9-oxo-9*H*-fluorene-2,7-dicarbohydrazide (229 mg, 0.77 mmol), salicylaldehyde (163 µL, 1.55 mmol), ethanol (2 mL), and acetic acid (2 drops). The reaction was refluxed 2.5 h and filtered to yield **L7.3** as a yellow solid (339 mg, 87%). ^{1}H NMR (400 MHz, DMSO-d_6) δ 12.29 (s, 2H); 11.20 (s, 2H); 8.69 (s, 2H); 8.28 (d, J=8.0 Hz, 2H); 8.27 (s, 2H); 8.11 (d, J=8.3 Hz, 2H); 7.59 (d, J=7.6 Hz, 2H); 7.32 (t, J=7.7 Hz, 2H); 6.96-6.92 (m, 4H); ^{13}C NMR (125 MHz, DMSO-d_6) δ 191.6; 161.4; 157.5; 148.5; 146.0; 135.4; 134.3; 134.0; 131.6; 129.4; 122.9; 122.3; 119.4; 118.7; 116.4; MS (ESI) *m/z* calcd for $C_{29}H_{20}N_4O_5$ $(M+H)^+$ 505.15; found 505.25.

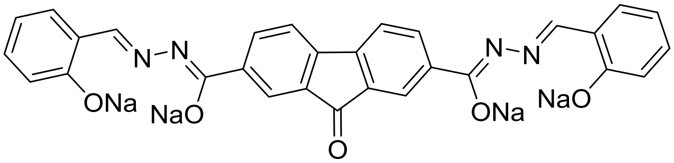

Ligand 7.3: ^{1}H NMR (400 MHz, DMSO-d_6) δ 8.29 (s, 2H); 8.27 (d, J=7.6 Hz, 2H); 8.12 (s, 2H); 7.59 (d, J=7.6 Hz, 2H); 6.80 (d, J=7.3 Hz, 2H); 6.69 (t, J=7.2 Hz, 2H); 6.17 (d, J=8.4 Hz, 2H); 5.93 (t, J=7.1 Hz, 2H); ^{13}C NMR (125 MHz, DMSO-d_6) δ 194.3; 171.1; 166.8; 152.8; 143.4; 143.2; 134.0; 133.3; 133.2; 128.5; 123.7; 123.2; 121.9; 119.6; 107.6.

Complex $Na_6[(7.3)_3Y_2]$: ^{1}H NMR (400 MHz, DMSO-*d*$_6$) δ 8.45 (s, 2H); 8.28-8.26 (m, 4H); 7.83 (dd, J=1.8, 8.1 Hz, 2H); 7.26 (d, J=7.6 Hz, 2H); 7.15 (t, J=7.6 Hz, 2H); 6.56-6.50 (m, 4H); MS (ESI) *m/z* calcd for $C_{87}H_{56}N_{12}O_{15}Y_2$ $[Y_2L_3\text{-}4H]^{2+}$ 843.11; found 843.00.

Complex $Na_6[(7.3)_3La_2]$: ^{1}H NMR (500 MHz, DMSO-*d*$_6$) δ 8.33 (s, 2H); 8.28 (s, 2H); 8.26 (d, J=7.6 Hz, 2H); 7.80 (d, J=7.7 Hz, 2H); 7.17 (d, J=7.7 Hz, 2H); 7.08 (t, J=7.3 Hz, 2H); 6.45-6.42 (m, 4H); ^{13}C NMR (125 MHz, DMSO-*d*$_6$) δ 193.1; 167.3; 166.0; 155.4; 144.3; 139.2; 134.4; 133.8; 133.8; 131.8; 123.1; 122.5; 120.8; 119.5; 113.2.

Complex $Na_6[(7.3)_3Sm_2]$: ^{1}H NMR (400 MHz, DMSO-*d*$_6$) δ 9.86 (d, J=7.1 Hz, 2H); 9.67 (s, 2H); 8.81 (d, J=7.8 Hz, 2H); 8.46 (d, J=7.5 Hz, 2H); 7.84 (s, 2H); 7.69 (t, J=7.5 Hz, 2H); 7.58 (d, 7.5 Hz, 2H); 6.87 (t, J=7.0 Hz, 2H).

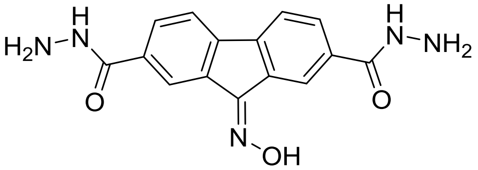

9-(hydroxyimino)-9*H*-fluorene-2,7-dicarbohydrazide (7.4a): To a round-bottomed flask equipped with stir bar and reflux condenser was added 9-oxo-9*H*-fluorene-2,7-dicarbohydrazide (159 mg, 0.54 mmol), hydroxylamine hydrochloride (54 mg, 0.78 mmol), and pyridine (1 mL). The reaction was refluxed for 1 h, cooled, and filtered to yield **7.4a** as a yellow solid (122 mg, 73%). ^{1}H NMR (400 MHz, DMSO-*d*$_6$) δ 12.88 (s, 1H); 9.95 (s, 1H); 9.92 (s, 1H); 8.80 (s, 1H); 8.17 (s, 1H); 8.04-7.91 (m, 4H); 4.68 (s, 4H).

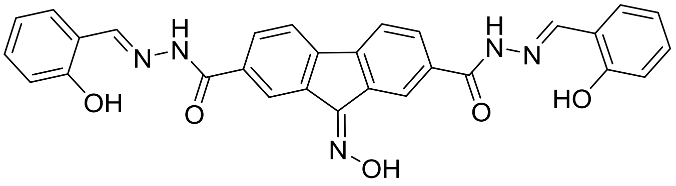

N'^{2},N'^{7}-bis((E)-2-hydroxybenzylidene)-9-(hydroxyimino)-9*H*-fluorene-2,7-dicarbohydrazide (L7.5a): To a round-bottomed flask equipped with stir bar and reflux condenser was added 9-(hydroxyimino)-9*H*-fluorene-2,7-dicarbohydrazide (90 mg, 0.29 mmol), salicylaldehyde (61 µL, 0.58 mmol), ethanol (2 mL), and acetic acid (2 drops). The reaction was refluxed 5 h, filtered, and washed with ethanol to yield **L7.5a** as a yellow solid (114 mg, 76%). ^{1}H NMR (400 MHz, DMSO-d_6) δ 13.06 (s, 1H); 12.29 (s, 2H); 11.31 (s, 2H); 8.94 (s, 1H); 8.69 (s, 2H); 8.35 (s, 1H); 8.21-8.08 (m, 4H); 7.56 (d, J=7.7 Hz, 2H); 7.32 (t, J=7.7 Hz, 2H); 6.96-6.91 (m, 4H); ^{13}C NMR (125 MHz, DMSO-d_6) δ 162.5; 162.3; 157.5; 150.0; 148.6; 148.5; 142.1; 141.3; 136.1; 133.6; 133.0; 131.5; 130.5; 130.2; 129.6; 129.6; 129.5; 127.8; 121.4; 121.2; 120.1; 119.4; 118.7; 116.5.; MS (ESI) *m/z* calcd for $C_{29}H_{21}N_5O_5$ $(M+H)^+$ 520.16; found 520.25.

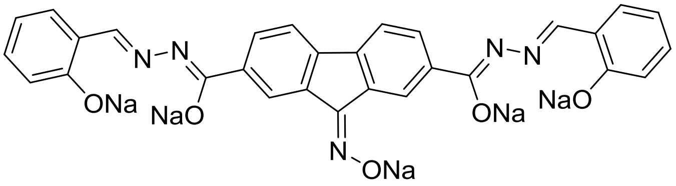

Ligand 7.5a: ^{1}H NMR (400 MHz, DMSO-d_6) δ 9.39 (s, 1H); 8.68 (s, 1H); 8.16 (s, 1H); 8.14 (s, 1H); 7.96 (d, J=8.0 Hz, 1H); 7.92 (d, J=8.1 Hz, 1H); 7.59 (d, J=8.0 Hz, 1H); 7.55 (d, J=8.1 Hz, 1H); 6.80 (t, J=7.2 Hz, 2H); 6.68 (t, J=7.6 Hz, 2H); 6.20 (dd, J=8.1, 4.4 Hz, 2H); 5.95 (d, J=6.1 Hz, 2H); ^{13}C NMR (125 MHz, DMSO-d_6) δ 171.0; 169.3; 169.2; 151.2; 140.7; 139.5; 139.2; 134.7; 134.1; 132.9; 128.9; 128.0; 124.9; 124.7; 124.3; 123.5; 123.2; 123.0; 121.8; 117.4; 117.2; 116.7.

Complex $Na_6[(7.5a)_3Y_2]$: ^{1}H NMR (400 MHz, DMSO-d_6) δ 9.07 (s, 1H); 8.43 (m, 3H); 8.23 (d, J=7.9 Hz, 1H); 8.13 (d, J=7.8 Hz, 1H); 7.88 (d, J=8.0 Hz, 1H); 7.84 (d, J=8.1 Hz, 1H); 7.24 (t, J=7.5 Hz, 2H); 7.14 (t, J=7.3 Hz, 2H); 6.53-6.49 (m, 4H); MS (ESI) *m/z* calcd for $C_{87}H_{59}N_{15}O_{15}Y_2$ $[Y_2L_3\text{-}4H]^{2+}$ 865.62; found 865.92.

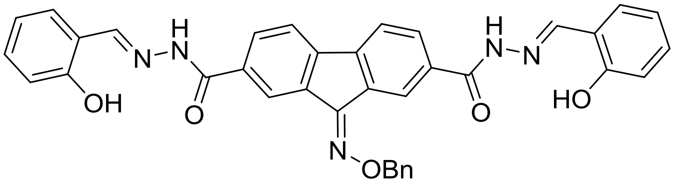

9-((benzyloxy)imino)-*N*'^{2},*N*'^{7}-bis((*E*)-2-hydroxybenzylidene)-9*H*-fluorene-2,7-dicarbohydrazide (L7.5b): To a round-bottomed flask equipped with stir bar and reflux condenser was added 9-oxo-9*H*-fluorene-2,7-dicarbohydrazide (190 mg, 0.64 mmol), *o*-benzylhydroxylamine hydrochloride (158 mg, 0.99 mmol), and pyridine (1 mL). After refluxing 1 h, water was added, the reaction filtered, and the solid recrystallized from ethanol. This solid was then combined with salicylaldehyde (135 µL, 1.28 mmol), ethanol (2 mL), and acetic acid (2 drops). The reaction was refluxed 4 h and filtered. The crude solid was filtered from hot nitromethane to yield **L7.5b** as a yellow solid (102 mg, 26%). ^{1}H NMR (300 MHz, DMSO-d_6) δ 12.29 (s, 1H); 12.27, (s, 1H); 11.28 (s, 1H); 11.23 (s, 1H); 8.81 (s, 1H); 8.69 (s, 1H); 8.66 (s, 1H); 8.31 (s, 1H); 8.19-8.13 (m, 4H); 7.60-7.46 (m, 4H); 7.41 (t, J=7.2 Hz, 2H); 7.38 (t, J=7.2 Hz, 1H); 7.32 (t, J=7.4 Hz, 2H); 6.97-6.91 (m, 4H); 5.59 (s, 2H); ^{13}C NMR (125 MHz, DMSO-d_6) δ 162.5; 162.1; 157.5; 150.7; 148.6; 148.5; 148.4; 146.0; 142.6; 141.7; 137.2; 135.2; 133.9; 133.2; 131.5; 131.1; 131.0; 131.0; 130.5; 130.1; 129.5; 129.4; 128.6; 128.2; 128.0; 121.7; 121.4; 120.5; 120.4; 119.4; 118.7; 116.5; 77.7; MS (ESI) *m/z* calcd for $C_{36}H_{28}N_5O_5$ $(M+H)^+$ 610.21; found 610.42.

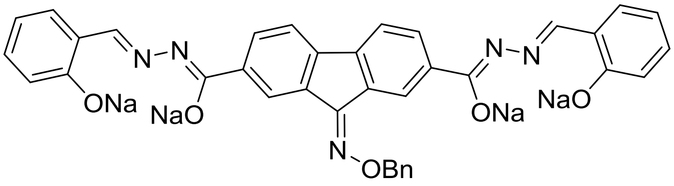

Ligand 7.5b ^{1}H NMR (400 MHz, DMSO-d_6) δ 9.02 (s, 1H); 8.27 (d, J=8.7 Hz, 1H); 8.23 (d, J=8.0 Hz, 1H); 8.13 (s, 2H); 8.10 (s, 1H); 7.65 (d, J=7.9 Hz, 1H); 7.62 (d, J=8.3 Hz, 1H); 7.57 (d, J=8.1 Hz, 2H); 7.44 (t, J=7.6 Hz, 2H); 7.35 (t, J=7.5 Hz, 1H); 6.80 (d, J=7.3 Hz, 2H); 6.69 (t, J=7.4 Hz, 2H); 6.19 (d, J=8.0 Hz, 2H); 5.94 (t, J=6.4 Hz, 2H); 5.51 (s, 2H).

Complex $Na_6[(7.5b)_3Y_2]$: ^{1}H NMR (400 MHz, DMSO-d_6) δ 9.01 (s, 1H); 8.47 (s, 1H); 8.45 (s, 1H); 8.37 (s, 1H); 8.23 (d, J=8.1 Hz, 1H); 8.14 (d, J=8.0 Hz, 1H); 7.90 (d, J=7.9 Hz, 1H); 7.84 (t, J=8.8 Hz, 1H); 7.53 (d, J=7.6 Hz, 2H); 7.46 (dd, J=6.5, 8.2 Hz, 2H); 7.39 (t, J=7.4 Hz, 1H); 7.25 (t, J=8.3 Hz, 2H); 7.15 (t, J=7.8 Hz, 2H); 6.56-6.50 (m, 4H); 5.55 (s, 2H).

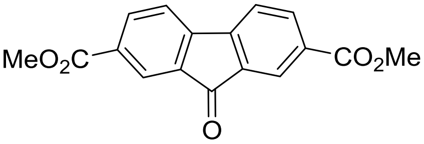

Dimethyl 9-oxo-9*H*-fluorene-2,7-dicarboxylate (7.6): To a round-bottomed flask equipped with stir bar was added 9-oxo-9*H*-fluorene-2,7-dicarboxylic acid (448 mg, 1.67 mmol), N,N'-dimethylformamide (1.5 mL), and 1,8-Diazabicyclo[5.4.0]undec-7-ene (750 μL, 5.02 mmol). The reaction was stirred for 3 h and iodomethane (415 μL, 6.67 mmol) was added. The reaction was stirred for an additional 24 h, water (7 mL) was added, and the resulting precipitate was filtered. The solid was suspended in chloroform, filtered, and the filtrate was evaporated to yield **7.6** as a yellow solid (333 mg, 67%). ^{1}H NMR

(500 MHz, $CDCl_3$) δ 8.32 (d, J=1.5 Hz, 2H); 8.24 (dd, J=1.5, 7.8 Hz, 2H); 7.67 (d, J=7.8 Hz, 2H); 3.95 (s, 6H); ^{13}C NMR (125 MHz, $CDCl_3$) δ 191.5; 165.9; 147.2; 136.6; 134.9; 132.1; 125.7; 121.2; 52.6.

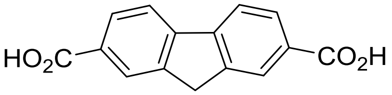

9*H*-fluorene-2,7-dicarboxylic acid (7.7): To a round-bottomed flask equipped with stir bar and reflux condenser was added Dimethyl 9-oxo-9*H*-fluorene-2,7-dicarboxylate (67 mg, 0.23 mmol), sodium hydroxide (162 mg, 2.89 mmol), ethylene glycol (1 mL) and hydrazine hydrate (173 µL, 3.55 mmol). The reaction was stirred at 180 °C for 16 h and cooled to room temperature. Concentrated HCl (1 mL) at 0 °C was added and the reaction was filtered and washed with water to yield **7.7** as an orange solid (56 mg, 97%). ^{1}H NMR (500 MHz, DMSO-d_6) δ 8.18 (s, 2H); 8.09 (d, J=8.0 Hz, 2H); 8.02 (d, J=7.9 Hz, 2H); 4.08 (s, 2H); ^{13}C NMR (125 MHz, $CDCl_3$) δ 167.5; 144.4; 144.3; 130.0; 128.5; 126.3; 120.9; 36.5.

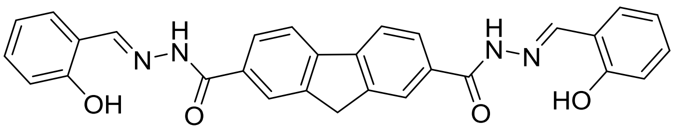

***N*'^{2},*N*'^{7}-bis((E)-2-hydroxybenzylidene)-9*H*-fluorene-2,7-dicarbohydrazide (L7.8):** To a round-bottomed flask equipped with stir bar was added 9*H*-fluorene-2,7-dicarboxylic acid (106 mg, 0.42 mmol), 2-(6-Chloro-1H-benzotriazole-1-yl)-1,1,3,3-tetramethylaminium hexafluoro-phosphate (HCTU) (373 mg, 0.90 mmol), acetonitrile (3 mL), chloroform (3 mL), and triethylamine (232 µL, 1.66 mmol). The reaction was stirred for 2 h and hydrazine hydrate (40 µL, 0.82 mmol) and triethylamine (230 µL, 1.65 mmol) were added. The reaction was stirred an additional 16 h and the resulting precipitate was filtered and washed with dichloromethane. This solid was transferred to a round-bottomed flask equipped with stir bar and reflux condenser and ethanol (2 mL), salicylaldehyde (88 µL, 0.84 mmol), and acetic acid (2 drops) were added. The reaction was refluxed 3 h and the resulting precipitate was filtered and washed with hot ethanol to yield **L7.8** as a yellow solid (118 mg, 58%). ^{1}H NMR (500 MHz, DMSO-*d*$_6$) δ 12.20 (s, 2H); 11.33 (s, 2H); 8.68 (s, 2H); 8.23 (s, 2H); 8.18 (d, J=8.0 Hz, 2H); 8.05 (d, J=8.2 Hz, 2H); 7.57 (d, J=7.5 Hz, 2H); 7.32 (t, J=7.6 Hz, 2H); 6.96-6.93 (m, 4H); 4.16 (s, 2H); ^{13}C NMR (125 MHz, CDCl$_3$) δ 162.8; 157.5; 148.2; 144.2; 143.6; 131.9; 131.4; 129.5; 126.9; 124.7; 120.9; 119.4; 118.7; 116.5; 36.6; MS (ESI) *m/z* calcd for $C_{29}H_{23}N_4O_4$ $(M+H)^+$ 491.17; found 491.33.

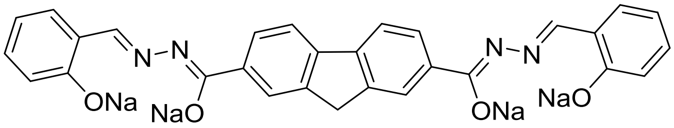

Ligand 7.8: ^{1}H NMR (300 MHz, DMSO-*d*$_6$) δ 8.27 (s, 2H); 8.12-8.09 (m, 4H); 7.68 (d, J=8.0 Hz, 2H); 6.79 (d, J=7.4 Hz, 2H); 6.67 (t, J=7.7 Hz, 2H); 6.18 (d, J=8.1 Hz, 2H); 5.93 (t, J=7.2 Hz, 2H); 3.87 (s, 2H); ^{13}C NMR (125 MHz, DMSO-*d*$_6$) δ 171.2; 167.9; 151.6; 142.2; 140.7; 133.0; 128.1; 126.3; 124.3; 123.1; 121.8; 119.4; 118.0; 107.0; 36.4.

Complex $Na_6[(7.8)_3Y_2]$: ^{1}H NMR (400 MHz, DMSO-*d*$_6$) δ 8.44 (s, 2H); 8.27 (s, 2H); 8.11 (d, J=7.9 Hz, 2H); 7.90 (d, J=8.0 Hz, 2H); 7.25 (d, J=7.8 Hz, 2H); 7.14 (td, J=7.6, 6.7, 1.7 Hz, 2H); 6.56-6.50 (m, 4H); 4.01 (s, 2H); ^{13}C NMR (125 MHz, DMSO-*d*$_6$) δ 169.2; 165.3; 156.1; 143.5; 142.3; 135.1; 133.6; 132.4; 126.8; 124.5; 122.1; 121.8; 119.7; 114.2.

Complex $Na_6[(7.8)_3La_2]$: ^{1}H NMR (400 MHz, DMSO-d_6) δ 8.32 (s, 2H); 8.27 (s, 2H); 8.10 (d, J=7.9 Hz, 2H); 7.85 (d, J=8.0 Hz, 2H); 7.16 (dd, J=1.9, 7.6 Hz, 2H); 7.06 (td, J=1.9, 7.6 Hz, 2H); 6.45-6.41 (m, 4H); 3.98 (s, 2H).

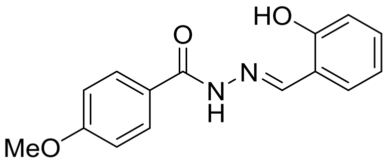

(*E*)-*N*-(2-hydroxystyryl)-4-methoxybenzamide (L7.11b): To a round-bottomed flask equipped with stir bar and reflux condenser was added methyl 4-methoxybenzoate (225 mg, 1.35 mmol), ethanol (1 mL), and hydrazine hydrate (1 mL). The reaction was refluxed 18 h, water was added, and the resulting precipitate was filtered. The solid was added to a round-bottomed flask equipped with stir bar and reflux condenser, and ethanol (1 mL), salicylaldehyde (213 mg, 2.02 mmol), and acetic acid (2 drops). The reaction was refluxed 16 h, water was added, and the resulting precipitate was filtered to yield **L7.11b** as a white solid (109 mg, 30%). ^{1}H NMR (500 MHz, DMSO-d_6) δ 12.00 (s, 1H); 11.38 (s, 1H); 8.62 (s, 1H); 7.93 (d, J=8.5 Hz, 2H); 7.52 (d, J=7.6 Hz, 1H); 7.29 (t, J=8.3 Hz, 1H); 7.08 (d, J=8.9 Hz, 2H); 6.94-6.90 (m, 2H); 3.84 (s, 3H); ^{13}C NMR (125 MHz, DMSO-d_6) δ 162.3; 162.3; 157.5; 147.9; 131.3; 129.6; 129.6; 124.8; 119.4; 118.7; 116.5; 113.9; 55.5; MS (ESI) *m/z* calcd for $C_{15}H_{15}N_2O_3$ $(M+H)^+$ 271.11; found 271.25.

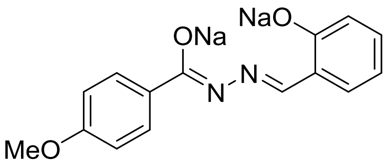

Ligand 7.11b: ^{1}H NMR (300 MHz, DMSO-d_6) δ 8.07 (s, 1H); 8.00 (d, J=8.7 Hz, 2H); 6.80-6.75 (m, 3H); 6.67 (t, J=6.5 Hz, 1H); 6.19 (d, J=8.2 Hz, 1H); 5.93 (t, J=7.0 Hz, 1H);

3.74 (s, 3H); ^{13}C NMR (125 MHz, DMSO-d_6) δ 171.0; 167.7; 159.0; 151.5; 134.6; 132.9; 128.9; 128.1; 124.1; 121.9; 112.1; 107.5; 55.0.

Complex Na$_3$[(7.11b)$_3$Y]: ^{1}H NMR (500 MHz, DMSO-d_6) δ 8.37 (s, 1H); 7.99 (d, J=8.6 Hz, 2H); 7.20 (dd, J=7.7, 1.9 Hz, 1H); 7.12 (td, J=8.2, 7.7, 1.7 Hz, 1H); 6.94 (d, J=8.3 Hz, 2H); 6.53 (d, J=8.4 Hz, 1H); 6.50 (t, J=7.4 Hz, 1H); 3.78 (s, 3H); ^{13}C NMR (125 MHz, DMSO-d_6) δ 168.6; 165.3; 161.0; 155.4; 133.6; 132.4; 129.5; 127.8; 121.7; 119.7; 114.2; 113.5; 55.4; MS (ESI) *m/z* calcd for $C_{45}H_{40}N_6O_9Y$ [(**L7.11b**)$_3$Y$_2$-2H]$^+$ 897.19; found 896.67.

Complex Na$_3$[(7.11b)$_3$La]: ^{1}H NMR (400 MHz, DMSO-d_6) δ 8.27 (s, 1H); 7.99 (d, J=8.8 Hz, 2H); 7.13 (dd, J=7.9, 1.9 Hz, 1H); 7.06 (t, J=7.7 Hz, 1H); 6.92 (d, J=8.3 Hz, 2H); 6.43-6.40 (m, 2H); 3.78 (s, 3H); ^{13}C NMR (125 MHz, DMSO-d_6) δ 168.5; 165.8; 160.3; 154.1; 133.6; 131.4; 129.6; 129.3; 122.8; 119.4; 113.1; 113.1; 55.2.

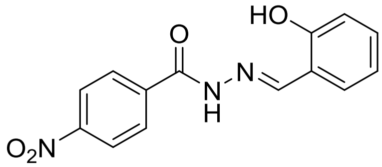

(*E*)-*N*-(2-hydroxystyryl)-4-nitrobenzamide (L7.11c): To a round-bottomed flask equipped with stir bar was added methyl 4-nitrobenzoate (244 mg, 1.35 mmol), ethanol (2 mL), and hydrazine hydrate (0.5 mL). The reaction was stirred 3.5 h, water was added, and the resulting precipitate was filtered and washed with cold ethanol. This solid was added to a round-bottomed flask equipped with stir bar and reflux condenser and ethanol (4 mL), salicylaldehyde (284 μL, 2.70 mmol), and acetic acid (2 drops) were added. The reaction was refluxed 2 h, filtered, and washed with ethanol to yield **L7.11c**

as a yellow solid (286 mg, 74%). ^{1}H NMR (500 MHz, DMSO-d_6) δ 12.35 (s, 1H); 11.10 (s, 1H); 8.68 (s, 1H); 8.38 (d, J=8.6 Hz, 2H); 8.18 (d, J=8.5 Hz, 2H); 7.60 (d, J=7.8 Hz, 1H); 7.32 (dd, J=7.0, 8.5 Hz, 1H); 6.95 (d, J=8.3 Hz, 1H); 6.93 (t, J=7.6 Hz, 1H); ^{13}C NMR (125 MHz, DMSO-d_6) δ161.2; 157.5; 149.4; 148.9; 138.5; 131.7; 129.2; 129.2 123.7; 119.4; 118.7; 116.4; MS (ESI) *m/z* calcd for $C_{14}H_{12}N_3O_4$ $(M+H)^+$ 286.08; found 286.25.

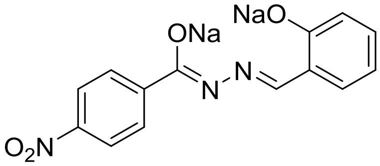

Ligand 7.11c: ^{1}H NMR (500 MHz, DMSO-d_6) δ 8.29 (d, J=8.8 Hz, 2H); 8.15 (s, 1H); 8.11 (d, J=9.0 Hz, 2H); 6.82 (dt, J=2.0, 7.3 Hz, 1H); 6.72 (ddd, J=1.2, 6.6, 8.6 Hz, 1H); 6.24 (d, J=8.2 Hz, 1H); 5.98 (t, J=7.1 Hz, 1H); ^{13}C NMR (125 MHz, DMSO-d_6) δ 171.5; 165.7; 153.8; 149.2; 146.6; 133.4; 128.7; 128.3; 123.4; 122.3; 122.1; 107.2.

Complex Na$_3$[(7.11c)$_3$Y]: ^{1}H NMR (500 MHz, DMSO-d_6) δ 8.43 (s, 1H); 8.26 (d, J=9.0 Hz, 2H); 8.24 (d, J=8.9 Hz, 2H); 7.24 (d, J=7.6 Hz, 1H); 7.14 (t, J=7.8 Hz, 1H); 6.54 (d, J=8.3 Hz, 1H); 6.50 (t, J=7.2 Hz, 1H); ^{13}C NMR (125 MHz, DMSO-d_6) δ 167.0; 165.7; 157.5; 148.1; 143.1; 133.9; 132.8; 128.8; 123.3; 121.7; 119.8; 114.2; MS (ESI) *m/z* calcd for $C_{42}H_{31}N_9O_{12}Y$ [(**L7.11c**)$_3$Y$_2$-2H]$^+$ 942.11; found 941.50.

Complex Na$_3$[(7.11c)$_3$La]: ^{1}H NMR (500 MHz, DMSO-d_6) δ 8.32 (s, 1H); 8.26 (d, J=8.9 Hz, 2H); 8.22 (d, J=9.0 Hz, 2H); 7.17 (d, J=8.1 Hz, 1H); 7.08 (t, J=8.7 Hz, 1H); 6.44-6.42 (m, 2H); ^{13}C NMR (125 MHz, DMSO-d_6) δ 166.8; 166.2; 156.5; 147.8; 144.3; 134.1; 132.1; 128.7; 123.2; 122.5; 119.7; 113.4.

General deprotonation procedure: Ligand was suspended in anhydrous methylene chloride (2 mL) and an excess of sodium hydride was added. The mixture was allowed to stir 1 h, quenched with nonanhydrous methylene chloride and hexanes, and stirred an additional 30 min. The deprotonated ligand was collected by centrifugation and dried to yield a light yellow solid in quantitative yield.

Complex formation: Ligand and metal triflate were combined in an NMR tube with 0.5 mL DMSO-*d*$_6$. The sample was shaken for 10 s for quantitative formation of Na$_6$[(**7.3**)$_3$Ln$_2$].

NMR titrations: Ligand **7.3** was dissolved in 0.5 mL DMSO-*d*$_6$ and a solution of metal triflate was slowly added with shaking to mix after each addition.

General procedure for displacement experiments: To a solution of **7.3** (3.7 mg, 6.23 μmol) in 0.42 mL DMSO-*d*$_6$ was added 8.31 μmol lanthanide triflate in 40 μL DMSO-*d*$_6$ and a ^{1}H NMR spectrum was acquired. An equimolar solution of the second lanthanide triflate was added in two portions with a spectrum acquired after each addition. Integration of the signals corresponding to each complex allowed for determination of the ratio of complexes.

General procedure for equilibrium experiments: To a solution of **7.3** (3.7 mg, 6.23 μmol) in 0.42 mL DMSO-*d*$_6$ was added 9.37 μmol each of two lanthanide triflates in 80 μL DMSO-*d*$_6$. ^{1}H NMR spectra were acquired after the first addition and periodically over approximately 26 h.

Representative procedure for mixing experiments: To a solution of **7.3** (1.8 mg, 3.04 μmol) and **7.8** (1.8 mg, 3.11 μmol) in 400 μL DMSO-d_6 was added Y(OTf)$_3$ (6.7 mg, 12.5 μmol) in 50 μL DMSO-d_6. ^{1}H NMR spectra were acquired immediately after metal addition and heating at 60 °C for 18 h.

8.8 Selected NMR Spectra

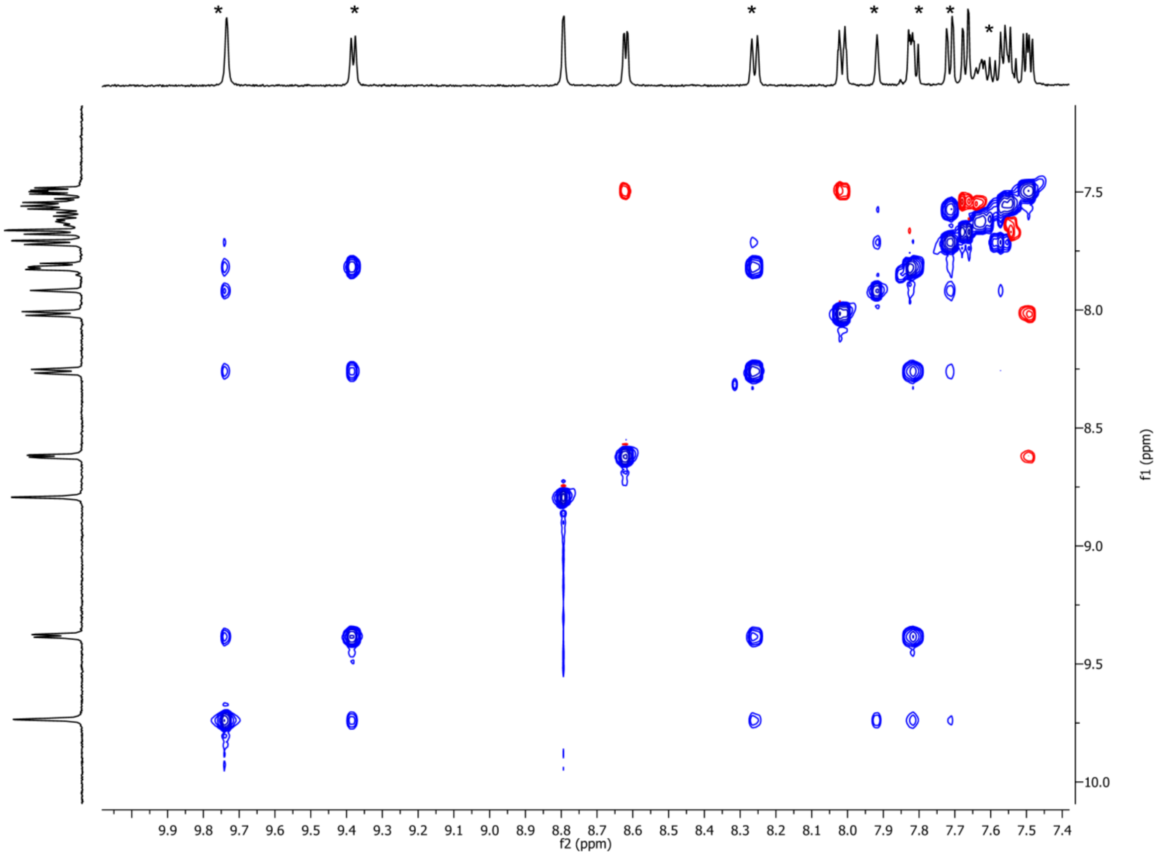

Figure 8.3: Upfield region of the 2D gNOESY NMR spectrum of the mixture of **2.3** and [(**2.3**)$_4$Pd$_2$](NO$_3$)$_4$ (1:1 ratio, 2 mM, 500 MHz, DMSO-*d*6, 2.0 sec mixing time, 298 K) illustrating the lack of self-exchange peaks between ligand and complex. Complex peaks are denoted by *. Crosspeaks are due to NOE enhancements.

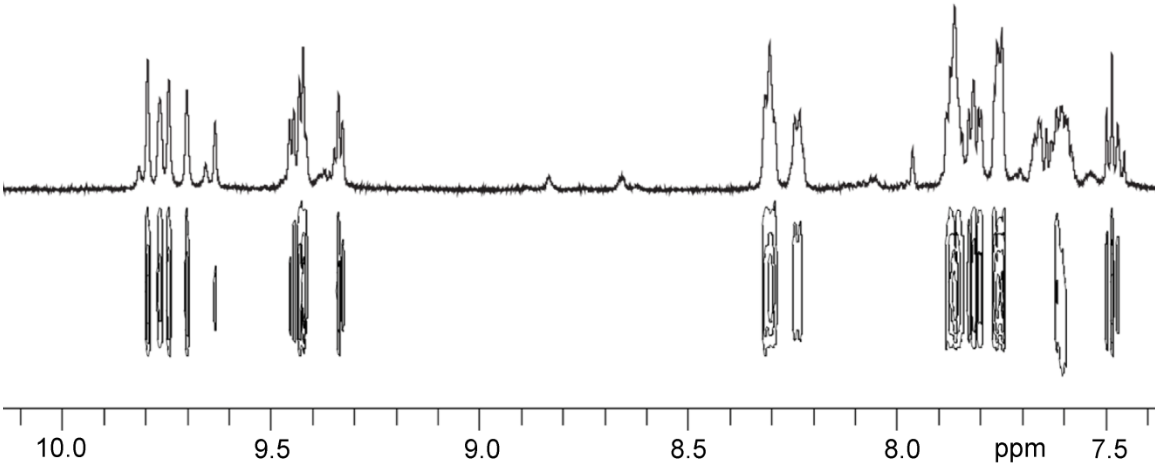

Figure 8.4: DOSY spectrum of the heterocluster $[(\textbf{2.3})_x(\textbf{2.6a})_y\text{Pd}_2](\text{NO}_3)_4$ (600 MHz, DMSO-*d*6, 298 K, relaxation delay 2.5 sec, Δ=250 msec, δ=1.6 msec).

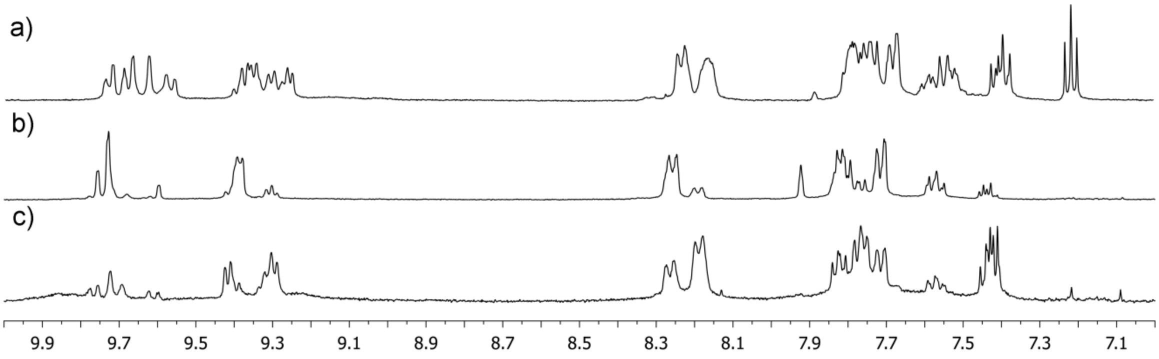

Figure 8.5: Identification of heterocomplex peaks (4 mM, 400 MHz, DMSO-d_6, 300 K): a) 1 eq. **2.3** + 1 eq. **2.6a** + $\text{Pd(NO}_3)_2$; b) 3 eq. **2.3** + 1 eq. **2.6a** + $\text{Pd(NO}_3)_2$; c) 1 eq. **2.3** + 3 eq. **2.6a** + $\text{Pd(NO}_3)_2$.

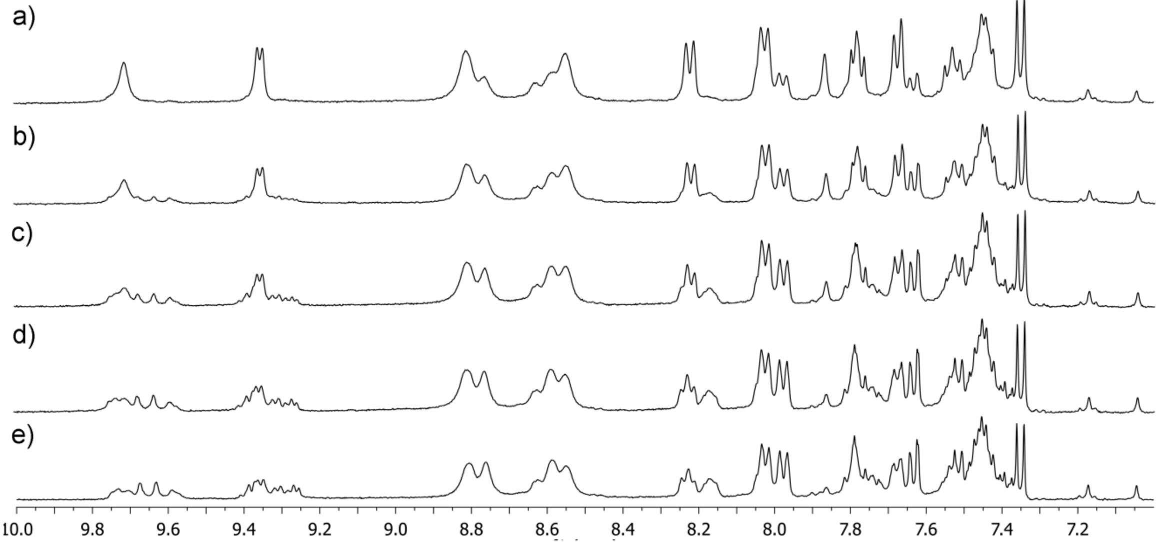

Figure 8.6: ^{1}H NMR spectra of the incorporation of ligand **2.6a** into complex $[(\textbf{2.3})_4\text{Pd}_2](\text{NO}_3)_4$ (400 MHz, DMSO-d_6, 14 mM, 300 K): a) 2 min; b) 15 min; c) 29 min; d) 42 min; e) 55 min.

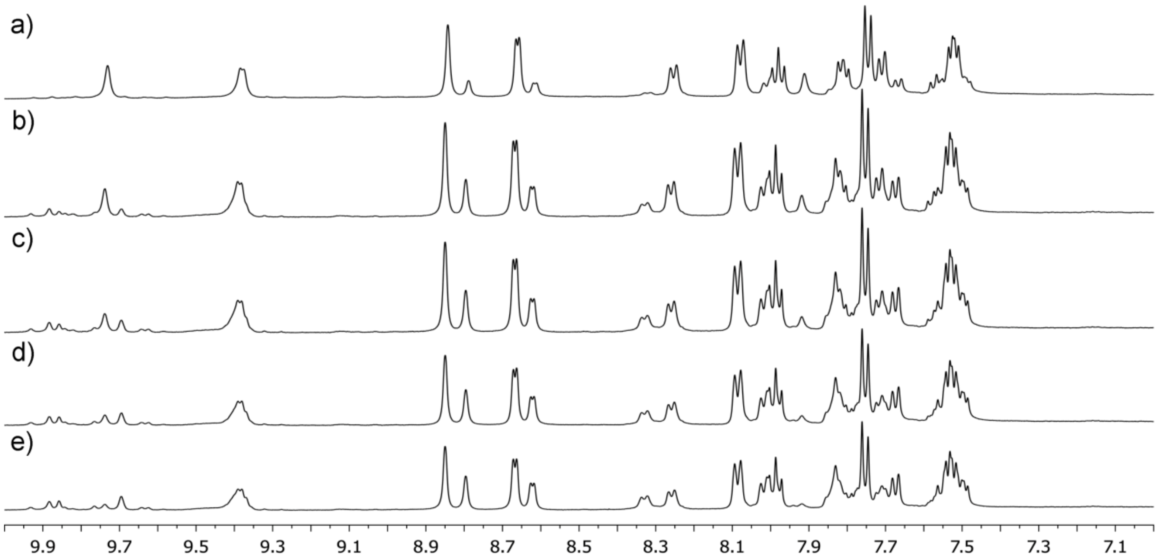

Figure 8.7: ^{1}H NMR spectra of the incorporation of ligand **2.6d** into complex $[(\mathbf{2.3})_4Pd_2](NO_3)_4$ (400 MHz, DMSO-d_6, 14 mM, 300 K): a) 7 min; b) 22 min; c) 32 min; d) 42 min; e) 51 min.

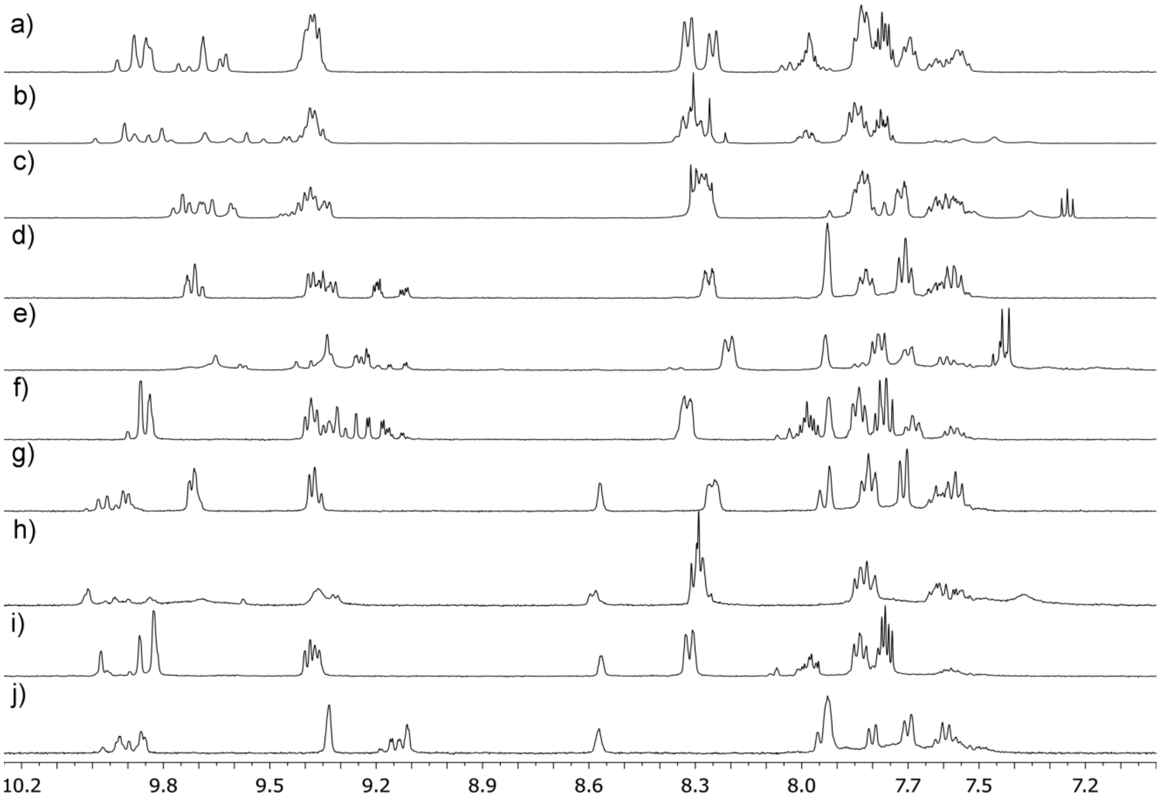

Figure 8.8: ^{1}H NMR spectra of mixing of ligands with different electronic properties: a) $[(\mathbf{2.3})_x(\mathbf{2.6d})_yPd_2](NO_3)_4$; b) $[(\mathbf{2.6b})_x(\mathbf{2.6d})_yPd_2](NO_3)_4$; c) $[(\mathbf{2.3})_x(\mathbf{2.6b})_yPd_2](NO_3)_4$; d) $[(\mathbf{2.3})_x(\mathbf{2.8a})_yPd_2](NO_3)_4$; e) $[(\mathbf{2.6a})_x(\mathbf{2.8a})_yPd_2](NO_3)_4$; f) $[(\mathbf{2.6d})_x(\mathbf{2.8a})_yPd_2](NO_3)_4$; g) $[(\mathbf{2.3})_x(\mathbf{2.8c})_yPd_2](NO_3)_4$; h) $[(\mathbf{2.6b})_x(\mathbf{2.8c})_yPd_2](NO_3)_4$; i) $[(\mathbf{2.6d})_x(\mathbf{2.8c})_yPd_2](NO_3)_4$; j) $[(\mathbf{2.8a})_x(\mathbf{2.8c})_yPd_2](NO_3)_4$ (400 MHz, DMSO-d_6, 298 K).

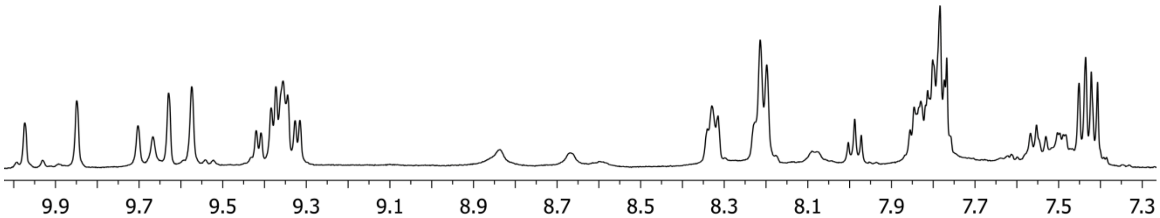

Figure 8.9: Full ^{1}H NMR spectrum of $[(\mathbf{2.6a})_x(\mathbf{2.6d})_y\mathrm{Pd}_2](\mathrm{NO}_3)_4$ (500 MHz, DMSO-d_6, 298 K).

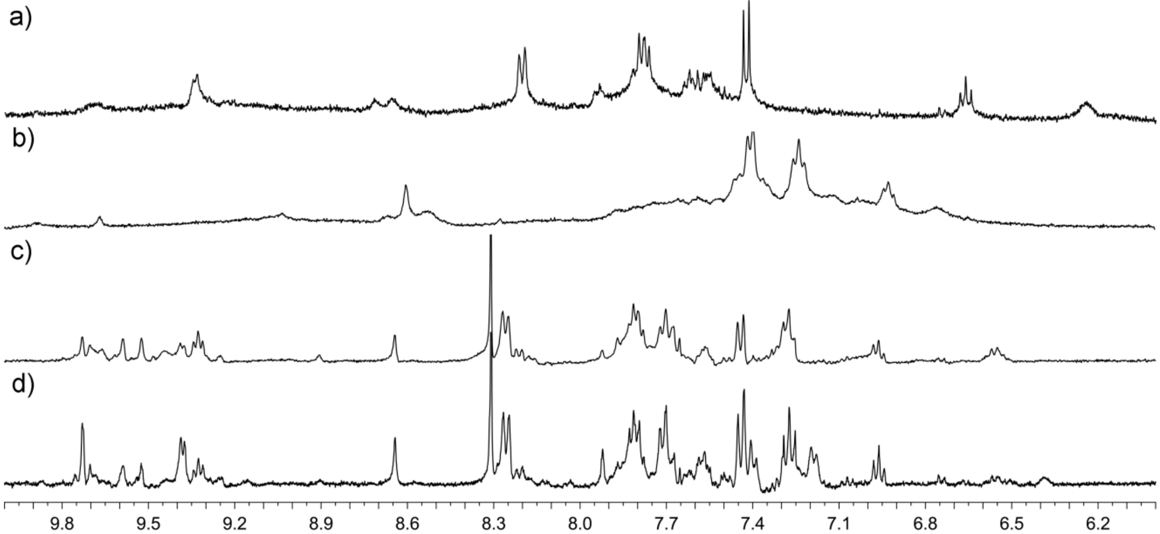

Figure 8.10: ^{1}H NMR spectra of mixing of ligands with different steric properties: a) **2.6a** + **2.9** + $\mathrm{Pd(NO_3)_2}$; b) **2.10** + $\mathrm{Pd(NO_3)_2}$; c) **2.3** + **2.10** + $\mathrm{Pd(NO_3)_2}$ (spectrum acquired after 1 h); d) **2.3** + **2.10** + $\mathrm{Pd(NO_3)_2}$ (spectrum acquired after 1 h) (7 mM, 400 MHz, DMSO-d_6, 298K).

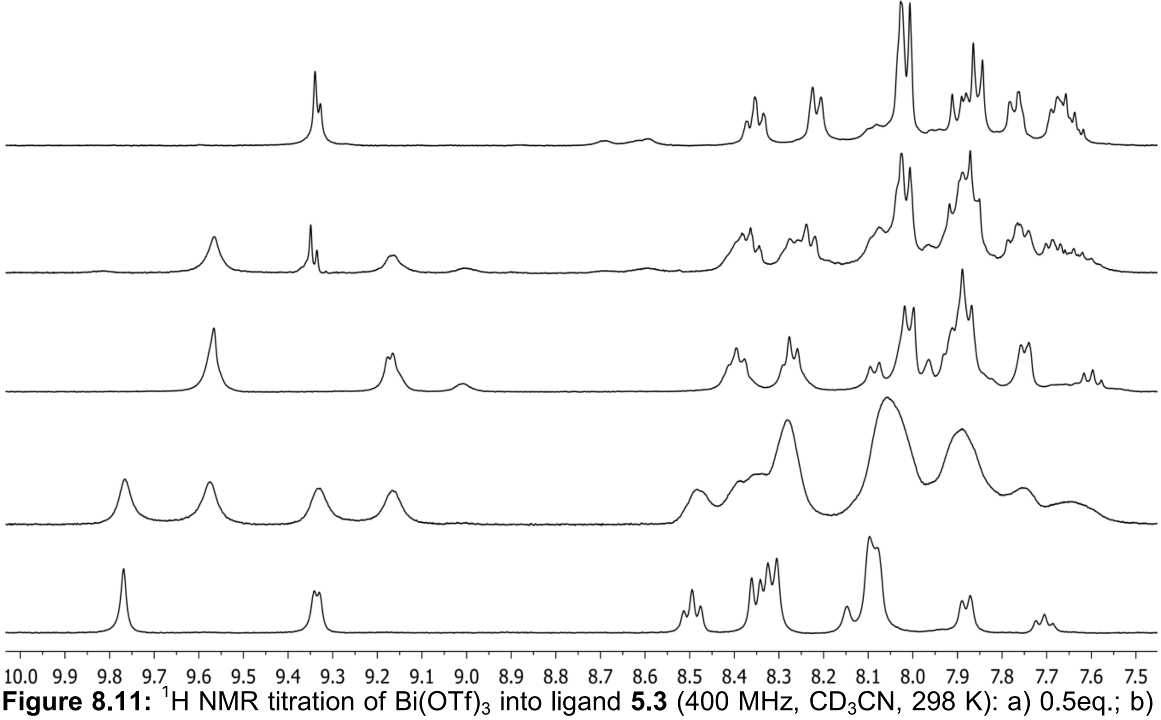

Figure 8.11: ^{1}H NMR titration of $\mathrm{Bi(OTf)_3}$ into ligand **5.3** (400 MHz, $\mathrm{CD_3CN}$, 298 K): a) 0.5eq.; b) 0.67 eq.; c) 1 eq.; d) 2 eq.; e) 3 eq.

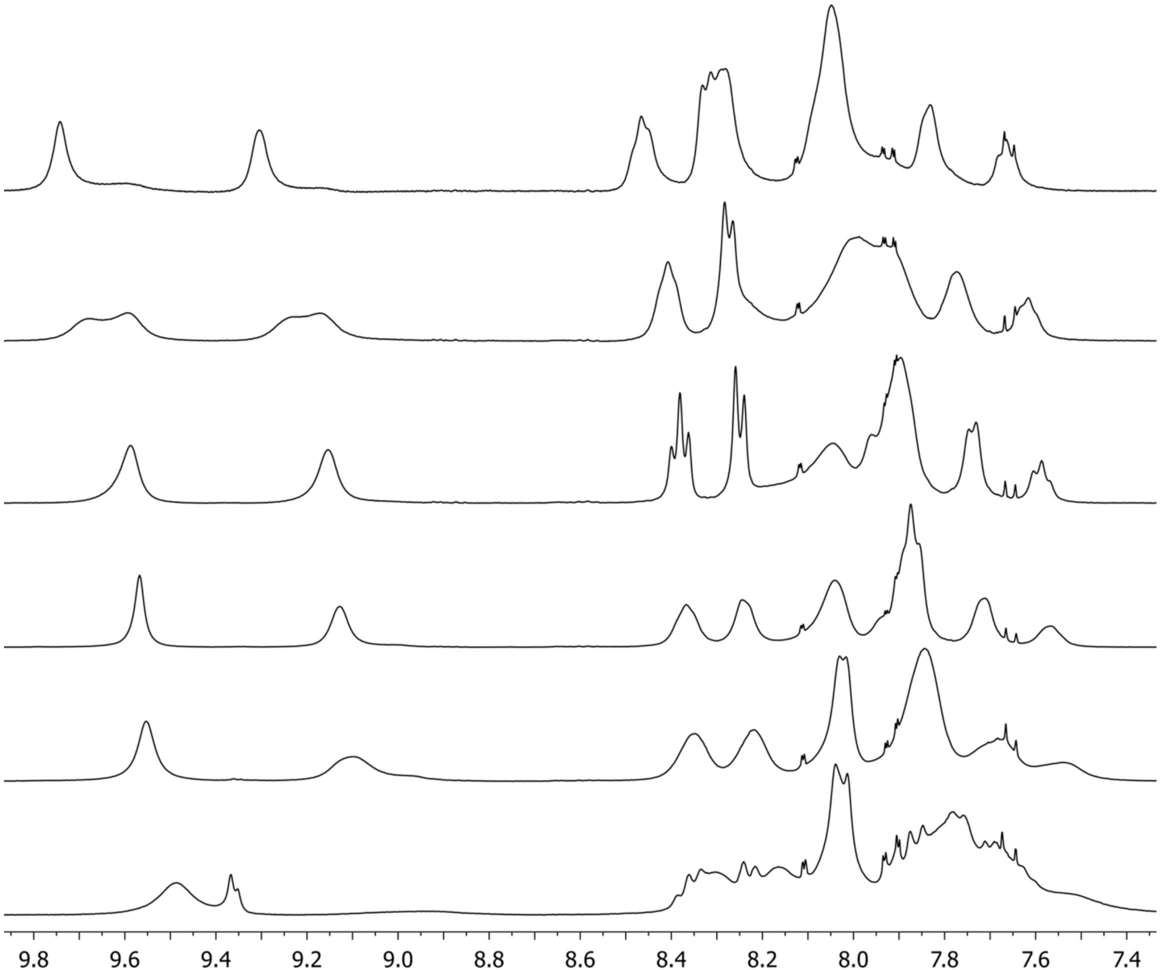

Figure 8.12: ^{1}H NMR titration of ligand **5.3** into [(**5.3**)$_2$Bi$_2$](OTf)$_6$: a) [(**5.3**)$_2$Bi$_2$](OTf)$_6$; b) 1.0 eq; c) 1.8 eq; d) 2.9 eq; e) 4.2 eq; f); 6.0 eq; (CD$_3$CN, 400 MHz, 298 K)

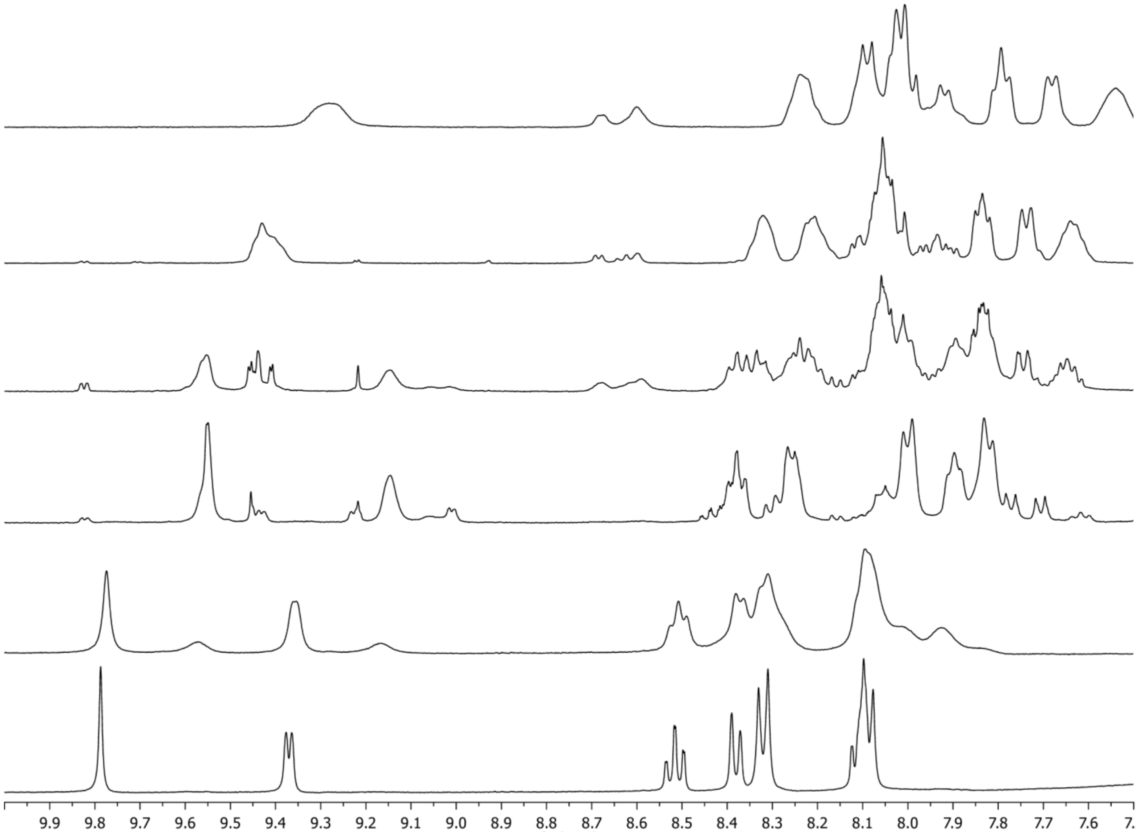

Figure 8.13: ^{1}H NMR titration of Bi(OTf)$_3$ into ligand **5.4**: (a) 0.33 eq; (b) 0.66 eq; (c) 1 eq; (d) 1.5 eq; (e) 2 eq; (f) 3 eq; (CD$_3$CN, 400 MHz, 298 K).

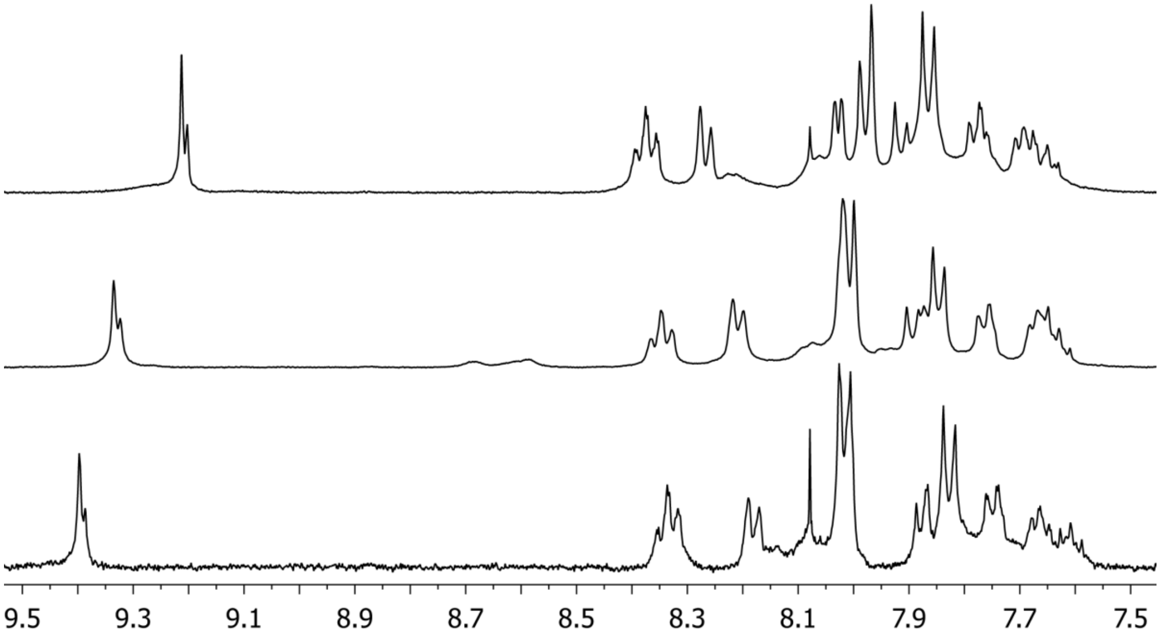

Figure 8.14: Addition of sodium triflate to [(**5.3**)$_2$Bi$_2$](BF$_4$)$_6$: a) [(**5.3**)$_2$Bi$_2$](BF$_4$)$_6$; b) [(**5.3**)$_2$Bi$_2$](OTf)$_6$; c) [(**5.3**)$_2$Bi$_2$](BF$_4$)$_6$ + NaOTf (CD$_3$CN, 400 MHz, 298 K).

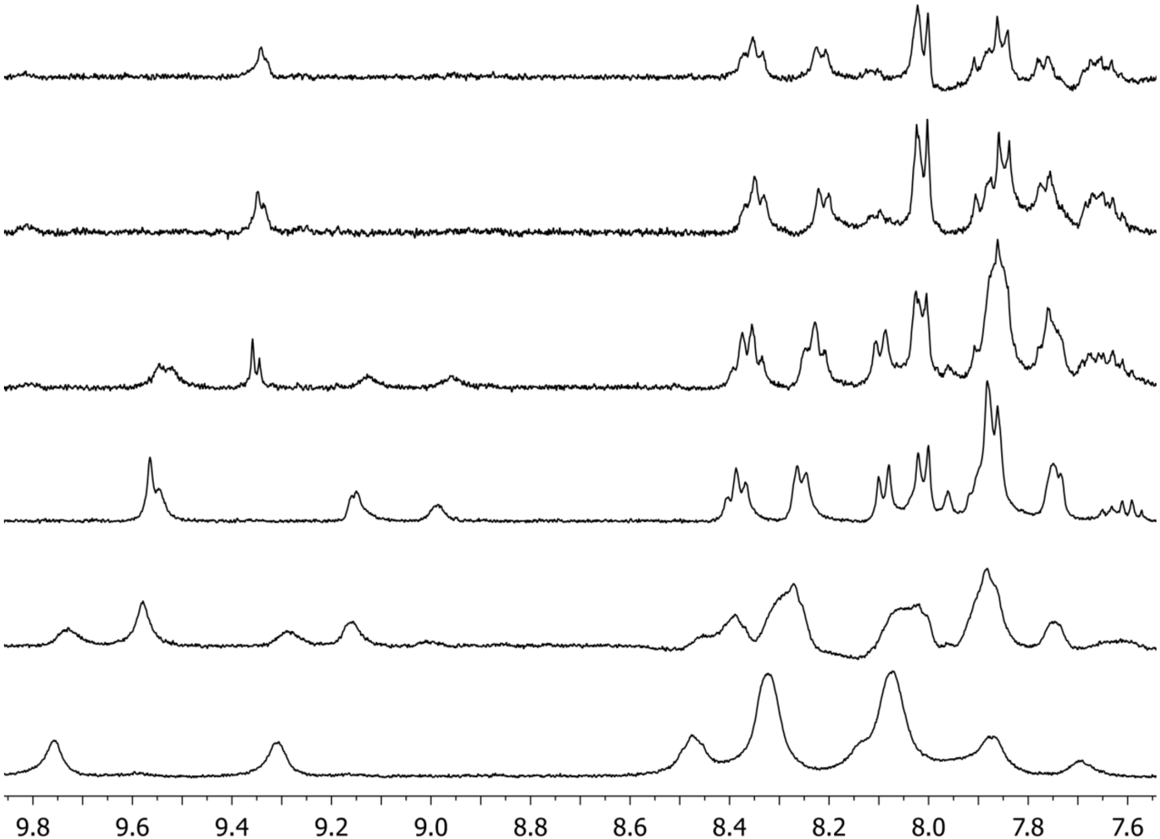

Figure 8.15: ^{1}H NMR titration of Bi(OTf)$_3$ into deprotonated **5.3**: a) 0.5 eq; b) 0.75 eq; c) 1 eq; d) 1.5 eq; e) 3 eq; f) 5 eq; (CD_3CN, 400 MHz, 298 K)

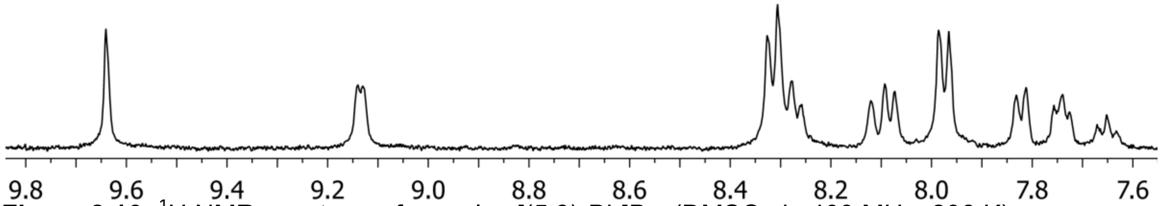

Figure 8.16: ^{1}H NMR spectrum of complex [(**5.3**)$_2$Bi$_2$]Br$_6$ (DMSO-d_6, 400 MHz, 298 K).

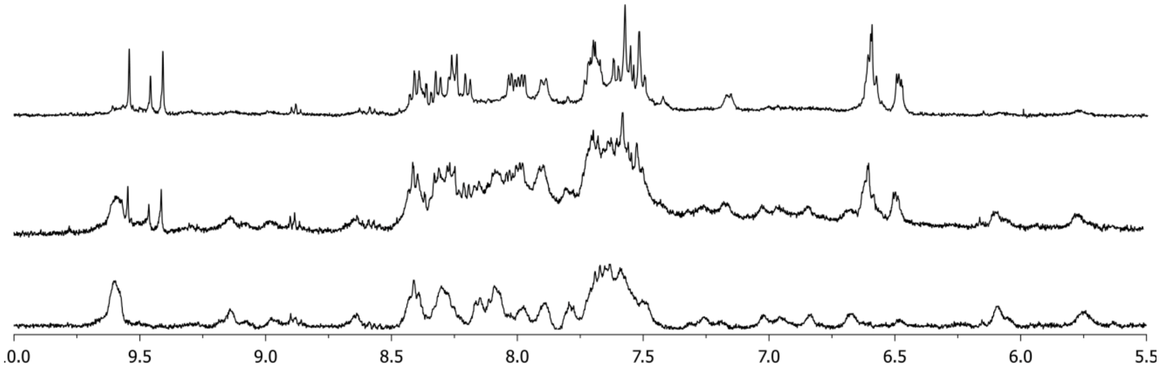

Figure 8.17: ^{1}H NMR titration of Bi(OTf)$_3$ into endohedral urea ligand: a) 0.5 eq.; b) 0.67 eq.; c) 1 eq. (400 MHz, CD_3CN, 298K).

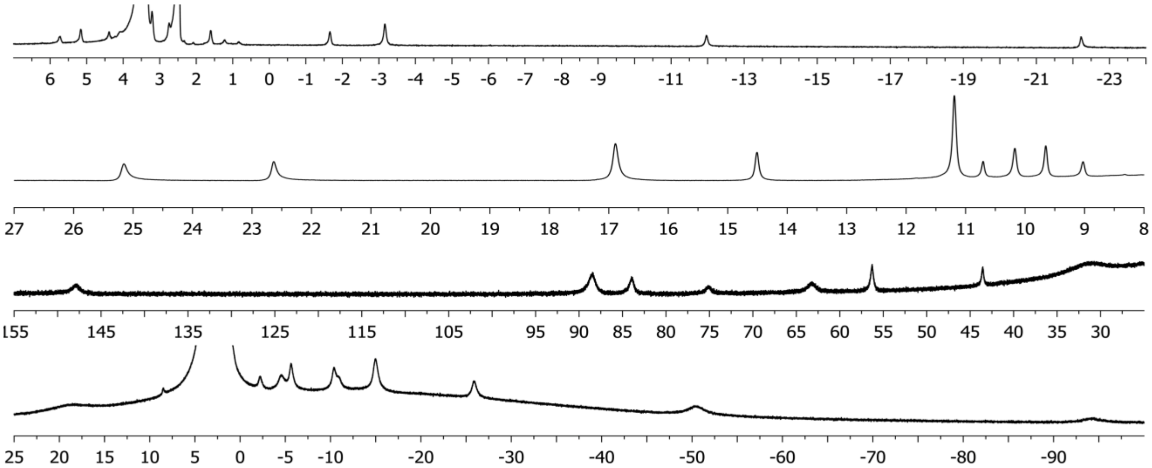

Figure 8.18: ^{1}H NMR spectra of self-assembled lanthanide helical complexes (400 MHz, DMSO-d_6, 298 K): a) $Na_6[(\mathbf{6.3})_3Eu_2]$; b) $Na_6[(\mathbf{6.3})_3Nd_2]$; c) $Na_6[(\mathbf{6.3})_3Dy_2]$; d) $Na_6[(\mathbf{6.3})_3Er_2]$.

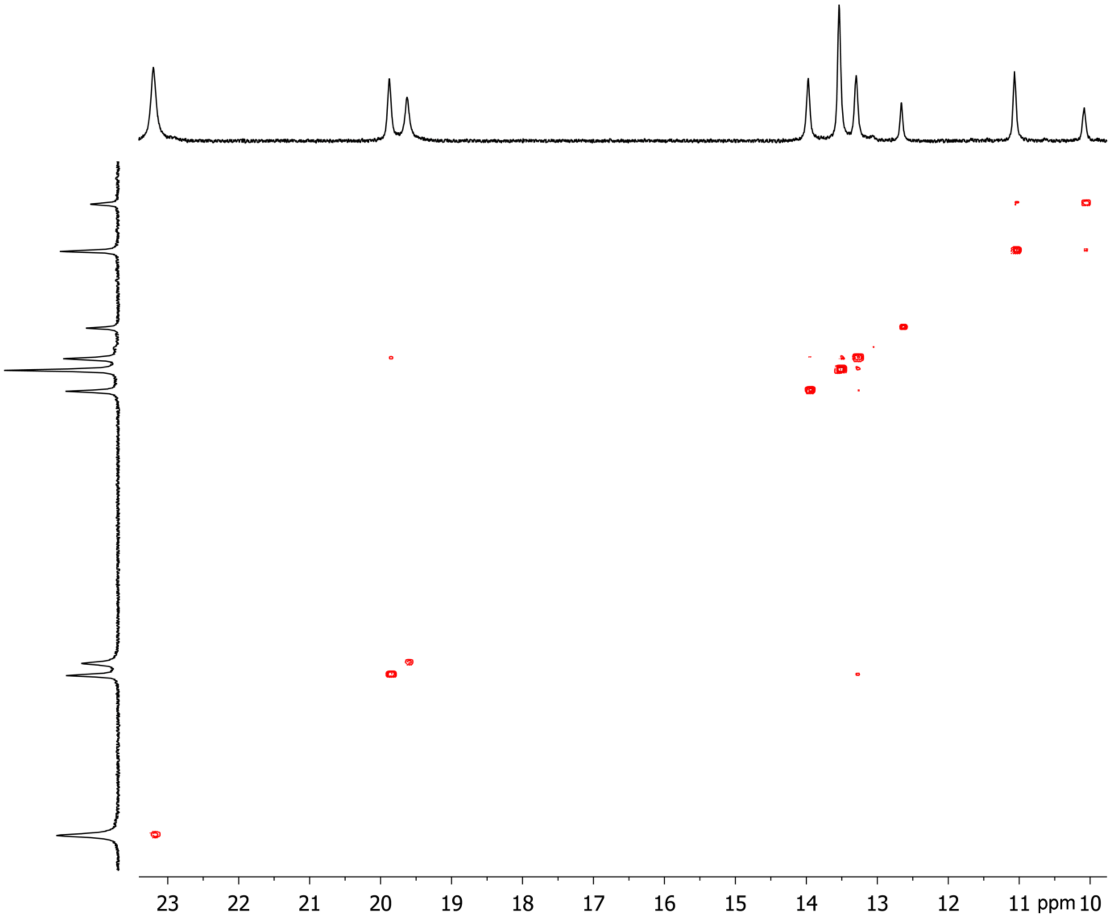

Figure 8.19: COSY NMR spectrum of $Na_6[(\mathbf{6.3})_3Pr_2]$ (400 MHz, DMSO-d_6, 298 K).

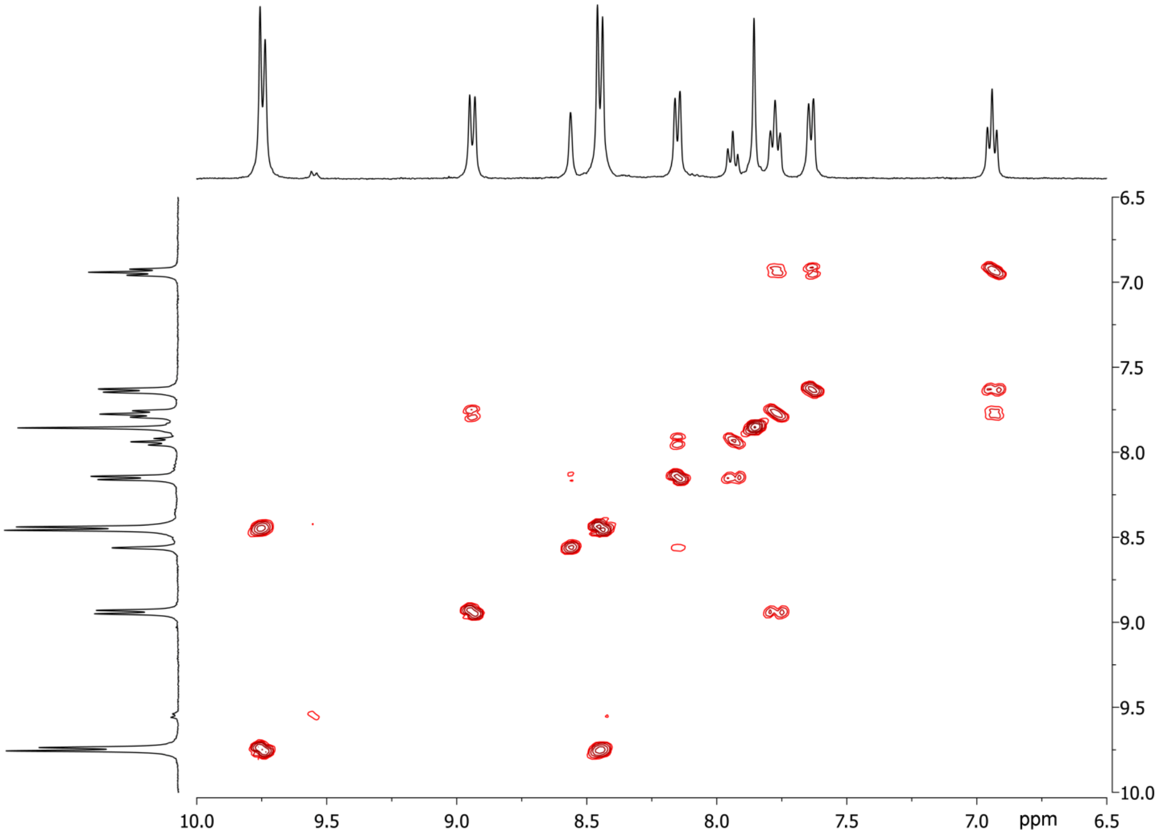

Figure 8.20: COSY NMR spectrum of Na$_6$[(**6.3**)$_3$Sm$_2$] (400 MHz, DMSO-d_6, 298 K).

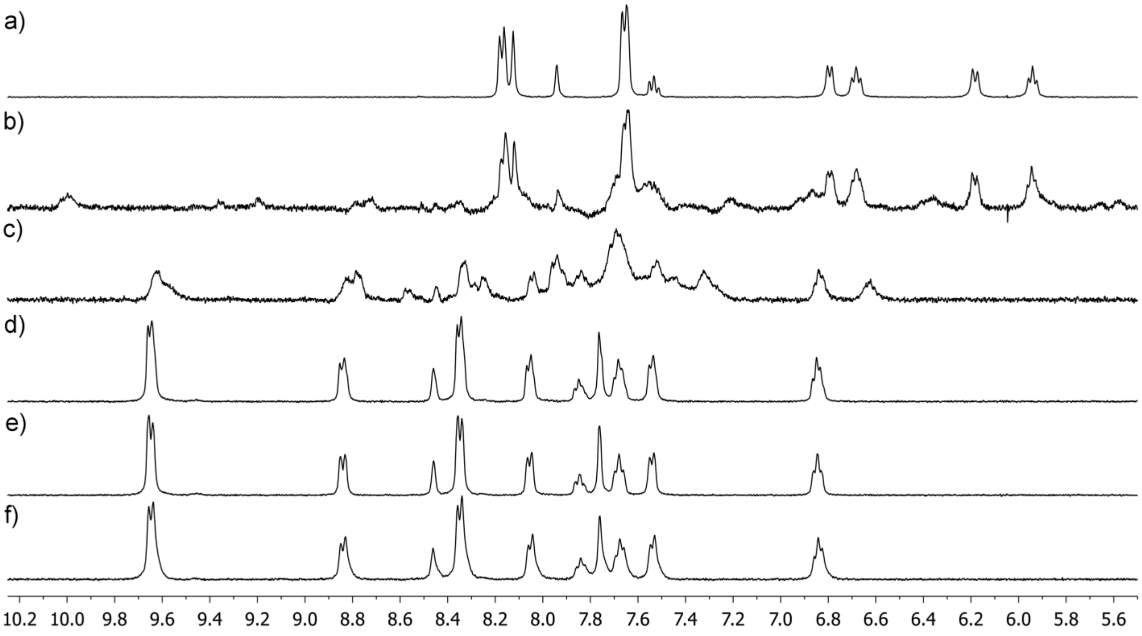

Figure 8.21: Titration of Sm(OTf)$_3$ into **6.3**: a) **6.3**; b) 0.25 eq; c) 0.5 eq; d) 0.75 eq; e) 1 eq; f) 3 eq (400 MHz, DMSO-d_6, 298 K).

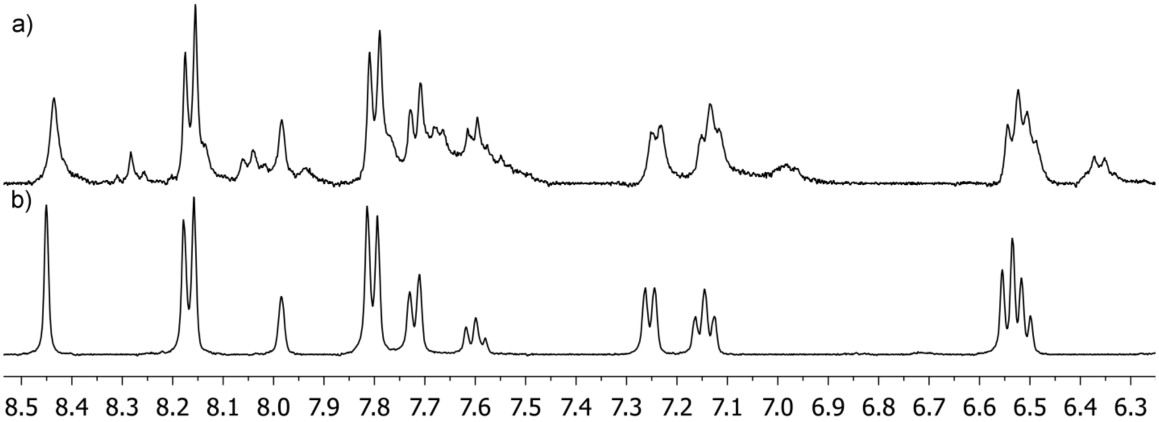

Figure 8.22: Titration of Y(OTf)$_3$ into **6.3**: a) 0.67 eq; b) 1 eq (400 MHz, DMSO-d_6, 298 K).

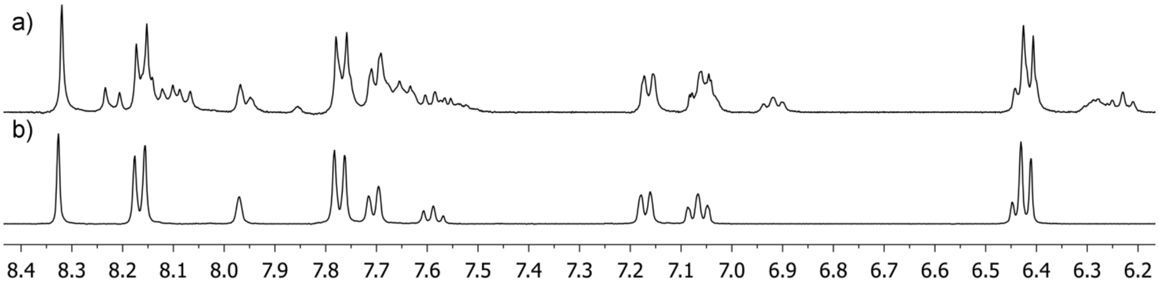

Figure 8.23: Titration of La(OTf)$_3$ into **6.3**: a) 0.67 eq; b) 1 eq (400 MHz, DMSO-d_6, 298 K).

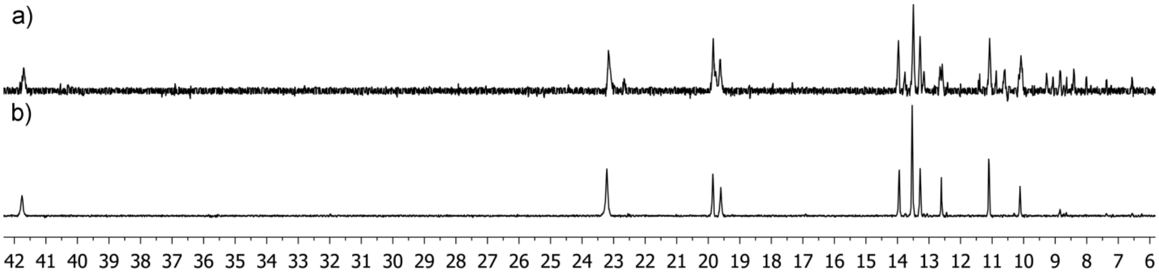

Figure 8.24: Titration of Pr(OTf)$_3$ into **6.3**: a) 0.67 eq; b) 1 eq (400 MHz, DMSO-d_6, 298 K).

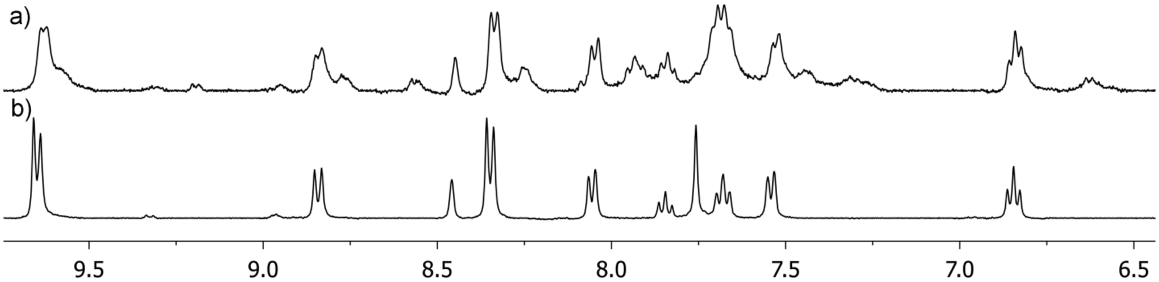

Figure 8.25: Titration of Sm(OTf)$_3$ into **6.3**: a) 0.67 eq; b) 1 eq (400 MHz, DMSO-d_6, 298 K).

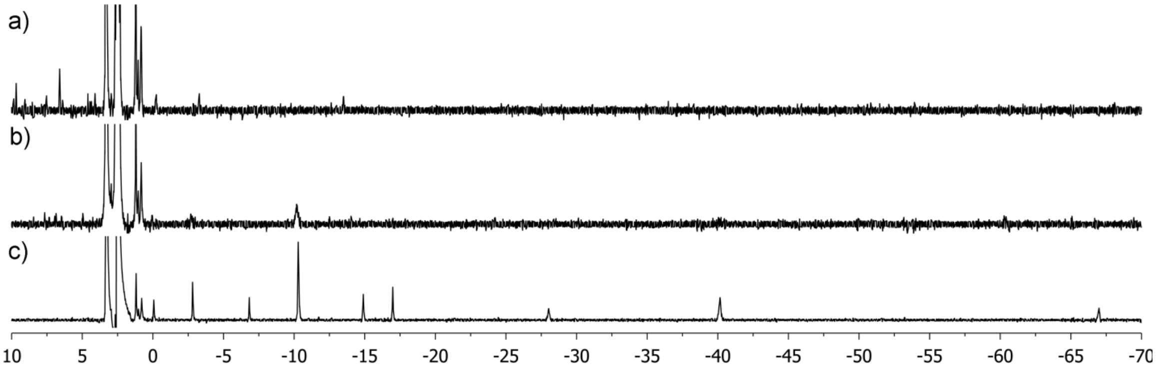

Figure 8.26: Titration of Yb(OTf)$_3$ into **6.3**: a) 0.67 eq; b) 1 eq; c) 1.33 eq (400 MHz, DMSO-d_6, 298 K).

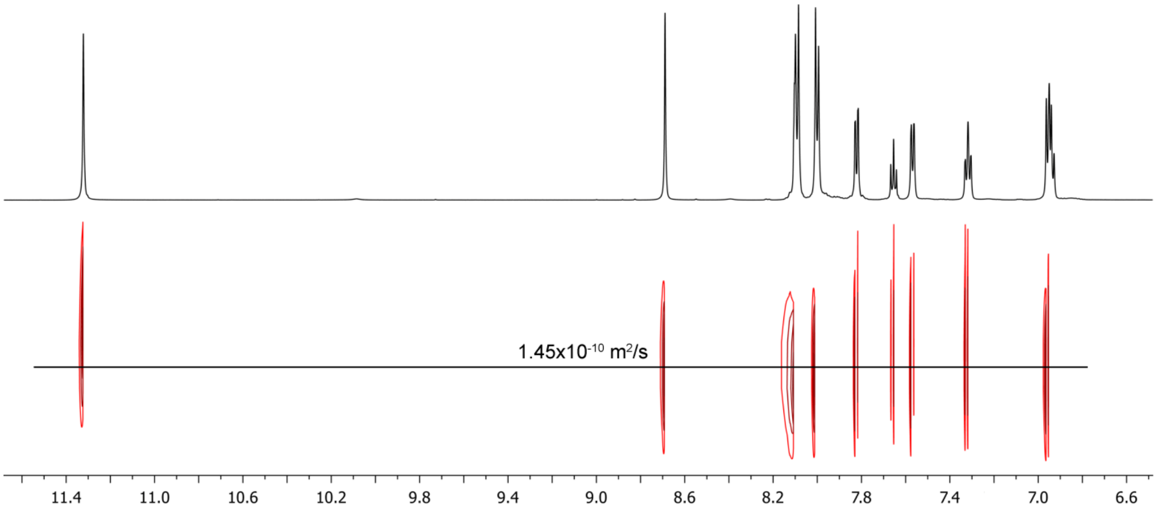

Figure 8.27: DOSY spectrum of ligand **6.2** (600 MHz, DMSO-d_6, 298 K, Δ=120 ms, δ=4.0 ms, Diffusion coefficient =1.45x10^{-10} ± 0.59x10^{-10} m^2/s for **6.2** and 6.07x10^{-10} m^2/s for DMSO-d_6).

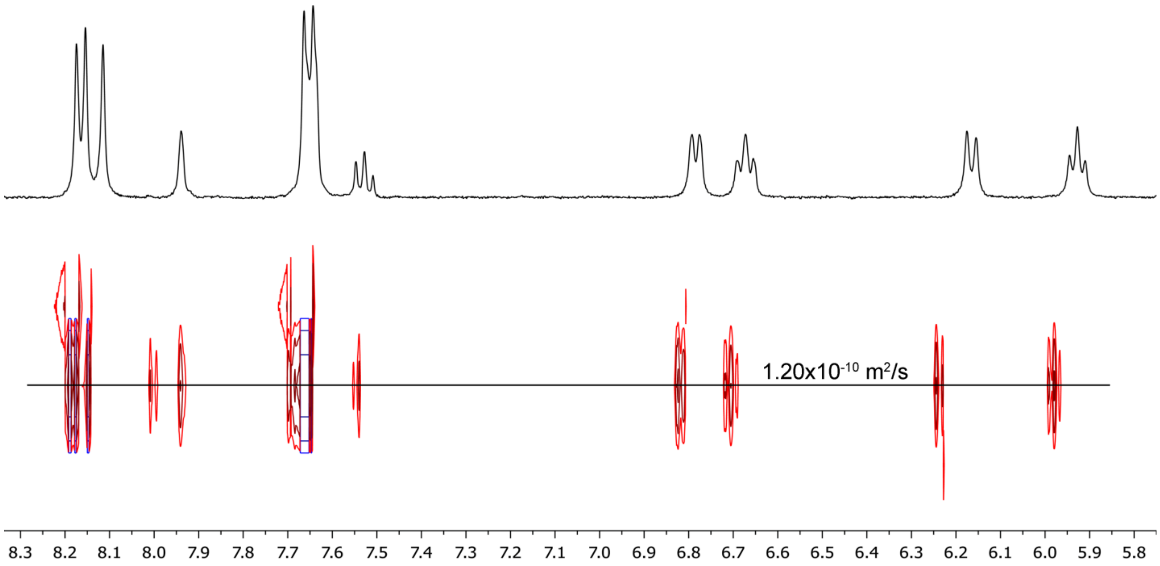

Figure 8.28: DOSY spectrum of ligand **6.3** (600 MHz, DMSO-d_6, 298 K, Δ=100 ms, δ=5.3 ms, Diffusion coefficient =$1.20\times10^{-10} \pm 0.51\times10^{-10}$ m^2/s for **6.3** and 8.13×10^{-10} m^2/s for DMSO-d_6).

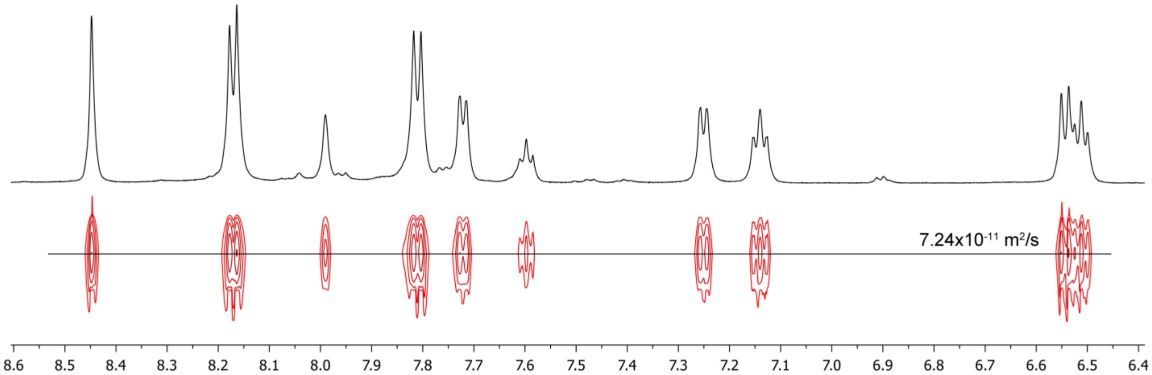

Figure 8.29: DOSY spectrum of $Na_6[(\mathbf{6.3})_3Y_2]$ (600 MHz, DMSO-d_6, 298 K, Δ=100 ms, δ=6.6 ms, Diffusion coefficient =$7.24\times10^{-11} \pm 2.8\times10^{-11}$ m^2/s for $Na_6[(\mathbf{6.3})_3Y_2]$ and 4.27×10^{-10} m^2/s for DMSO-d_6).

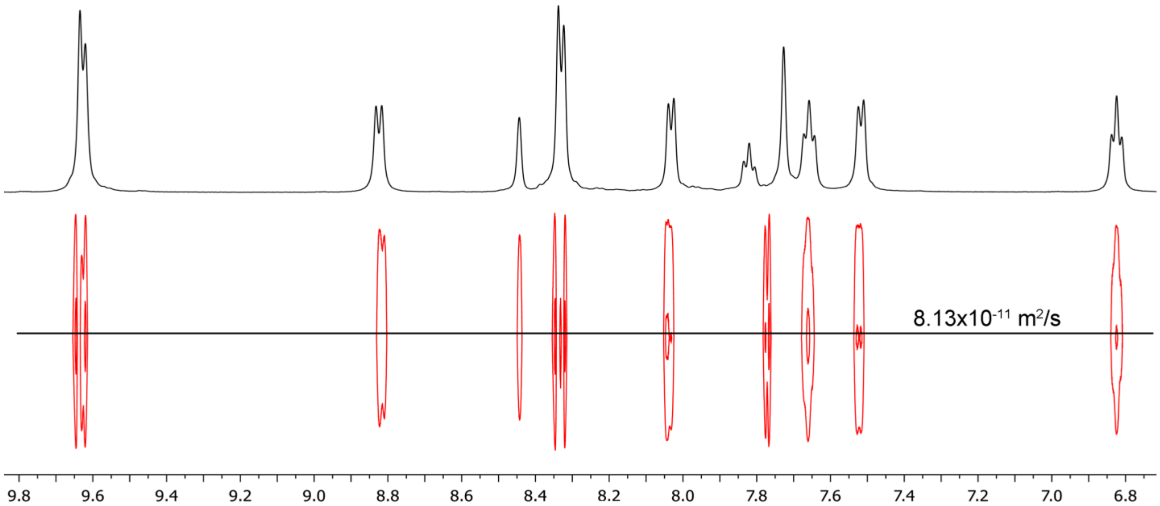

Figure 8.30: DOSY spectrum of $Na_6[(\mathbf{6.3})_3Sm_2]$ (600 MHz, DMSO-d_6, 298 K, Δ=100 ms, δ=6.6 ms, Diffusion coefficient =8.13×10^{-11} ±3.4×10^{-11} m^2/s for $Na_6[(\mathbf{6.3})_3Sm_2]$ and 4.27×10^{-10} m^2/s for DMSO-d_6).

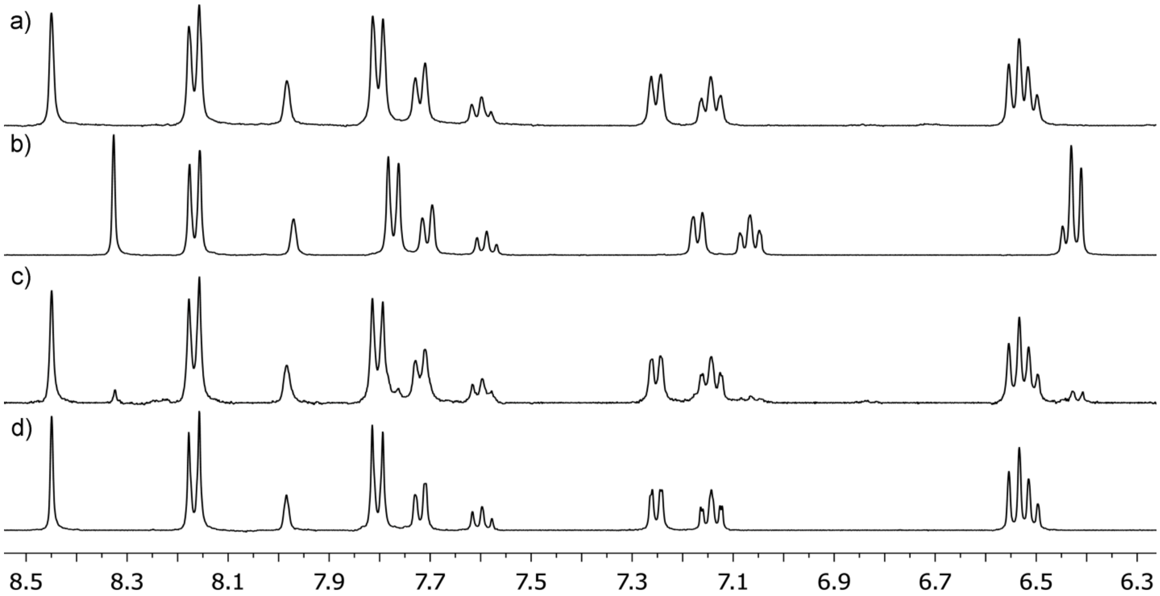

Figure 8.31: Displacement of La by Y: a) $Na_6[(\mathbf{6.3})_3Y_2]$; b) $Na_6[(\mathbf{6.3})_3La_2]$; c) $Na_6[(\mathbf{6.3})_3Y_2]$ + 1.33 eq $La(OTf)_3$; d) $Na_6[(\mathbf{6.3})_3La_2]$ + 1.33 eq $Y(OTf)_3$ (400 MHz, DMSO-d_6, 298 K).

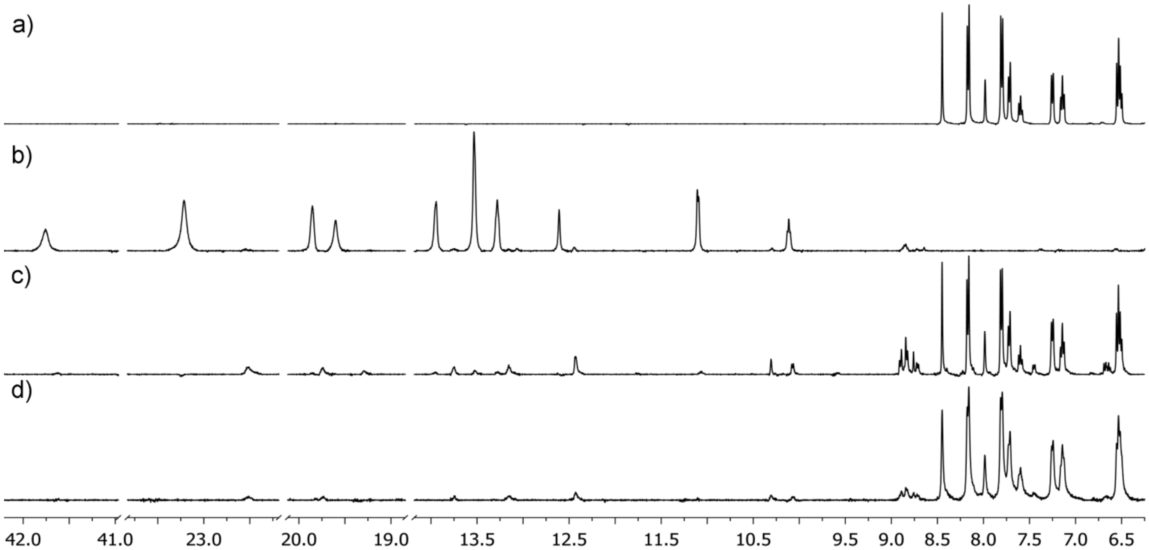

Figure 8.32: Displacement of Pr by Y: a) $Na_6[(\mathbf{6.3})_3Y_2]$; b) $Na_6[(\mathbf{6.3})_3Pr_2]$; c) $Na_6[(\mathbf{6.3})_3Y_2]$ + 1.33 eq $Pr(OTf)_3$; d) $Na_6[(\mathbf{6.3})_3Pr_2]$ + 1.33 eq $Y(OTf)_3$ (400 MHz, DMSO-d_6, 298 K).

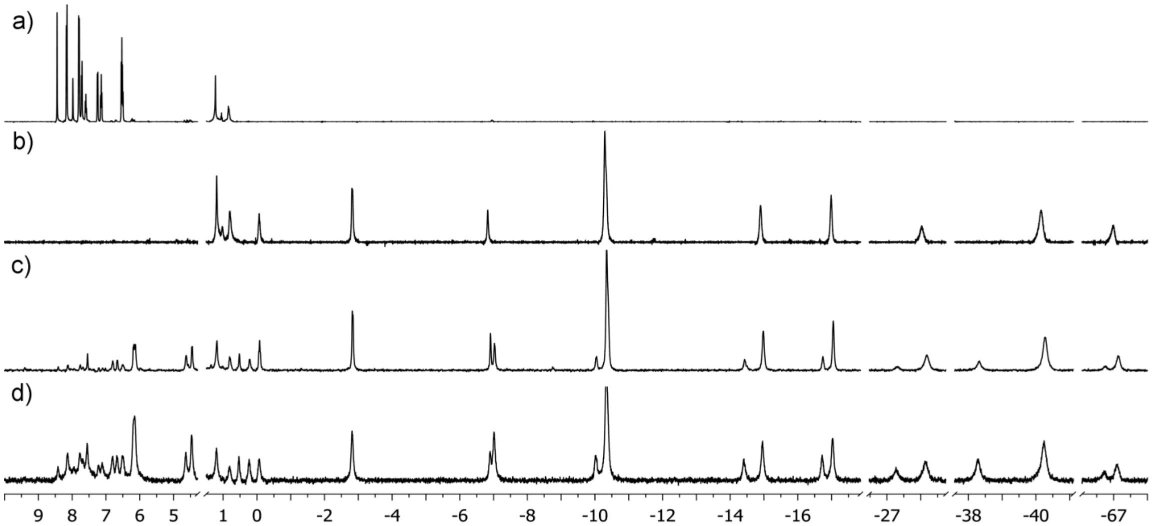

Figure 8.33: Displacement of Y by Yb: a) $Na_6[(\mathbf{6.3})_3Y_2]$; b) $Na_2[(\mathbf{6.3})_2Yb_2]$; c) $Na_6[(\mathbf{6.3})_3Y_2]$ + 1.33 eq $Yb(OTf)_3$; d) $Na_2[(\mathbf{6.3})_2Yb_2]$ + 1.33 eq $Y(OTf)_3$ (400 MHz, DMSO-d_6, 298 K).

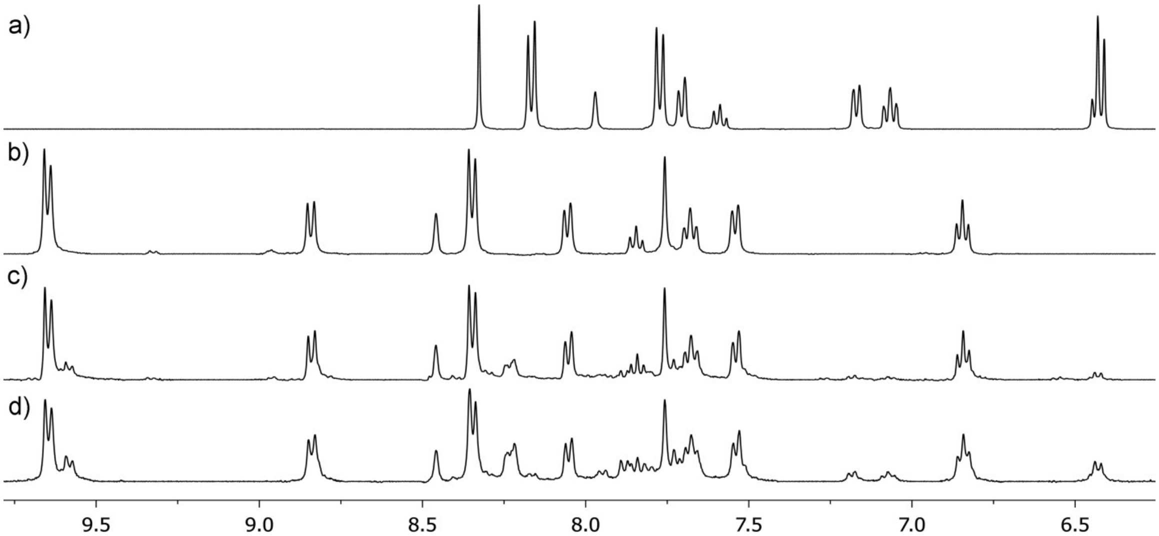

Figure 8.34: Displacement of La by Sm: a) $Na_6[(\mathbf{6.3})_3La_2]$; b) $Na_6[(\mathbf{6.3})_3Sm_2]$; c) $Na_6[(\mathbf{6.3})_3La_2]$ + 1.33 eq $Sm(OTf)_3$; d) $Na_6[(\mathbf{6.3})_3Sm_2]$ + 1.33 eq $La(OTf)_3$ (400 MHz, DMSO-d_6, 298 K).

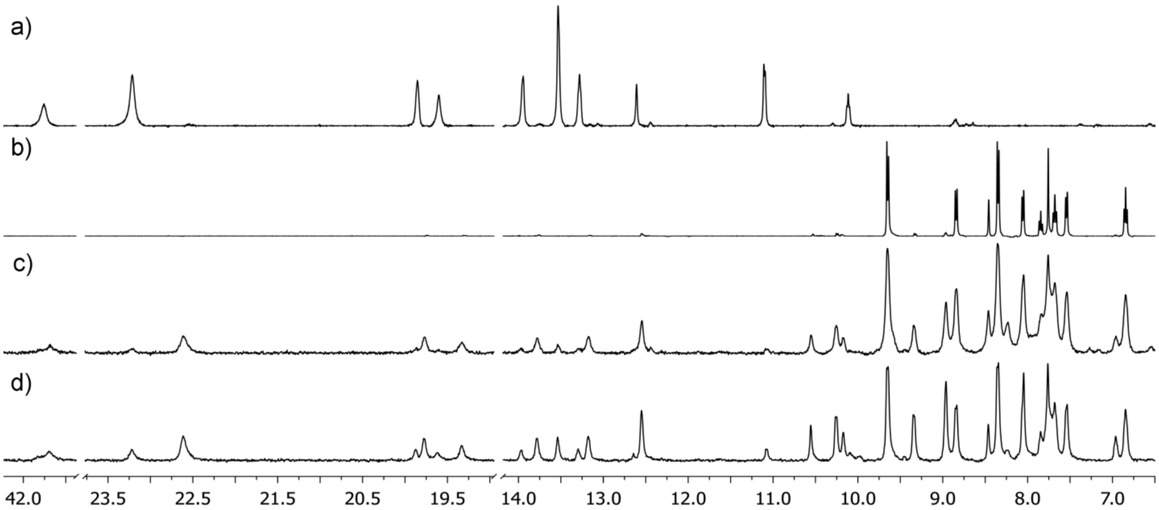

Figure 8.35: Displacement of Pr by Sm: a) $Na_6[(\mathbf{6.3})_3Pr_2]$; b) $Na_6[(\mathbf{6.3})_3Sm_2]$; c) $Na_6[(\mathbf{6.3})_3Pr_2]$ + 1.33 eq $Sm(OTf)_3$; d) $Na_6[(\mathbf{6.3})_3Sm_2]$ + 1.33 eq $Pr(OTf)_3$ (400 MHz, DMSO-d_6, 298 K).

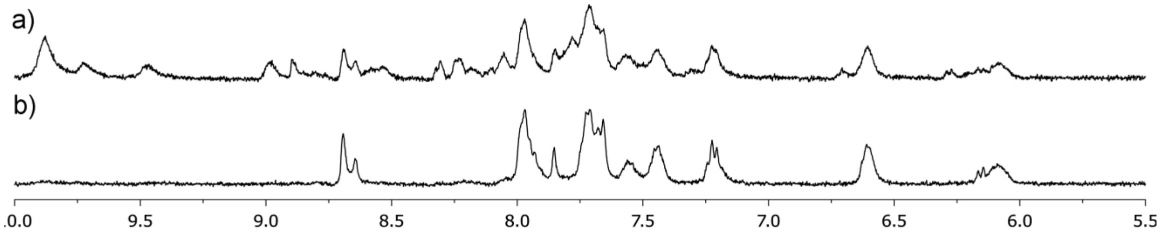

Figure 8.36: Titration of $Ce(OTf)_4$ into **6.3**: a) 0.67 eq; b) 1 eq (400 MHz, DMSO-d_6, 298 K).

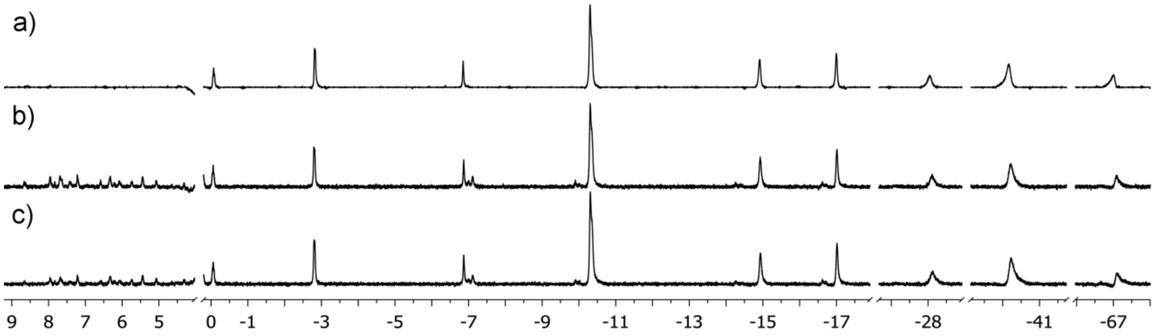

Figure 8.37: Displacement of Ce by Yb: a) $Na_2[(\mathbf{6.3})_2Yb_2]$; b) $Na_2[(\mathbf{6.3})_2Ce_2]$ + 1.33 eq $Yb(OTf)_3$; c) $Na_2[(\mathbf{6.3})_2Yb_2]$ + 1.33 eq $Ce(OTf)_4$ (400 MHz, DMSO-d_6, 298 K).

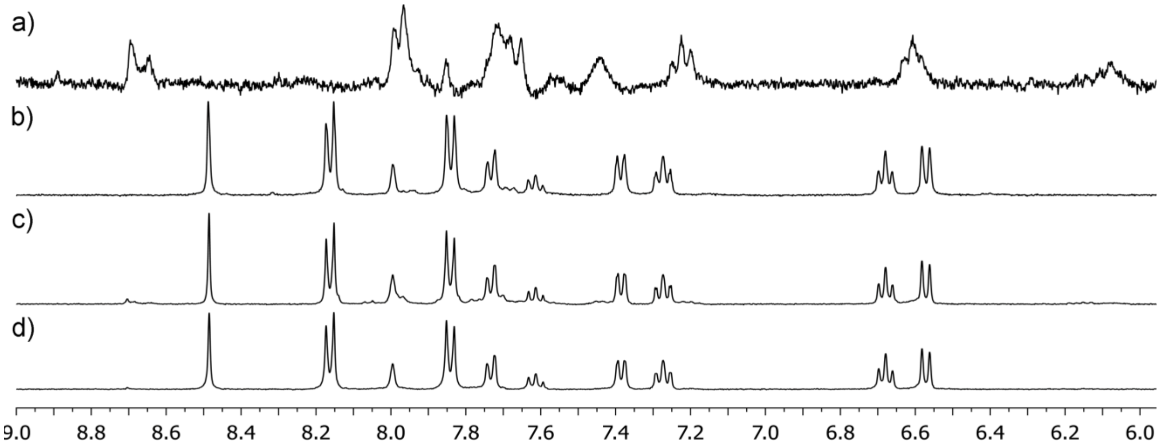

Figure 8.38: Displacement of Ce by Th: a) $Na_2[(\mathbf{6.3})_2Ce_2]$; b) $Na_6[(\mathbf{6.3})_2Th_2]$; c) $Na_2[(\mathbf{6.3})_2Ce_2]$ + 1.33 eq $Th(NO_3)_4$; d) $Na_6[(\mathbf{6.3})_3Th_2]$ + 1.33 eq $Ce(OTf)_4$ (400 MHz, DMSO-d_6, 298 K).

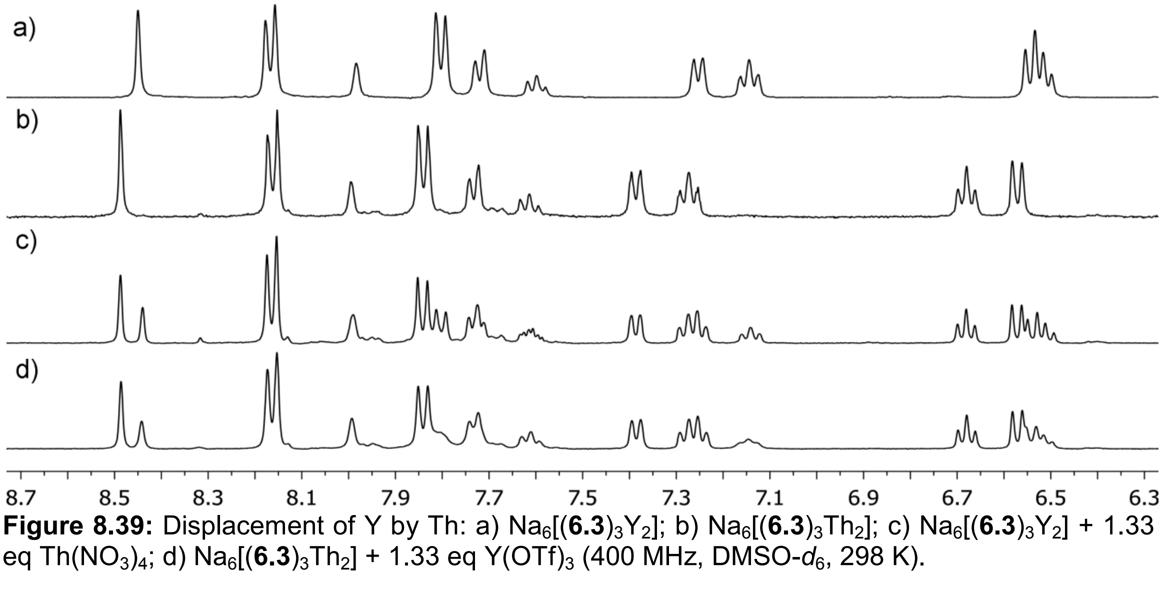

Figure 8.39: Displacement of Y by Th: a) $Na_6[(\mathbf{6.3})_3Y_2]$; b) $Na_6[(\mathbf{6.3})_3Th_2]$; c) $Na_6[(\mathbf{6.3})_3Y_2]$ + 1.33 eq $Th(NO_3)_4$; d) $Na_6[(\mathbf{6.3})_3Th_2]$ + 1.33 eq $Y(OTf)_3$ (400 MHz, DMSO-d_6, 298 K).

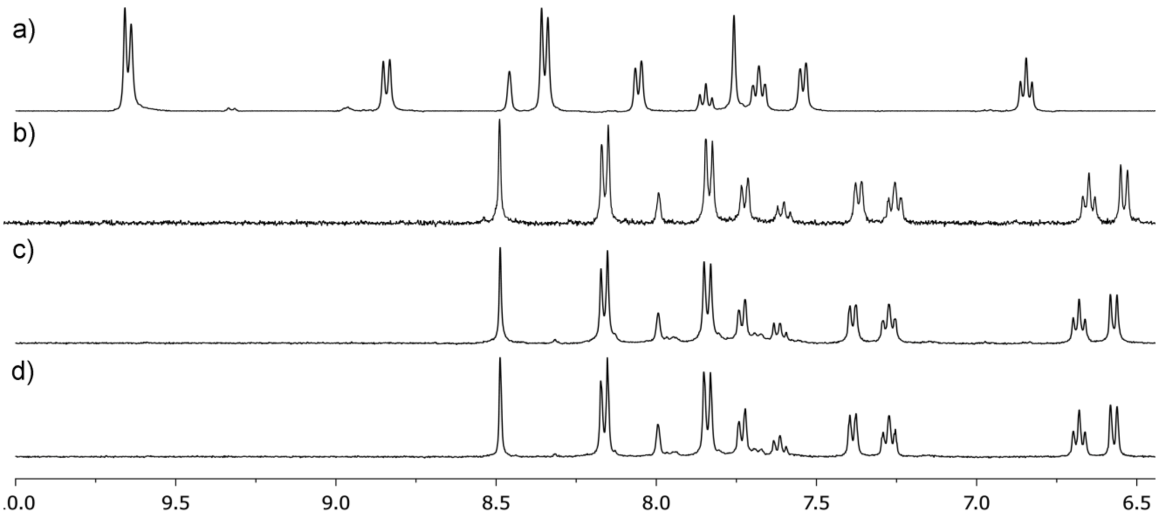

Figure 8.40: Displacement of Sm by Th: a) $Na_6[(\textbf{6.3})_3Sm_2]$; b) $Na_6[(\textbf{6.3})_3Th_2]$; c) $Na_6[(\textbf{6.3})_3Sm_2]$ + 1.33 eq $Th(NO_3)_4$; d) $Na_6[(\textbf{6.3})_3Th_2]$+ 1.33 eq $Sm(OTf)_3$ (400 MHz, DMSO-d_6, 298 K).

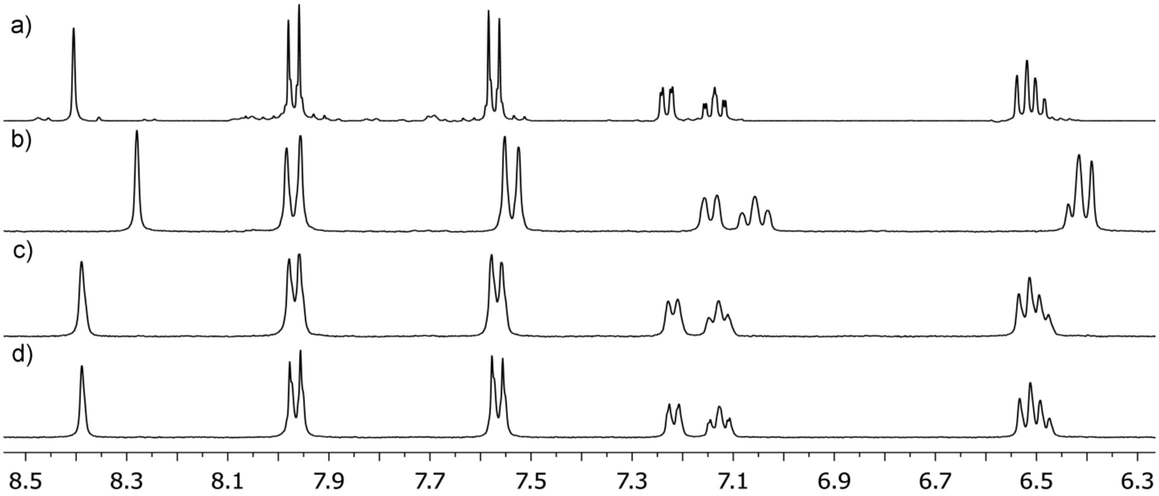

Figure 8.41: Displacement of La by Y: a) $Na_3[(\textbf{6.5})_3Y]$; b) $Na_3[(\textbf{6.5})_3La]^-$; c) $Na_3[(\textbf{6.5})_3Y]$ + 0.67 eq $La(OTf)_3$; d) $Na_3[(\textbf{6.5})_3La]$ + 0.67 eq $Y(OTf)_3$ (400 MHz, DMSO-d_6, 298 K).

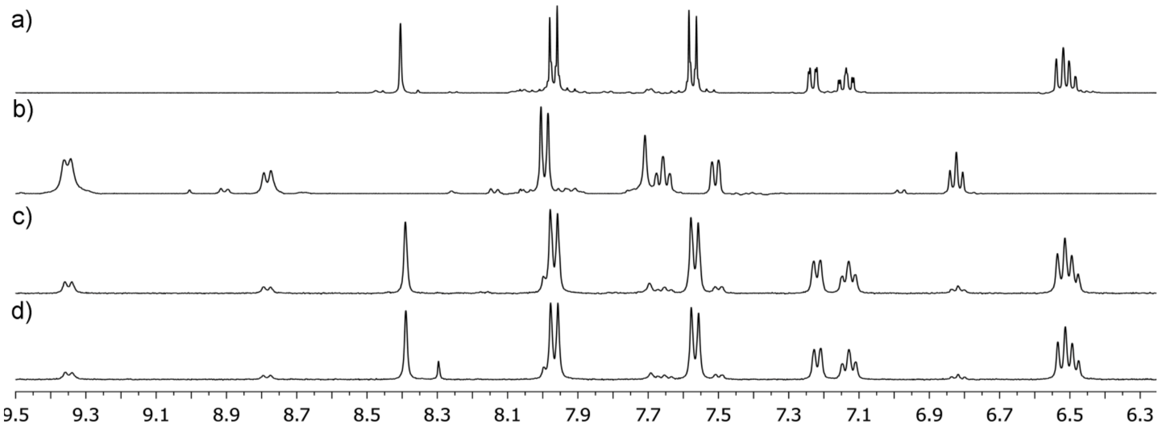

Figure 8.42: Displacement of Sm by Y: a) Na$_3$[(**6.5**)$_3$Y]; b) Na$_3$[(**6.5**)$_3$Sm]; c) Na$_3$[(**6.5**)$_3$Y] + 0.67 eq Sm(OTf)$_3$; d) Na$_3$[(**6.5**)$_3$Sm] + 0.67 eq Y(OTf)$_3$ (400 MHz, DMSO-d_6, 298 K).

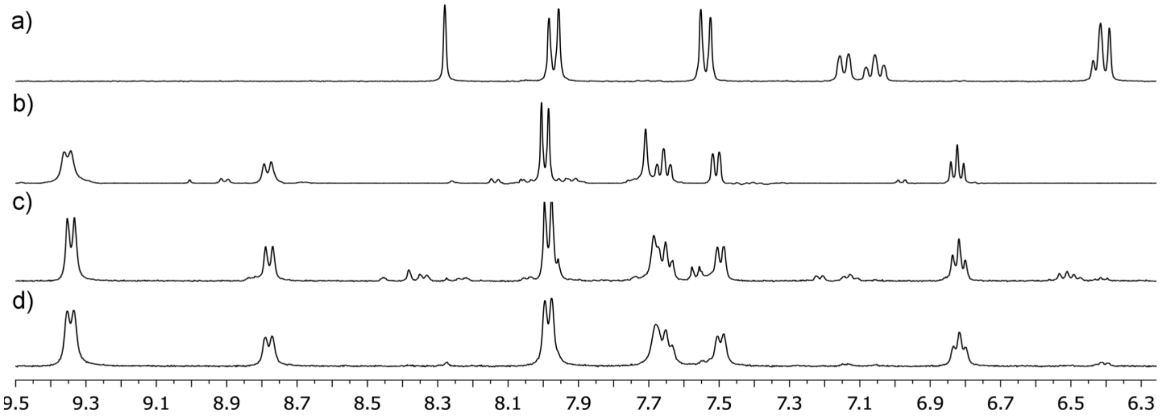

Figure 8.43: Displacement of La by Sm: a) Na$_3$[(**6.5**)$_3$La]; b) Na$_3$[(**6.5**)$_3$Sm]; c) Na$_3$[(**6.5**)$_3$La] + 0.67 eq Sm(OTf)$_3$; d) Na$_3$[(**6.5**)$_3$Sm] + 0.67 eq La(OTf)$_3$ (400 MHz, DMSO-d_6, 298 K).

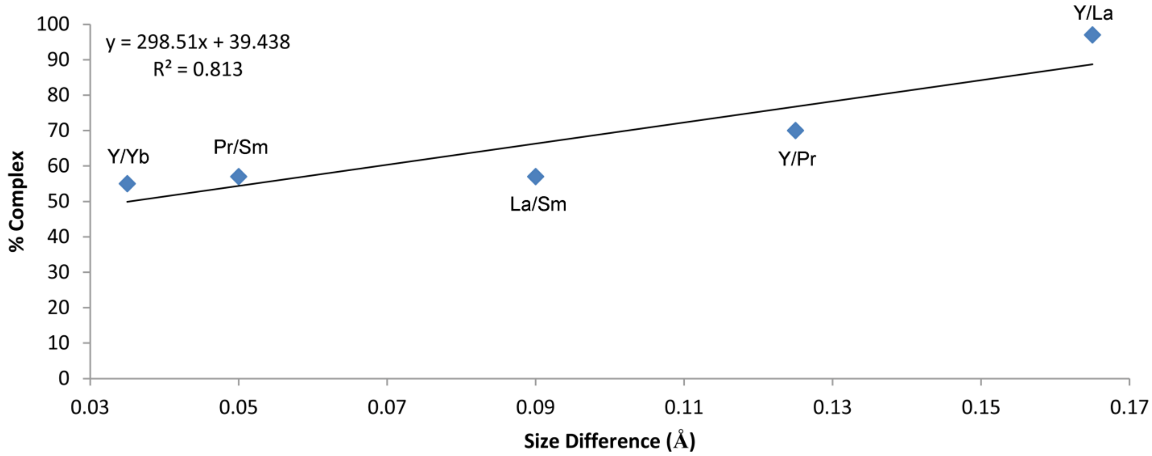

Figure 8.44: Graph of percent Na$_x$[(**6.3**)$_y$Ln(small)$_2$] versus effective ionic radius difference in displacement experiments with Na$_x$[(**6.3**)$_y$Ln$_2$].

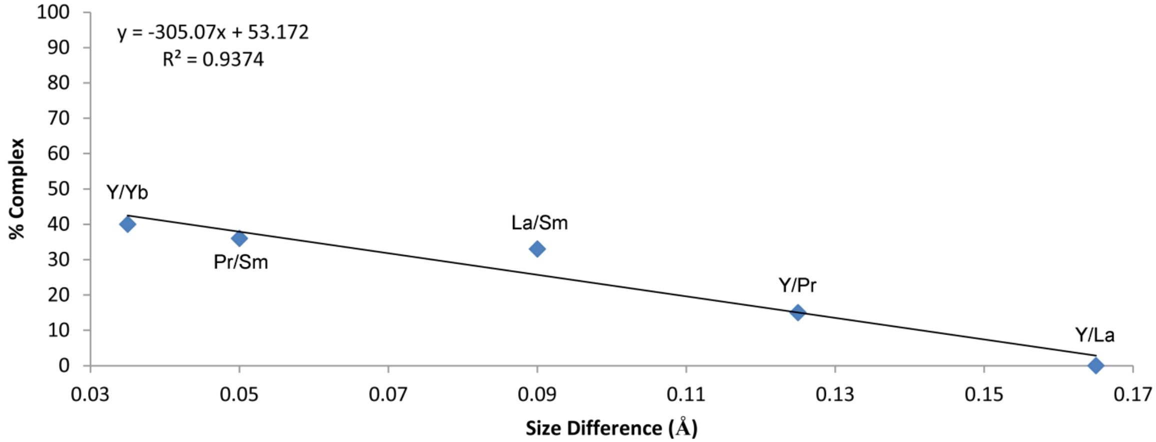

Figure 8.45: Graph of percent $Na_x[(\mathbf{6.3})_yLn^ALn^B]$ versus effective ionic radius difference in displacement experiments with $Na_x[(\mathbf{6.3})_yLn_2]$.

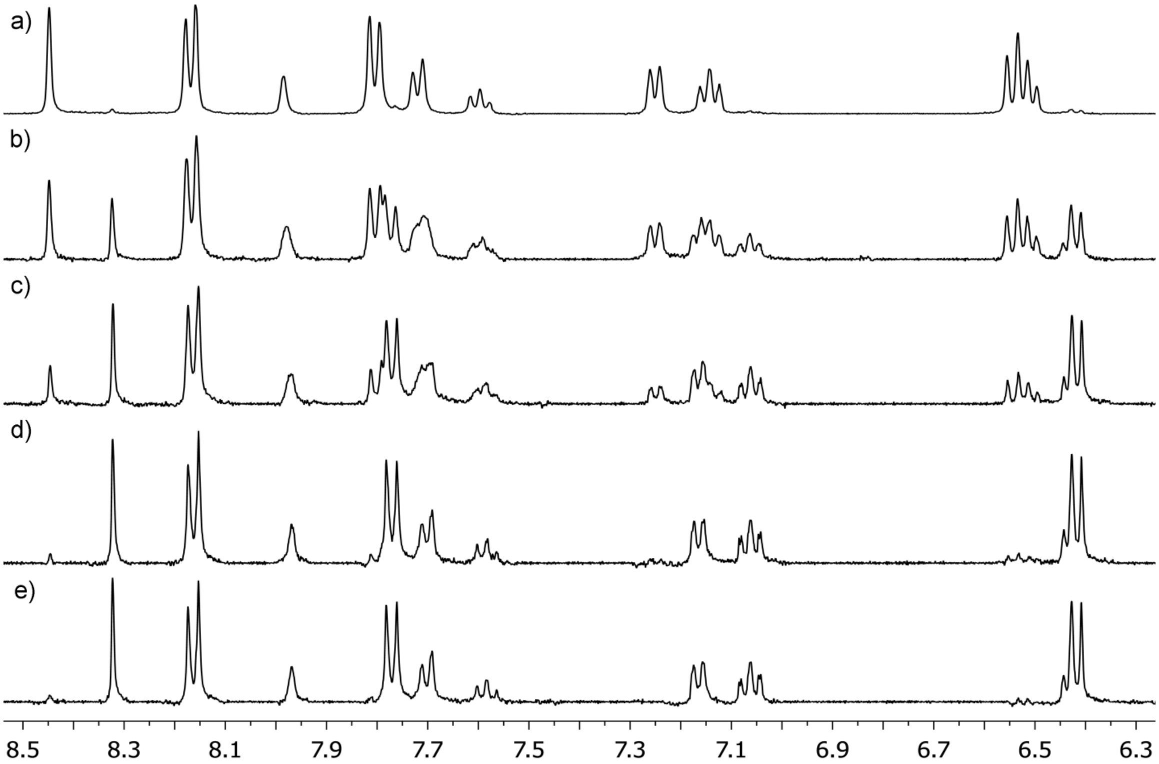

Figure 8.46: Equilibration of $Na_6[(\mathbf{6.3})_3Y_2]$ and $Na_6[(\mathbf{6.3})_3La_2]$: a) 0 h; b) 3.97 h; c)8.75 h; d) 23.95 h; e) 30.43 h (400 MHz, DMSO-d_6, 298 K).

time (h)	$Na_6[(\mathbf{6.3})_3Y_2]$ (mM)	$Na_6[(\mathbf{6.3})_3La_2]$ (mM)
0	3.70	0.15
3.97	2.39	1.46
8.75	1.23	2.62
23.95	0.19	3.66
30.43	0.23	3.62

Table 8.3: Concentration of $Na_6[(\mathbf{6.3})_3Y_2]$ and $Na_6[(\mathbf{6.3})_3La_2]$ versus time.

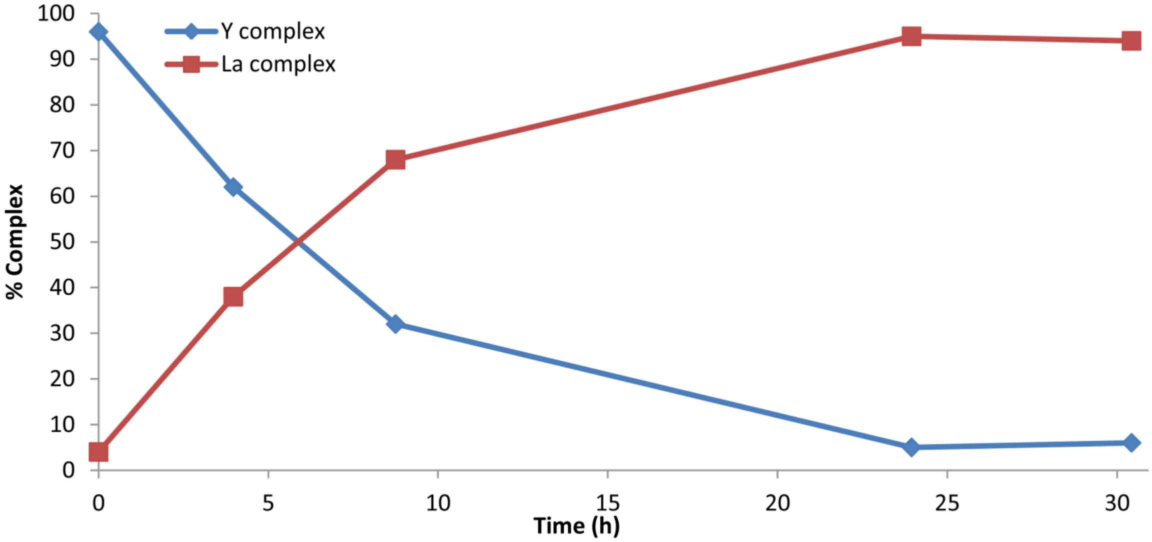

Figure 8.47: Graph of percent ligand versus time in equilibration of $Na_6[(\mathbf{6.3})_3Y_2]$ and $Na_6[(\mathbf{6.3})_3La_2]$.

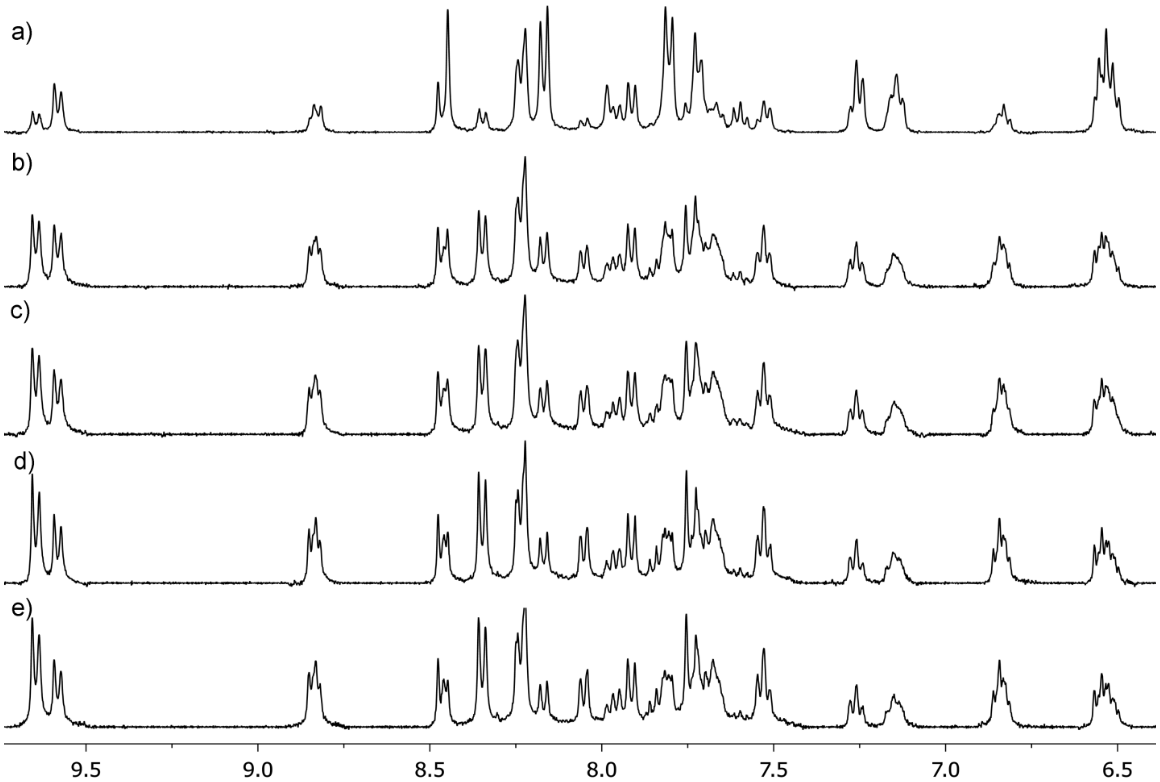

Figure 8.48: Equilibration of $Na_6[(\mathbf{6.3})_3Y_2]$ and $Na_6[(\mathbf{6.3})_3Sm_2]$: a) 0 h; b) 3.95 h; c) 8.73 h; d) 23.93 h; e) 30.42 h (400 MHz, DMSO-d_6, 298 K).

time (h)	$Na_6[(\mathbf{6.3})_3Y_2]$ (mM)	$[Na_6[(\mathbf{6.3})_3Sm_2]$ (mM)	$Na_6[(\mathbf{6.3})_3YSm]$ (mM)
0	1.93	0.34	1.58
3.95	0.86	1.10	1.89
8.73	0.81	1.21	1.84
23.93	0.72	1.34	1.79
30.42	0.64	1.42	1.79

Table 8.4: Concentration of $Na_6[(\mathbf{6.3})_3Y_2]$, $Na_6[(\mathbf{6.3})_3Sm_2]$, and $Na_6[(\mathbf{6.3})_3YSm]$ versus time.

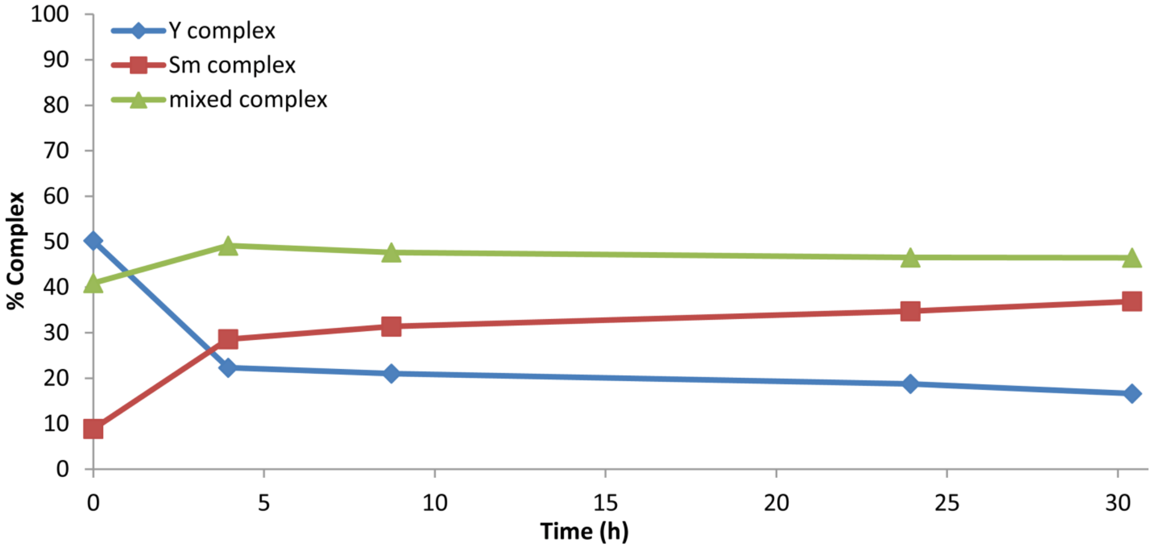

Figure 8.49: Graph of percent ligand versus time in equilibration of $Na_6[(\mathbf{6.3})_3Y_2]$ and $Na_6[(\mathbf{6.3})_3Sm_2]$.

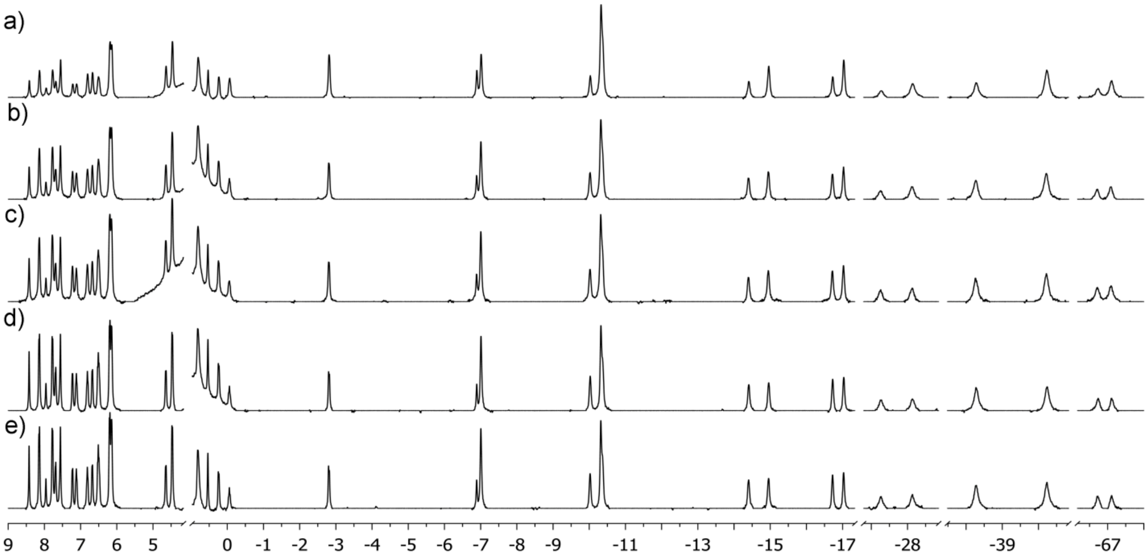

Figure 8.50: Equilibration of $Na_2[(\mathbf{6.3})_2Yb_2]$ and $Na_6[(\mathbf{6.3})_3Y_2]$: a) 0 h; b) 3.92 h; c) 8.68 h; d) 23.88 h; e) 30.37 h (400 MHz, DMSO-d_6, 298 K).

time (h)	$Na_2[(\mathbf{6.3})_2Yb_2]$ (mM)	$Na_6[(\mathbf{6.3})_3Y_2]$ (mM)	$Na_2[(\mathbf{6.3})_2YYb]$ (mM)
0	2.52	0.46	2.57
3.92	1.81	0.77	2.81
8.68	1.74	0.81	2.82
23.88	1.61	0.90	2.82
30.37	1.60	0.90	2.83

Table 8.5: Concentration of $Na_2[(\mathbf{6.3})_2Yb_2]$, $Na_6[(\mathbf{6.3})_3Y_2]$, and $Na_2[(\mathbf{6.3})_2YYb]$ versus time.

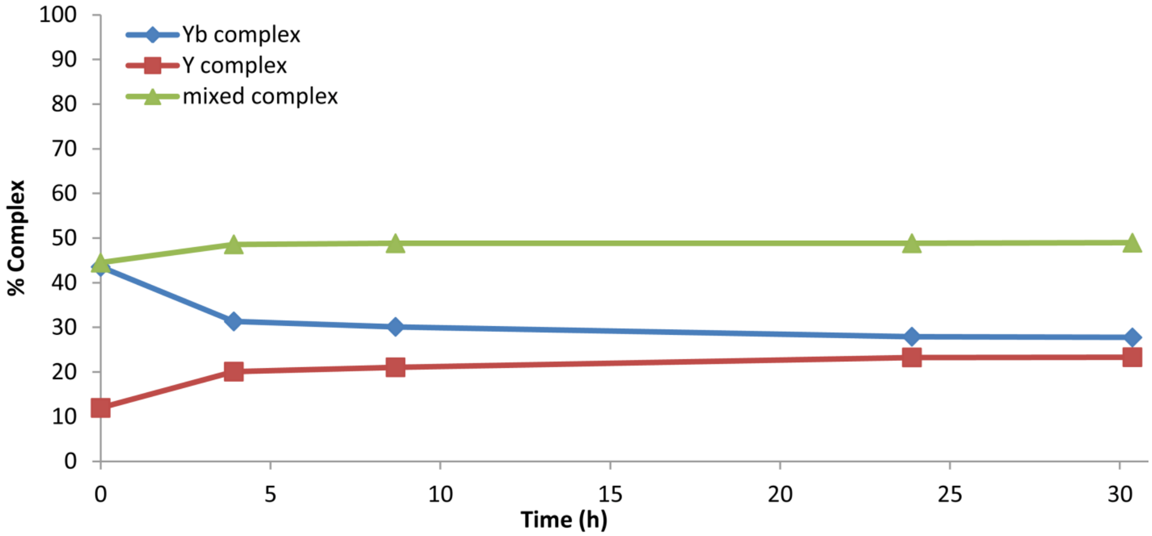

Figure 8.51: Graph of percent ligand versus time in equilibration of $Na_2[(\mathbf{6.3})_2Yb_2]$ and $Na_6[(\mathbf{6.3})_3Y_2]$.

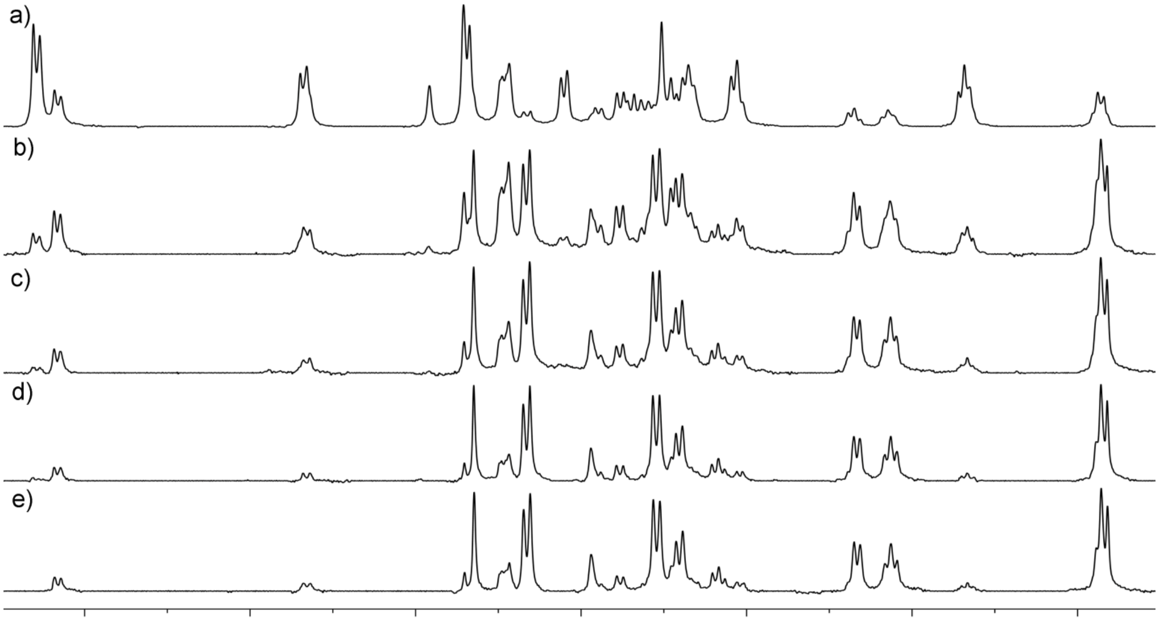

Figure 8.52: Equilibration of $Na_6[(\mathbf{6.3})_3Sm_2]$ and $Na_6[(\mathbf{6.3})_3La_2]$: a) 0 h; b) 3.87 h; c) 8.65 h; d) 23.85 h; e) 30.33 h (400 MHz, DMSO-d_6, 298 K).

time (h)	$Na_6[(\mathbf{6.3})_3Sm_2]$ (mM)	$Na_6[(\mathbf{6.3})_3La_2]$ (mM)	$Na_6[(\mathbf{6.3})_3LaSm]$ (mM)
0	1.89	0.42	1.54
3.87	0.35	1.97	1.53
8.65	0.13	2.62	1.10
23.85	0.09	2.85	0.91
30.33	0	2.96	0.89

Table 8.6: Concentration of $Na_6[(\mathbf{6.3})_3Sm_2]$, $Na_6[(\mathbf{6.3})_3La_2]$, and $Na_6[(\mathbf{6.3})_3LaSm]$versus time.

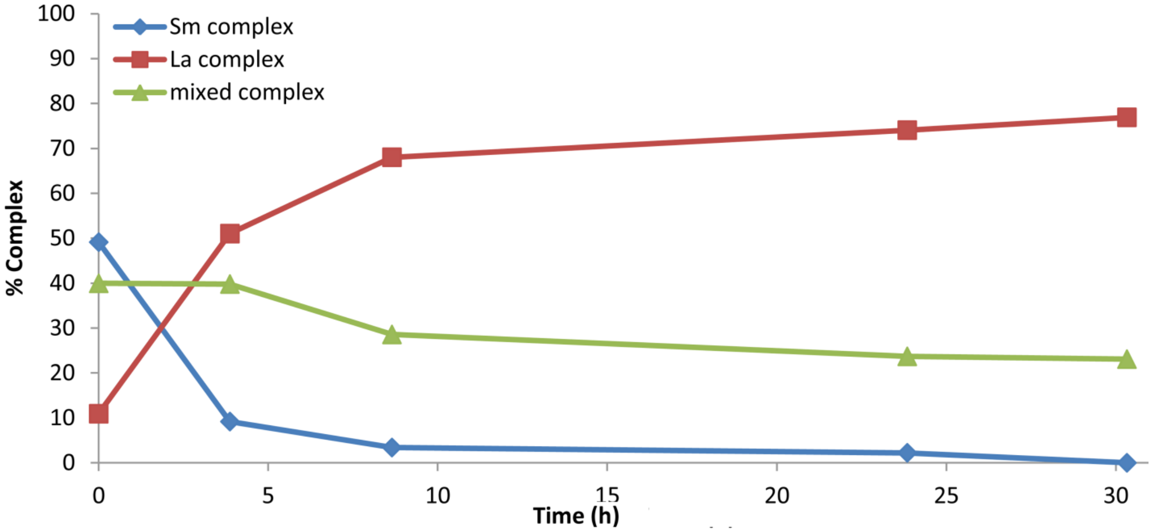

Figure 8.53: Graph of percent ligand versus time in equilibration of $Na_6[(\mathbf{6.3})_3Sm_2]$ and $Na_6[(\mathbf{6.3})_3La_2]$.

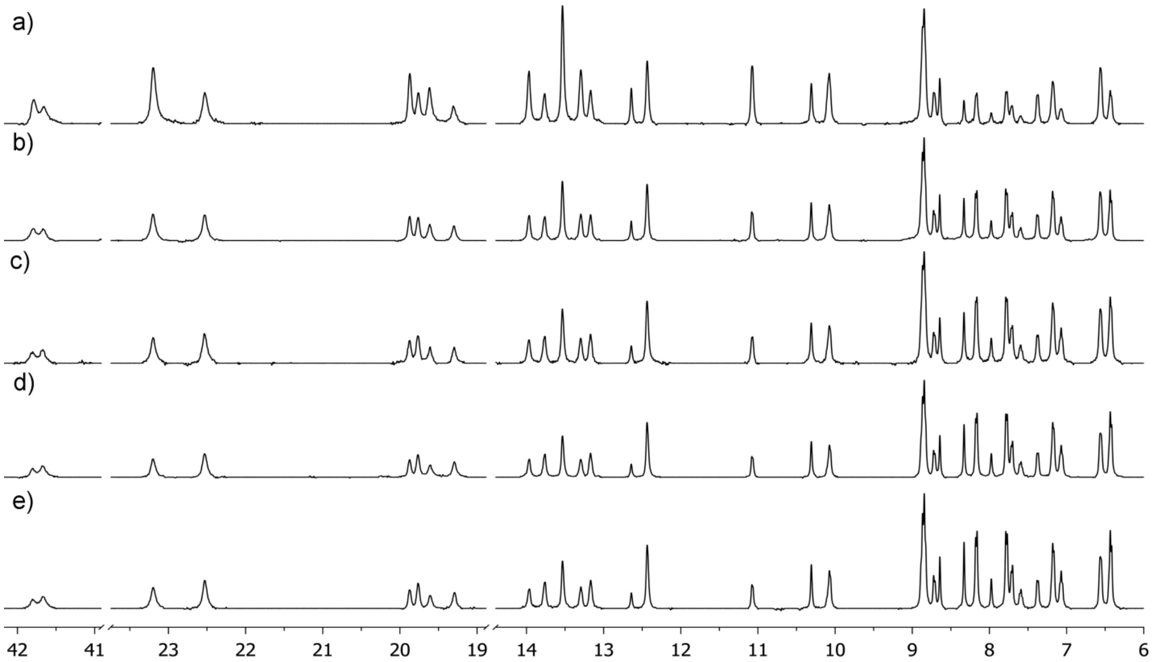

Figure 8.54: Equilibration of $Na_6[(\mathbf{6.3})_3Pr_2]$and $Na_6[(\mathbf{6.3})_3La_2]$: a) 0 h; b) 3.90 h; c) 8.63 h; d) 23.87 h; e) 30.35 h (400 MHz, DMSO-d_6, 298 K).

time (h)	$Na_6[(\mathbf{6.3})_3Pr_2]$ (mM)	$Na_6[(\mathbf{6.3})_3La_2]$ (mM)	$Na_6[(\mathbf{6.3})_3LaPr]$ (mM)
0	1.53	0.43	1.90
3.9	0.93	0.99	1.94
8.63	0.83	1.10	1.93
23.87	0.75	1.14	1.96
30.35	0.72	1.15	1.98

Table 8.7: Concentration of $Na_6[(\mathbf{6.3})_3Pr_2]$, $Na_6[(\mathbf{6.3})_3La_2]$, and $Na_6[(\mathbf{6.3})_3LaPr]$versus time.

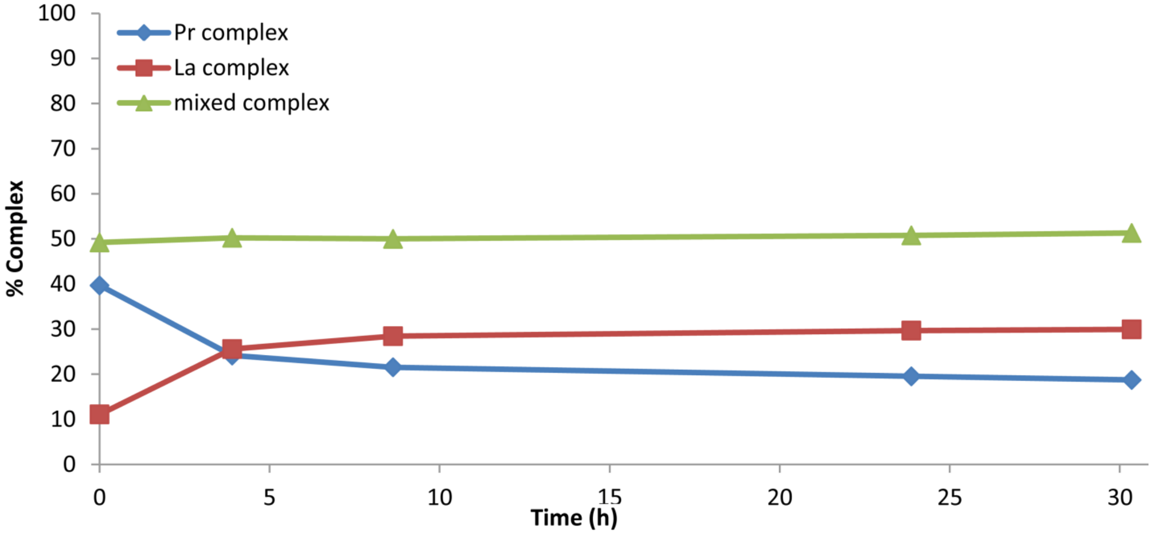

Figure 8.55: Graph of percent ligand versus time in equilibration of $Na_6[(\mathbf{6.3})_3Pr_2]$ and $Na_6[(\mathbf{6.3})_3La_2]$.

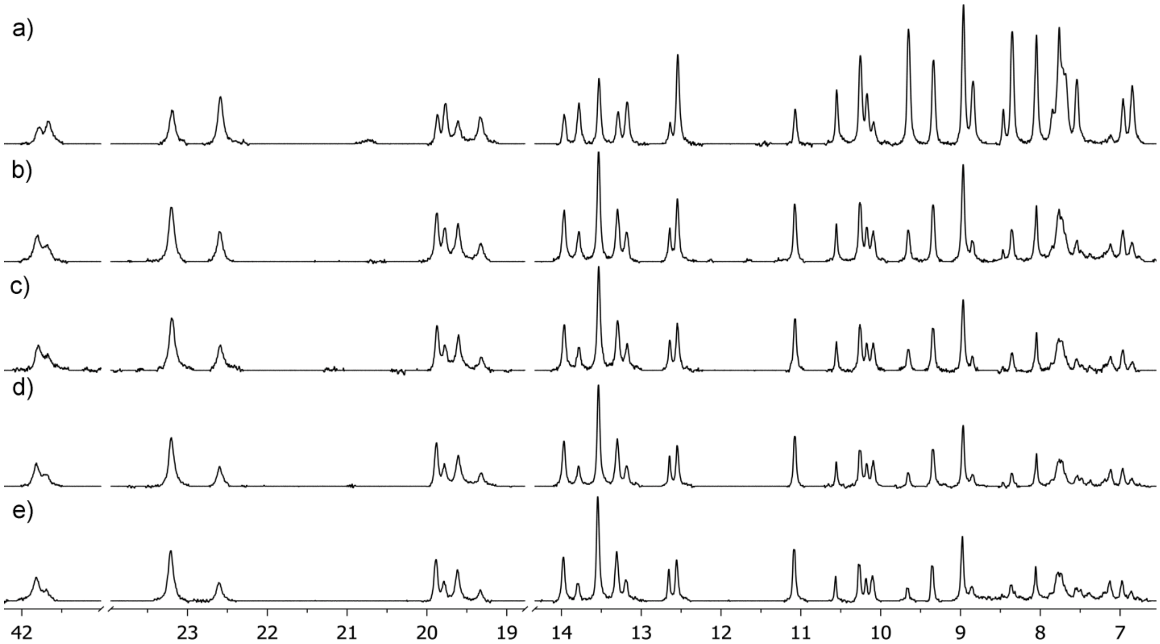

Figure 8.56: Equilibration of $Na_6[(\mathbf{6.3})_3Pr_2]$ and $Na_6[(\mathbf{6.3})_3Sm_2]$: a) 0 h; b) 3.97 h; c) 8.67 h; d) 23.93 h; e) 30.38 h (400 MHz, DMSO-d_6, 298 K).

20time (h)	$Na_6[(\mathbf{6.3})_3Sm_2]$ (mM)	$Na_6[(\mathbf{6.3})_3Pr_2]$ (mM)	$Na_6[(\mathbf{6.3})_3PrSm]$ (mM)
0	1.30	0.62	1.93
3.97	0.45	1.47	1.94
8.67	0.38	1.61	1.87
23.93	0.24	1.81	1.81
30.38	0.28	1.88	1.69

Table 8.8: Concentration of $Na_6[(\mathbf{6.3})_3Pr_2]$, $Na_6[(\mathbf{6.3})_3Sm_2]$, and $Na_6[(\mathbf{6.3})_3PrSm]$ versus time.

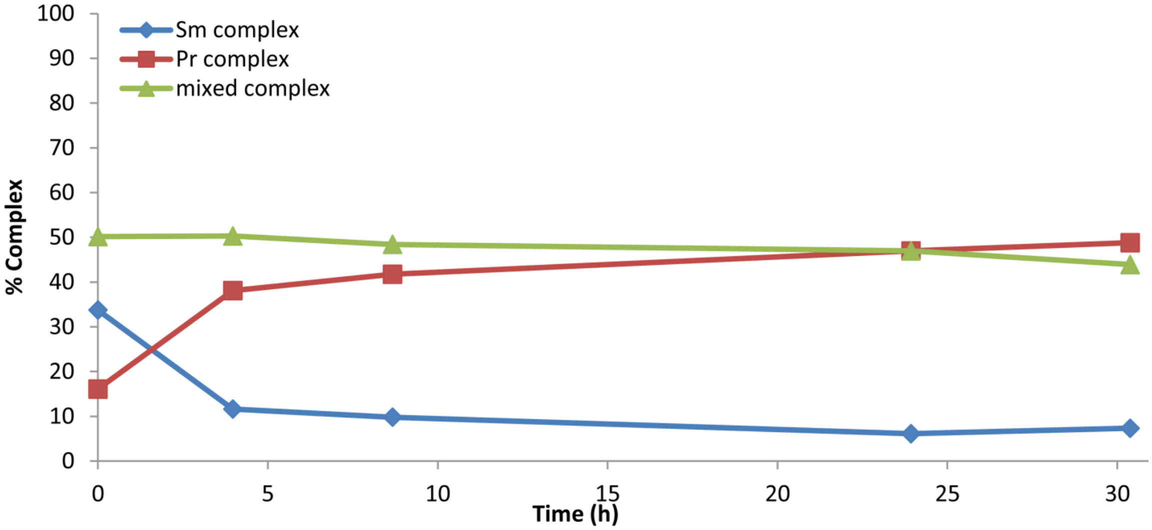

Figure 8.57: Graph of percent ligand versus time in equilibration of $Na_6[(\mathbf{6.3})_3Pr_2]$ and $Na_6[(\mathbf{6.3})_3Sm_2]$.

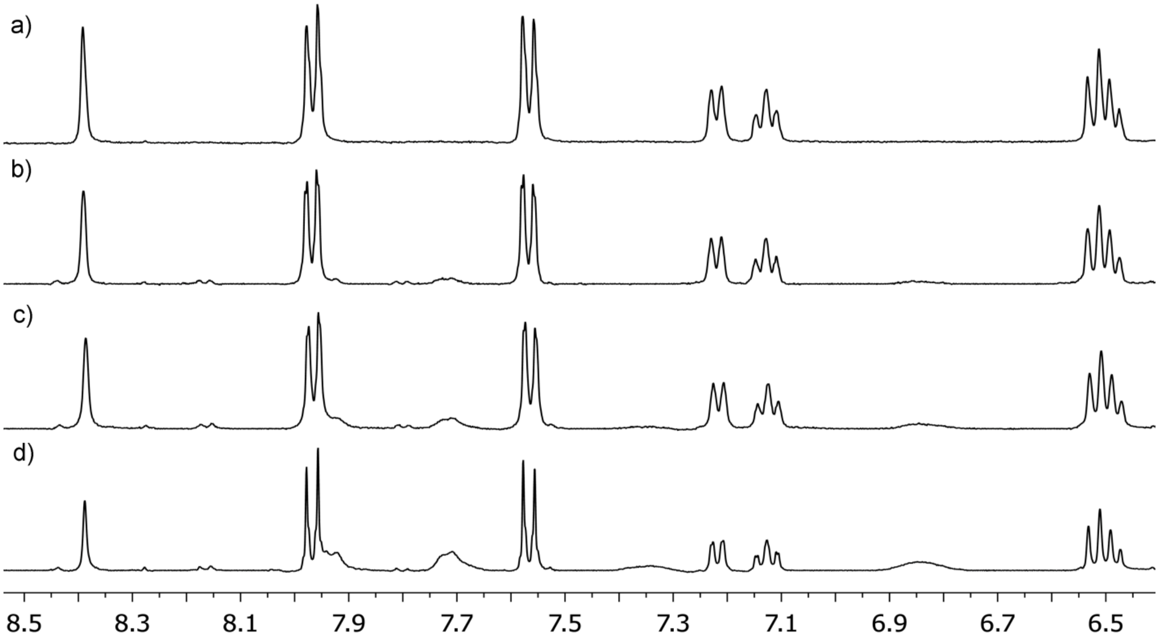

Figure 8.58: Equilibration of $Na_3[(\mathbf{6.5})_3Y]$ and $Na_3[(\mathbf{6.5})_3La]$: a) 0 h; b) 3.50 h; c) 7.47 h; d) 30.83 h (400 MHz, DMSO-d_6, 298 K).

time (h)	$Na_3[(\mathbf{6.5})_3Y]$ (mM)	$Na_3[(\mathbf{6.5})_3La]$ (mM)
0	4.67	0.42
3.5	5.04	0.05
7.47	4.94	0.15
30.83	4.99	0.10

Table 8.9: Concentration of $Na_3[(\mathbf{6.5})_3Y]$ and $Na_3[(\mathbf{6.5})_3La]$ versus time.

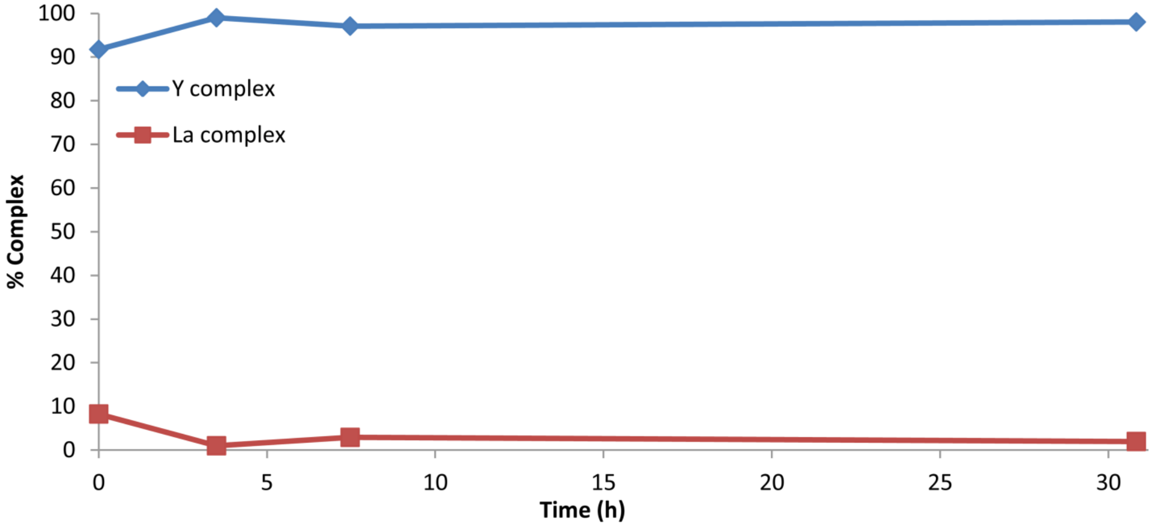

Figure 8.59: Graph of percent ligand versus time in equilibration of $Na_3[(\mathbf{6.5})_3Y]$ and $Na_3[(\mathbf{6.5})_3La]$.

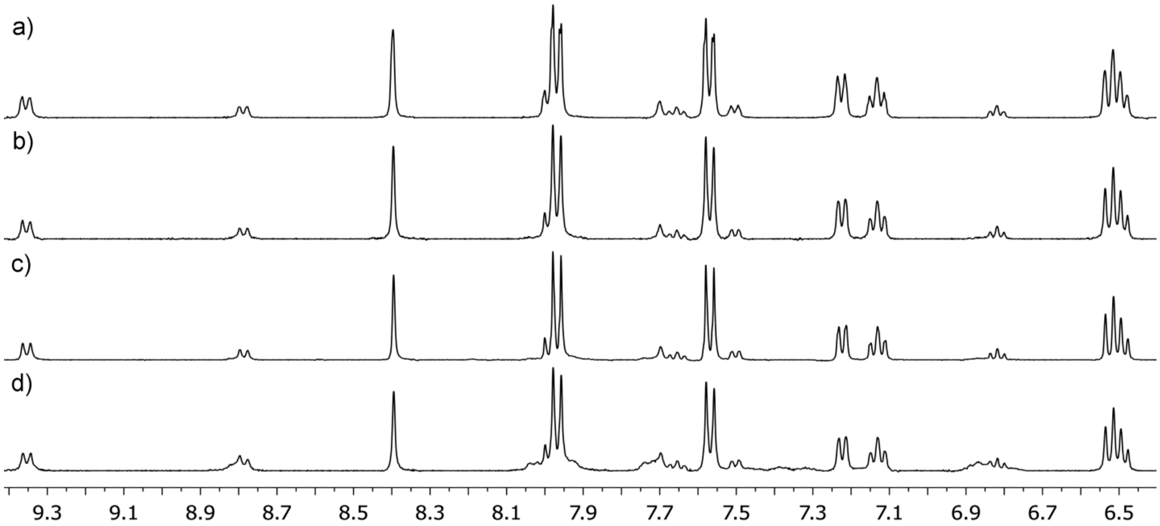

Figure 8.60: Equilibration of Na$_3$[(**6.5**)$_3$Y]and Na$_3$[(**6.5**)$_3$Sm]: a) 0 h; b) 3.97 h; c) 7.45 h; d) 30.83 h (400 MHz, DMSO-d_6, 298 K).

time (h)	Na$_3$[(**6.5**)$_3$Y] (mM)	Na$_3$[(**6.5**)$_3$Sm] (mM)
0	4.20	0.89
3.97	3.95	1.15
7.45	3.85	1.24
30.83	3.29	1.80

Table 8.10: Concentration of Na$_3$[(**6.5**)$_3$Y] and Na$_3$[(**6.5**)$_3$Sm]versus time.

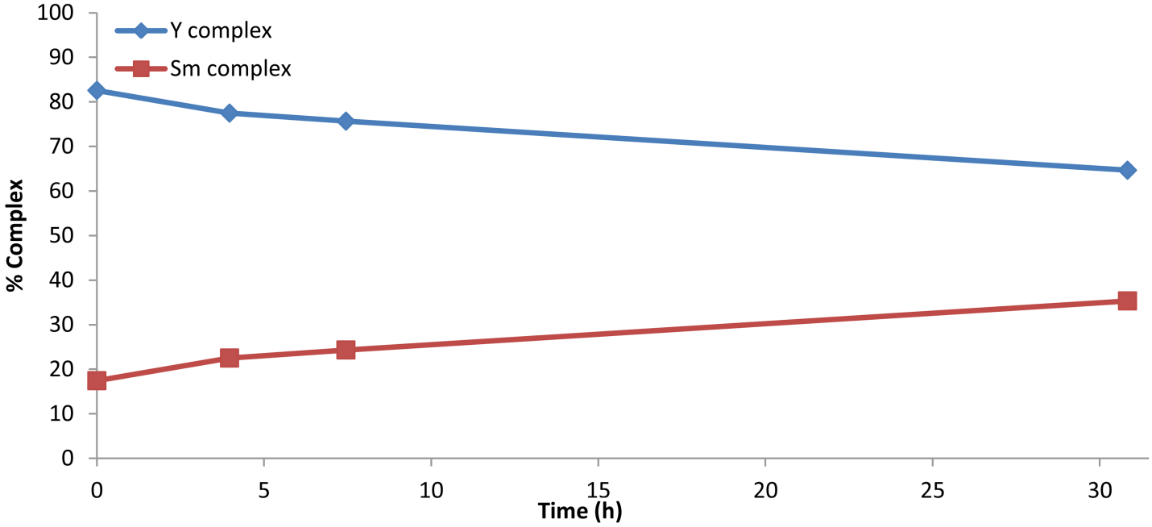

Figure 8.61: Graph of percent ligand versus time in equilibration of Na$_3$[(**6.5**)$_3$Y]and Na$_3$[(**6.5**)$_3$Sm].

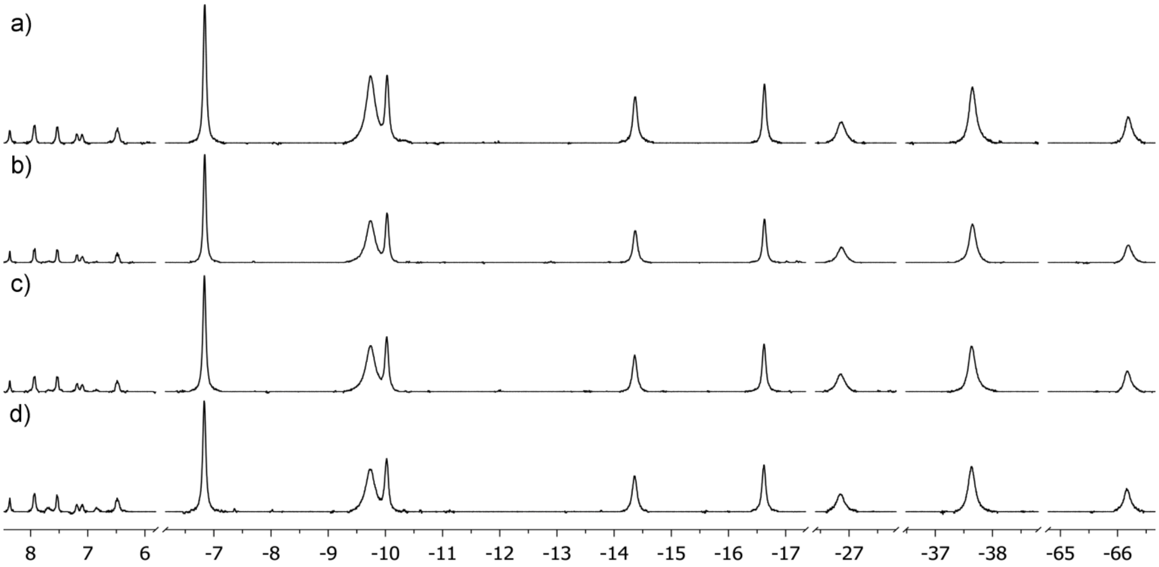

Figure 8.62: Equilibration of Na[(**6.5**)$_2$Yb] and Na$_3$[(**6.5**)$_3$Y]: a) 0 h; b) 3.47 h; c) 7.48 h; d) 30.85 h (400 MHz, DMSO-*d*$_6$, 298 K).

time (h)	Na[(**6.5**)$_2$Yb] (mM)	Na$_3$[(**6.5**)$_3$Y] (mM)
0	6.99	0.44
3.47	6.97	0.46
7.48	7.05	0.40
30.85	6.89	0.51

Table 8.11: Concentration of Na[(**6.5**)$_2$Yb] and Na$_3$[(**6.5**)$_3$Y] versus time.

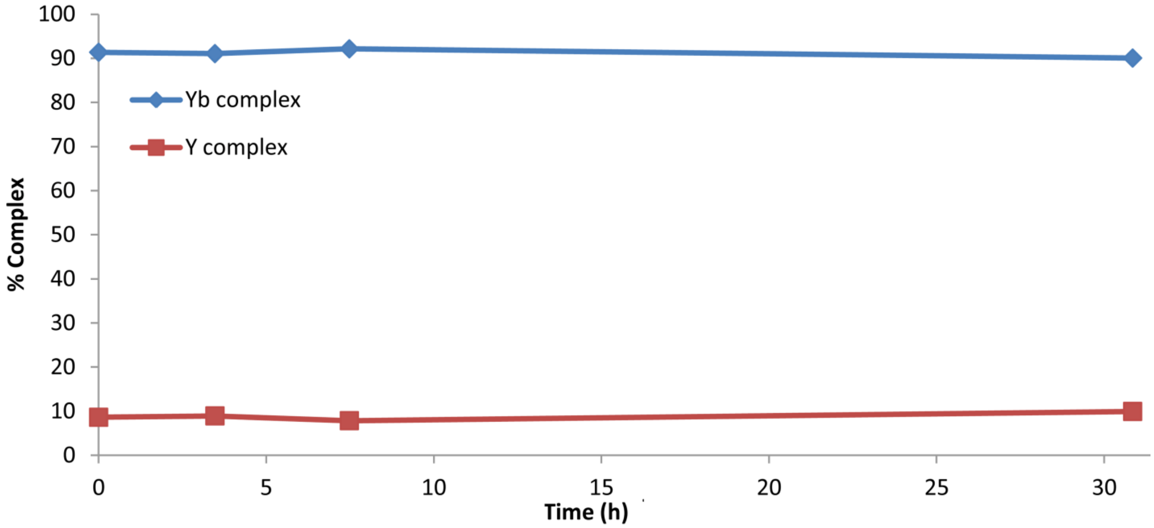

Figure 8.63: Graph of percent ligand versus time in equilibration of Na[(**6.5**)$_2$Yb] and Na$_3$[(**6.5**)$_3$Y].

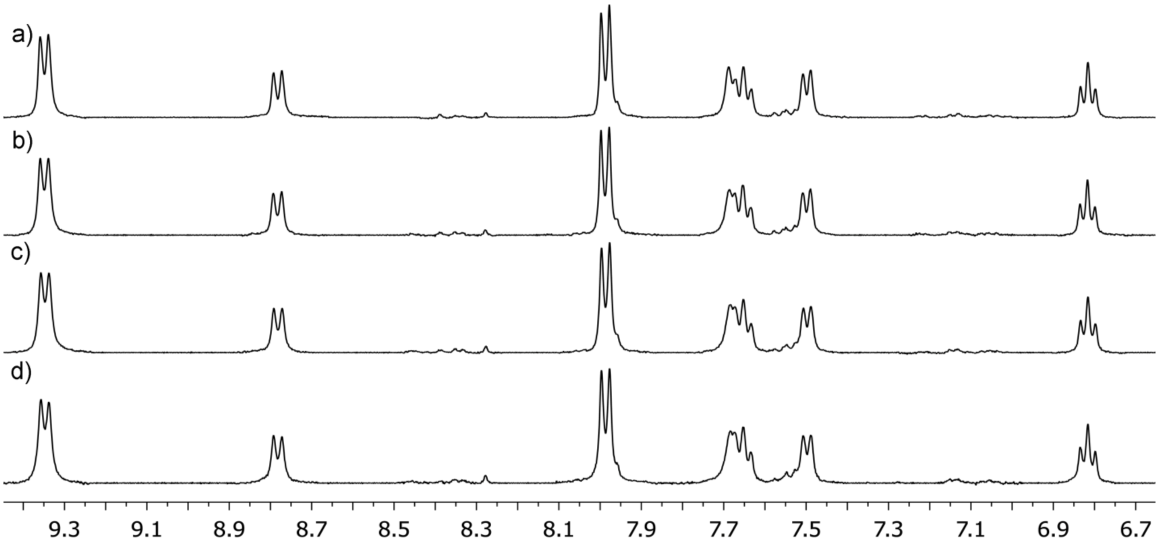

Figure 8.64: Equilibration of $Na_3[(\mathbf{6.5})_3Sm]$and $Na_3[(\mathbf{6.5})_3La]$: a) 0 h; b) 3.45 h; c) 7.47 h; d) 30.83 h (400 MHz, DMSO-d_6, 298 K).

time (h)	$Na_3[(\mathbf{6.5})_3Sm]$ (mM)	$Na_3[(\mathbf{6.5})_3La]$ (mM)
0	4.94	0.15
3.45	4.90	0.10
7.47	4.90	0.10
30.83	4.85	0.24

Table 8.12: Concentration of $Na_3[(\mathbf{6.5})_3Sm]$and $Na_3[(\mathbf{6.5})_3La]$ versus time.

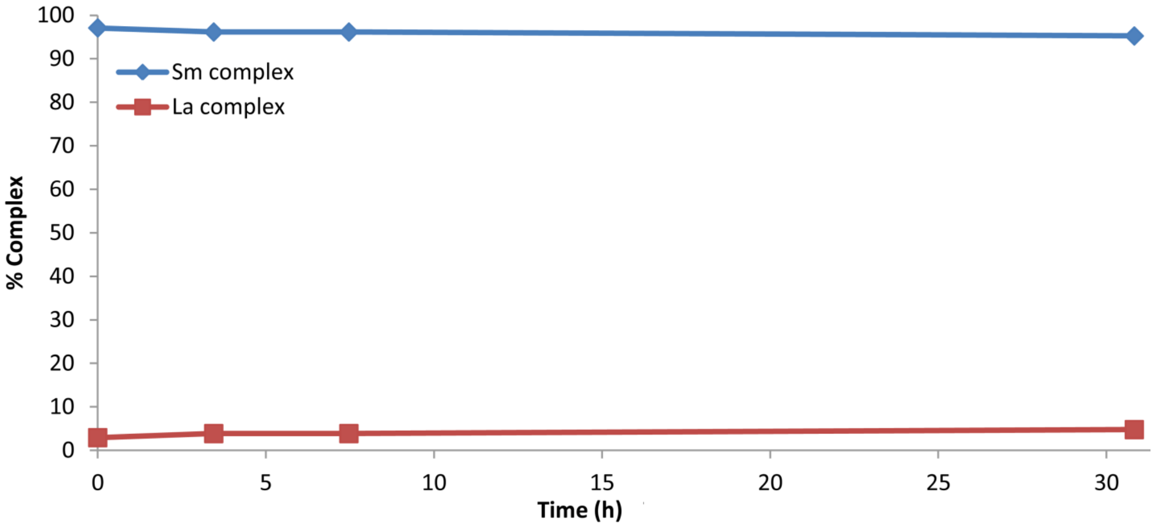

Figure 8.65: Graph of percent ligand versus time in equilibration of $Na_3[(\mathbf{6.5})_3Sm]$ and $Na_3[(\mathbf{6.5})_3La]$.

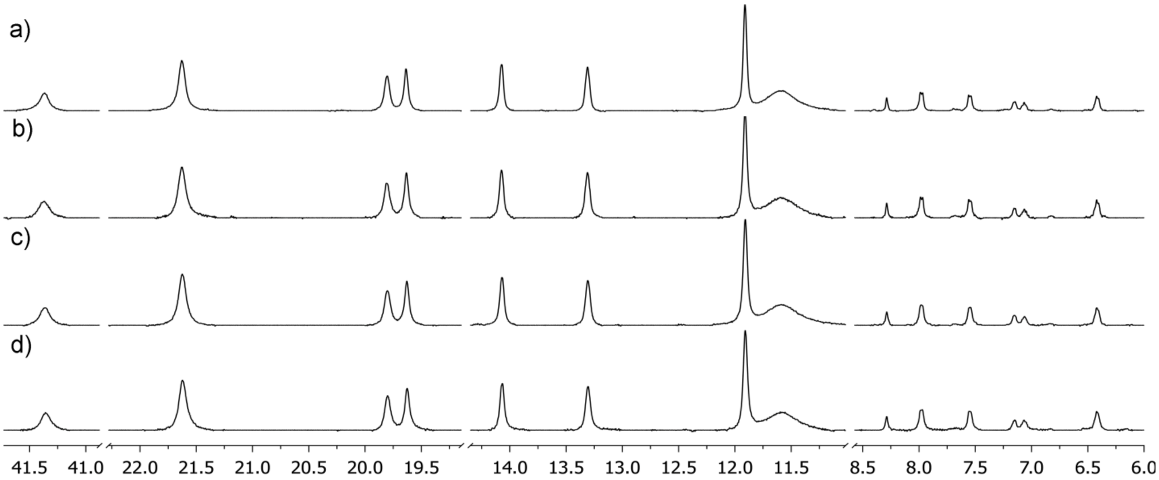

Figure 8.66: Equilibration of $Na_3[(\mathbf{6.5})_3Pr]$ and $Na_3[(\mathbf{6.5})_3La]$: a) 0 h; b) 3.40 h; c) 7.48 h; d) 30.83 h (400 MHz, DMSO-d_6, 298 K).

time (h)	$Na_3[(\mathbf{6.5})_3Pr]$ (mM)	$Na_3[(\mathbf{6.5})_3La]$ (mM)
0	4.47	0.63
3.4	4.43	0.66
7.48	4.43	0.66
30.83	4.35	0.74

Table 8.13: Concentration of $Na_3[(\mathbf{6.5})_3Pr]$and $Na_3[(\mathbf{6.5})_3La]$ versus time.

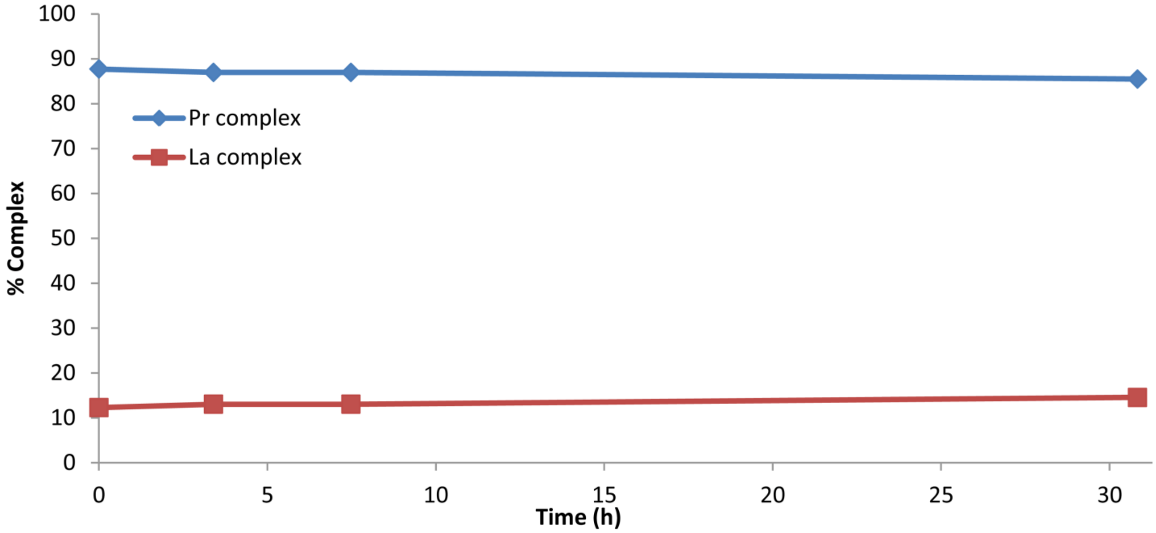

Figure 8.67: Graph of percent ligand versus time in equilibration of $Na_3[(\mathbf{6.5})_3Pr]$ and $Na_3[(\mathbf{6.5})_3La]$.

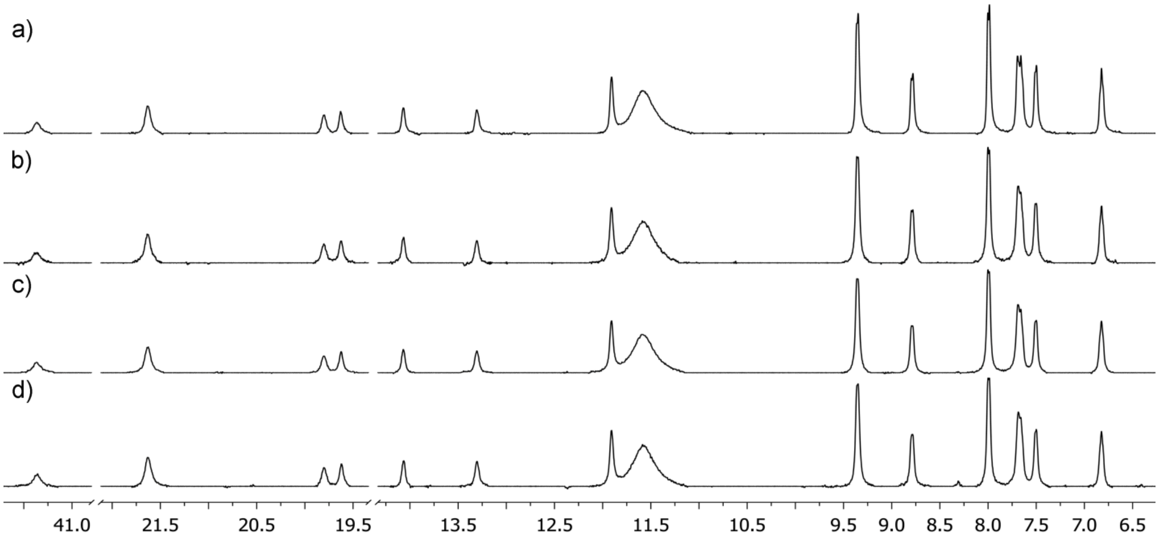

Figure 8.68: Equilibration of Na$_3$[(**6.5**)$_3$Pr] and Na$_3$[(**6.5**)$_3$Sm]: a) 0 h; b) 3.35 h; c) 7.47 h; d) 30.83 h (400 MHz, DMSO-d_6, 298 K).

time (h)	Na$_3$[(**6.5**)$_3$Sm] (mM)	Na$_3$[(**6.5**)$_3$Pr] (mM)
0	3.60	1.49
3.35	3.51	1.58
7.47	3.52	1.58
30.83	3.56	1.53

Table 8.14: Concentration of Na$_3$[(**6.5**)$_3$Sm]and Na$_3$[(**6.5**)$_3$Pr] versus time.

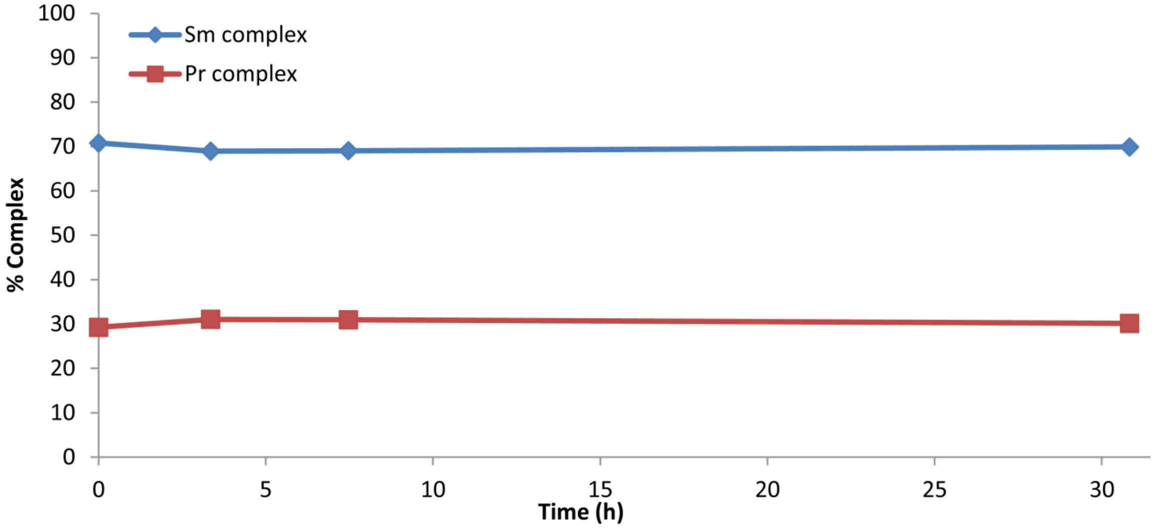

Figure 8.69: Graph of percent ligand versus time in equilibration of Na$_3$[(**6.5**)$_3$Sm] and Na$_3$[(**6.5**)$_3$Pr].

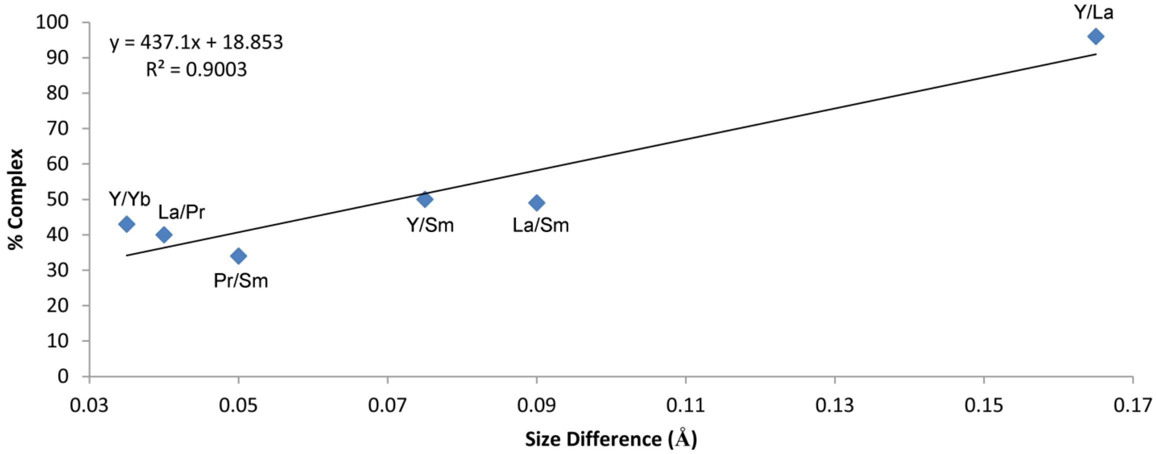

Figure 8.70: Graph of percent $Na_x[(\mathbf{6.3})_yLn(small)_2]$ versus effective ionic radius difference before equilibration in equilibrium experiments with $Na_x[(\mathbf{6.3})_yLn_2]$.

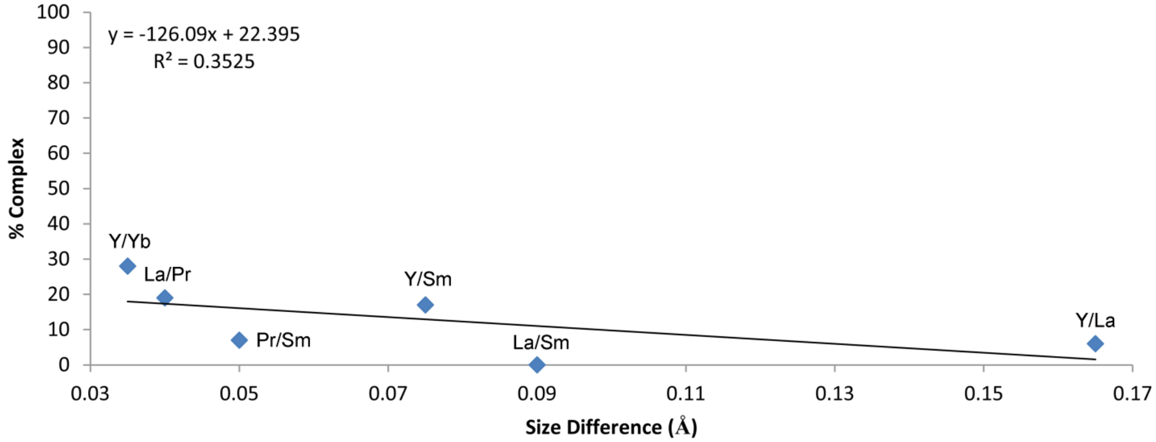

Figure 8.71: Graph of percent $Na_x[(\mathbf{6.3})_yLn(small)_2]$ versus effective ionic radius difference after equilibration in equilibrium experiments with $Na_x[(\mathbf{6.3})_yLn_2]$.

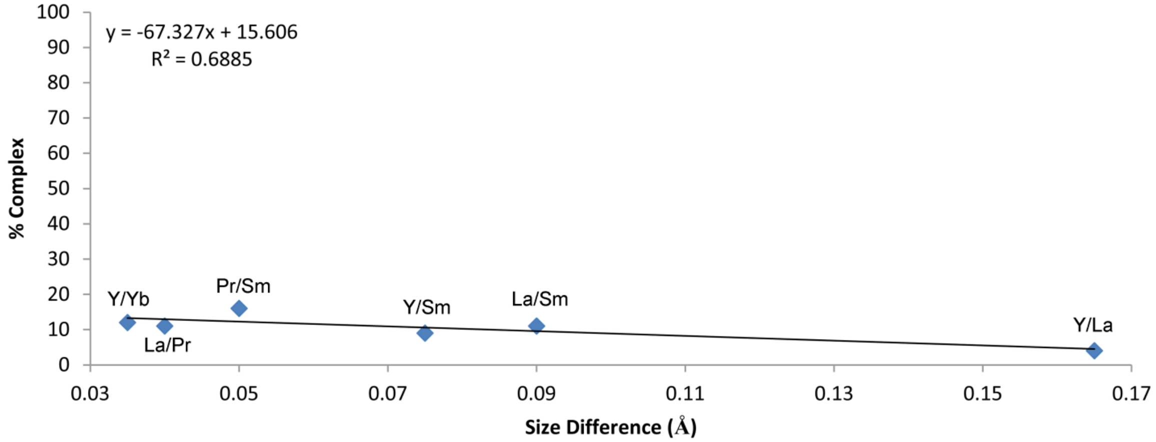

Figure 8.72: Graph of percent $Na_x[(\mathbf{6.3})_yLn(large)_2]$ versus effective ionic radius difference before equilibration in equilibrium experiments with $Na_x[(\mathbf{6.3})_yLn_2]$.

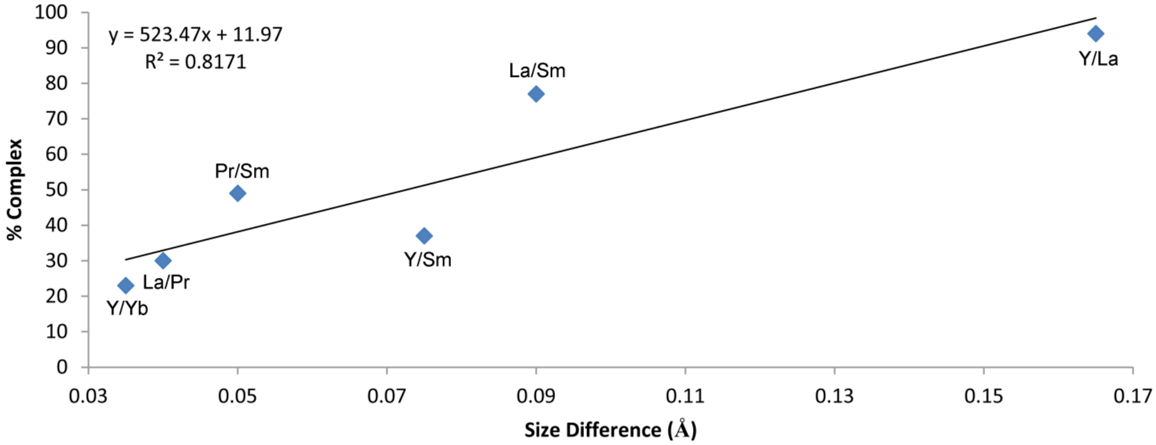

Figure 8.73: Graph of percent $Na_x[(\mathbf{6.3})_yLn(large)_2]$ versus effective ionic radius difference after equilibration in equilibrium experiments with $Na_x[(\mathbf{6.3})_yLn_2]$.

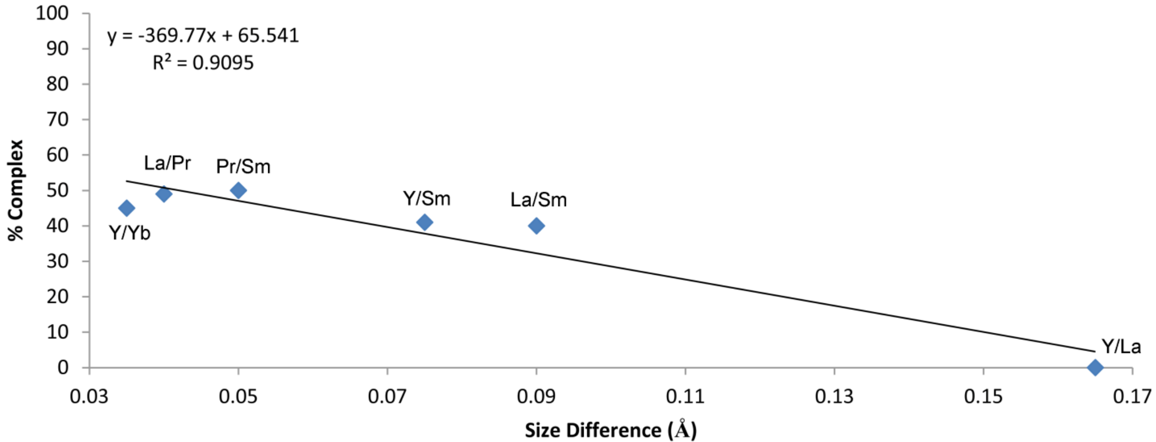

Figure 8.74: Graph of percent $Na_x[(\mathbf{6.3})_yLn^ALn^B]$ versus effective ionic radius difference before equilibration in equilibrium experiments with $Na_x[(\mathbf{6.3})_yLn_2]$.

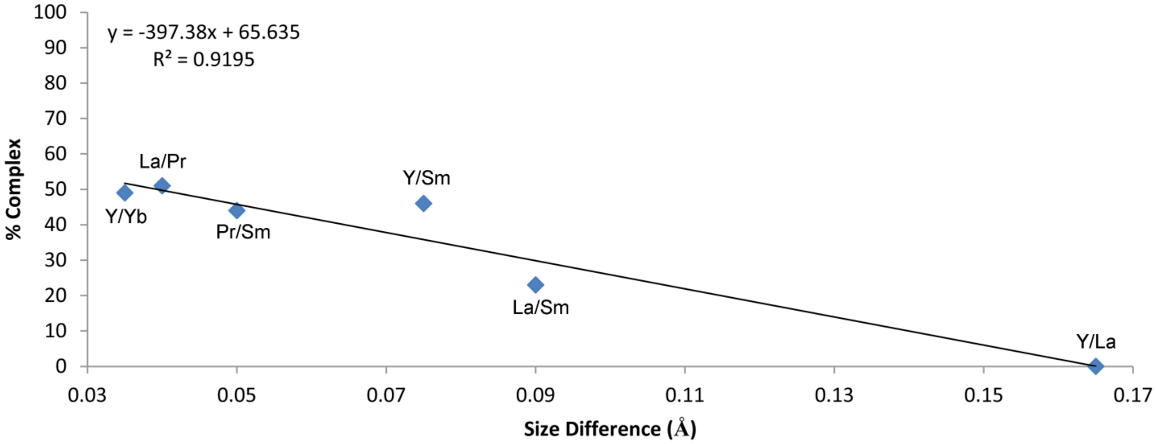

Figure 8.75: Graph of percent $Na_x[(\mathbf{6.3})_yLn^ALn^B]$ versus effective ionic radius difference after equilibration in equilibrium experiments with $Na_x[(\mathbf{6.3})_yLn_2]$.

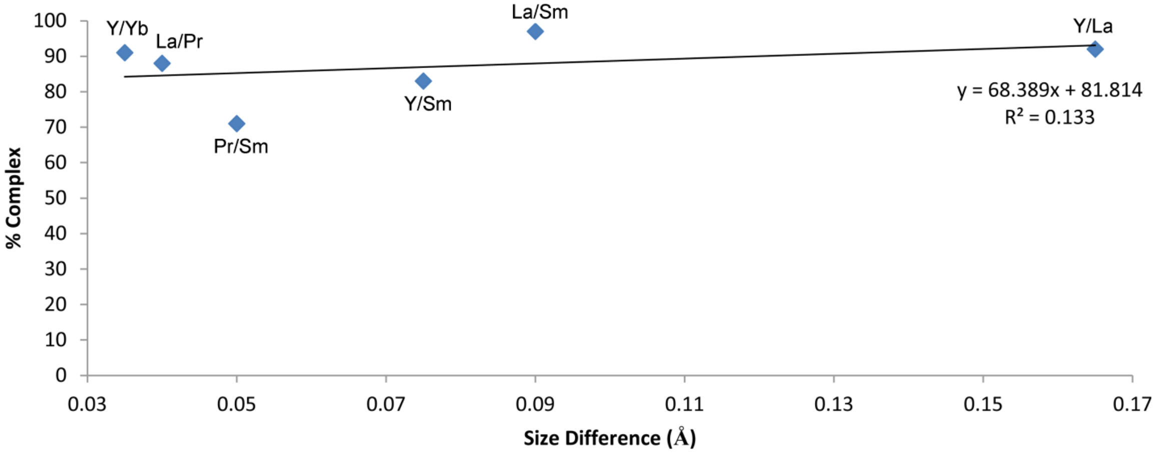

Figure 8.76: Graph of percent $Na_x[(\mathbf{6.5})_yLn(small)]$ versus effective ionic radius difference before equilibration in equilibrium experiments with $Na_x[(\mathbf{6.3})_yLn]$.

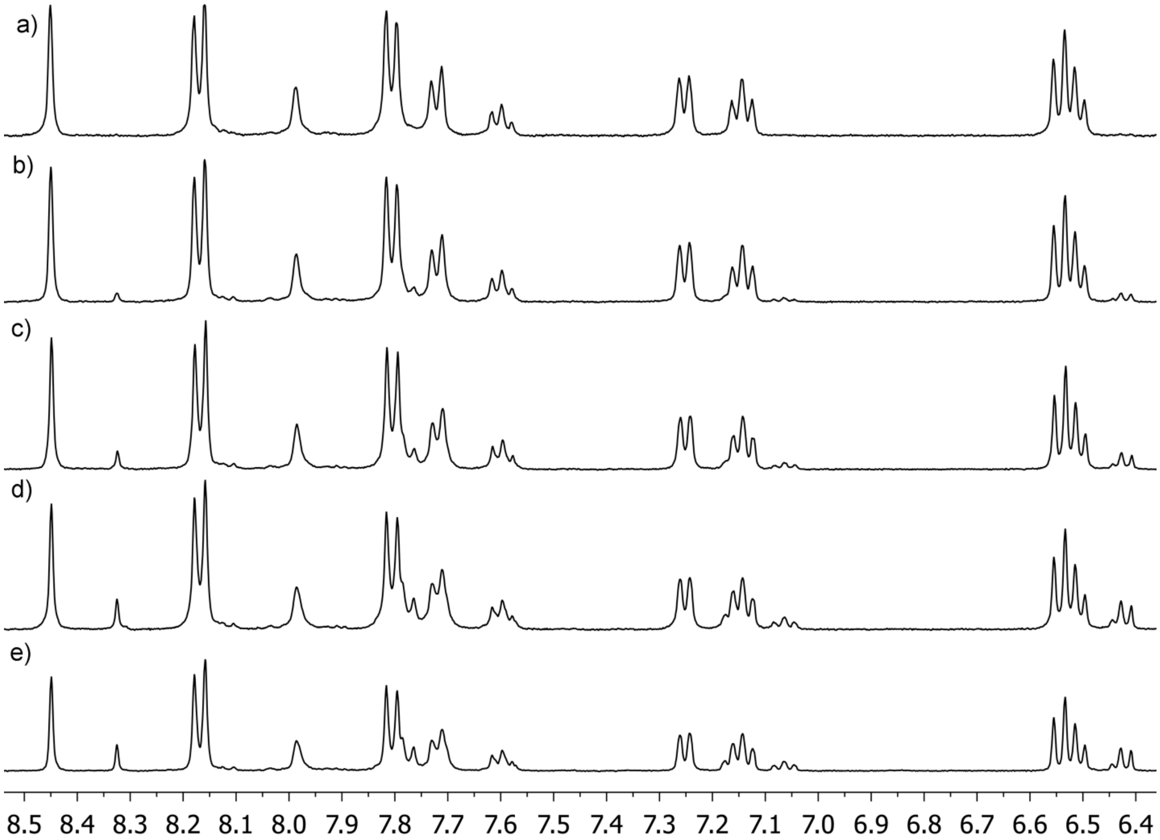

Figure 8.77: Equilibration of $Na_6[(\mathbf{6.3})_3Y_2]$ and $Na_6[(\mathbf{6.3})_3La_2]$ with 50 mM initial water concentration: a) 0.25 h; b) 3.53 h; c) 8.17 h; d) 22.5 h; e) 29.5 h (400 MHz, DMSO-d_6, 298 K).

time (h)	$Na_6[(\mathbf{6.3})_3Y_2]$ (mM)	$Na_6[(\mathbf{6.3})_3La_2]$ (mM)
0.25	4.16	0
3.53	3.93	0.24
8.17	3.71	0.45
22.5	3.47	0.69
29.5	3.38	0.78

Table 8.15: Concentration of $Na_6[(\mathbf{6.3})_3Y_2]$ and $Na_6[(\mathbf{6.3})_3La_2]$ versus time with 50 mM initial water concentration.

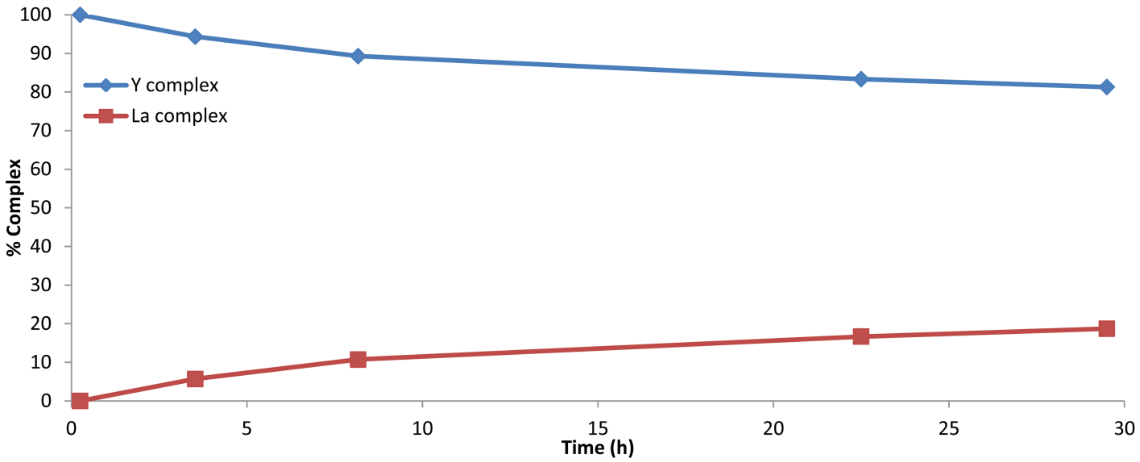

Figure 8.78: Graph of percent ligand versus time in equilibration of $Na_6[(\mathbf{6.3})_3Y_2]$ and $Na_6[(\mathbf{6.3})_3La_2]$ with 50 mM initial water concentration.

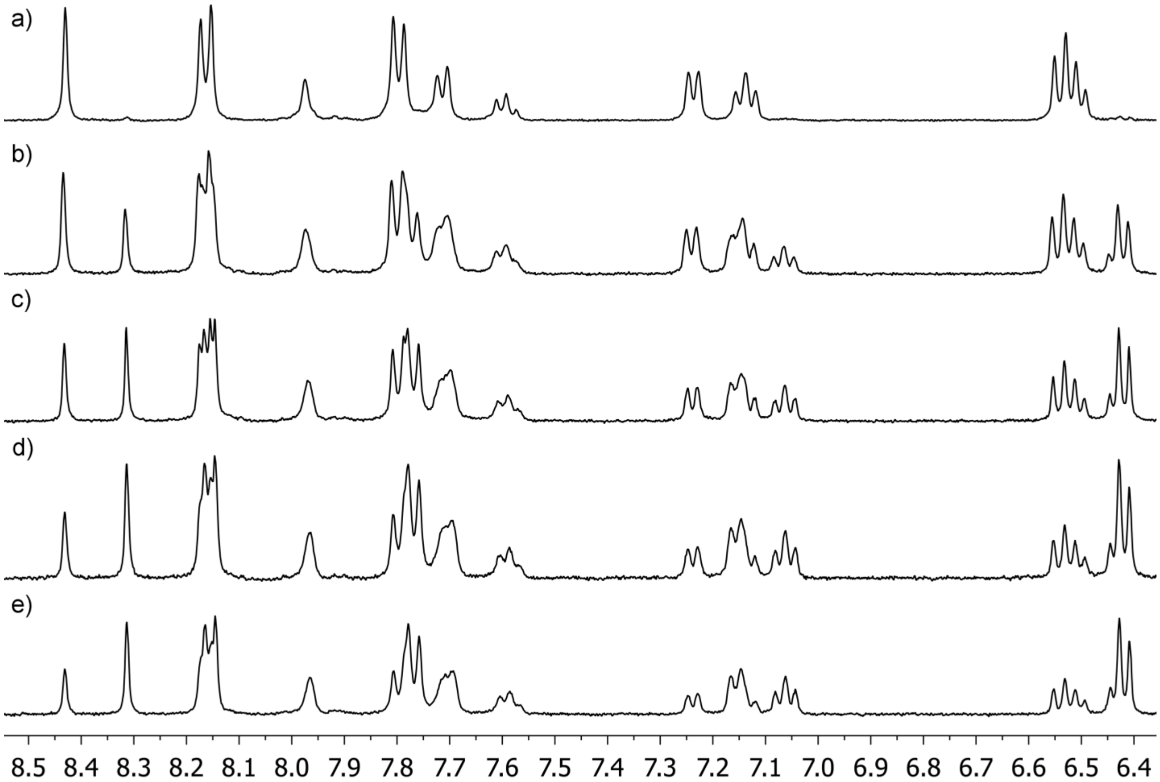

Figure 8.79: Equilibration of $Na_6[(\mathbf{6.3})_3Y_2]$ and $Na_6[(\mathbf{6.3})_3La_2]$ with 158 mM initial water concentration: a) 0.08 h; b) 3.25 h; c) 7.98 h; d) 22.32 h; e) 29.30 h (400 MHz, DMSO-d_6, 298 K).

time (h)	$Na_6[(\mathbf{6.3})_3Y_2]$ (mM)	$Na_6[(\mathbf{6.3})_3La_2]$ (mM)
0.08	97.09	2.91
3.25	60.98	39.02
7.98	47.39	52.61
22.32	36.90	63.10
29.30	33.11	66.89

Table 8.16: Concentration of $Na_6[(\mathbf{6.3})_3Y_2]$ and $Na_6[(\mathbf{6.3})_3La_2]$ versus time with 158 mM initial water concentration.

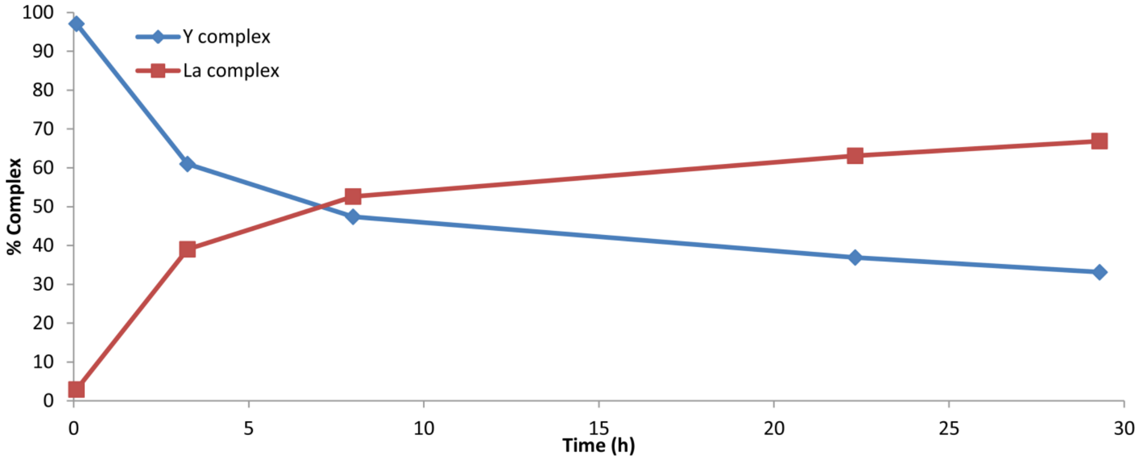

Figure 8.80: Graph of percent ligand versus time in equilibration of $Na_6[(\mathbf{6.3})_3Y_2]$ and $Na_6[(\mathbf{6.3})_3La_2]$ with 158 mM initial water concentration.

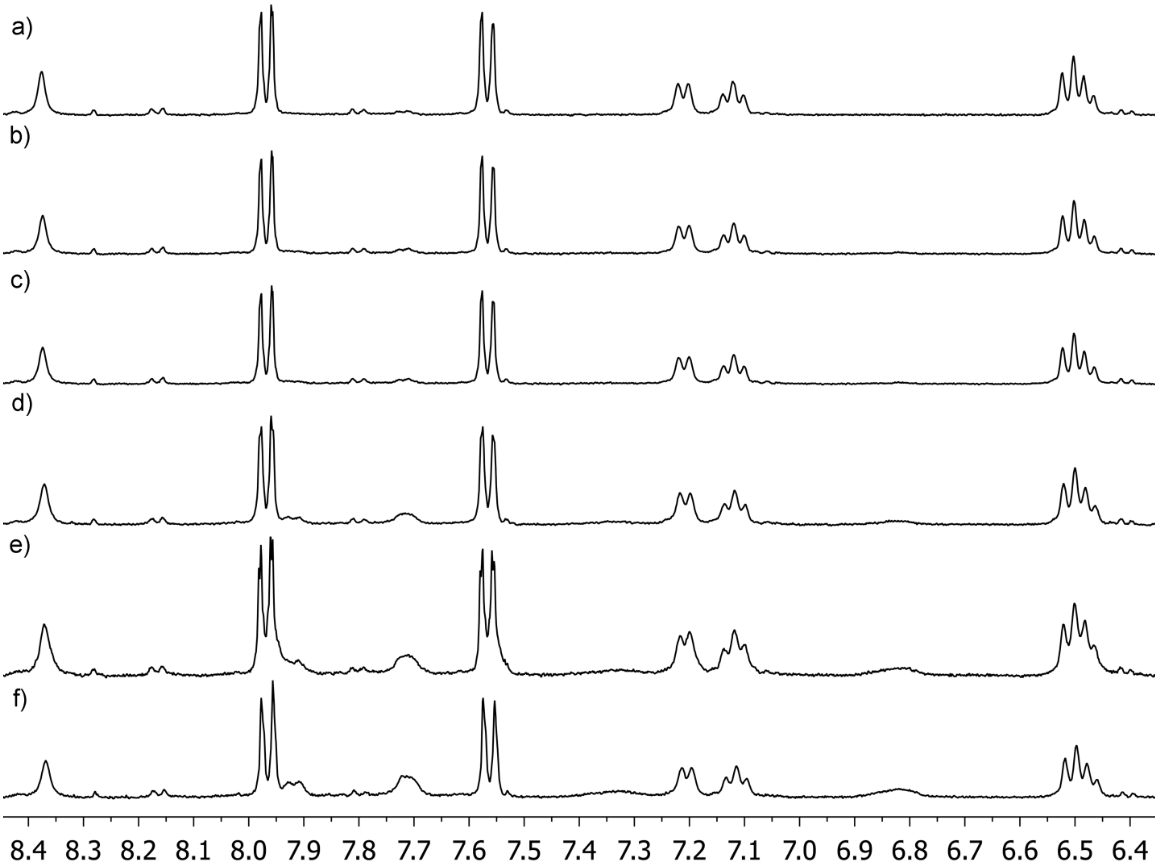

Figure 8.81: Equilibration of $Na_3[(\mathbf{6.5})_3Y]$ and $Na_3[(\mathbf{6.5})_3La]$ with 114 mM initial water concentration: a) 0 h; b) 1.72 h; c) 4.10 h; d) 6.35 h; e) 22.18 h; f) 29.18 h (400 MHz, DMSO-d_6, 298 K).

time (h)	$Na_3[(\mathbf{6.5})_3Y]$ (mM)	$Na_3[(\mathbf{6.5})_3La]$ (mM)
0	95.24	4.76
1.72	95.24	4.76
4.10	95.24	4.76
6.35	95.24	4.76
22.18	95.24	4.76
29.18	94.34	5.66

Table 8.17: Concentration of $Na_3[(\mathbf{6.5})_3Y]$ and $Na_3[(\mathbf{6.5})_3La]$ versus time with 114 mM initial water concentration.

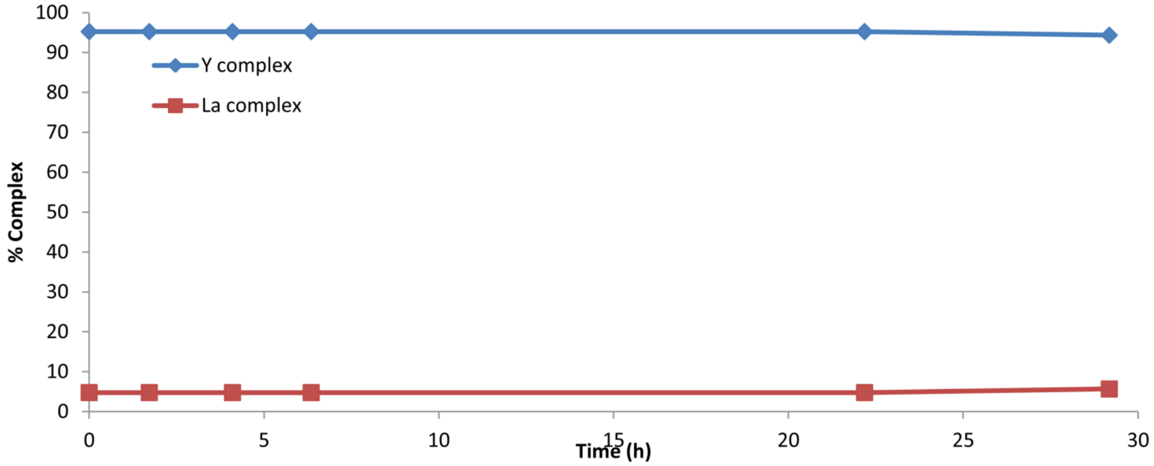

Figure 8.82: Graph of percent ligand versus time in equilibration of $Na_3[(\mathbf{6.5})_3Y]$ and $Na_3[(\mathbf{6.5})_3La]$ with 114 mM initial water concentration.

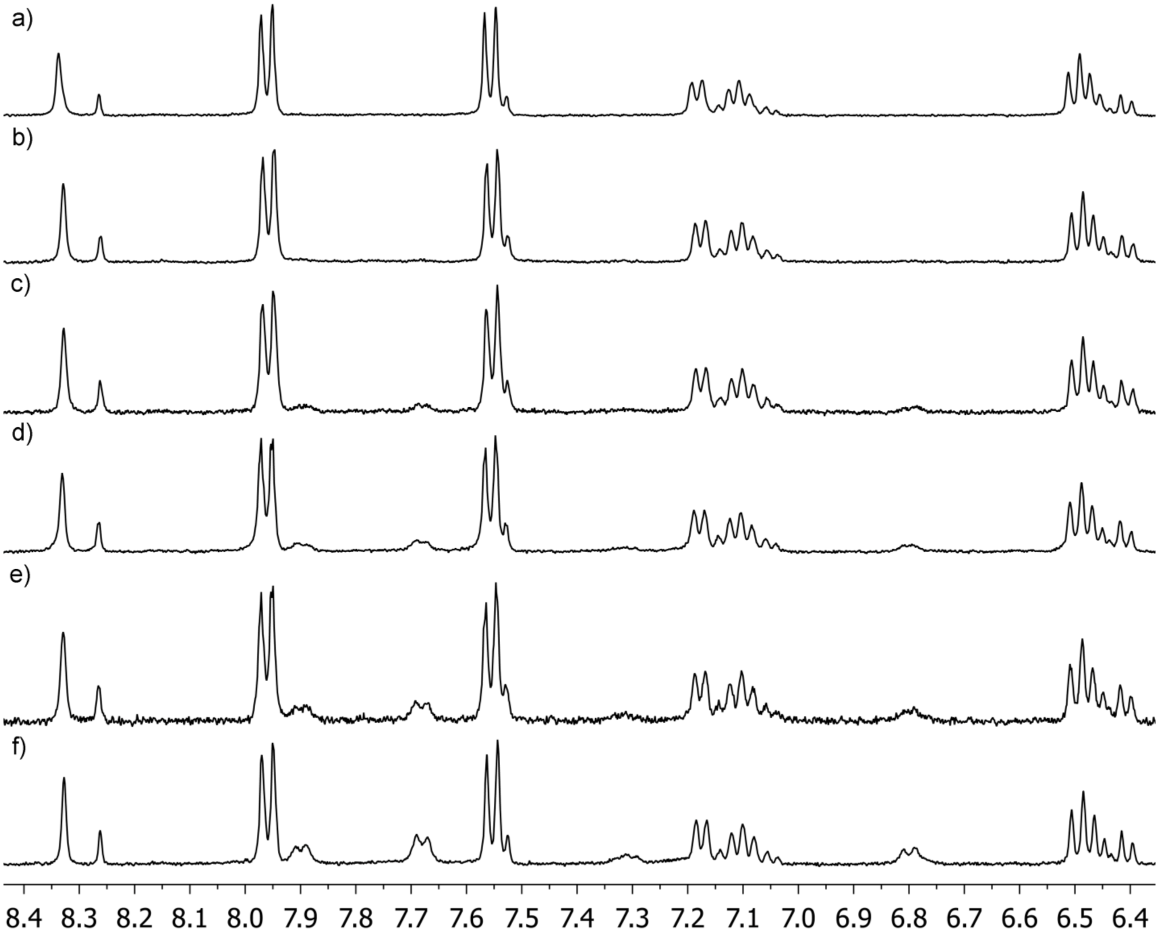

Figure 8.83: Equilibration of $Na_3[(\mathbf{6.5})_3Y]$ and $Na_3[(\mathbf{6.5})_3La]$ with 298 mM initial water concentration: a) 0 h; b) 1.58 h; c) 3.97 h; d) 6.20 h; e) 22.08 h; f) 29.05 h (400 MHz, DMSO-d_6, 298 K).

time (h)	$Na_3[(\mathbf{6.5})_3Y]$ (mM)	$Na_3[(\mathbf{6.5})_3La]$ (mM)
0	82.64	17.36
1.58	80.00	20.00
3.97	79.34	20.66
6.20	78.13	21.87
22.08	76.92	23.08
29.05	77.52	22.48

Table 8.18: Concentration of $Na_3[(\mathbf{6.5})_3Y]$ and $Na_3[(\mathbf{6.5})_3La]$ versus time with 298 mM initial water concentration.

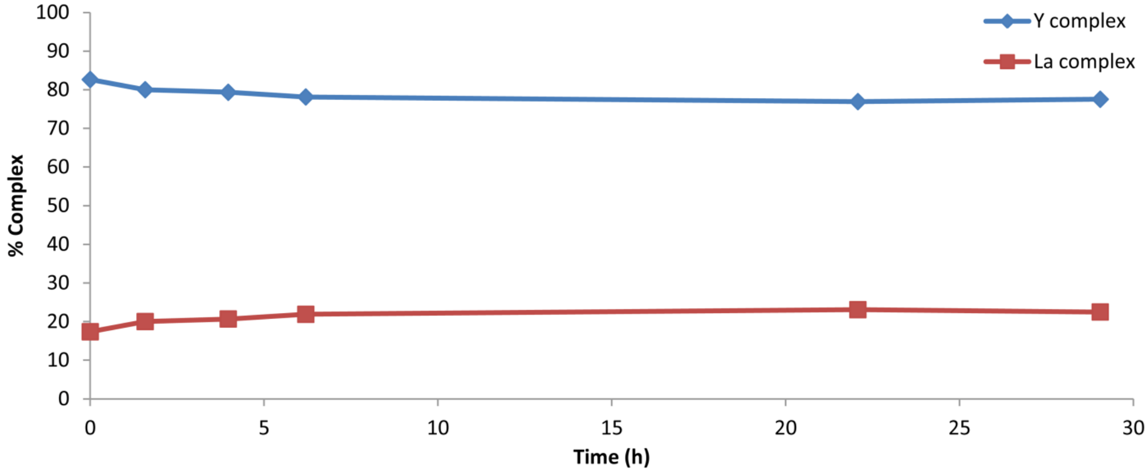

Figure 8.84: Graph of percent ligand versus time in equilibration of $Na_3[(\mathbf{6.5})_3Y]$ and $Na_3[(\mathbf{6.5})_3La]$ with 208 mM initial water concentration.

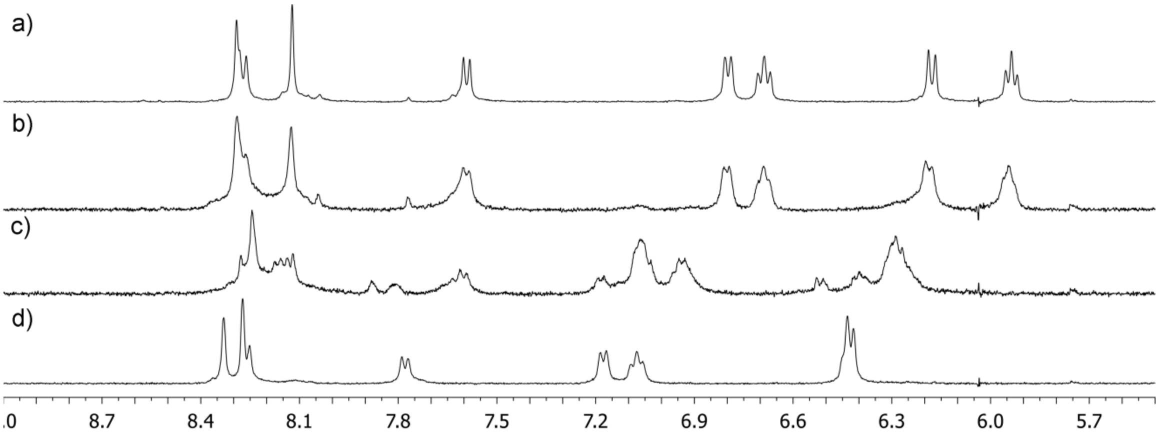

Figure 8.85: Titration of $La(OTf)_3$ into **7.3**: a) **7.3**; b) 0.25 eq.; c) 0.67 eq.; d) 1 eq. (400 MHz, DMSO-d_6, 298 K).

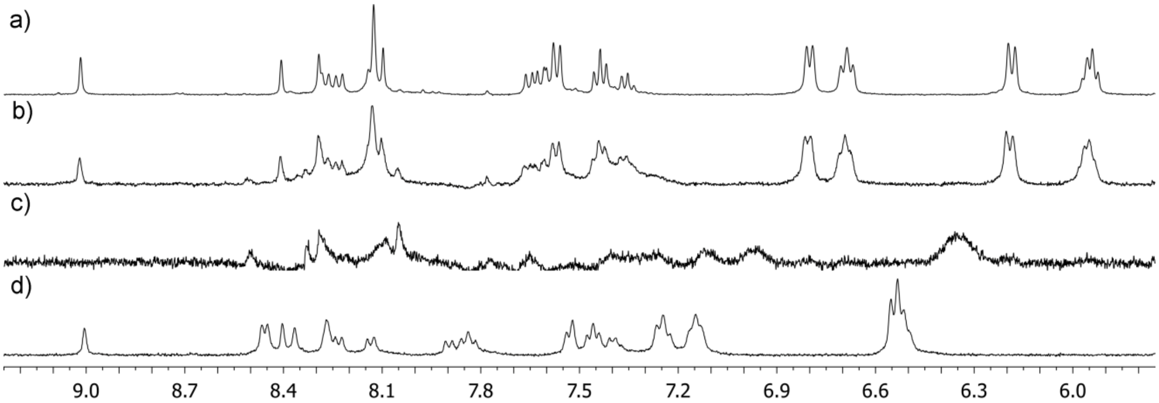

Figure 8.86: Titration of $Y(OTf)_3$ into **7.5b**: a) **7.5b**; b) 0.33 eq.; c) 0.67 eq.; d) 1.5 eq. (400 MHz, DMSO-d_6, 298 K).

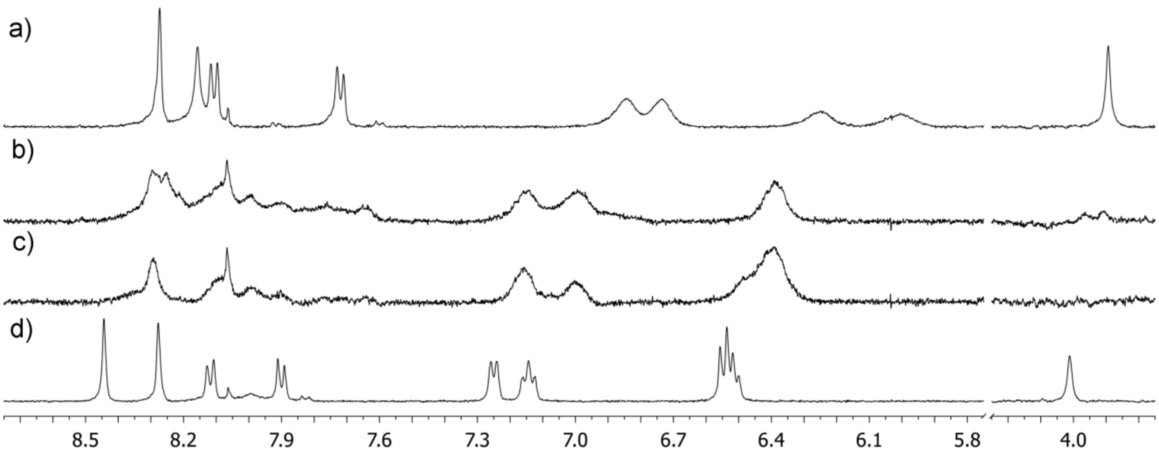

Figure 8.87: Titration of Y(OTf)$_3$ into **7.8**: a) **7.8**; b) 0.33 eq.; c) 0.67 eq.; d) 1.5 eq. (400 MHz, DMSO-d_6, 298 K).

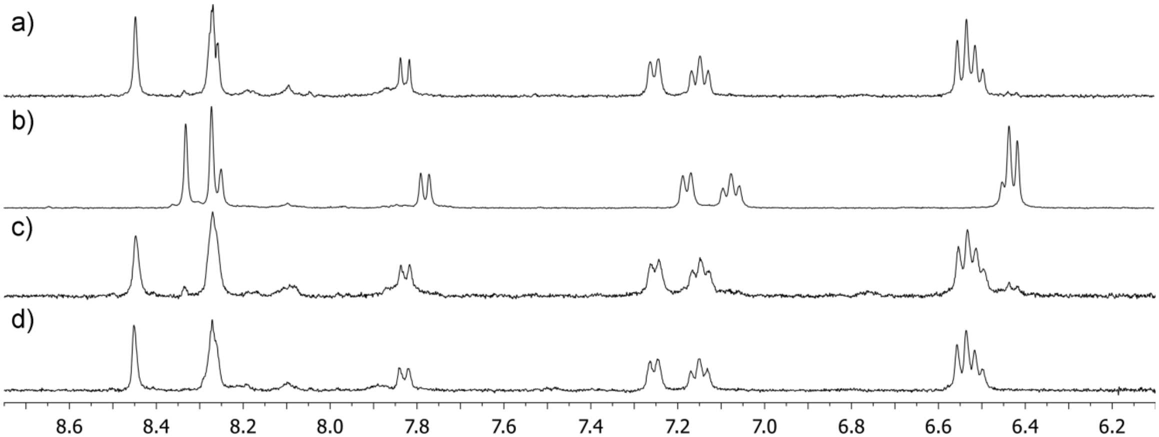

Figure 8.88: Displacement of La by Y: a) Na$_6$[(**7.3**)$_3$Y$_2$]; b) Na$_6$[(**7.3**)$_3$La$_2$]; c) Na$_6$[(**7.3**)$_3$Y$_2$] + 0.67 eq La(OTf)$_3$; d) Na$_6$[(**7.3**)$_3$La$_2$] + 0.67 eq Y(OTf)$_3$ (400 MHz, DMSO-d_6, 298 K).

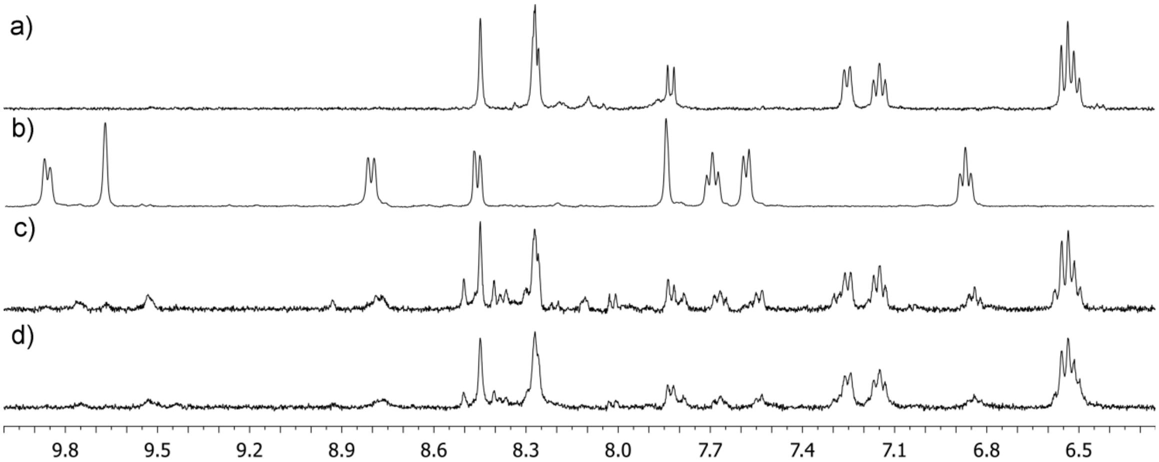

Figure 8.89: Displacement of Sm by Y: a) Na$_6$[(**7.3**)$_3$Y$_2$]; b) Na$_6$[(**7.3**)$_3$Sm$_2$]; c) Na$_6$[(**7.3**)$_3$Y$_2$] + 0.67 eq Sm(OTf)$_3$; d) Na$_6$[(**7.3**)$_3$Sm$_2$] + 0.67 eq Y(OTf)$_3$ (400 MHz, DMSO-d_6, 298 K).

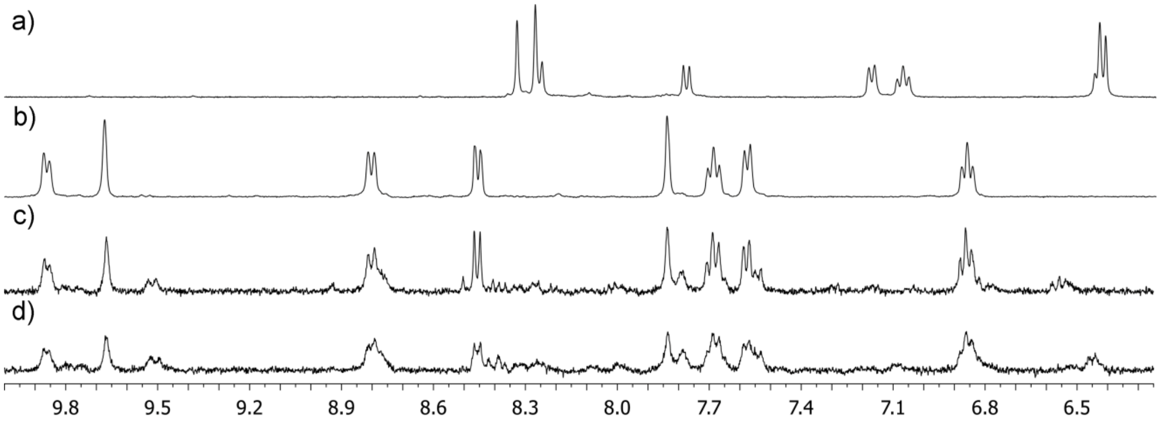

Figure 8.90: Displacement of La by Sm: a) $Na_6[(\mathbf{7.3})_3La_2]$; b) $Na_6[(\mathbf{7.3})_3Sm_2]$; c) $Na_6[(\mathbf{7.3})_3La_2]$ + 0.67 eq $Sm(OTf)_3$; d) $Na_6[(\mathbf{7.3})_3Sm_2]$ + 0.67 eq $La(OTf)_3$ (400 MHz, DMSO-d_6, 298 K).

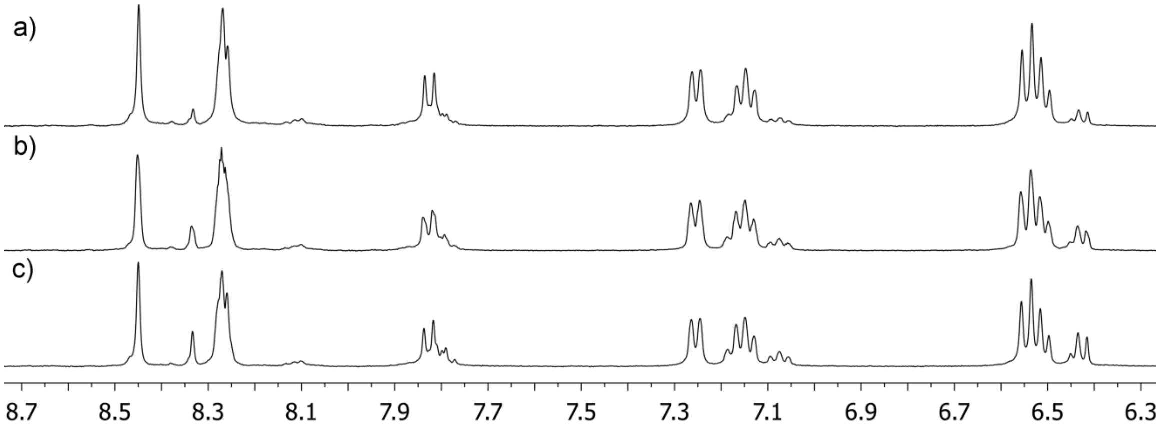

Figure 8.91: Equilibration of $Na_6[(\mathbf{7.3})_3Y_2]$ and $Na_6[(\mathbf{7.3})_3La_2]$: a) 0 h; b) 5.6 h; c) 25.6 h (400 MHz, DMSO-d_6, 298 K).

time (h)	$Na_6[(\mathbf{7.3})_3Y_2]$ (mM)	$Na_6[(\mathbf{7.3})_3La_2]$ (mM)
0	4.39	0.57
5.57	4.02	0.94
25.58	3.86	1.1

Table 8.19: Concentration of $Na_3[(\mathbf{7.3})_3Y_2]$ and $Na_3[(\mathbf{7.3})_3La_2]$ versus time.

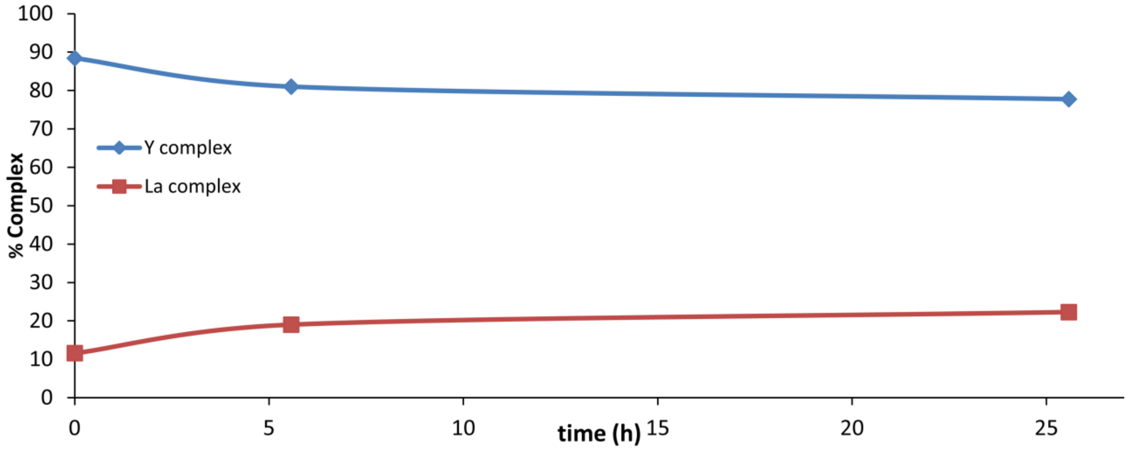

Figure 8.92: Graph of percent ligand versus time in equilibration of Na$_6$[(**7.3**)$_3$Y$_2$] and Na$_6$[(**7.3**)$_3$La$_2$].

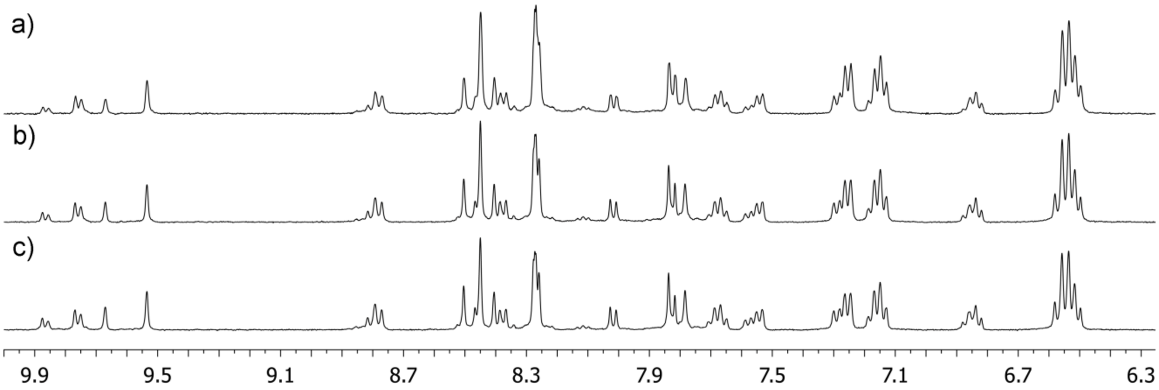

Figure 8.93: Equilibration of Na$_6$[(**7.3**)$_3$Y$_2$] and Na$_6$[(**7.3**)$_3$Sm$_2$]: a) 0 h; b) 5.6 h; c) 25.6 h (400 MHz, DMSO-d_6, 298 K).

time (h)	Na$_6$[(**7.3**)$_3$Y$_2$] (mM)	Na$_6$[(**7.3**)$_3$Sm$_2$] (mM)	Na$_6$[(**7.3**)$_3$YSm] (mM)
0	2.73	0.38	1.84
5.55	2.41	0.51	2.03
25.58	2.22	0.62	2.12

Table 8.20: Concentration of Na$_3$[(**7.3**)$_3$Y$_2$] and Na$_3$[(**7.3**)$_3$Sm$_2$] versus time.

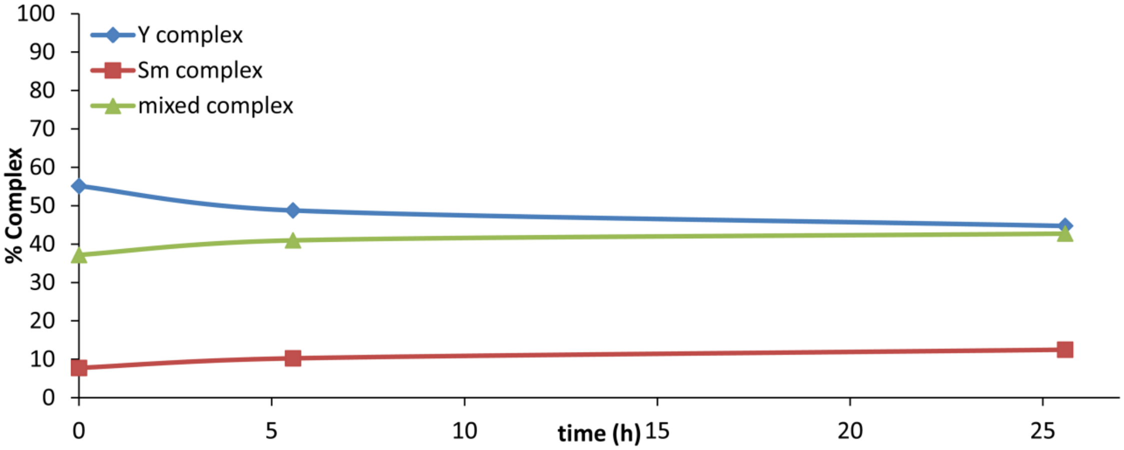

Figure 8.94: Graph of percent ligand versus time in equilibration of $Na_6[(\mathbf{7.3})_3Y_2]$ and $Na_6[(\mathbf{7.3})_3Sm_2]$.

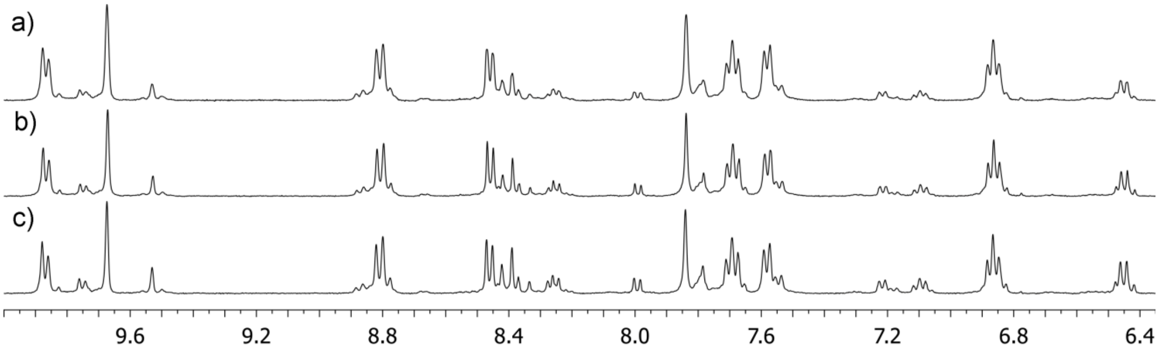

Figure 8.95: Equilibration of $Na_6[(\mathbf{7.3})_3La_2]$ and $Na_6[(\mathbf{7.3})_3Sm_2]$: a) 0 h; b) 5.6 h; c) 25.6 h (400 MHz, DMSO-d_6, 298 K).

time (h)	$Na_6[(\mathbf{7.3})_3La_2]$ (mM)	$Na_6[(\mathbf{7.3})_3Sm_2]$ (mM)	$Na_6[(\mathbf{7.3})_3LaSm]$ (mM)
0	0.18	3.54	3.54
5.55	0.22	3.26	1.48
25.58	0.32	3.02	1.62

Table 8.21: Concentration of $Na_3[(\mathbf{7.3})_3La_2]$ and $Na_3[(\mathbf{7.3})_3Sm_2]$ versus time.

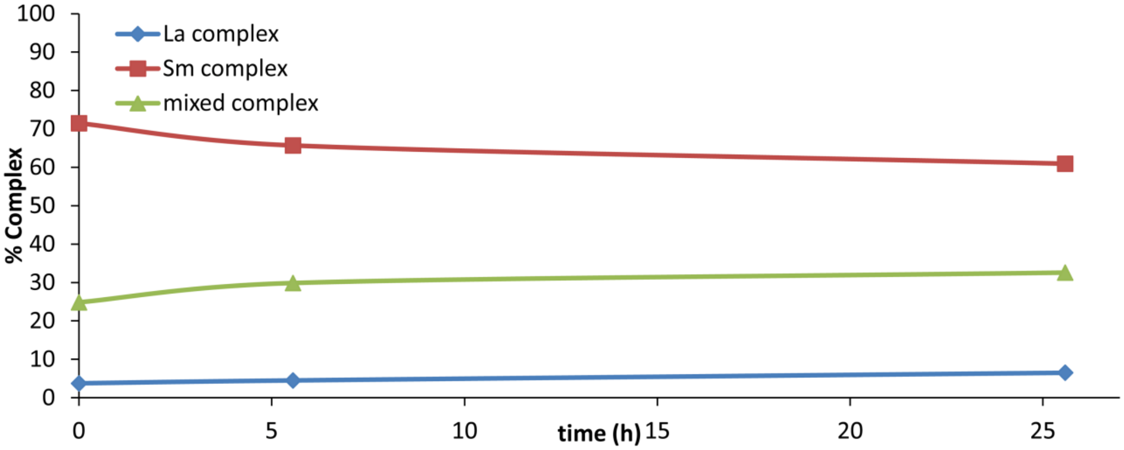

Figure 8.96: Graph of percent ligand versus time in equilibration of $Na_6[(\mathbf{7.3})_3La_2]$ and $Na_6[(\mathbf{7.3})_3Sm_2]$.

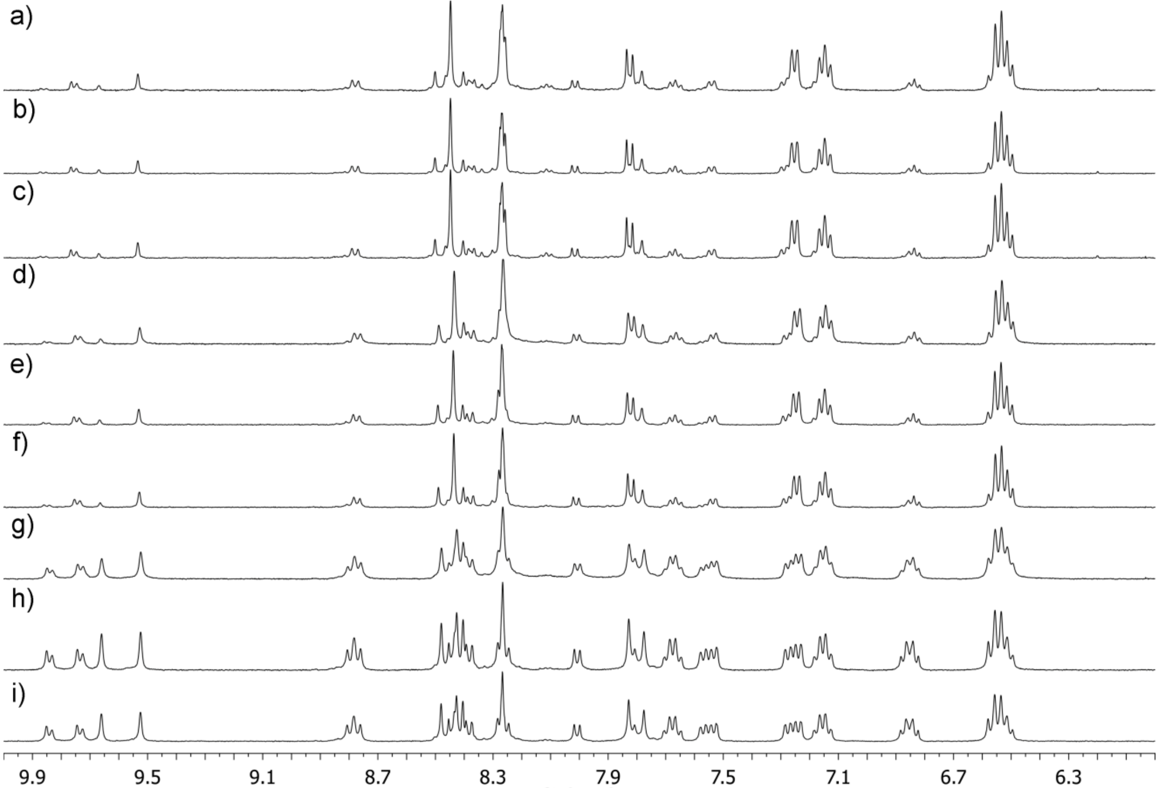

Figure 8.97: Effect of water on equilibration in $Na_6[(\mathbf{7.3})_3Y_2]$ and $Na_6[(\mathbf{7.3})_3Sm_2]$: a) **7.3** + $Y(OTf)_3$ + $Sm(OTf)_3$; b) 6.5 h; c) 23.5 h; d) **7.3** + $Y(OTf)_3$ + $Sm(OTf)_3$ + 10 μL D_2O; e) 6.5 h; f) 23.5 h; g) **7.3** + $Y(OTf)_3$ + $Sm(OTf)_3$ + 20 μL D_2O; h) 6.5 h; i) 23.5 h.

	0 h	6.47 h	23.47 h
$Na_6[(\mathbf{7.3})_3Y_2]$ (mM)	2.88	2.79	2.81
$Na_6[(\mathbf{7.3})_3Sm_2]$ (mM)	0.17	0.18	0.17
$Na_6[(\mathbf{7.3})_3YSm]$ (mM)	1.11	1.19	1.19
$Na_6[(\mathbf{7.3})_3Y_2]$ (mM) 10 µL D_2O	2.53	2.55	2.50
$Na_6[(\mathbf{7.3})_3Sm_2]$ (mM) 10 µL D_2O	0.20	0.20	0.18
$Na_6[(\mathbf{7.3})_3YSm]$ (mM) 10 µL D_2O	1.35	1.33	1.39
$Na_6[(\mathbf{7.3})_3Y_2]$ (mM) 20 µL D_2O	1.73	1.43	1.46
$Na_6[(\mathbf{7.3})_3Sm_2]$ (mM) 20 µL D_2O	0.63	0.83	0.82
$Na_6[(\mathbf{7.3})_3YSm]$ (mM) 20 µL D_2O	1.64	1.73	1.72

Table 8.22: Concentration of $Na_3[(\mathbf{7.3})_3Y_2]$ and $Na_3[(\mathbf{7.3})_3Sm_2]$ versus time in samples with varying amounts of water.

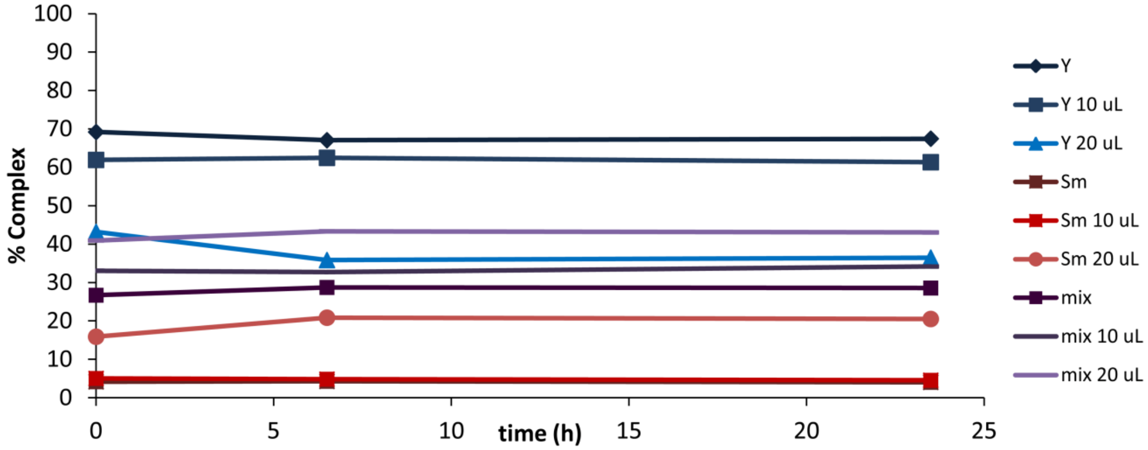

Figure 8.98: Graph of percent ligand versus time in equilibration of $Na_6[(\mathbf{7.3})_3La_2]$ and $Na_6[(\mathbf{7.3})_3Sm_2]$.

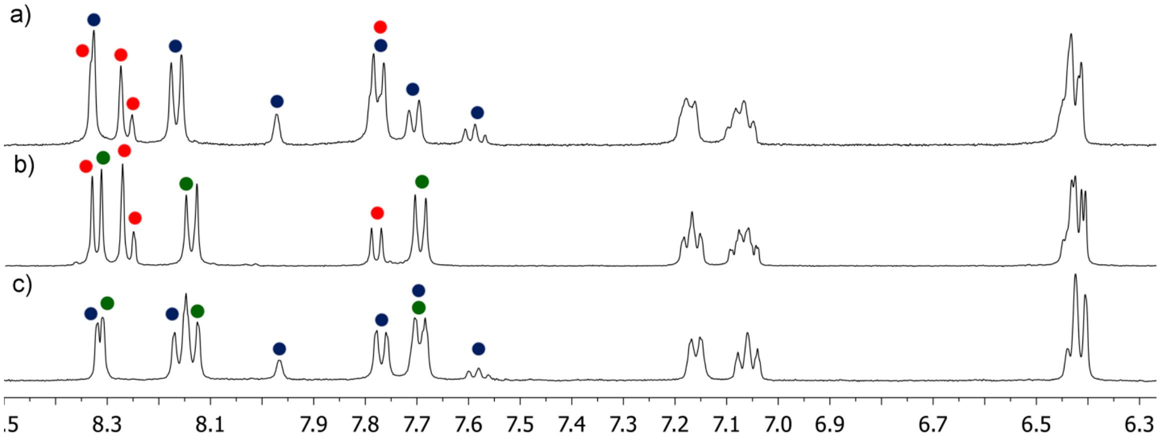

Figure 8.99: Narcissistic self-sorting in La complexes of **7.3**, **7.9**, and **7.10**: a) **7.3** + **7.9** + La(OTf)$_3$; b) **7.3** + **7.10** + La(OTf)$_3$; c) **7.9** + **7.10** + La(OTf)$_3$ (400 MHz, DMSO-d_6, 298 K). Red=Na$_6$[(**7.3**)$_3$La$_2$], blue= Na$_6$[(**7.9**)$_3$La$_2$], green= Na$_{12}$[(**7.10**)$_6$La$_4$].

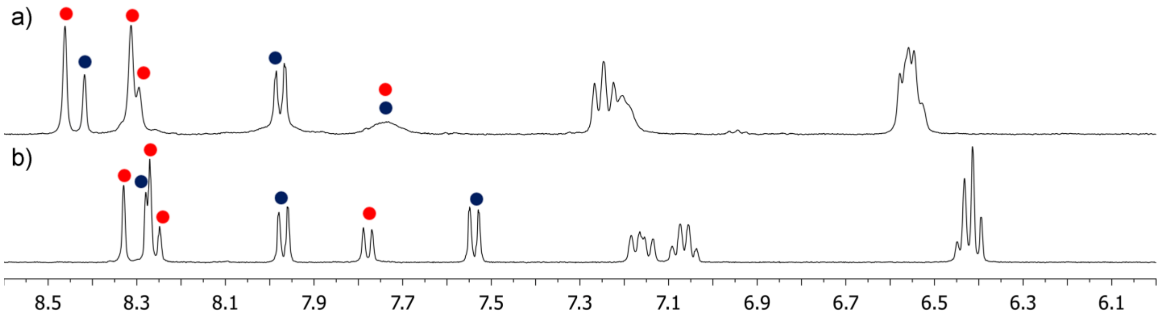

Figure 8.100: Narcissistic self-sorting in Y and La complexes of **7.3** and **7.11a**: a) **7.3** + **7.11a** + Y(OTf)$_3$; b) **7.3** + **7.11a** + La(OTf)$_3$ (400 MHz, DMSO-d_6, 298 K). Red= Na$_6$[(**7.3**)$_3$Ln$_2$], blue= Na$_3$[(**7.3**)$_3$Ln].

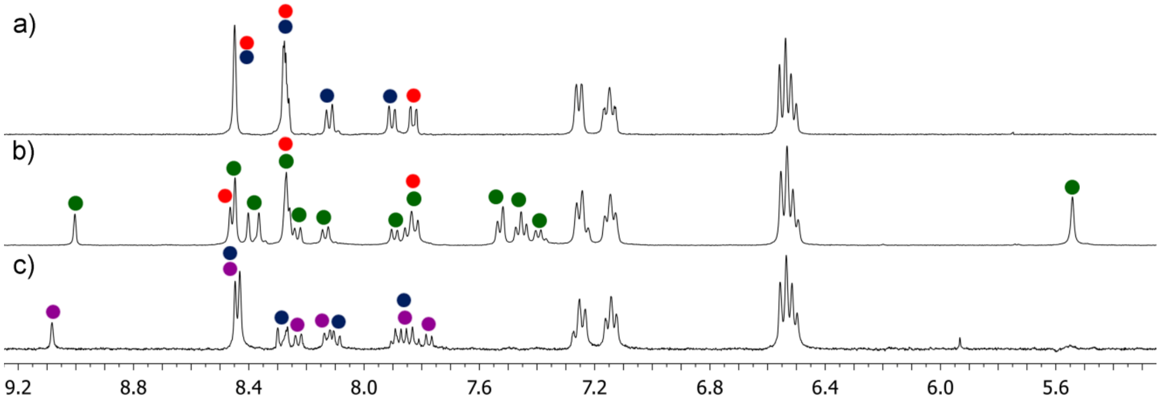

Figure 8.101: Narcissistic self-sorting in Y complexes of **7.3**, **7.5a**, **7.5b**, and **7.8**: a) **7.3** + **7.8** + Y(OTf)$_3$; b) **7.3** + **7.5b** + Y(OTf)$_3$; c) **7.5a** + **7.8** + Y(OTf)$_3$ (400 MHz, DMSO-d_6, 298 K). Red=Na$_6$[(**7.3**)$_3$Y$_2$], blue=Na$_6$[(**7.8**)$_3$Y$_2$], green=Na$_6$[(**7.5b**)$_3$Y$_2$], purple=Na$_6$[(**7.5a**)$_3$Y$_2$].

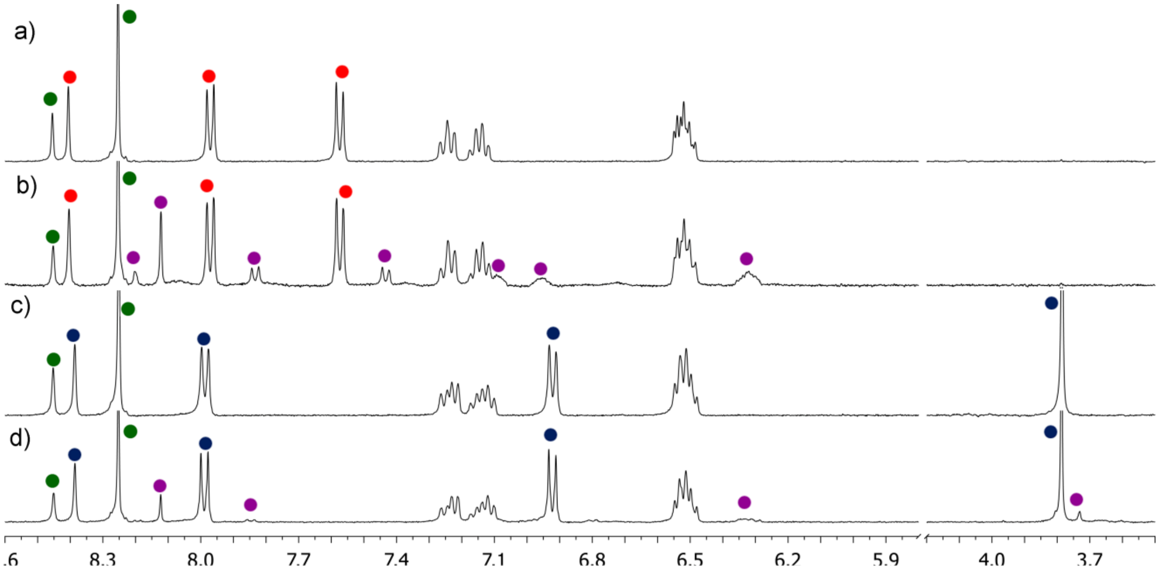

Figure 8.102: Mixing in Y complexes of controls: a) **7.11a** + **7.11c** + Y(OTf)$_3$; b) **7.11a** + **7.11c** + Y(OTf)$_3$ 60 °C overnight; c) **7.11b** + **7.11c** + Y(OTf)$_3$; c) **7.11b** + **7.11c** + Y(OTf)$_3$ 60 °C overnight (400 MHz, DMSO-*d*$_6$, 298 K). Red=Na$_3$[(**7.11a**)$_3$Y], blue=Na$_3$[(**7.11b**)$_3$Y], green=Na$_3$[(**7.11c**)$_3$Y], purple=heterocomplexes.

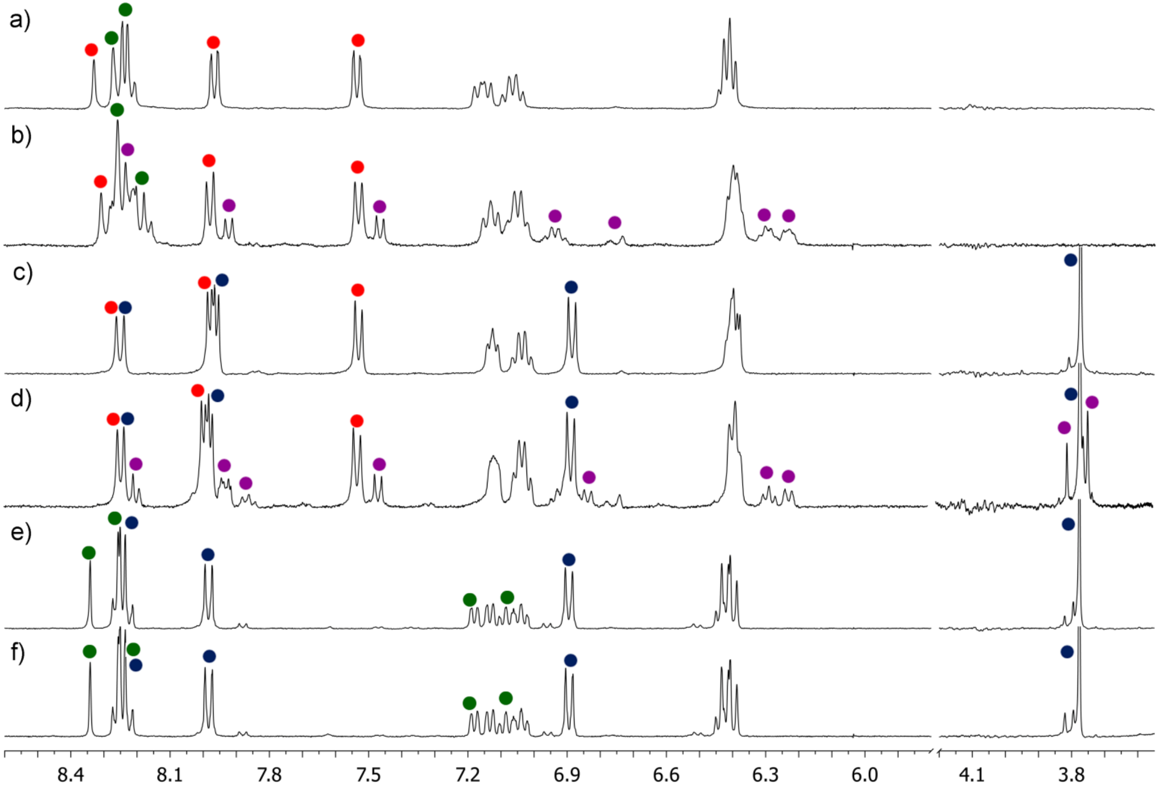

Figure 8.103: Mixing in La complexes of controls: a) **7.11a** + **7.11c** + La(OTf)$_3$; b) **7.11a** + **7.11c** + La(OTf)$_3$ 60 °C overnight; c) **7.11a** + **7.11b** + La(OTf)$_3$; d) **7.11a** + **7.11b** + La(OTf)$_3$ 60 °C overnight; e) **7.11b** + **7.11c** + La(OTf)$_3$; f) **7.11b** + **7.11c** + La(OTf)$_3$ 60 °C overnight (400 MHz, DMSO-*d*$_6$, 298 K). Red=Na$_3$[(**7.11a**)$_3$La], blue=Na$_3$[(**7.11b**)$_3$La], green=Na$_3$[(**7.11c**)$_3$La], purple=heterocomplexes.

8.9 Selected Mass Spectra

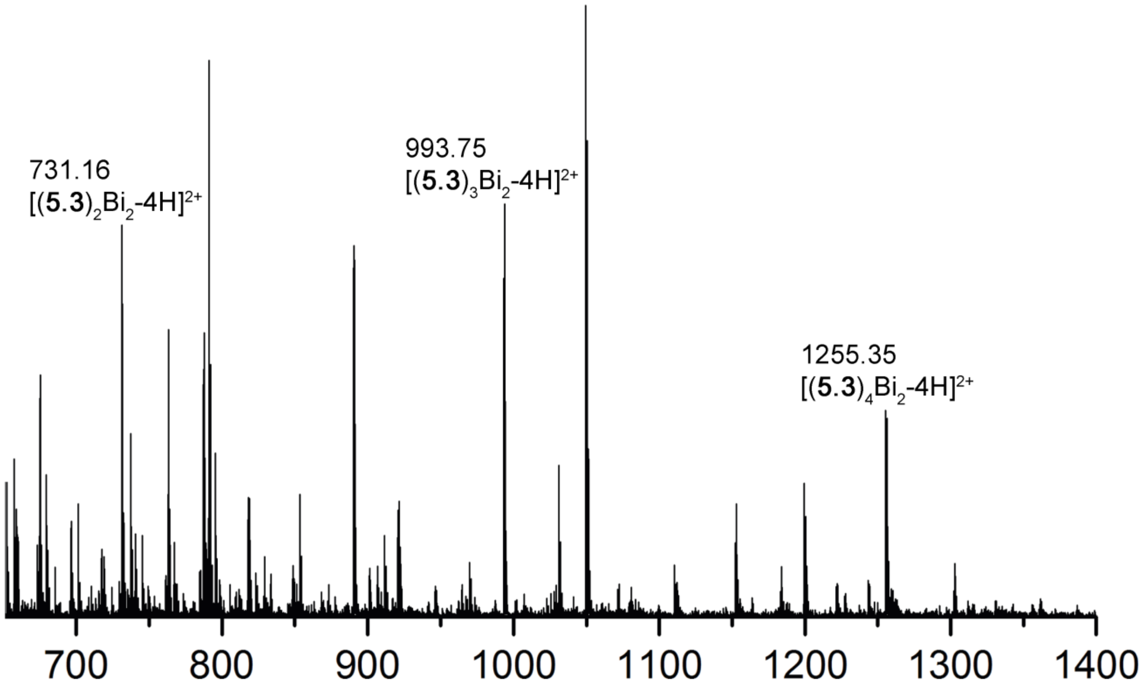

Figure 8.104: ESI-MS spectra (MeCN) of **5.3** + 0.5 eq Bi(OTf)$_3$ showing enhancement of the M$_2$L$_4$ complex.

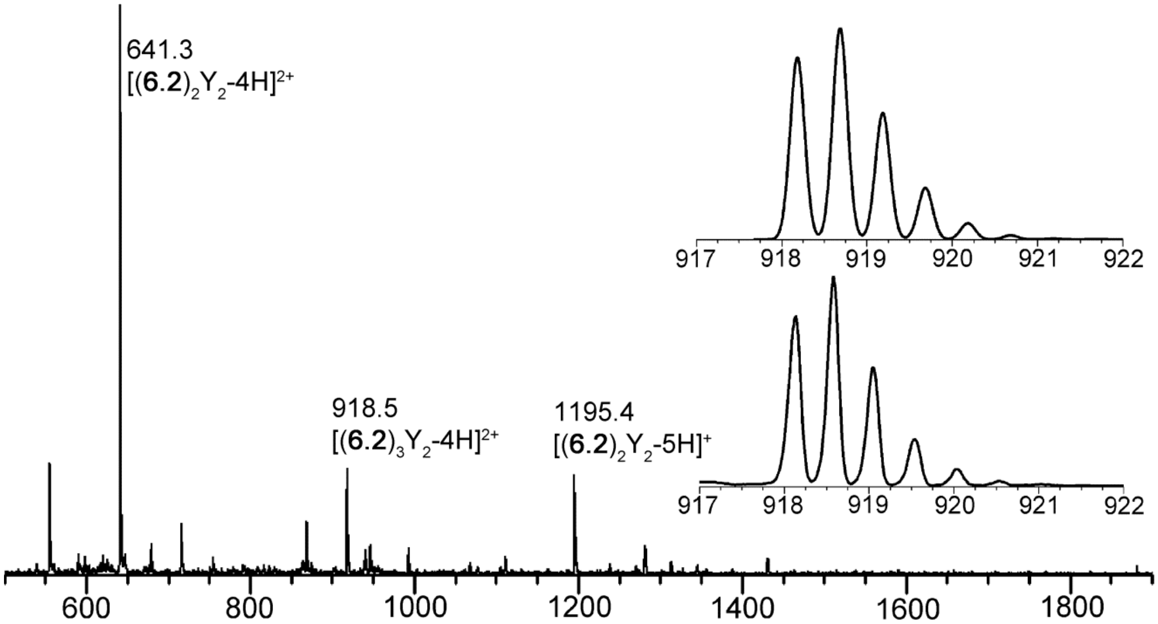

Figure 8.105: ESI-MS (THF) of [(**6.2**)$_3$Y$_2$-6H] with predicted and experimental isotopic distributions.

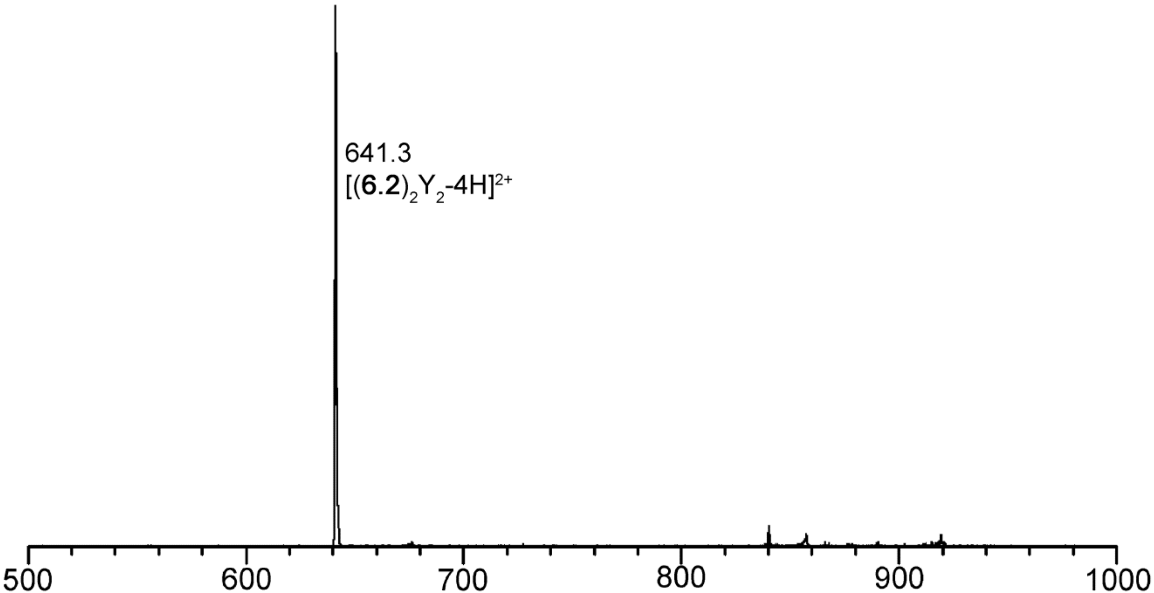

Figure 8.106: MS/MS of [(**6.2**)$_3$Y$_2$-4H]$^{2+}$ showing fragmentation into [**1**$_2$Y$_2$-4H]$^{2+}$.

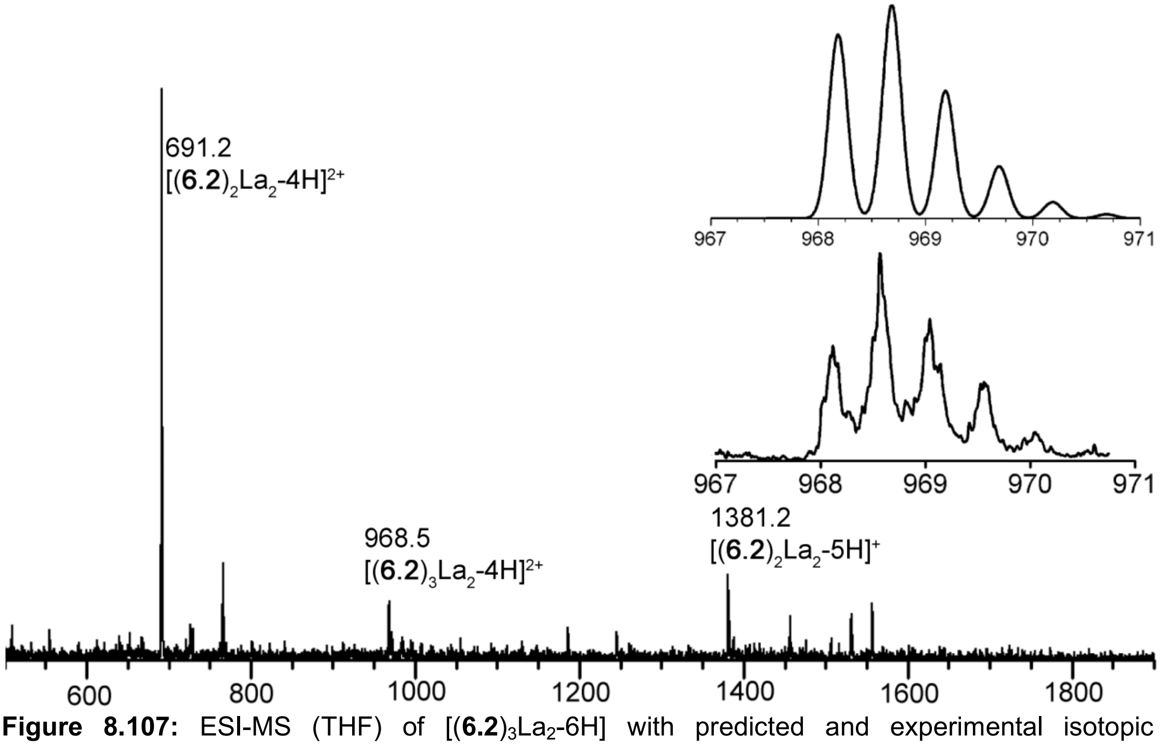

Figure 8.107: ESI-MS (THF) of [(**6.2**)$_3$La$_2$-6H] with predicted and experimental isotopic distributions.

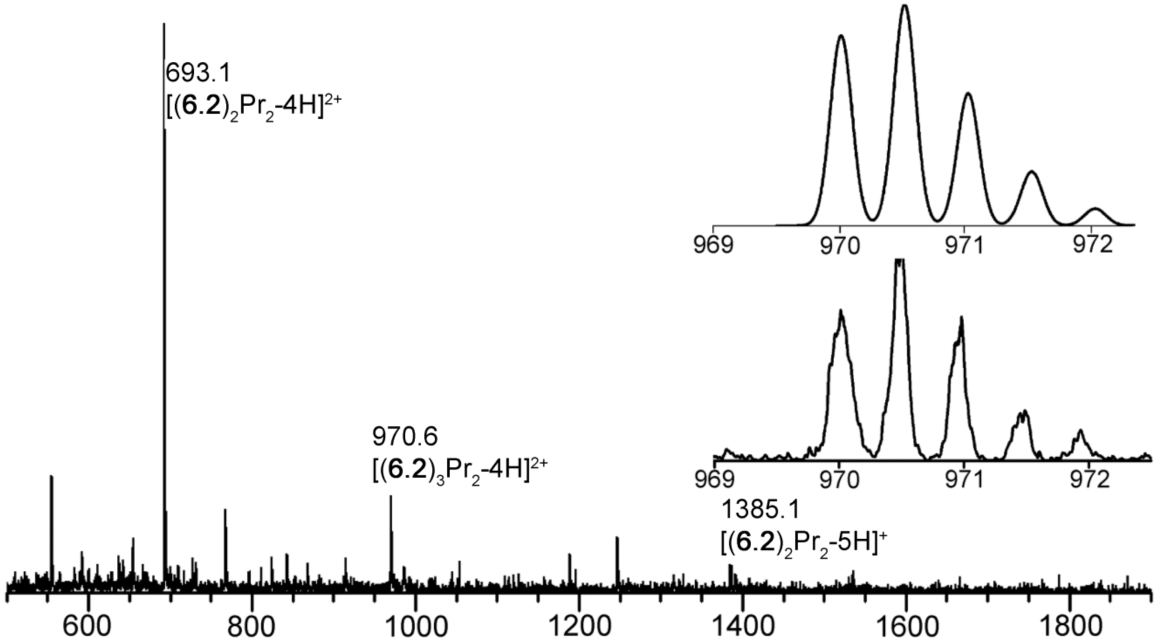

Figure 8.108: ESI-MS (THF) of [(**6.2**)$_3$Pr$_2$-6H] with predicted and experimental isotopic distributions.

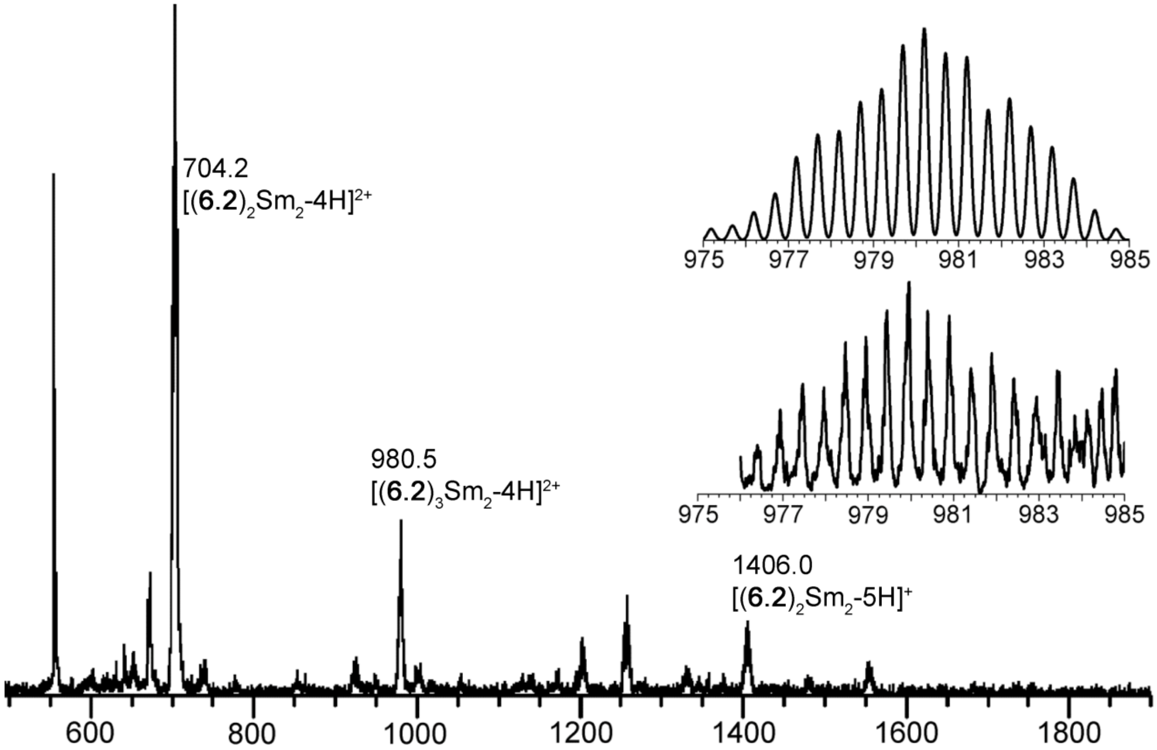

Figure 8.109: ESI-MS (THF) of [(**6.2**)$_3$Sm$_2$-6H]with predicted and experimental isotopic distributions.

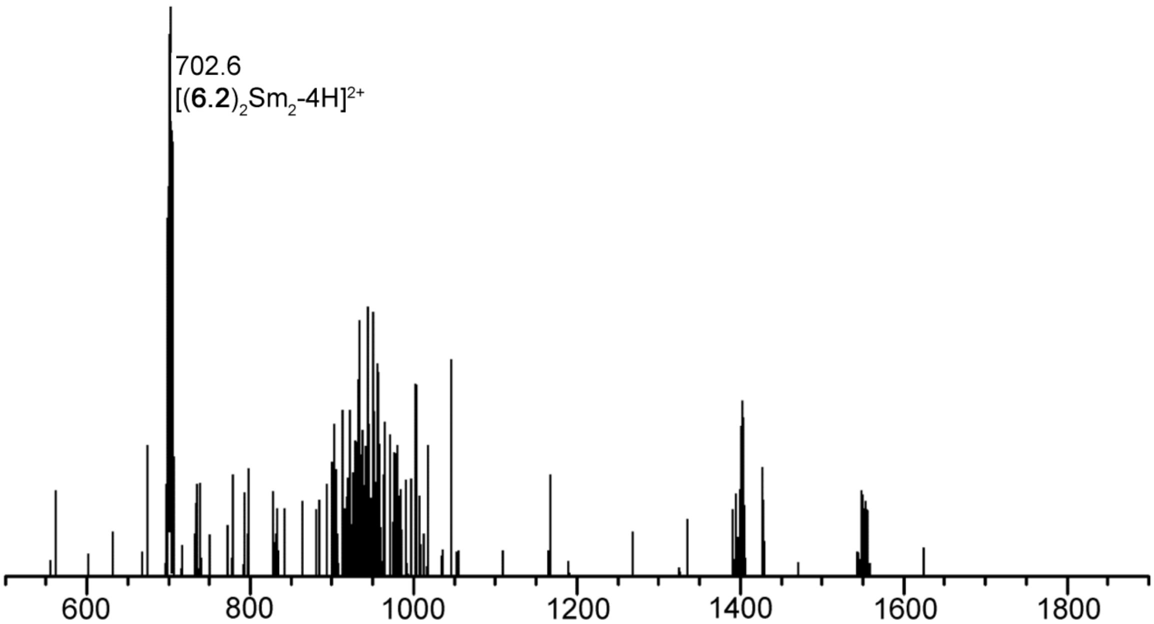

Figure 8.110: MS/MS of [(**6.2**)$_3$Sm$_2$-4H]$^{2+}$ showing fragmentation into [(**6.2**)$_2$Sm$_2$-4H]$^{2+}$.

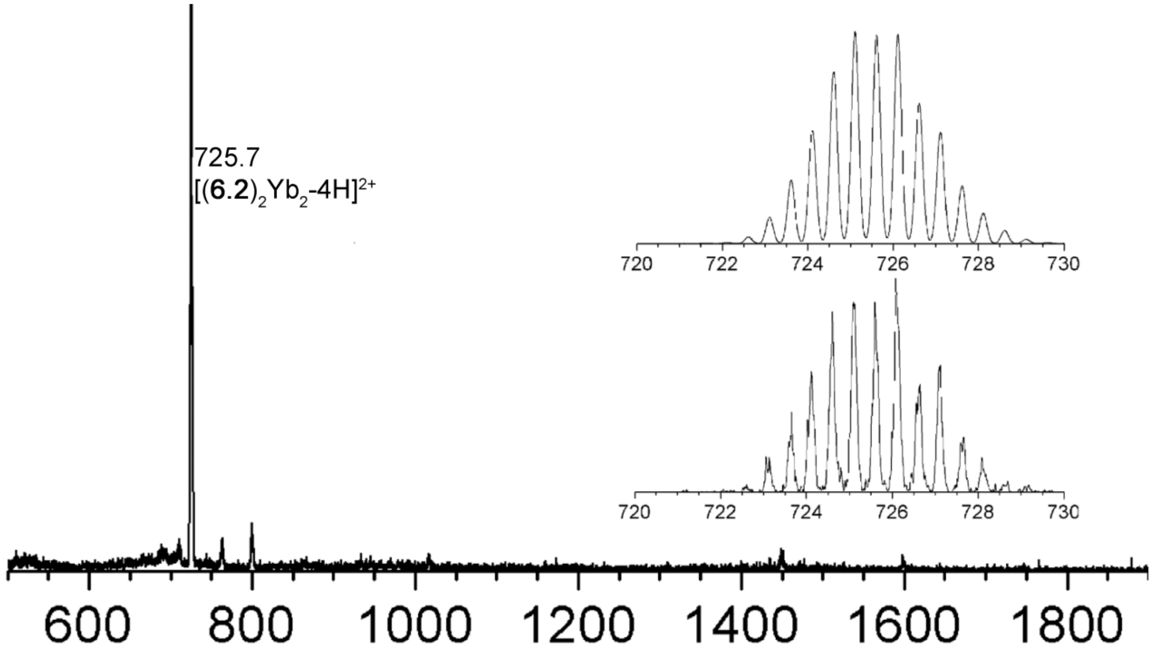

Figure 8.111: ESI-MS (THF) of [(**6.2**)$_2$Yb$_2$-4H](OTf)$_2$ with predicted and experimental isotopic distributions.

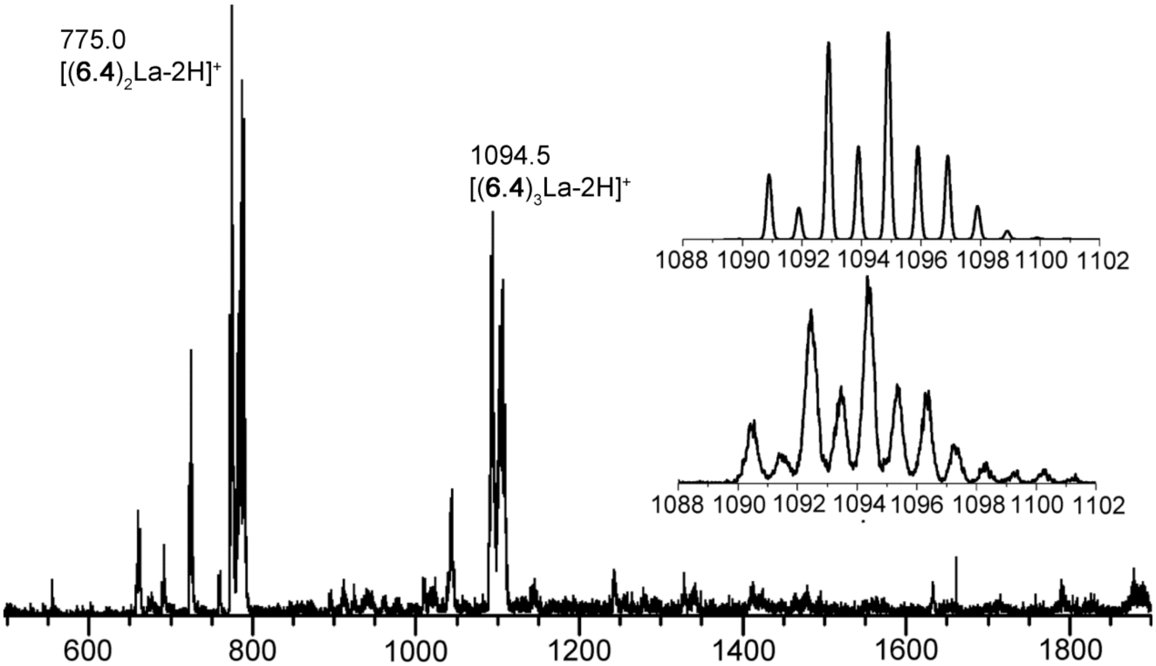

Figure 8.112: ESI-MS (THF) of [(**6.4**)$_3$La-3H] with predicted and experimental isotopic distributions.

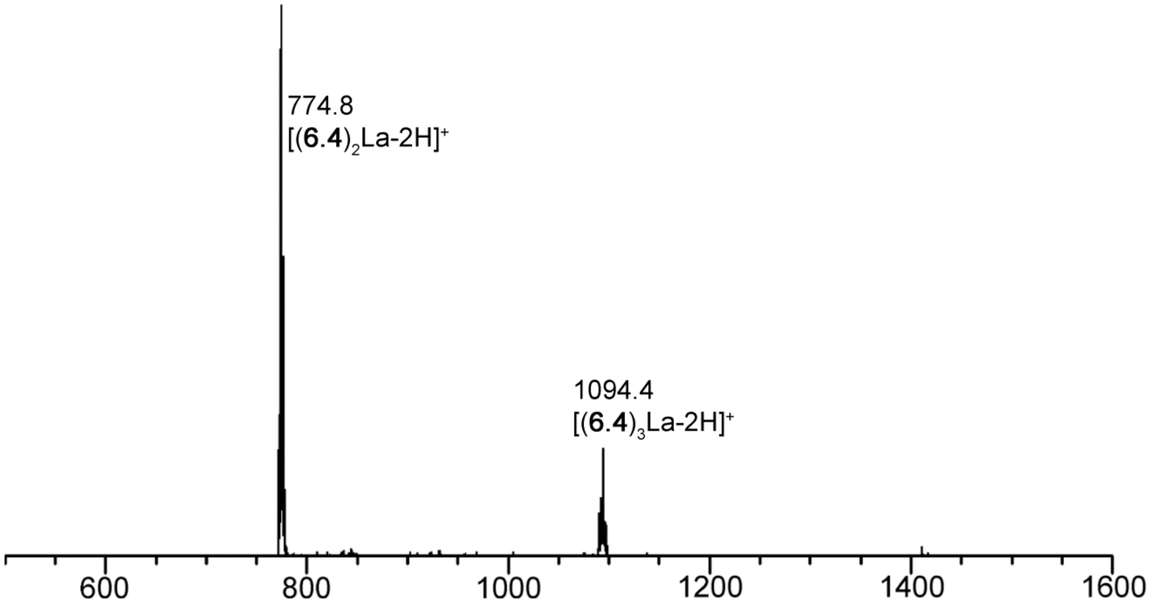

Figure 8.113: MS/MS of [(**6.4**)$_3$La-2H]$^+$ showing fragmentation into [(**6.4**)$_2$La-2H]$^+$.

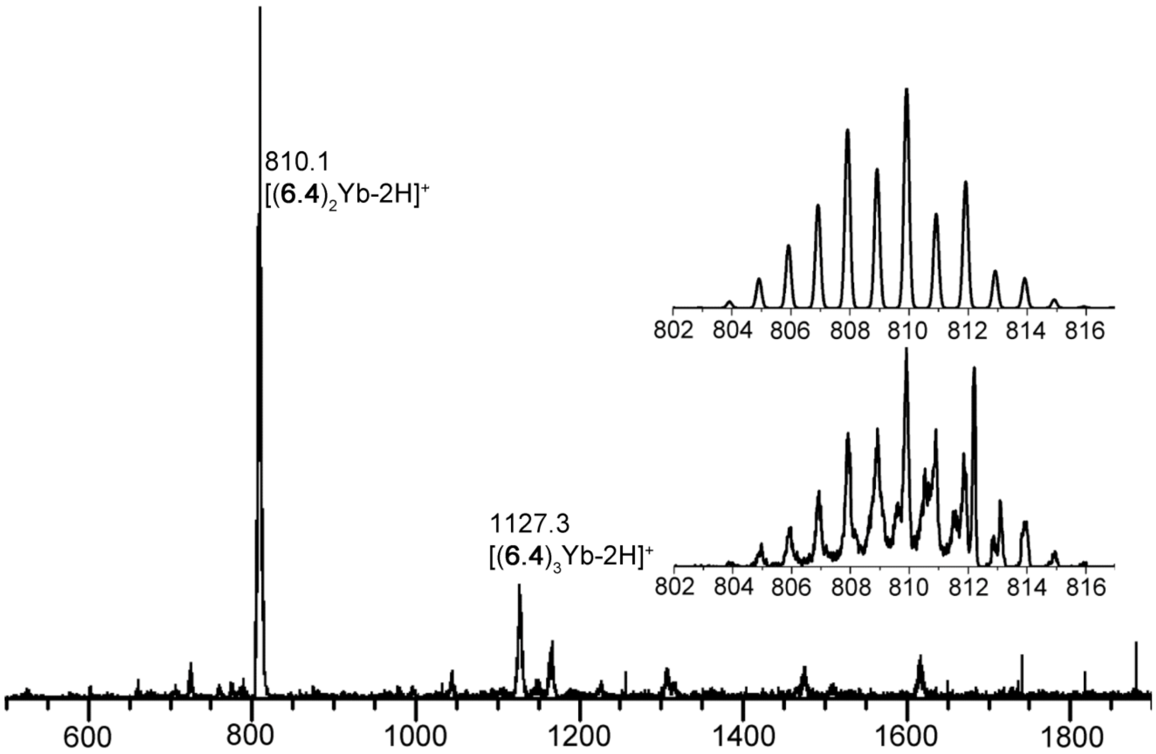

Figure 8.114: ESI-MS (THF) of [(**6.4**)$_2$Yb-3H] with predicted and experimental isotopic distributions.

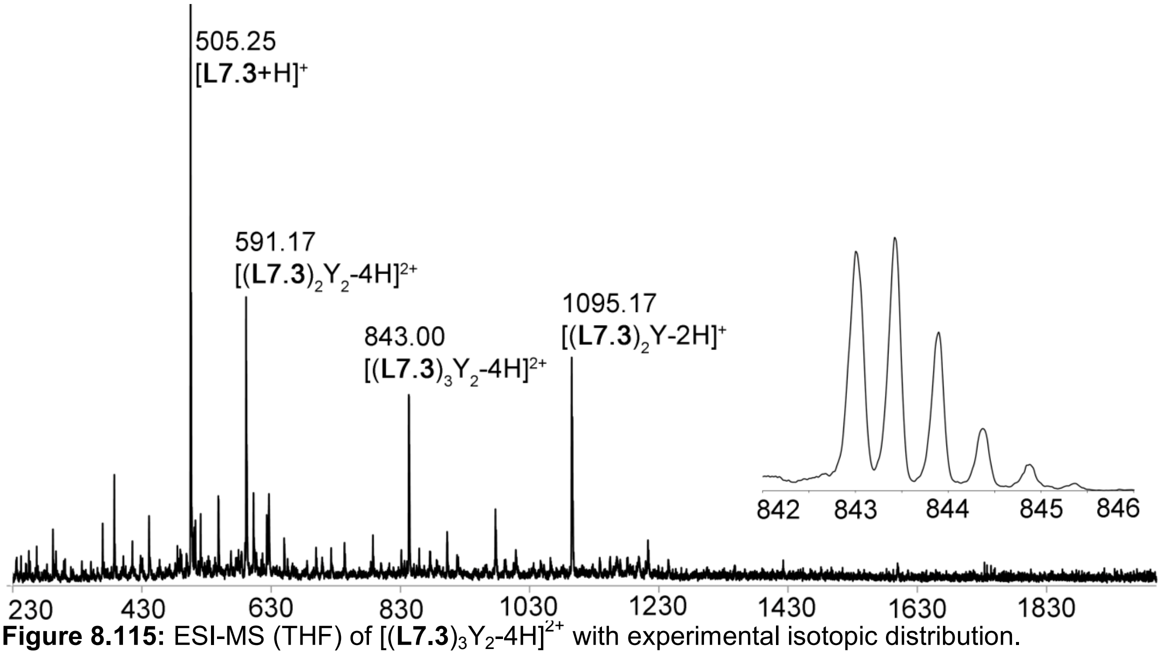

Figure 8.115: ESI-MS (THF) of [(**L7.3**)$_3$Y$_2$-4H]$^{2+}$ with experimental isotopic distribution.

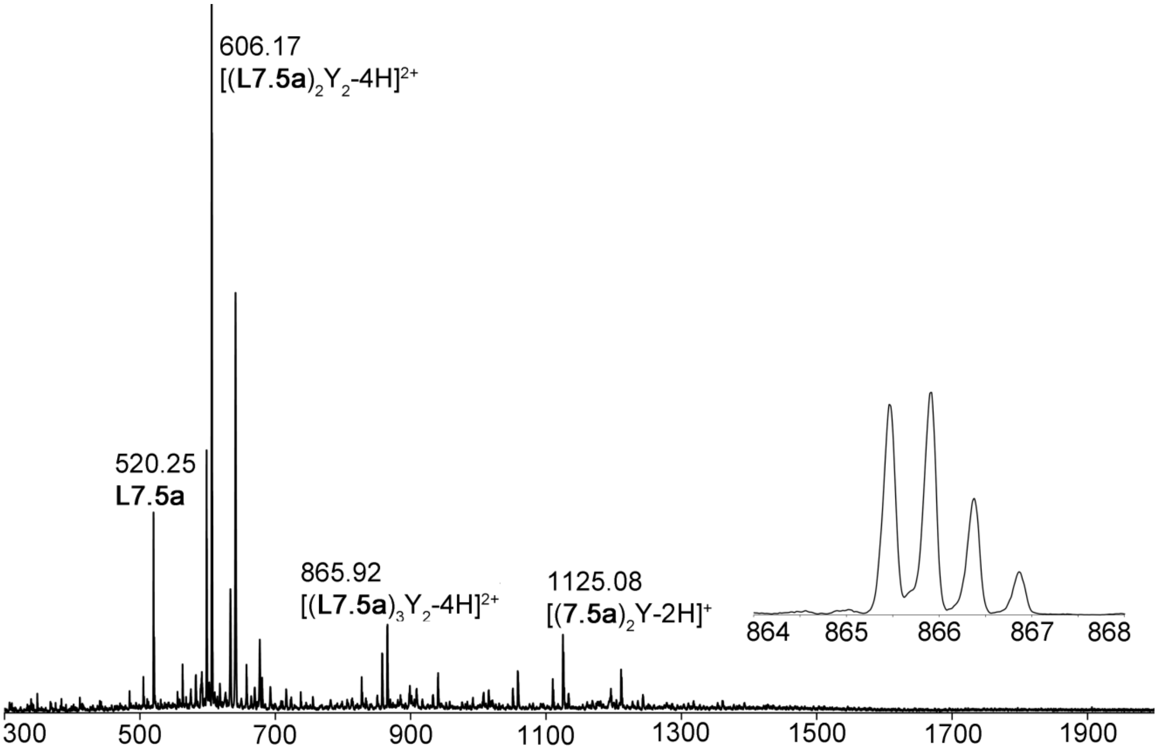

Figure 8.116: ESI-MS (THF) of $[(\mathbf{L7.5a})_3Y_2\text{-}4H]^{2+}$ with experimental isotopic distribution.

8.10 X-Ray Crystallographic Data

X-Ray Structure determination of $[(2.3)_4Pd_2](OTf)_4$:

A colorless prism fragment (0.40 x 0.38 x 0.35 mm^3) was used for the single crystal x-ray diffraction study of $[C_{80}H_{48}N_8Pd_2]^{4+}[CF_3SO_3]^{-4}$ ((4•OTf)4.). The crystal was coated with paratone oil and mounted on to a cryo-loop glass fiber. X-ray intensity data were collected at 100(2) K on a Bruker APEX2[3] platform-CCD x-ray diffractometer system (Mo-radiation, λ = 0.71073 Å, 50KV/40mA power). The CCD detector was placed at a distance of 4.8550 cm from the crystal.

A total of 2400 frames were collected for a hemisphere of reflections (with scan width of 0.3° in ω, starting ω and 2θ angles at –30°, and φ angles of 0°, 90°, 180°, and 270° for every 600 frames, 10 sec/frame exposure time). The frames were integrated using the Bruker SAINT software package[4] and using a narrow-frame integration algorithm. Based on a monoclinic crystal system, the integrated frames yielded a total of 44210 reflections at a maximum 2θ angle of 60.06° (0.71 Å resolution), of which 16961 were independent reflections (R_{int} = 0.0236, R_{sig} = 0.0282, redundancy = 2.6, completeness = 99.7%) and 15443 (91.1%) reflections were greater than 2σ(I). Absorption corrections were applied to the raw intensity data using the SADABS program.[5]

The Bruker SHELXTL software package[6] was used for phase determination and structure refinement. The distribution of intensities (E^2-1 = 0.852) and systematic absent reflections indicated three possible space groups, C2, C2/m, and Cm. The space group Cm (#8) was later determined to be correct (one of the four triflate anions is located on a pseudo 2-fold rotation or a pseudo inversion symmetry if space group C2 or C2/m is selected, respectively, with O-O and S-S close contact warnings). Direct methods of phase determination followed by two Fourier cycles of refinement led to an electron density map from which most of the non-hydrogen atoms were identified in the asymmetry unit of the unit cell. With subsequent isotropic refinement, all of the non-hydrogen atoms were identified. There were half a cation of $[C_{80}H_{48}N_8Pd_2]^{4+}$, four half anions of $[CF_3SO_3]^-$, one half water, seven half solvent molecules of CH_3CN, one disordered and one non-disordered CH_3CN solvent molecules present in the asymmetry unit of the unit cell. The four anions, one cation, one H_2O, and seven CH_3CN solvent molecules were located on the mirror planes perpendicular to the **b**-axis. Two CH_3CN molecules were in general positions, where one was modeled as 50%/50% disordered CH_3CN solvent. The structure was refined as a racemic twin and the major/minor component ratio was 86%/14%. DFIX, SADI, DELU, and SIMU commands were used to stabilize the refinement of all the CH_3CN, H_2O molecules and the four CF_3SO_3 anions.

Atomic coordinates, isotropic and anisotropic displacement parameters of all the non-hydrogen atoms were refined by means of a full matrix least-squares procedure on F^2. The H-atoms were included in the refinement in calculated positions riding on the atoms to which they were attached, except the water hydrogen atoms. The refinement converged at R1 = 0.0326, wR2 = 0.0877, with intensity $I>2\sigma$ (I). The largest peak/hole in the final difference map was 1.109/-0.583 e/Å$_3$.

Table 8.23: Crystal data and structural refinement for $[(\mathbf{2.3})_4Pd_2](OTf)_4$:

Empirical formula	$C_{106}\ H_{83}\ F_{12}\ N_{19}\ O_{13}\ Pd_2\ S_4$	
Formula weight	2399.95	
Temperature	100(2) K	
Wavelength	0.71073 Å	
Crystal system	Monoclinic	
Space group	Cm	
Unit cell dimensions	*a* = 27.6097(22) Å	α= 90°.
	b = 15.0085(12) Å	β= 107.6573(11)°.
	c = 14.2322(11) Å	γ = 90°.
Volume	5619.7(8) Å^3	
Z	2	
Density (calculated)	1.418 Mg/m^3	
Absorption coefficient	0.482 mm^{-1}	
F(000)	2440	
Crystal size	0.40 x 0.38 x 0.35 mm^3	
Theta range for data collection	2.32 to 30.03°.	
Index ranges	$-38<=h<=38$, $-21<=k<=21$, $-20<=l<=20$	
Reflections collected	44210	
Independent reflections	16961 [R_{int} = 0.0236]	
Completeness to θ = 30.03°	99.7 %	
Absorption correction	Semi-empirical from equivalents	
Max. and min. transmission	0.8495 and 0.8292	
Refinement method	Full-matrix least-squares on F^2	
Data / restraints / parameters	16961 / 372 / 837	
Goodness-of-fit on F^2	1.032	
Final *R* indices [$I>2\sigma(I)$]	$R1$ = 0.0326, $wR2$ = 0.0877	
R indices (all data)	$R1$ = 0.0372, $wR2$ = 0.0913	
Absolute structure parameter	0.141(14)	
Largest diff. peak and hole	1.109 and -0.583 *e*.Å$^-$	

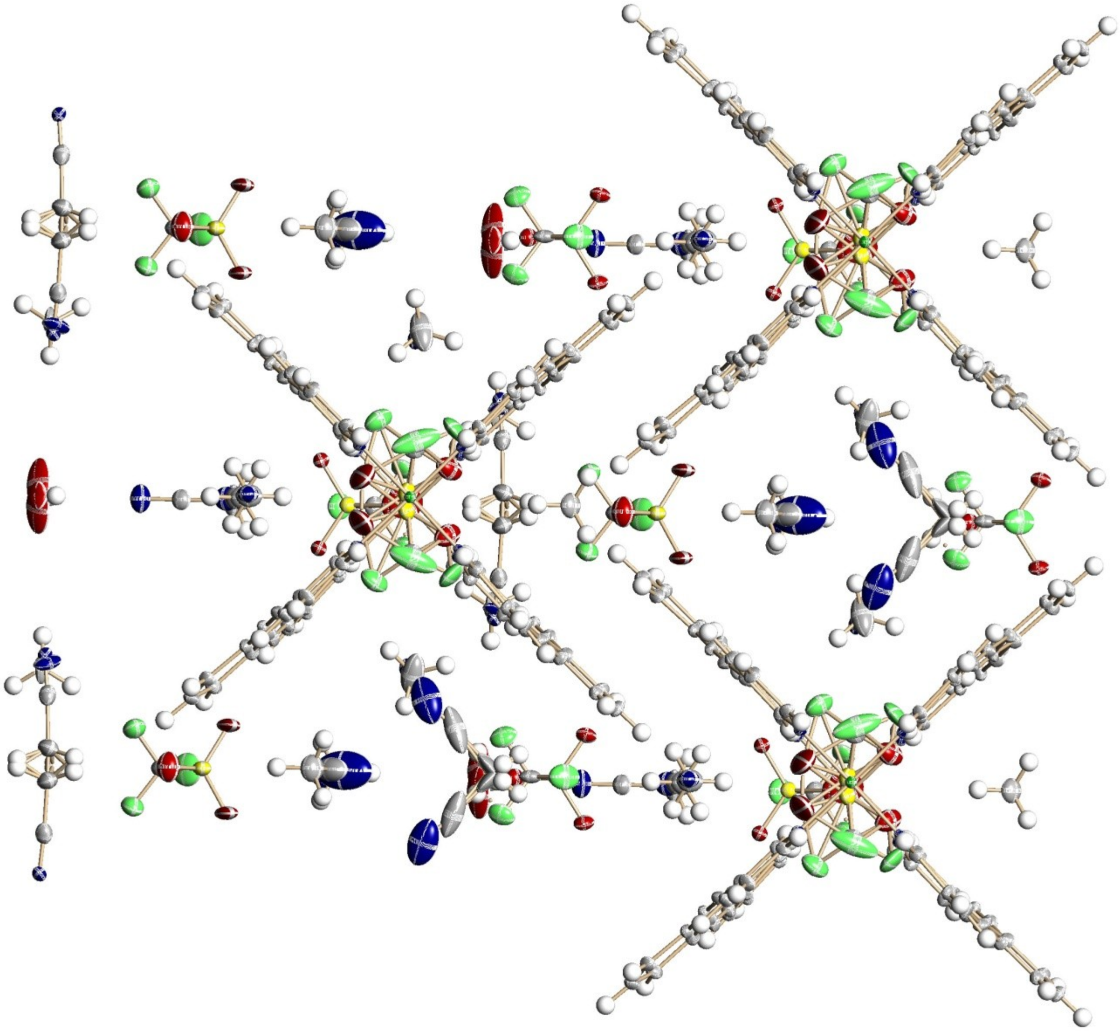

Figure 8.117: ORTEP representation of the unit cell of [(**2.3**)$_4$Pd$_2$](OTf)$_4$, indicating disordered solvent molecules and triflate ions.

X-Ray Structure Determination for [(2.6a)$_4$Pd$_2$](OTf)$_4$:

A light yellow fragment of a prism (0.43 x 0.27 x 0.18 mm^3) was used for the single crystal x-ray diffraction study of $[C_{80}H_{52}N_{12}Pd_2]_{4+}[CF_3SO_3]^{-4}$. The crystal was coated with paratone oil and mounted on to a cryo-loop glass fiber. X-ray intensity data were collected at 100(2) K on a Bruker APEX2 (platform-CCD x-ray diffractometer system (fine focus Mo-radiation, λ = 0.71073 Å, 50KV/30mA power).[3] The CCD detector was placed at a distance of 4.9890 cm from the crystal.

A total of 3600 frames were collected for a sphere of reflections (with scan width of 0.3° in ω, starting ω and 2θ angles of –30°, and φ angles of 0°, 90°, 120°, 180°, 240°, and 270° for every 600 frames, 80 sec/frame exposure time). Bruker Cell_now software[7] was used to separate the non-merohedral twinning components of the thresholded reflections. The frames were integrated using the Bruker SAINT software package[4] and using a narrow-frame integration algorithm. Based on a triclinic crystal system, the integrated frames yielded a total of 36788 reflections at a maximum 2θ angle of 59.14° (0.73 Å resolution), of which 25380 were independent reflections (R_{int} = 0.0461, redundancy = 1.4, completeness = 99.6%) and 19754 (77.8%) reflections were greater than 2σ(I). The unit cell parameters were, **a** = 12.6089(15) Å, **b** = 19.950(2) Å, **c** = 21.233(3) Å, α = 63.3356(16) °**,** β = 73.1549(17) °**,** γ = 75.7105(17) °**,** V = 4525.4(9) $Å^3$, Z = 2, calculated density D_c = 1.550 g/cm^3. Absorption corrections were applied (absorption coefficient μ = 0.586 mm^{-1}; max/min transmission = 0.9004/0.7864) to the raw intensity data using the TWINABS program.[5]

The Bruker SHELXTL software package[6] was used for phase determination and structure refinement. The distribution of intensities (E^2-1 = 0.837) and no systematic absent reflections indicated two possible space groups, P-1 and P1. The space group P-1 (#2) was later determined to be correct. Direct methods of phase determination followed by two Fourier cycles of refinement led to an electron density map from which most of the non-hydrogen atoms were identified in the asymmetry unit of the unit cell. With subsequent isotropic refinement, all of the non-hydrogen atoms were identified. There were one cation of $[C_{80}H_{52}N_{12}Pd_2]^{4+}$, four disordered anions of $[CF_3SO_3]^-$, one disordered CH_3CN, one 45% occupied disordered toluene (refined isotropically) at the inversion center, and all unresolved solvents were assumed to be partially occupied water oxygen present in the asymmetry unit of the unit cell. The structure was refined as a non-merohedral twin (twinning: 180° rotation about the real axis 2 1 1) and the major/minor component twin-ratio was 54%/46%. DFIX, SADI, DELU, SIMU, FLAT, EADP, ISOR, FVAR, BASF and SUMP commands were used to stabilize the refinement of all the CH_3CN, C_7H_8, H_2O molecules and the four CF_3SO_3 anions. The disordered site occupancy ratios for the four triflates S1E/S1F, S1G/S1H, S1I/S1J, and S1K/S1L/S1M/S1N are 63%/37%, 51%/49%, 45%/55%, and 23%/27%/18%/32%, respectively. The partially site occupancy factor for the water O-atoms were, O1W = 44%, O1X = 17%, O1Y = 39%, O2W = 50%, O3W = 50%, O4W = 41%.

Atomic coordinates, isotropic and anisotropic displacement parameters of all the non-hydrogen atoms were refined by means of a full matrix least-squares procedure on F^2. The H-atoms were included in the refinement in calculated positions riding on the atoms to which they were attached, except the water H-atoms were not included in the final refinement because the H-atoms could not be identified from the difference electron density map. The refinement converged at R1 = 0.0685, wR2 = 0.1647, with intensity, $I>2\sigma(I)$. The largest peak/hole in the final difference map was 2.195/-1.186e/$Å^3$. The high electron density peak/hole close to the two Pd-atoms were probably due to the absorption correction and possible Fourier truncation errors.

Table 8.24: Crystal data and structural refinement for $[(\mathbf{2.6a})_4\mathrm{Pd}_2](\mathrm{OTf})_4$.

Empirical formula	C89.17 H58.61 F12 N13 O14.41 Pd2 S4	
Formula weight	2111.77	
Temperature	100(2) K	
Wavelength	0.71073 Å	
Crystal system	Triclinic	
Space group	P-1	
Unit cell dimensions	*a* = 12.6089(15) Å	α= 63.3356(16)°
	b = 19.950(2) Å	β= 73.1549(17)°
	c = 21.233(3) Å	γ = 75.7105(17)°
Volume	4525.4(9) Å^3	
Z	2	
Density (calculated)	1.550 Mg/m^3	
Absorption coefficient	0.586 mm^{-1}	
F(000)	2128	
Crystal size	0.43 x 0.27 x 0.18 mm^3	
Theta range for data collection	1.70 to 29.57°	
Index ranges	$-16<=h<=17$, $-24<=k<=27$, $0<=l<=29$	
Reflections collected	36788	
Independent reflections	25380 [R_{int} = 0.0461]	
Completeness to theta = 29.57°	99.6 %	
Absorption correction	Semi-empirical from equivalents	
Max. and min. transmission	0.9004 and 0.7864	
Refinement method	Full-matrix least-squares on F^2	
Data / restraints / parameters	25380 / 2341 / 1696	
Goodness-of-fit on F^2	1.105	
Final *R* indices [I>2σ(I)]	*R*1 = 0.0685, *wR*2 = 0.1647	
R indices (all data)	*R*1 = 0.0948, *wR*2 = 0.1845	
Largest diff. peak and hole	2.195 and -1.186 *e*.Å^{-3}	

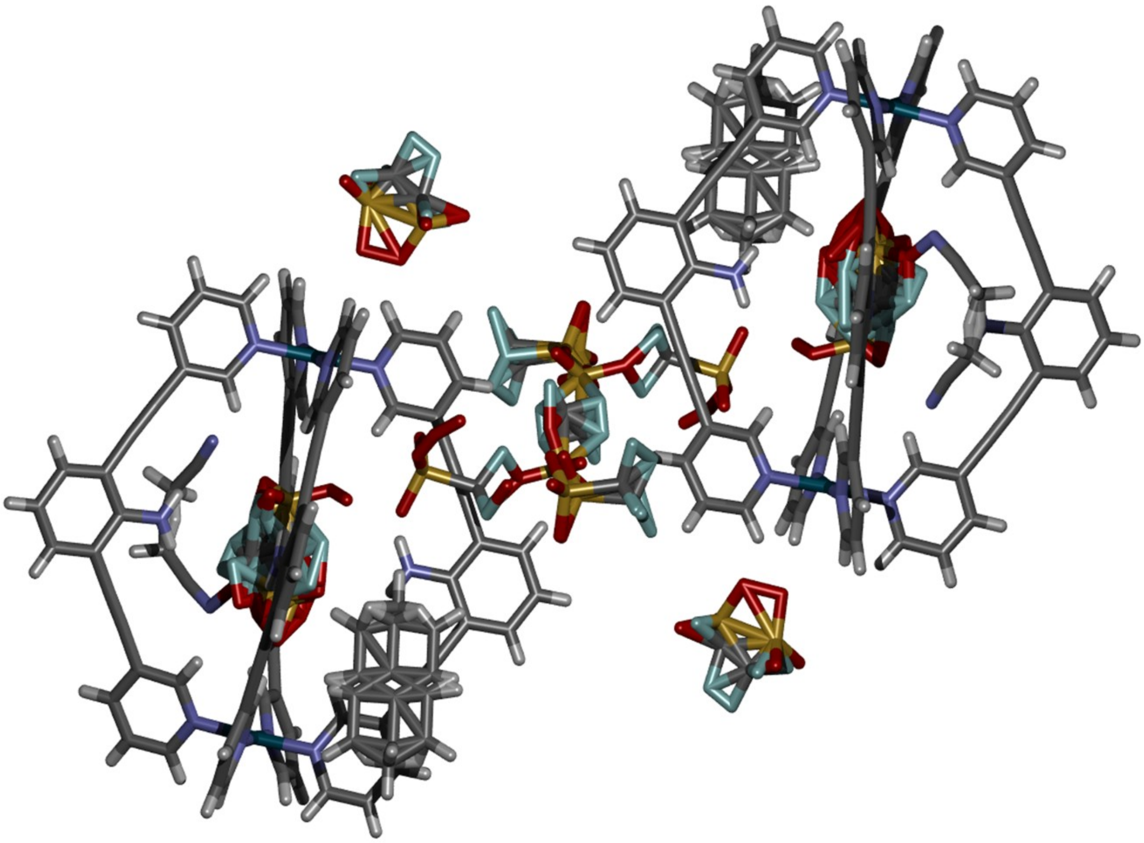

Figure 8.118: Structure of the unit cell of [(**2.6a**)$_4$Pd$_2$](OTf)$_4$, indicating disordered solvent molecules and triflate ions.

X-Ray Structure Determination for [(5.3)$_2$Bi$_2$](OTf)$_6$:

A colorless fragment of a prism (0.35 x 0.17 x 0.07 mm^3) was used for the single crystal X-ray diffraction study of [(**5.3**)$_2$Bi$_2$](OTf)$_6$ (CCDC submission #892045). The crystal was coated with paratone oil and mounted on to a cryo-loop glass fiber. X-ray intensity data were collected at 100(2) K on a Bruker APEX2[3] platform-CCD X-ray diffractometer system (fine focus Mo-radiation, λ = 0.71073 Å, 50KV/35mA power). The CCD detector was placed at a distance of 5.0000 cm from the crystal.

A total of 4800 frames were collected for a sphere of reflections (with scan width of 0.3° in ω or ϕ, starting ω and 2θ angles of –30°, and ϕ angles of 0°, 90°, 120°, 180°, 240°, and 270° for every 600 frames, and 1200 frames with ϕ-scan from 0-360°, 20 sec/frame exposure time). The frames were integrated using the Bruker SAINT software package[5] and using a narrow-frame integration algorithm. Based on a triclinic crystal system, the integrated frames yielded a total of 68323 reflections at a maximum 2θ angle of 54.96° (0.77 Å resolution), of which 13040 were independent reflections (R_{int} = 0.0256, R_{sig} = 0.0194, redundancy = 5.2, completeness = 99.8%) and 12130 (93.0%) reflections were greater than $2\theta(I)$. The unit cell parameters were, **a** = 10.5697(3) Å, **b** = 13.7043(4) Å, **c** = 20.0249(6) Å, **α** = 98.057(1) **β** = 92.112(1)°**,** **γ** = 96.452(1) V = 2849.71(14) $Å^3$, Z = 2, calculated density D_c = 1.622 g/cm^3. Absorption corrections were applied (absorption coefficient □ = 3.433 mm^{-1}; max/min transmission = 0.8001/0.3770) to the raw intensity data using the SADABS program.[5]

The Bruker SHELXTL software package[6] was used for phase determination and structure refinement. The distribution of intensities and no systematic absent reflections indicated two possible space groups, P-1 and P1. The space group P-1 (#2) was later determined to be correct. Direct methods of phase determination followed by two Fourier cycles of refinement led to an electron density map from which most of the non-hydrogen atoms were identified in the asymmetry unit of the unit cell. With subsequent isotropic refinement, all of the non-hydrogen atoms were identified. There were one ligand of $C_{32}H_{24}N_6O_2$, one Bi-cation, three disordered SO_3CF_3 anions (site occupancy ratios are 80%/20%, 81%/19%, 75%/25%), one disordered $CHCl_3$ (site occupancy ratio is 58%/42%), one disordered CH_3CN (site occupancy ratio is 73%/27%), one partially occupied CH_3CN (80% occupied), and two partially occupied H_2O (66% and 39% occupied) present in the asymmetry unit of the unit cell. The 39% occupied water molecule near the inversion centered was modeled without its hydrogen atoms. One of the two H-atoms of the 66% occupied water didn't have an H-atom acceptor within the rigid model distance as the H-acceptor. All the alerts level B, C and G warning are either because of disordered and partially occupied solvents (water, acetonitrile and chloroform) or the disordered SO_3CF_3 anions. All possible hydrogen bonding distances and angles are given in Table 7. The DFIX, SADI, SIMU, DELU, and EADP, restraints were to stabilize the final refinement of the atomic positions. Although the distribution of intensities (E^2-1 = 0.705) indicated a possible racemic twin P1 chiral space group, the refinement using the racemic twin P1 space group was highly unstable for most of the solvent molecules giving rise to non-definite positive thermal parameters. The final structure model was refined using the P-1 space group.

Atomic coordinates, isotropic and anisotropic displacement parameters of all the non-hydrogen atoms were refined by means of a full matrix least-squares procedure on F^2. The H-atoms were included in the refinement in calculated positions riding on the atoms to which they were attached, except the two NH-group hydrogen atoms were refined unrestrained. The refinement converged at R1 = 0.0293, wR2 = 0.0774, with intensity, I>2□(I). The largest peak/hole in the final difference map was 1.675/-0.680 e/$Å^3$. The high electron density peak/hole ratio (2.46) near the Bi-atom was probably due to absorption correction error.

Table 8.25: Crystal data and structure refinement for [(**5.3**)$_2$Bi$_2$](OTf)$_6$:

Empirical formula	$[C_{32}H_{24}N_6O_2]_2[Bi]_2[SO_3CF_3]_6$	
Formula weight	1391.94	
Temperature	100(2) K	
Wavelength	0.71073 Å	
Crystal system	Triclinic	
Space group	P-1 (#2)	
Unit cell dimensions	*a* = 10.5697(3) Å	α = 98.057(1)°.
	b = 13.7043(4) Å	β = 92.112(1)°.
	c = 20.0249(6) Å	γ = 96.452(1)°.
Volume	2849.71(14) Å^3	
Z	2	
Density (calculated)	1.622 Mg/m^3	
Absorption coefficient	3.433 mm^{-1}	
F(000)	1366	
Crystal size	0.35 x 0.17 x 0.07 mm^3	
Theta range for data collection	1.51 to 27.48°.	
Index ranges	$-13<=h<=13$, $-17<=k<=17$, $-25<=l<=25$	
Reflections collected	68323	
Independent reflections	13040 [R_{int} = 0.0256]	
Completeness to θ = 27.48°	99.8 %	
Absorption correction	Semi-empirical from equivalents	
Max. and min. transmission	0.8001 and 0.3770	
Refinement method	Full-matrix least-squares on *F*2	
Data / restraints / parameters	13040 / 849 / 981	
Goodness-of-fit on *I*2	1.077	
Final *R* indices [I>2σ(I)]	*R*1 = 0.0293, *wR*2 = 0.0774	
RI indices (all data)	*R*1 = 0.0328, *wR*2 = 0.0795	
Largest diff. peak and hole	1.675 and -0.680 *e*.Å^{-3}	

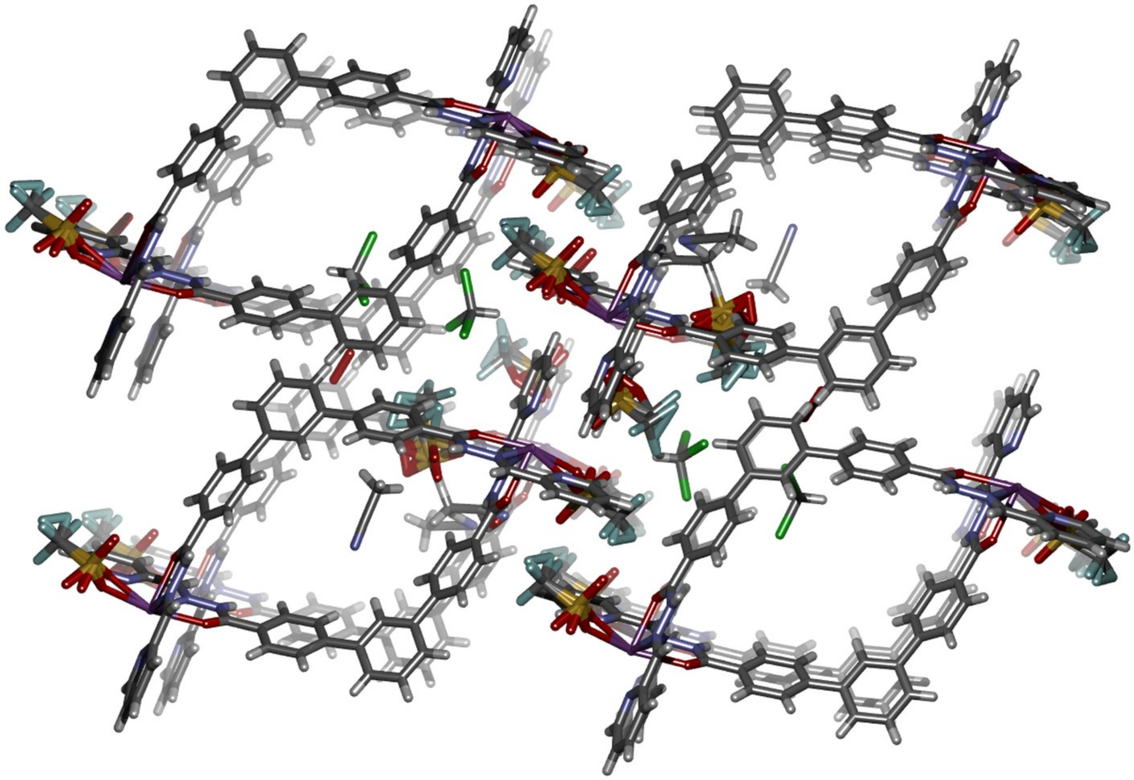

Figure 8.119: Structure of the unit cell of complex [(**5.3**)$_2$Bi$_2$](OTf)$_6$, indicating disordered solvent molecules and triflate counterions.

8.11 References

1) Dewar, M. J. S.; Zoebisch, E. G.; Healy, E. F.; Stewart, J. J. P. "AM1; A new general purpose quantum mechanical molecular model." *J. Am. Chem. Soc*. **1985**, *107*, 3902–3909. Calculations were performed on SPARTAN 06; Wavefunction Inc: Irvine, CA, 2006.

2) Nilsson, M. "The DOSY toolbox: A new tool for processing PFG NMR diffusion data." *J. Magn. Reson*. **2009**, *200*, 296–302.

3) *APEX 2,* version 2010.11-3, Bruker (2010), Bruker AXS Inc., Madison, Wisconsin, USA.

4) *SAINT,* version V7.60A, Bruker (2009), Bruker AXS Inc., Madison, Wisconsin, USA.

5) *TWINABS,* version 2008/2, Bruker (2008), Bruker AXS Inc., Madison, Wisconsin, USA.

6) *SHELXTL,* version 2008/4, Bruker (2008), Bruker AXS Inc., Madison, Wisconsin, USA.

7) *CELL_NOW*, version 2008/2, Bruker (2008), Bruker AXS Inc., Madison, Wisconsin, USA.